AN INTEGRATED WELL PERFORMANCE STUDY FOR SHALE RESERVOIR SYSTEMS – APPLICATION TO THE MARCELLUS SHALE

A Thesis

by

LANDON JESS RISER

Submitted to the Office of Graduate and Professional Studies of
Texas A&M University
in partial fulfillment of the requirements for the degree of

MASTER OF SCIENCE

Chair of Committee,	Thomas A. Blasingame
Committee Members,	Maria A. Barrufet
	Eduardo Gildin
Head of Department,	A. Daniel Hill

December 2013

Major Subject: Petroleum Engineering

ABSTRACT

In this work we focus on the integration of two independent analyses, time-rate analysis and model-based production analysis, as an approach to resolve the uncertainty in estimating ultimate recovery (EUR) for wells in unconventional reservoirs. In particular, we seek to establish a relationship between time-rate parameters from modern time-rate models and the reservoir and completion properties obtained from model-based production analysis. Establishing agreement between these independent analyses will support the practice of EURs in unconventional reservoir systems.

In this work we provide a study of 55 (fifty-five) shale gas wells taken from the Marcellus shale (USA), complete with an integrated workflow of model-based production analysis and time-rate analysis accompanied by a discussion of challenges and methodologies. In addition, we present a study on pressure transient analysis (PTA) for selected pressure buildup tests conducted on a series of Marcellus shale wells. We include field cases complete with orientation, diagnostic, and analysis plots; as well as commentary on the observed behavior of the pressure transient tests themselves and what these pressure buildup tests may yield with regard to insight into the well/reservoir that production data in isolation cannot provide.

DEDICATION

I dedicate this work to my parents.

ACKNOWLEDGEMENTS

I'd like to thank the chair of my committee, Dr. Tom Blasingame, for his steadfast demand for excellence. I am appreciative of Dr. Maria Barrufet and Dr. Eduardo Gildin for serving as committee members. I owe a special thanks to Viannet Okouma for providing the data used in this study. I acknowledge and appreciate the use of software created by Dave Symmons for a portion of this study.

TABLE OF CONTENTS

Page

ABSTRACT ii

DEDICATION iii

ACKNOWLEDGEMENTS iv

TABLE OF CONTENTS v

LIST OF FIGURES vii

LIST OF TABLES xi

CHAPTER

I INTRODUCTION 1

1.1 Statement of the Problem 1
1.2 Objectives 3
1.3 Validation of Study 3

II LITERATURE REVIEW 12

2.1 Classical Rate-Time Analysis 12
2.2 Modern Rate-Time Analysis 13
2.3 Modern Model-Based Production Analysis 14
2.4 Pressure Transient Analysis of Fractured Wells 14

III RATE-TIME ANALYSIS 16

IV MODEL-BASED PRODUCTION ANALYSIS 28

V INTEGRATION OF PERFORMANCE AND WELL/RESERVOIR METRICS 38

VI PRESSURE TRANSIENT ANALYSIS 48

6.1 High- Frequency Bottomhole Gauge Buildup Analysis 49
6.2 Daily- Measured Surface Gauge Buildup Analysis 55

VII SUMMARY, CONCLUSIONS, AND RECOMMENDATIONS FOR FUTURE WORK 62

7.1 Summary 62
7.2 Conclusions 62
7.3 Recommendations for Future Work 63

NOMENCLATURE 64

REFERENCES 65

APPENDIX A INVENTORY OF WELL AND RESERVOIR DATA 67

APPENDIX B RATE-TIME ANALYSIS 73

APPENDIX C MODEL-BASED PRODUCTION ANALYSIS 129

APPENDIX D PRESSURE TRANSIENT ANALYSIS 158

LIST OF FIGURES

FIGURE Page

1.1 (Log-log Plot): Production data diagnostic plot — inverse productivity index and its Bourdet derivative versus material balance time: Well 21 high permeability case 4

1.2 (Log-log Plot): Production data diagnostic plot — inverse productivity index and its Bourdet derivative versus material balance time: Well 21 low permeability case 5

1.3 (Cartesian Plot): Production history plot — gas flowrate (q_g), cumulative gas production (G_p), calculated bottomhole pressure (p_{wfc}) and high permeability model matches for Well 21 6

1.4 (Cartesian Plot): Production history plot — gas flowrate (q_g), cumulative gas production (G_p), calculated bottomhole pressure (p_{wfc}) and low permeability model matches for Well 21 6

1.5 (Cartesian Plot): Cumulative gas production plot — cumulative gas production (G_p) and high permeability and low permeability model cumulative gas production forecasts 7

1.6 (Log-log Plot): Production data diagnostic plot — Well 9 high permeability model case 8

1.7 (Log-log Plot): Production data diagnostic plot — Well 9 low permeability model case 8

1.8 (Cartesian Plot): Production history plot — gas flowrate (q_g), cumulative gas production (G_p) and calculated bottomhole pressure (p_{wfc}) and high permeability model matches 9

1.9 (Cartesian Plot): Production history plot — gas flowrate (q_g), cumulative gas production (G_p) and calculated bottomhole pressure (p_{wfc}) and high permeability model matches 10

1.10 (Cartesian Plot): Cumulative gas production plot — cumulative gas production (G_p) and high permeability and low permeability model cumulative gas production forecasts 11

3.1 (Log-log Plot): *qDb* plot — gas flow rate (q_g), *D*- and *b*-parameters versus production time and modified hyperbolic model matches for Well 3 17

3.2 (Log-log Plot): *qDb* plot — gas flow rate (q_g), *D*- and *b*-parameters versus production time and power-law exponential model matches for Well 3 18

3.3 (Log-log Plot): *qDb* plot — gas flow rate (q_g), *D*- and *b*-parameters versus production time and modified hyperbolic model matches for Well 4 19

3.4 (Log-log Plot): *qDb* plot — gas flow rate (q_g), *D*- and *b*-parameters versus production time and power-law exponential model matches for Well 4 20

3.5 (Log-log Plot): *qDb* plot — gas flow rate (q_g), *D*- and *b*-parameters versus production time and modified hyperbolic model matches for Well 5 21

3.6 (Log-log Plot): *qDb* plot — gas flow rate (q_g), *D*- and *b*-parameters versus production time and power-law exponential model matches for Well 5 22

FIGURE Page

3.7 (Log-log Plot): *qDb* plot — gas flow rate (q_g), *D*- and *b*-parameters versus production time and modified hyperbolic model matches for Well 6 23

3.8 (Log-log Plot): *qDb* plot — gas flow rate (q_g), *D*- and *b*-parameters versus production time and power-law exponential model matches for Well 6 24

3.9 (Log-log Plot): *qDb* plot — gas flow rate (q_g), *D*- and *b*-parameters versus production time and modified hyperbolic model matches for Well 7 25

3.10 (Log-log Plot): *qDb* plot — gas flow rate (q_g), *D*- and *b*-parameters versus production time and power-law exponential model matches for Well 7 26

4.1 (Log-log Plot): Production data diagnostic plot — inverse productivity index and its Bourdet derivative versus material balance time: data and model matches for Well 1 28

4.2 (Log-log Plot): Production data diagnostic plot — inverse productivity index and its Bourdet derivative versus material balance time: data and model matches for Well 2 29

4.3 (Log-log Plot): Production data diagnostic plot — inverse productivity index and its Bourdet derivative versus material balance time: Well 1 and Well 2 comparison 30

4.4 (Log-log Plot): Production data diagnostic plot — inverse productivity index and its Bourdet derivative versus material balance time: Well 2 "normalized" to Well 1 31

4.5 (Log-log Plot): Production data diagnostic plot — inverse productivity index and its Bourdet derivative versus material balance time: Well 15 and Well 18 comparison 32

4.6 (Log-log Plot): Production data diagnostic plot — inverse productivity index and its Bourdet derivative versus material balance time: Well 15 "normalized" to Well 18 33

4.7 (Log-log Plot): Production data diagnostic plot — inverse productivity index and its Bourdet derivative versus material balance time: Wells 39-42 "normalized" to Well 43 34

4.8 (Log-log Plot): Production data diagnostic plot — inverse productivity index and its Bourdet derivative functions: data and model matches for Well 35 35

4.9 (Log-log Plot): Production data diagnostic plot — inverse productivity index and its Bourdet derivative: data and model matches for Well 36 36

4.10 (Log-log Plot): Production data diagnostic plot — inverse productivity index and its Bourdet derivative: data and model matches for Well 37 36

5.1 (Cartesian Plot): Formation permeability as a function of modified hyperbolic rate-time model *b*-parameter — a sample of 30 wells 39

5.2 (Cartesian Plot): EUR comparison crossplot — EUR from modified hyperbolic rate-time model versus EUR from model-based production analysis 40

5.3 (Histogram): Modified hyperbolic *b*-parameter — Distribution of *b*-parameter values from 30 well sample 41

FIGURE Page

5.4 (Histogram): Model-based analysis permeability values — Distribution of permeability values from model-based production analysis of 30 well sample 42

5.5 (Histogram): EUR values — Distributions of EUR values from modified hyperbolic model and model-based production analysis: 30 wells 43

5.6 (Cartesian Plot): EUR comparison crossplot — EUR from the power-law exponential rate-time model versus EUR from model-based production analysis 44

5.7 (Histogram): Power-law exponential *n*-parameter — Distribution of *n*-parameter values from 30 well sample 45

5.8 (Histogram): Power-law exponential $\check{D}_i$-parameter — Distribution of the logarithm of the $\check{D}_i$ -parameter values from 30 well sample 45

5.9 (Semi-log Plot): Power-law exponential model parameters — exponential relationship between the $\check{D}_i$ -parameter and *n*-parameter: 30 well sample 46

5.10 (Histogram): EUR values — Distributions of EUR values from the power-law exponential model and model-based production analysis: 30 wells 47

6.1 (Log-log Plot): Pressure buildup diagnostic plot — pseudopressure drop and Bourdet derivative of pseudopressure drop functions for Well 9 49

6.2 (Log-log Plot): Production data diagnostic plot — inverse productivity index and its Bourdet derivative versus material balance time: data and model matches for Well 9 50

6.3 (Log-log Plot): Pressure buildup diagnostic plot — pseudopressure drop and Bourdet derivative of pseudopressure drop functions for Well 49 52

6.4 (Log-log Plot): Production data diagnostic plot — inverse productivity index and its Bourdet derivative versus material balance time: data and model matches for Well 49 53

6.5 (Log-log Plot): Combination diagnostic plot — pressure buildup and production data diagnostic curves for Well 49 with a unique model 54

6.6 (Log-log Plot): Pressure buildup diagnostic plot — pseudopressure drop, Bourdet derivative of pseudopressure drop and primary pressure derivative functions for Well PBU1 55

6.7 (Log-log Plot): Pressure buildup diagnostic plot — high-frequency bottomhole gauge and daily surface gauge comparison for Well 9 56

6.8 (Log-log Plot): Pressure buildup diagnostic plot — high-frequency bottomhole gauge and daily surface gauge comparison for Well 49 57

6.9 (Log-log Plot): Pressure buildup diagnostic plot — high-frequency bottomhole gauge and daily surface gauge comparison for Well PBU1 57

FIGURE Page

6.10 (Log-log Plot): Pressure buildup diagnostic plot — daily surface pressure buildup response and model matches with parameters from production diagnostic analysis for Well 1 58

6.11 (Log-log Plot): Pressure buildup diagnostic plot — daily surface pressure buildup response and model matches with parameters from production diagnostic analysis for Well 2 59

6.12 (Log-log Plot): Pressure buildup diagnostic plot — daily surface pressure buildup response: comparison of Well 1 and Well 2 60

6.13 (Log-log Plot): Combination diagnostic plot — pressure buildup and production data diagnostic curves for Well 10 with a diagnostic flow regime lines 61

LIST OF TABLES

TABLE		Page
3.1	Three modified hyperbolic model forecast scenarios with unique D_{limit} values and the corresponding EUR values for Well 3	17
3.2	Modified hyperbolic model analysis results from wells 3 through 7	26
3.3	Power-law exponential model analysis results for wells 3 through 7	27
4.1	Key flow parameters from matched models of Wells 1 and 2	29
4.2	EUR values and key flow parameters from matched models of Wells 39-43	34
6.1	Key flow parameters in production drawdown and pressure buildup models of Well 9	51
6.2	Key flow parameters in production drawdown and pressure buildup models of Well 49	53
6.3	Key flow parameters in the model matching both the pressure buildup and production diagnostic data of Well 49	54

CHAPTER I
INTRODUCTION

1.1 Statement of the Problem

Unconventional reservoir systems (*i.e.,* shale gas/oil, tight gas sands, and coalbed methane) have recently emerged as an integral and perhaps dominant resource in the global energy supply. An essential feature of many of these unconventional systems is their typically vast size, which is helpful in the acquisition of land and later in development planning. However; because of the ultra-low permeabilities of these large hydrocarbon accumulations the wells used to exploit these reservoirs must be stimulated with multiple hydraulic fractures along a horizontal wellbore. Multi-fracture horizontal wells are believed to have made the development of unconventional reservoirs economically viable; and at present, we recognize that this is essentially our only mechanism for exploiting unconventional (ultra-low permeability) resources. Given only this degree of freedom in the well completion, we have to accept considerable uncertainty in our ability to optimize production from such reservoir systems.

The necessity of stimulating the rock to increase flux area brings with it complications in analyzing the flow response. Not surprisingly, the well completion-related parameters for a horizontal multi-fractured well (x_f, n_f, F_c) must be accounted for in model-based analysis. Non-uniqueness in estimating well and formation properties presents a challenge in describing the well/reservoir with any degree of certainty. Given the interdependence of some parameters, it is extremely difficult to establish a unique set (or combination) of parameters for modeling a given interval of well performance. Certain flow regimes (*e.g.*, linear flow and compound linear flow) while often quite robust, depend on combinations of parameters such that the determination of an individual parameter (*e.g.*, fracture half-length or permeability) become impossible to distinguish in isolation. Present practices include considering "sensitivity cases" where multiple groups of parameters are modeled in an effort to establish "bounds" on a particular variable. Given an approach such as using sensitivity cases, we will continue to observe differences in performance predictions and recovery.

Time-rate (or decline curve) analysis has long been a staple of the petroleum industry used for obtaining estimated ultimate recovery (EUR). Modern time-rate relations have been developed for use in unconventional reservoirs — when applied using diagnostics, these time-rate relations can be useful tools for EUR. These new time-rate models are empirical and are therefore independent of a physical model. Being empirical, these relations are often applied as "best fit" models, which (while simplistic) lends no rigor to the process of forecasting and prediction of reserves.

One pitfall of time-rate analysis is the need for smooth data with minimal interruptions — as an aside; time-rate-pressure analyses (*i.e.*, reservoir model-based analyses) are more tolerant (as these methods combine rates and pressures), but this approach requires a reference model for the analysis/interpretation process — which also leads to uncertainty. In the time-rate analysis approach, we strongly recommend the use of the "diagnostic" approach of where $D(t)$ and $b(t)$ parameter functions are computed for each time point. This approach requires numerical differentiation to estimate the $D(t)$ and $b(t)$ parameter functions, where said differentiation is not tolerant of erratic production rate data. Data editing is used to minimize the effect of erratic data on the $D(t)$ and $b(t)$ functions, but even the best editing cannot resolve a highly erratic data set.

In these cases with highly erratic production histories; we propose that model-based interpretation/analysis be used. We will demonstrate that reasonably high resolution diagnostic plots can be obtained using time-rate-pressure data, even for cases with highly erratic flowrate data. In our work we utilize a workflow of production data "diagnostic" plots consisting of rate-normalized pseudopressure and the Bourdet derivative of rate-normalized pseudopressure versus material balance time (t_e) on log-log scale. This plot displays the data in a form analogous to a constant-rate solution and allows for an estimate of well/reservoir parameters in addition to revealing the dominant flow regimes.

The two data functions shown on the "log-log" diagnostic plots are given by the following relations:

$$I(t_e) = \frac{1}{t_e}\int_0^{t_e} \frac{m(p_i) - m(p_w(\tau))}{q_g(\tau)} d\tau \quad \text{..... Integral of rate-normalized pseudopressure}$$

$$I'(t_e) = \frac{\partial I(t_e)}{\partial \ln(t_e)} \quad \text{..... Bourdet derivative of the integral of rate-normalized pseudopressure}$$

In our work, we include a chapter on pressure-transient analysis (PTA), which includes pressure buildup tests obtained from a subset of wells in this study. We will exhibit how non-uniqueness is a major issue in determining well and reservoir properties using model-based analysis, while acknowledging the diagnostic (*i.e.,* interpretative) aspects of the analysis. We examine the differences in results and considerations given for production and pressure transient analyses. We note that the analysis of pressure transient data is not a direct method for determining *EUR* (and certainly this approach would never be valid in ultra-low permeability reservoirs). However; the diagnostics afforded to us by PTA allow us to compare and contrast different features when compared to production analysis, and we may be able to establish certain flow regimes with more certainty.

1.2 Objectives

The objectives of this work are:

- To present a specialized workflow for modern dynamic data analyses applied to production history data obtained from the Marcellus shale (USA).
- To discuss the challenges encountered in the analysis of well performance from ultra-low permeability shale reservoirs.
- To demonstrate a correlation or "tuning" concept for the integration of results obtained from time-rate (decline curve) analysis along with results obtained from rigorous model-based analyses (*i.e.*, time-rate-pressure analyses).
- To address the void in the literature of modern pressure transient analysis in shale reservoirs with illustration and discussion of a selection of field cases.

1.3 Validation of Study

In this section we demonstrate using illustrative examples the non-uniqueness of model-based production analysis in ultra-low permeability shale reservoirs. Horizontal multi-fractured wells present a complex physical inflow system that is difficult to characterize mathematically. The analyst has at his disposal two dynamic data streams (flowrate and pressure) that must be used in conjunction with the many static subsurface parameters. These dynamic data are measured at a single point along the flow stream – often at a great distance from the sandface. This becomes increasingly problematic when attempting to characterize the subsurface system that produces these two data streams since the response at the point of measurement (gauge) is the combined response of a collection of many individual responses in the form of multiple discrete fractures.

The predominant properties that govern flow in horizontal multi-fractured shale wells are permeability, fracture half-length, and to a lesser extent fracture conductivity. Analytical models, particularly multi-fracture horizontal models, do not discriminate between permeability and flux area as components of flow capacity. This is particularly true in transient flow where we often see the diagnostic signatures of linear or bilinear flow as straight, sloped lines on log-log scale. A well can be matched, within limits, with a high permeability and low flux area, or a lower permeability and higher flux area. It is the reconciliation of these governing flow properties that is key in creating an accurate model that can be forecasted and can produce a reliable *EUR* value.

We begin with an illustrative example of a well matched with two individual models: a "high" permeability case and a "low" permeability case. The diagnostic plot of the high permeability model match is presented in **Fig. 1.1**.

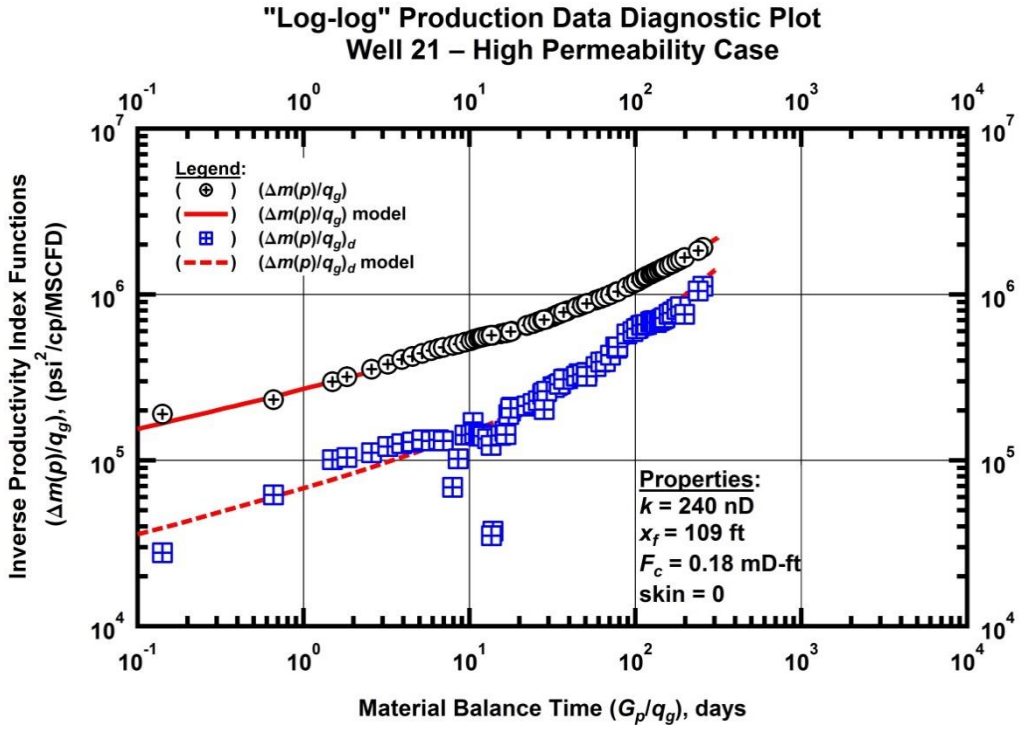

Figure 1.1 — (Log-log Plot): Production data diagnostic plot — inverse productivity index and its Bourdet derivative versus material balance time: Well 21 high permeability case.

The diagnostic plot for the "low" permeability case is presented in **Fig. 1.2**. Examining Figs. 1.1 and 1.2 we find little difference in the quality of the match of the models with the data. The early-time behavior of the low-permeability case model suggests a skin effect, considering the prescribed skin factor value required to match the data. The low-permeability model has a higher fracture half-length and higher fracture conductivity to account for the lost flow capacity from a lower formation permeability. It is worth noting that the flow capacity is effectively matched by both models.

To further illustrate our point, we present the corresponding production "history plots" for the respective high and low permeability cases. These plots are shown in **Figs. 1.3** and **1.4**. These plots show the matches for flowrate as a function of pressure ($q_g[p_{wf}]$), pressure as a function of flowrate ($p_{wf}[q_g]$), and cumulative production as an integral function of rate versus time based on the prescribed analytical models. This serves to further validate the notion that non-uniqueness is a real issue in the analysis of ultra-low permeability reservoir systems produced from multi-fractured horizontal wells. The ultimate goal in well performance analysis is to obtain a high level understanding of the nature of the flow behavior so that confidence can be had in forecasting a model and obtaining a reliable *EUR* value. We depict in **Fig. 1.5** a plot of cumulative gas production from Well 21 and the 30 year forecasted cumulative

production from the high and low permeability cases. We assume a constant bottomhole pressure for the forecast.

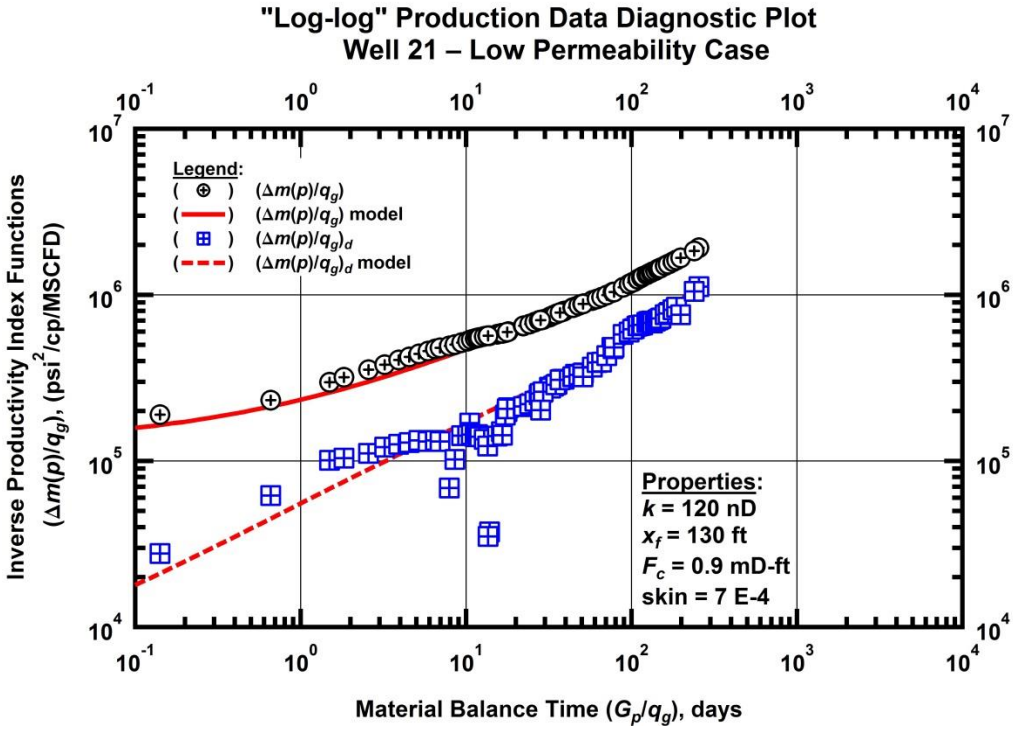

Figure 1.2 — (Log-log Plot): Production data diagnostic plot — inverse productivity index and its Bourdet derivative versus material balance time: Well 21 low permeability case.

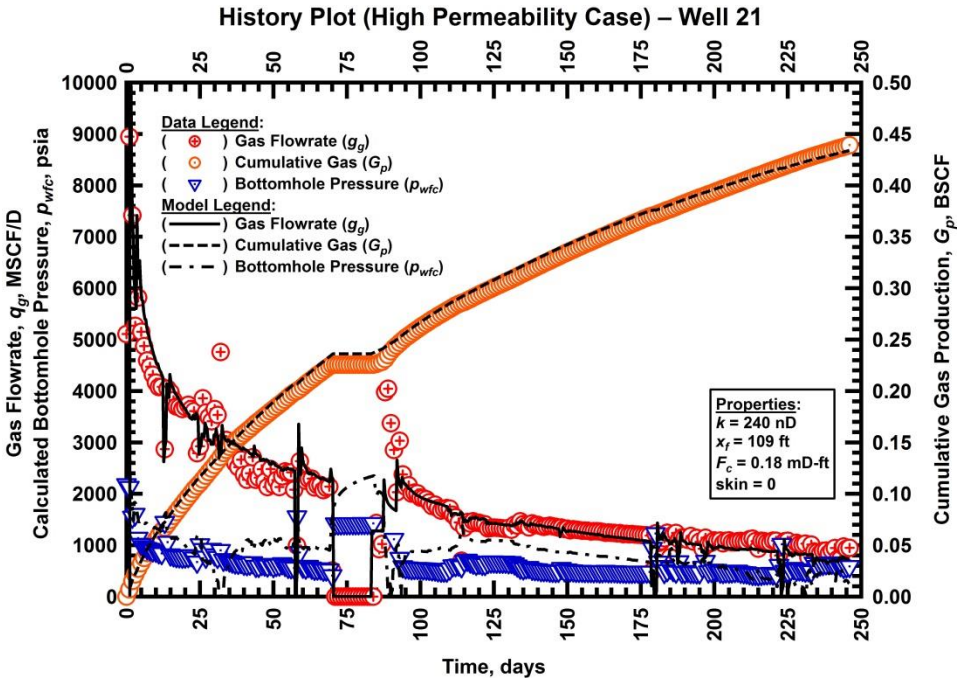

Figure 1.3 — (Cartesian Plot): Production history plot — gas flowrate (q_g), cumulative gas production (G_p), calculated bottomhole pressure (p_{wfc}) and high permeability model matches for Well 21.

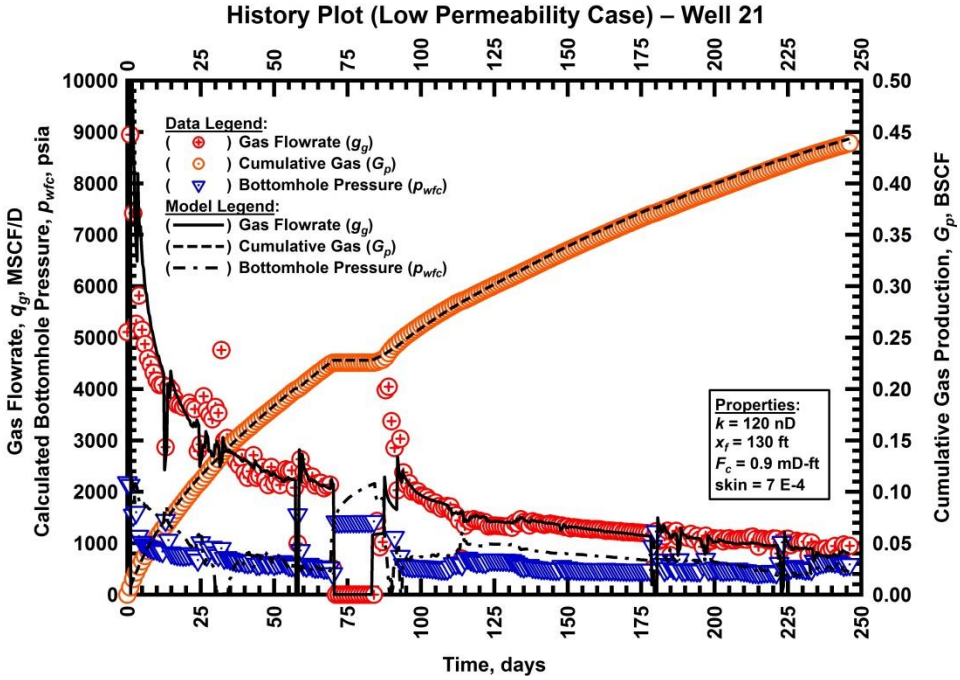

Figure 1.4 — (Cartesian Plot): Production history plot — gas flowrate (q_g), cumulative gas production (G_p), calculated bottomhole pressure (p_{wfc}) and low permeability model matches for Well 21.

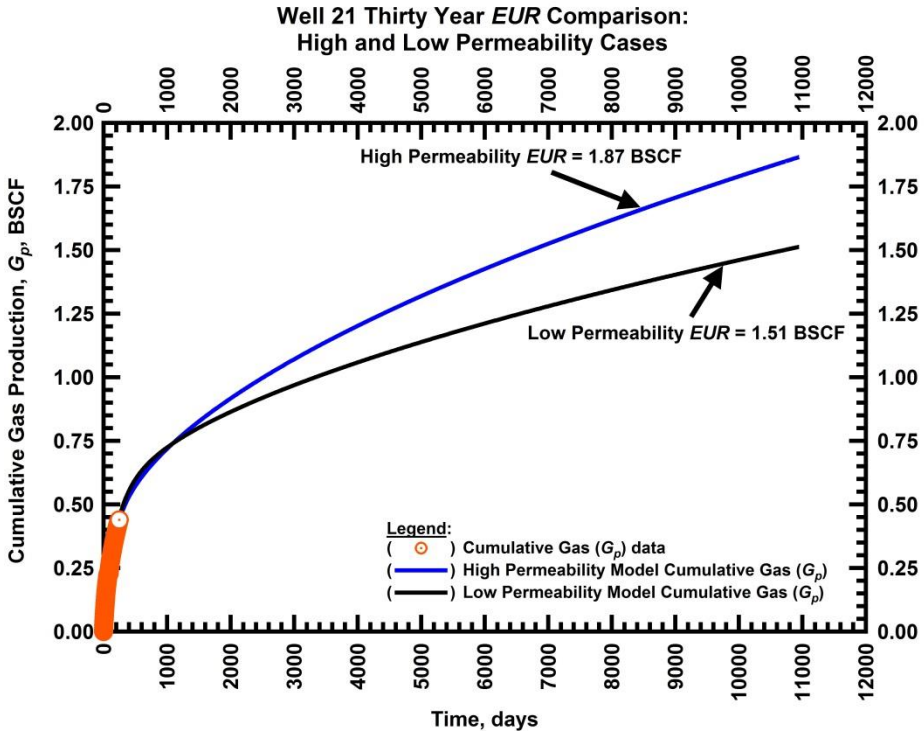

Figure 1.5 — (Cartesian Plot): Cumulative gas production plot — cumulative gas production (G_p) and high permeability and low permeability model cumulative gas production forecasts.

We see two distinct characteristic trends in the two models of Fig. 1.5. The high permeability case has a 24 percent higher EUR than the low permeability case, or a difference in 0.36 BSCF. This is a considerable difference, particularly on a percentage basis. Aside from the difference in EUR in the two models, we see two distinct behaviors in arriving at the ultimate values. While the high permeability model results in a higher EUR, the low permeability model maintains a higher cumulative production for the first 1200 days before taking a lesser final trend. This suggests the greater flux area and fracture conductivity of the low permeability model provide a higher flow capacity initially before giving way to the high permeability case where productivity index stabilizes from a deeper extent of diffusion (lower pressure gradient) resulting from the higher permeability.

We continue this exercise by presenting an additional case that further illustrates the long-term implications of erroneous interpretation stemming from the non-uniqueness of model-based production analysis. We present the diagnostic plots of a "high" permeability and a "low" permeability model used to match the data of Well 9 in **Figs. 1.6** and **1.7**.

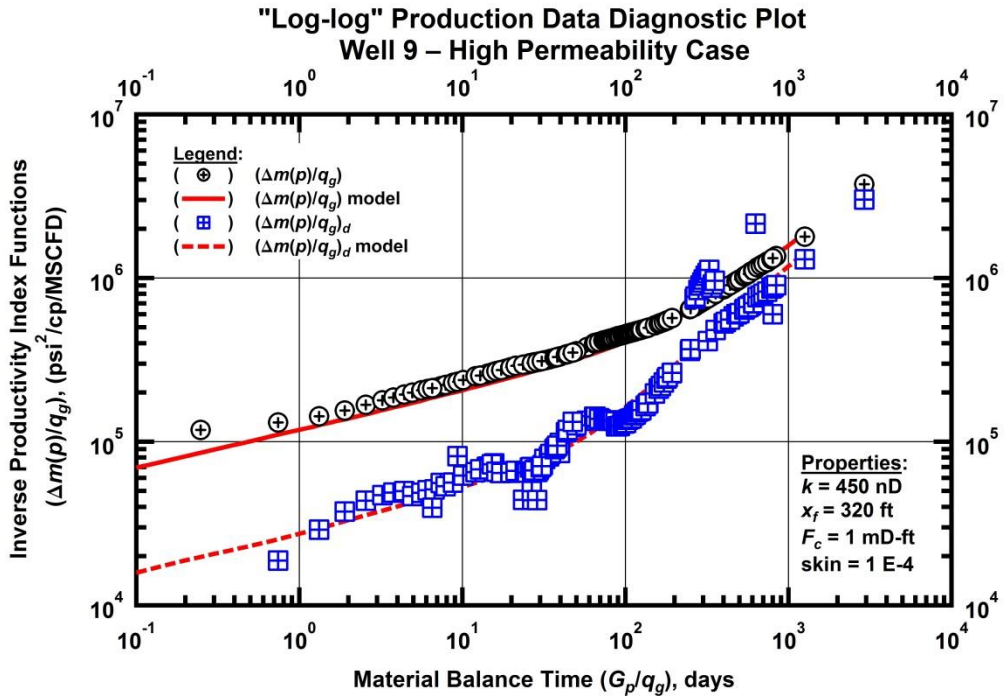

Figure 1.6 — (Log-log Plot): Production data diagnostic plot — Well 9 high permeability model case.

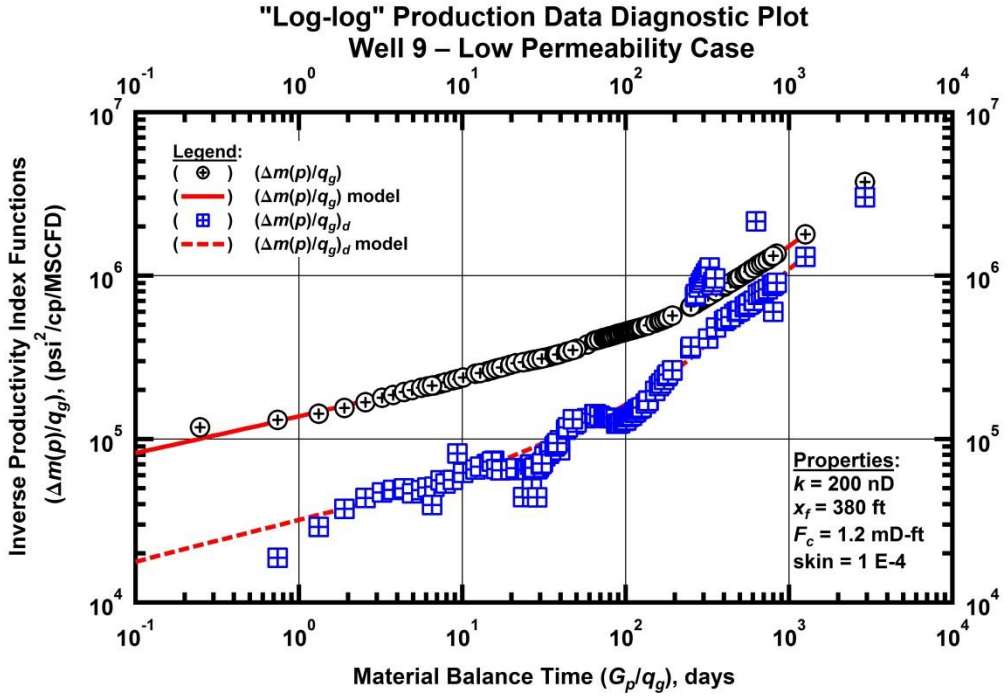

Figure 1.7 — (Log-log Plot): Production data diagnostic plot — Well 9 low permeability model case.

As with the case of Well 21 we see very little difference in the quality of the diagnostic match for Well 9. Both the high-permeability and low-permeability cases are modeled with low fracture conductivity (F_c) values. Both models provide the requisite flow capacity to reconcile flowrate and pressure drop, they just achieve this in different ways.

The "history plots" for these two cases are displayed in **Figs. 1.8** and **1.9**.

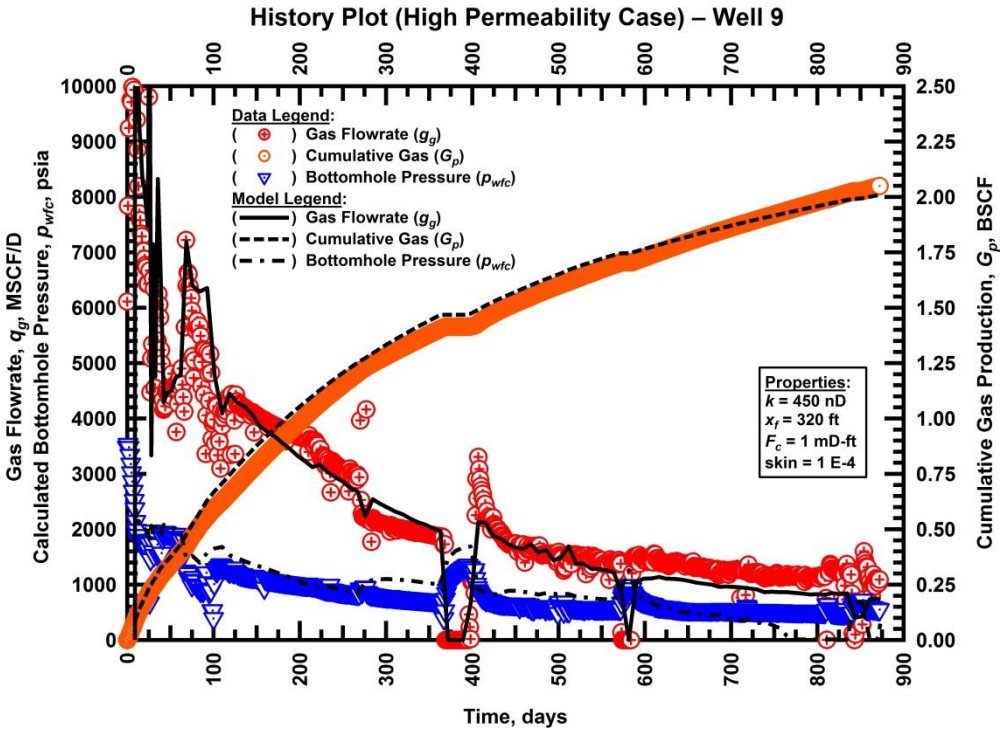

Figure 1.8 — (Cartesian Plot): Production history plot — gas flowrate (q_g), cumulative gas production (G_p) and calculated bottomhole pressure (p_{wfc}) and high permeability model matches.

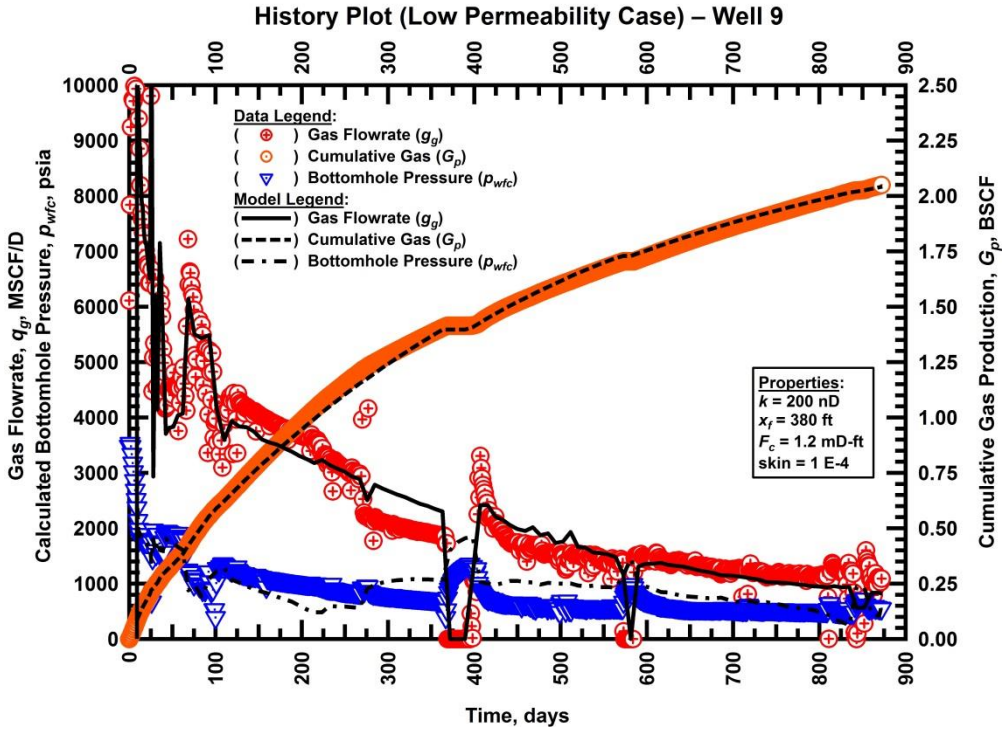

Figure 1.9 — (Cartesian Plot): Production history plot — gas flowrate (q_g), cumulative gas production (G_p) and calculated bottomhole pressure (p_{wfc}) and high permeability model matches.

The thirty-year cumulative gas production forecasts of the high-permeability and low-permeability models are shown in **Fig. 1.10**. The high-permeability model forecasts an EUR of 0.57 BSCF more than the low-permeability case. This is a difference in almost 15 percent. We recall from the previous example (Well 21) that there was a difference in EUR values from the "high" and "low" permeability cases of 0.36 BSCF which was a 24 percent difference percentage wise. This lack of harmony in gross difference versus percentage difference owes to a concept akin to economies of scale. The completion for Well 9 is larger than Well 21 by every measure and we should expect to see a diminishing increase in percentage difference of EUR between models for larger wells. However, difference in the raw numbers is of great import. The difference in 0.57 BSCF and 0.36 BSCF from a mere two wells has strong economic implications when expanded throughout an entire development area.

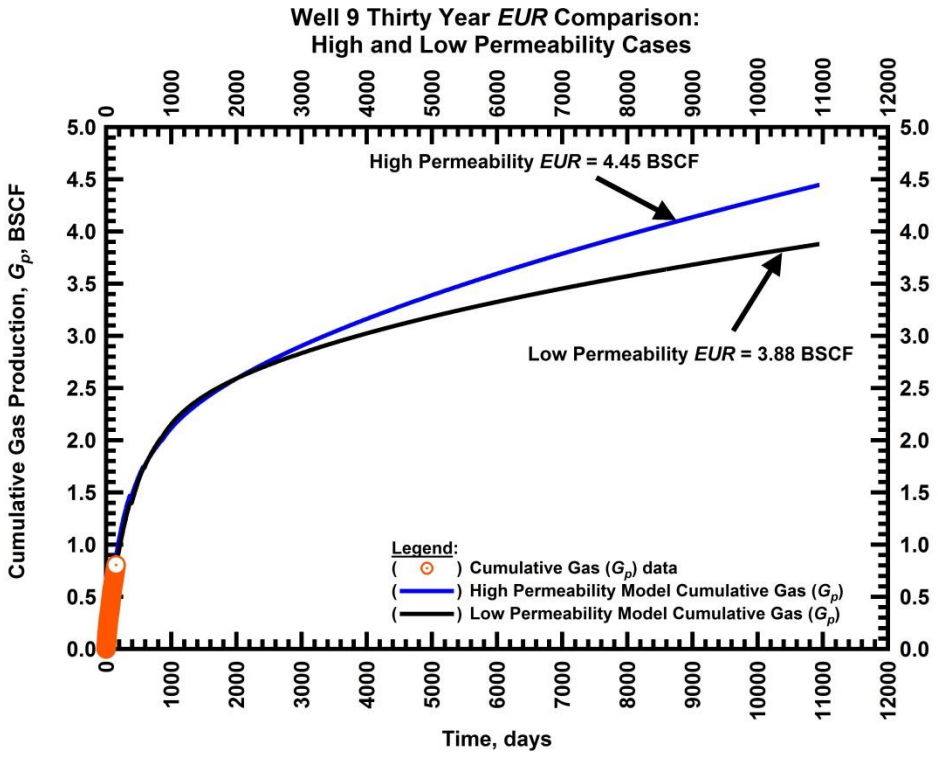

Figure 1.10 — (Cartesian Plot): Cumulative gas production plot — cumulative gas production (G_p) and high permeability and low permeability model cumulative gas production forecasts.

Along these lines, we will demonstrate a "tuning" concept where matrix permeability is modeled as a function of the *b*-parameter from the modified hyperbolic rate-time model. We suggest that there is a fundamental relationship between the rate decline character of a producing well and its bulk matrix permeability. Once a well has surpassed its early time transient behavior and has reached an equilibrium, we should observe a decline related to its permeability. As an example, we propose that a well's permeability can be loosely predicted based on an inverse relationship with its modified hyperbolic *b*-parameter. The lower the *b*-parameter, the more rapid the decline will be and therefore the higher the permeability will be.

CHAPTER II
LITERATURE REVIEW

The literature on the subject of production data analysis (of one form or another) dates back almost a century. The sophistication of the analysis has evolved with the advancement in technology – in a serial manner — each advancement buttressed by those that came before. This chapter will serve to review the publications relevant to this study.

2.1 Classical Rate-Time Analysis

The earliest published work on empirical methods for the estimation of oil and gas reserves was that of Lewis and Beal (1918) where the authors used "percentage decline" and "cumulative percentage" concepts to forecast production. This use of percentages served also as a normalizing technique that allowed for a great number of wells over a large area with a variety of conditions to be compared to one another. Later, Johnson and Bollens (1927) built on the work by Lewis and Beal and developed what they called the "loss-ratio" and its first derivative. Arps (1944) made decline curve analysis famous with the development of the exponential and hyperbolic decline curve relations. These relations were formulated by solving differential equations for cases where the loss-ratio and the loss-ratio derivative were constant, respectively. The definition of the loss-ratio and loss ratio derivative are given by Eqs. 2.1 and 2.2, respectively.

$$\frac{1}{D} = -\frac{q}{dq/dt} \quad \text{..... (2.1)}$$

$$b = \frac{d}{dt}\left[\frac{1}{D}\right] = -\frac{d}{dt}\left[\frac{q}{dq/dt}\right] \quad \text{..... (2.2)}$$

Arps' exponential and hyperbolic decline relations are given by Eq. 2.3 and Eq. 2.4, respectively.

$$q(t) = q_i \exp[-Dt] \quad \text{..... (2.3)}$$

$$q(t) = \frac{q_i}{(1 + bD_i t)^{1/b}} \quad \text{..... (2.4)}$$

Both of these relations are applicable only in the case of boundary-dominated flow. This condition is very limiting for the use in unconventional reservoirs as boundary-dominated behavior is rarely observed in a

timeframe when rate-time analysis is performed. Therefore, using the Arps' relations will lead to erroneous results — often in the form of overestimations.

Fetkovich (1980) introduced type curves combining analytical solutions from infinite and closed reservoir models with the Arps decline curve relations. What resulted was a matching technique similar to the one employed in pressure transient analysis that was applicable to both the transient period of the data and the boundary-dominated period.

2.2 Modern Rate-Time Analysis

Gentry and McCray (1978) showed that the hyperbolic b-parameter can exceed unity for a variety of cases. Using numerical simulation they demonstrated how reservoir heterogeneity (e.g. layered reservoirs) can produce *b*-parameter values greater than one. Before this, it was assumed that the b-parameter must be bounded between 0 and 1. Maley (1985) confirmed the conclusions of Gentry and McCray by analyzing fractured tight-gas wells and observing that *b*-parameter values often exceed 1 in tight gas wells or other wells exhibiting linear flow. Unconventional reservoirs often exhibit periods of transient flow on the order of several years because of their characteristic ultra-low permeabilities. The need for rate-time relations applicable to wells in unconventional reservoirs was addressed by Ilk et al. (2008). The authors developed new empirical relations based on characteristic behavior of rate-time data in unconventional reservoirs. They observed power-law behavior of the *D*-parameter when calculated continuously. This led to the implementation of the power-law exponential (PLE) rate-time function. The authors believe that the PLE function adequately represents the transient and transition flow regimes exhibited in the production data of unconventional reservoirs. For reference, the PLE relation is given as:

$$q(t) = q_i \exp\left[-D_\infty t - D_i t^n\right] \quad \text{..... (2.5)}$$

Robertson (1988) observed that it was common to observe hyperbolic behavior early in the life of a well followed by an exponential "tail" for the later stages of production. This led to the development of the modified hyperbolic rate-time relation. The modified hyperbolic relation is a piecewise function that imposes a lower limit for the decline parameter, *D*, below which the function switches from hyperbolic decline to exponential decline. The modified hyperbolic relation is given below as:

$$q(t) = \begin{cases} \dfrac{q_i}{[1+bD_i t]^{\frac{1}{b}}}, D > D_{\lim it} \\ q_i \exp\left[-D_{\lim it} t\right], D \le D_{\lim it} \end{cases} \quad \text{..... (2.6)}$$

The piecewise nature of the modified hyperbolic function serves as a means of avoiding overestimation that can occur from extrapolating a pure hyperbolic function. A shortfall of this relation is that it requires

either a best-guess or considerable experience to determine the value for D_{limit} as it can take years to see a response in the data that indicates a transition in behavior.

2.3 Modern Model-Based Production Analysis

Al-Ahmadi et al. (2010) proposed a procedure to calculate the size of the drainage volume and the flux area of the fracture-reservoir interfaces of multiply-fractured horizontal shale wells. They also commented on an observed "skin effect" often encountered in shale wells that can mask early linear behavior. Aboaba and Cheng (2010) presented a procedure for estimating fracture properties for horizontal wells with multiple transverse fractures. The procedure was based on quantifying the slope of the pseudopressure drop curve when plotted against the square-root of time and implementing it into linear flow equations. Ilk et al. (2011b) attempted to integrate model-based production analysis and rate-time analysis by the use of parametric correlations. They performed rate-time analysis and production analysis independently and then correlated their respective model parameters. The authors noted that the quality of the correlation is highly dependent sample size (number of wells) and data quality.

Ilk et al. (2011c) discussed the challenges involved with analyzing production data in unconventional reservoirs and suggested that production analysis should include multiple independent techniques. They demonstrate their methodology with multiple field examples from a range of unconventional reservoirs. Ilk et al. (2011a) focus on the diagnostic characteristics of unconventional well performance. The authors proposed the use of various rate-time-pressure and rate-time plots, as a means to account for the large degree of uncertainty in unconventional reservoir analysis.

2.4 Pressure Transient Analysis of Fractured Wells

Cinco-Ley et al. (1978) pioneered the analysis of transient analysis of fractured wells. They developed a type-curve matching procedure used to analyze early-time transient pressure data to estimate fracture and formation properties. In addition, the authors demonstrated that the assumption of infinite fracture conductivity is valid when the dimensionless fracture conductivity exceeds 300. Cinco-Ley and Samaniego (1981) discovered the bilinear flow regime and its quarter-slope pressure transient signature. Larson and Hegre (1994) showed that fracture performance depends on both magnitude and distribution of conductivity. Kobaisi et al. (2006) discuss analysis of pressure-transient testing of finite conductivity multiply-fractured horizontal wells. Through the use of a semi-analytical model the authors simulate the sensitivity of fracture properties on the early-time flow regimes. The results of their work suggest that non-Darcy flow, fracture geometry and well location within the formation strongly influence flow convergence and produce flow characteristics unique from vertical well fractures. Cheng (2011) simulated the characteristics of pressure transient response in reservoirs having properties on the order of the Marcellus shale. It was concluded that both gas desorption and stress-dependent fracture conductivity

have negligible impact on the pseudopressure drop and pseudopressure drop derivative responses. Mayerhofer et al. (2011) integrated microseismic fracture mapping, diagnostic injection tests, bottomhole pressure gauges, chemical tracer data and post fracture pressure transient analysis in order to gain a better knowledge on fracture effectiveness. Downhole pressure gauge data indicated hydraulic communication between adjacent wells. This was corroborated by microseismic mapping during fracturing operations indicating activity beyond the "halfway" point in adjacent wells.

CHAPTER III
RATE-TIME ANALYSIS

We present a group of associated shale gas wells with analyzed rate-time data. We independently use two "modern" rate-time models, *the modified hyperbolic model* and the *power-law exponential model*, to analyze the production behavior and to forecast production in order to obtain EUR values. The analysis process begins with editing rate data by removing points that deviate from the dominant trend. This is a crucial measure in the analysis of flowrate data as the *D*-parameter and *b*-parameter are calculated from numerical differentiation (Bourdet algorithm) and noise in the data is amplified greatly in these calculations.

Once the rate data has been appropriately edited, we examine the rate data, and calculated *D*-parameter and *b*-parameter data on a log-log coordinate plot called the "*qDb*" plot. For both the modified hyperbolic model and the power-law exponential model we inspect the behavior of the *D*- and *b*-parameter trends and adjust the model parameters so that we match both simultaneously. Once we establish an agreement between the model parameters and the diagnostic parameters of the data (*D* and *b*) we adjust the initial production rate value, q_{gi}, of the model until the rate model matches the rate data. This is the final step in the process for the PLE model. We simply set a forecast schedule — based on a fixed time (30 years) - and we obtain a value for EUR.

For the modified hyperbolic model there is an additional parameter that needs to be resolved before we obtain a EUR value. This parameter is called D_{limit} and it is an imposed lower limit for the *D*-parameter – below which the model switches from hyperbolic to exponential decline. As previously mentioned, this switch in decline behaviors serves to avoid overestimation of EUR that comes from modeling with an unrealistically small decline rate in the latter years of a well's productive life. This additional parameter provides the analyst with great flexibility in the determination of EUR, however the choice of D_{limit} can be problematic when we do not see boundary-dominated behavior in the data and therefore must speculate as to its value. We illustrate the non-uniqueness of applying the D_{limit} parameter to field cases.

In **Fig 3.1** we present a case with 410 days of production data matched with the modified hyperbolic model. This well shows strong linearity in the *D*-parameter and relatively constant *b*-parameter behavior. The rate data is also matched exceedingly well over the entire production period suggesting that the modified hyperbolic model is suitable for modeling this well's decline. However, we are still in transient flow and have not yet observed any boundary influence. As a result, we must speculatively choose a D_{limit} value based on a best guess. For this particular well, the difference between a liberal terminal decline

value (5 percent) and a conservative value (15 percent) is the difference in 1 BCF of EUR over 30 years. We present three potential outcomes from three unique terminal decline values in **Table 3.1**. The second column of Table 3.1 (t^*) is the time at which the model will reach the prescribed D_{limit} value. The higher the value the sooner it will be reached, however this could take several years to observe.

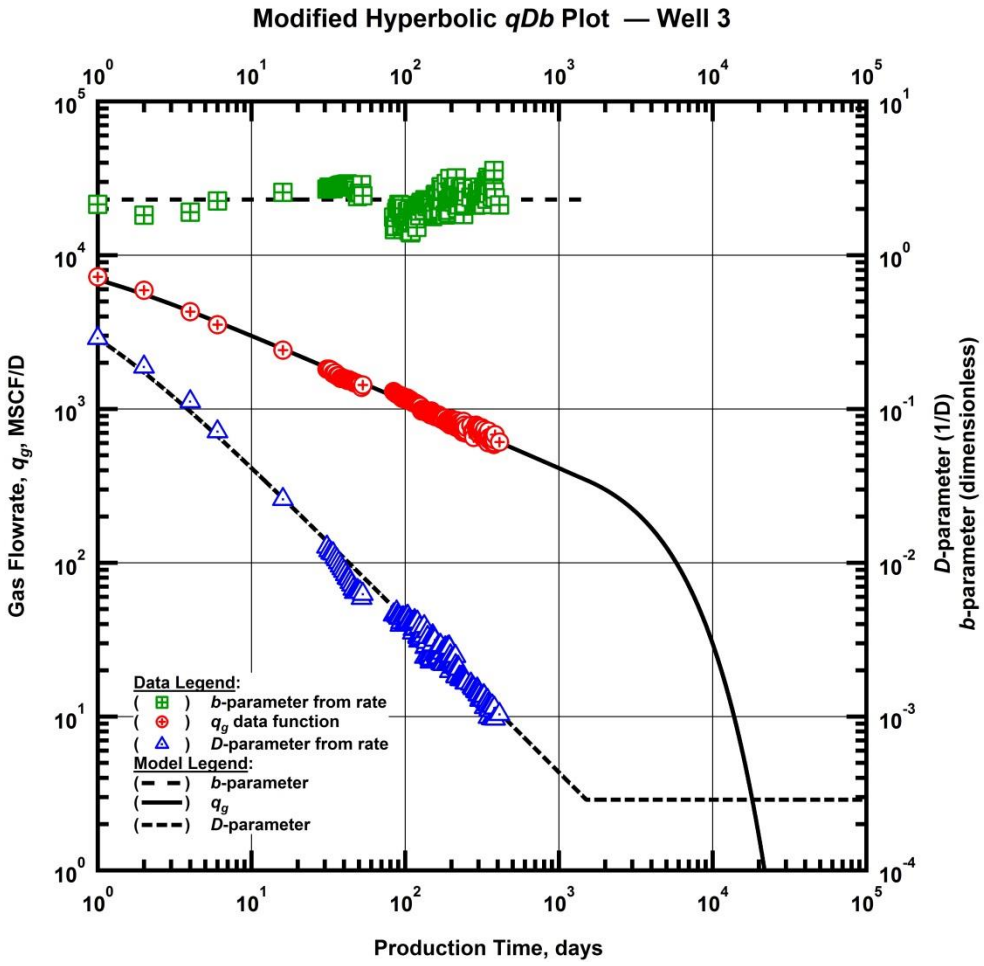

Figure 3.1 — (Log-log Plot): *qDb* plot — gas flow rate (q_g), *D*- and *b*-parameters versus production time and modified hyperbolic model matches for Well 3.

Table 3.1 — Three modified hyperbolic model forecast scenarios with unique D_{limit} values and the corresponding EUR values for Well 3.

D_{limit} (percent)	t^* (years)	*EUR* (BSCF)
5	8.5	2.47
10	4.1	1.93
15	2.67	1.53

A D_{limit} value of 10 percent was used in **Fig. 3.1** which resulted in a EUR of 1.93 BSCF. However, the model-based production analysis EUR was 1.59 BSCF. If a D_{limit} value of 14 percent is used instead of 10 percent then the modified hyperbolic model *EUR* will equal the model-based EUR. It is almost universal in this study for rate-time analysis EUR to be greater than model-based EUR.

In **Fig. 3.2** we have a power-law exponential model match for Well 3. The modified hyperbolic model of **Fig. 3.1** provides a better match of the rate profile of Well 3 despite the *D*-parameter exhibiting power-law straight-line behavior. In addition, the PLE model predicts a higher EUR value than the modified hyperbolic – which is a rare occurrence in this study.

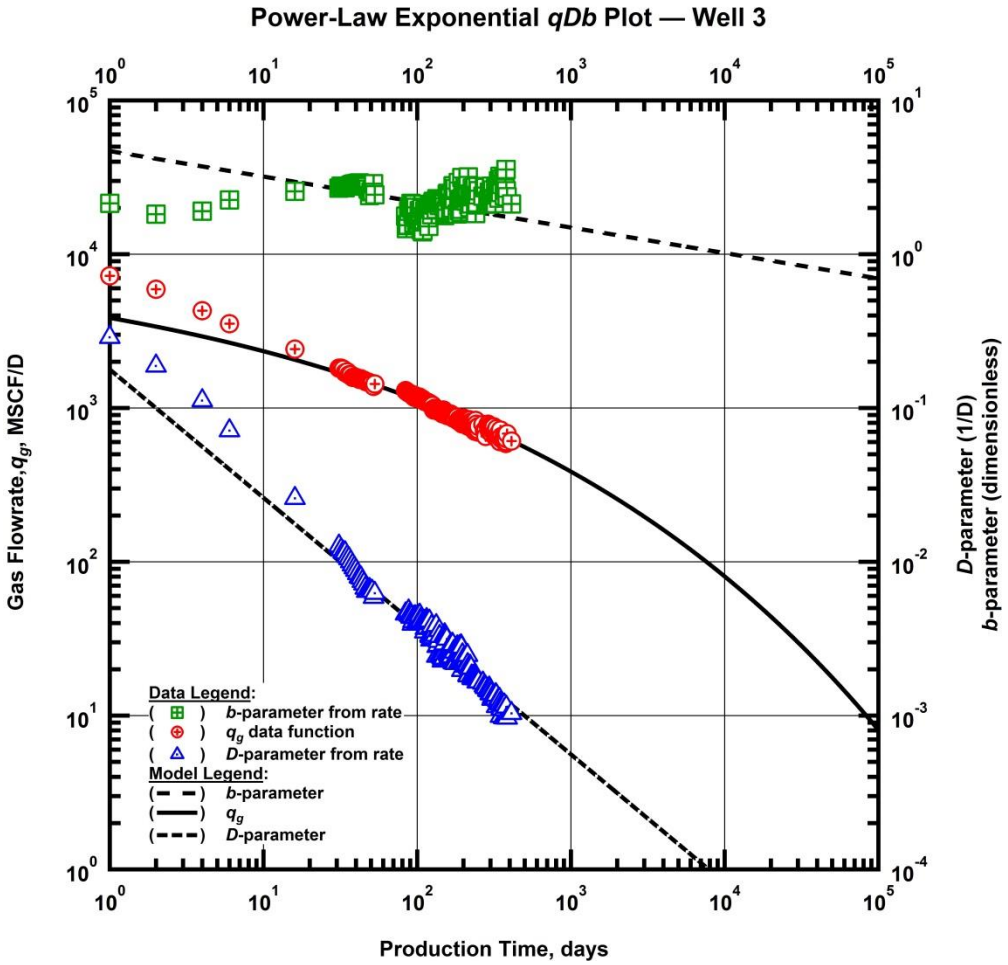

Figure 3.2 — (Log-log Plot): *qDb* plot — gas flow rate (q_g), *D*- and *b*-parameters versus production time and power-law exponential model matches for Well 3.

We present Well 4, a neighboring well to Well 3, in **Fig. 3.3** and observe differences in behavior of the *D*- and *b*-parameters between the two. The *D*-parameter data does not show straight line behavior, but instead shows a relatively low D_i value and a *b* value of 1.9. The resulting modified hyperbolic EUR values for wells 3 and 4 are 1.59 and 2.61 BSCF, respectively. This chasm in EUR is corroborated by a similar difference obtained from model-based production analysis. A D_{limit} of 12.3 percent will forecast a EUR equivalent to the model-based forecast.

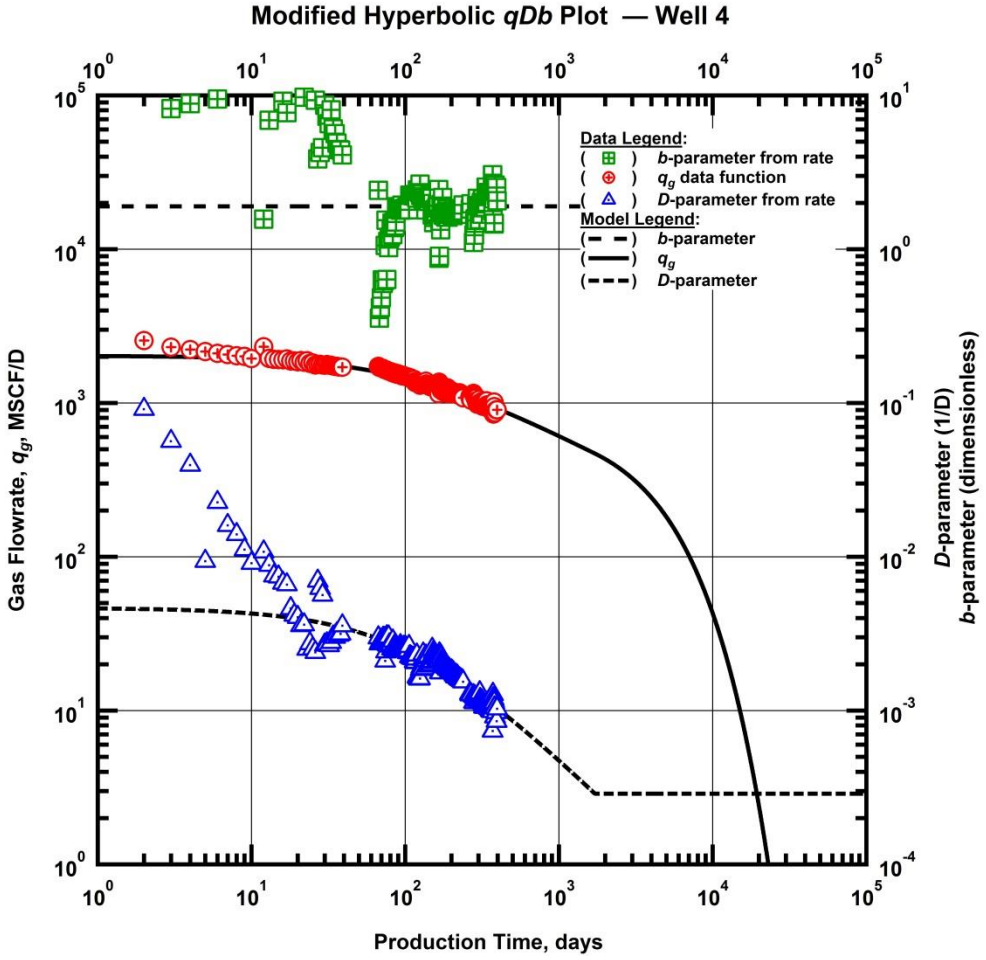

Figure 3.3 — (Log-log Plot): *qDb* plot — gas flow rate (q_g), *D*- and *b*-parameters versus production time and modified hyperbolic model matches for Well 4.

The PLE model match for Well 4 is shown in **Fig. 3.4**. The discontinuity in the data at 50 days is the result of a 10 day shut-in. The data, particularly the *D*-parameter, resume a diagnostic character that we

capture with the straight-line *D*-parameter model. EUR from both rate-time models are very similar for Well 4 and are quite close in value to the model-based EUR.

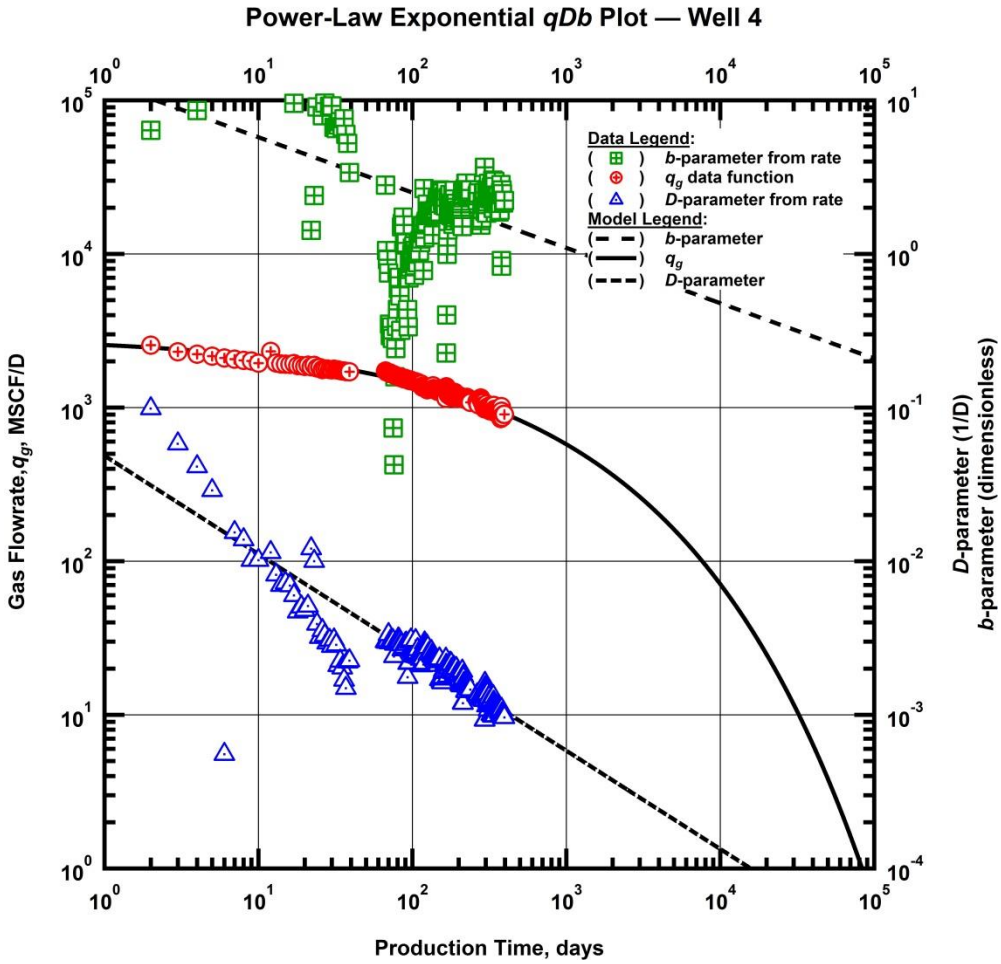

Figure 3.4 — (Log-log Plot): *qDb* plot — gas flow rate (q_g), *D*- and *b*-parameters versus production time and power-law exponential model matches for Well 4.

Well 5, illustrated in **Fig. 3.5** with a modified hyperbolic model match shows hyperbolic behavior in the *D*-parameter beginning at 80 days. This well undergoes several periods of shut-in from 400 days through the end of the history, but the predominant decline character is mostly preserved.

The PLE model match for Well 5 is depicted in **Fig. 3.6**. Both the *D*- and *b*-parameters are matched well with power-law straight lines, indicating that this is an effective model for matching this well. The *D*-parameter data can be effectively matched with either a power-law function or a hyperbolic function for

this well. The *b*-parameter does not approach a constant level until around 200 days. The EUR values from the two models of **Figs. 3.5 and 3.6** are within 4 percent of one another, so the choice of which model to invest more confidence in is less of an issue in this case.

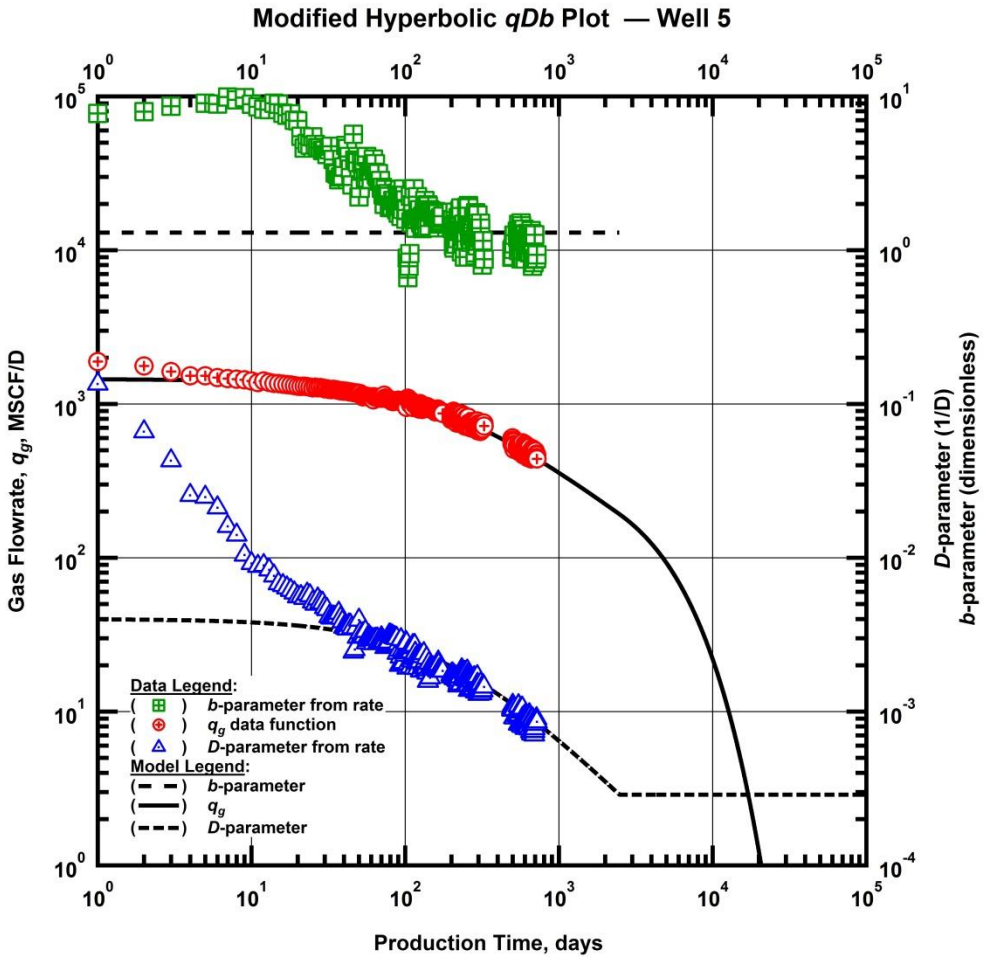

Figure 3.5 — (Log-log Plot): *qDb* plot — gas flow rate (q_g), *D*- and *b*-parameters versus production time and modified hyperbolic model matches for Well 5.

In **Figs. 3.7** and **3.8** we show model matches for Well 6. This well is from the same pad as the previous wells and it shows similar diagnostic behavior to Well 5. In both wells the *b*-parameter steadily decreases with time and eventually drops below 1, which is an indication of boundary-dominated flow. It is for this reason that the power-law exponential model is the optimal model for this particular case.

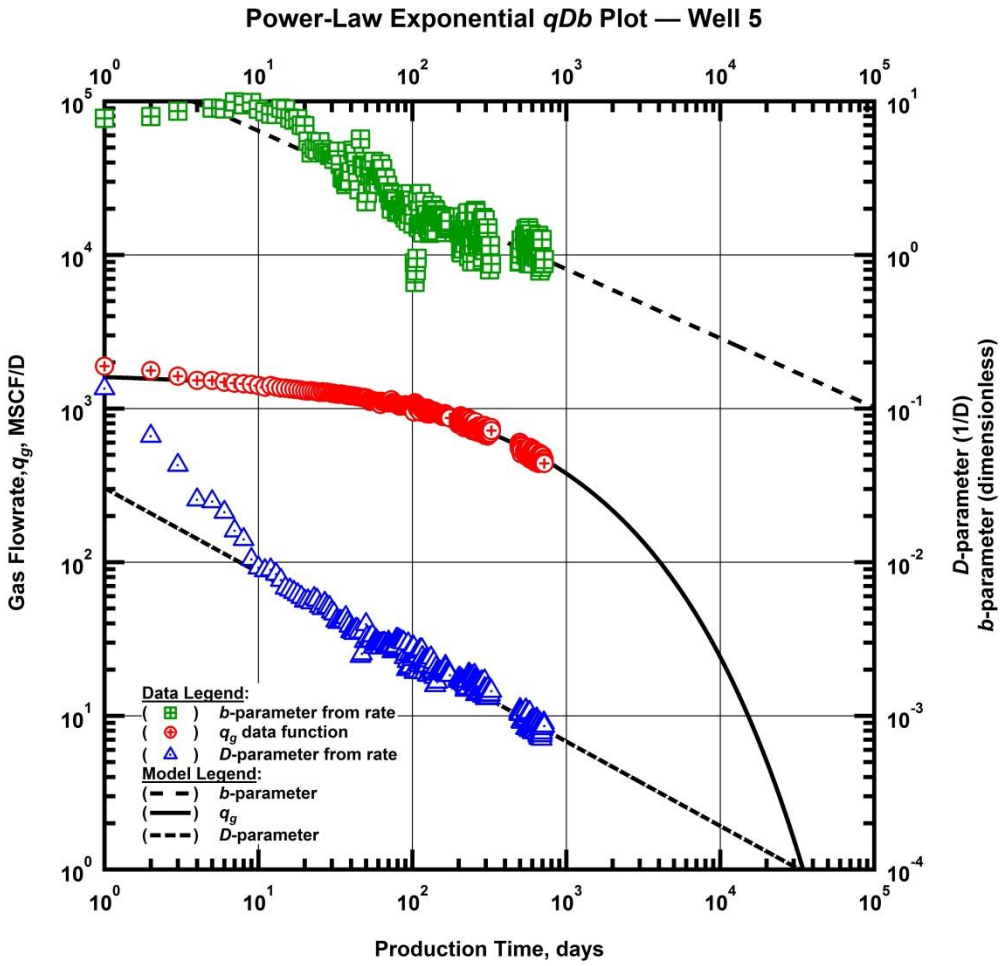

Figure 3.6 — (Log-log Plot): *qDb* plot — gas flow rate (q_g), *D*- and *b*-parameters versus production time and power-law exponential model matches for Well 5.

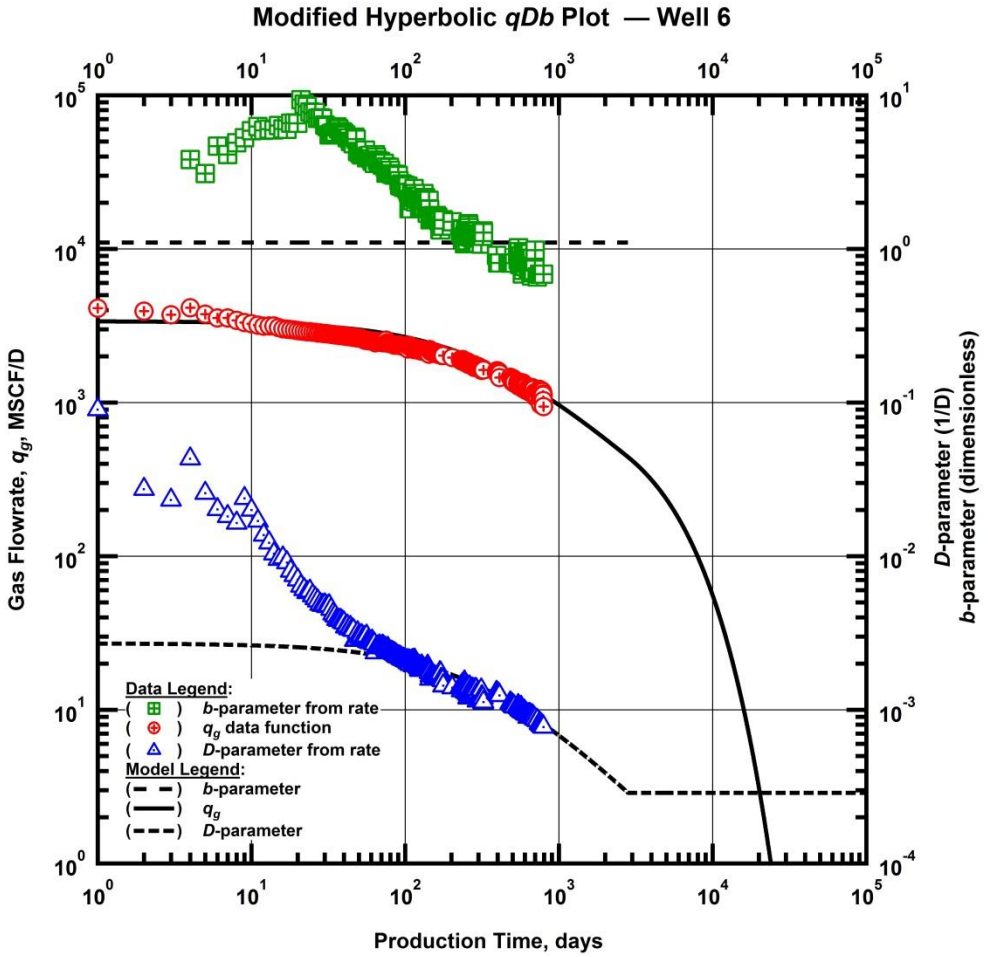

Figure 3.7 — (Log-log Plot): *qDb* plot — gas flow rate (q_g), *D*- and *b*-parameters versus production time and modified hyperbolic model matches for Well 6.

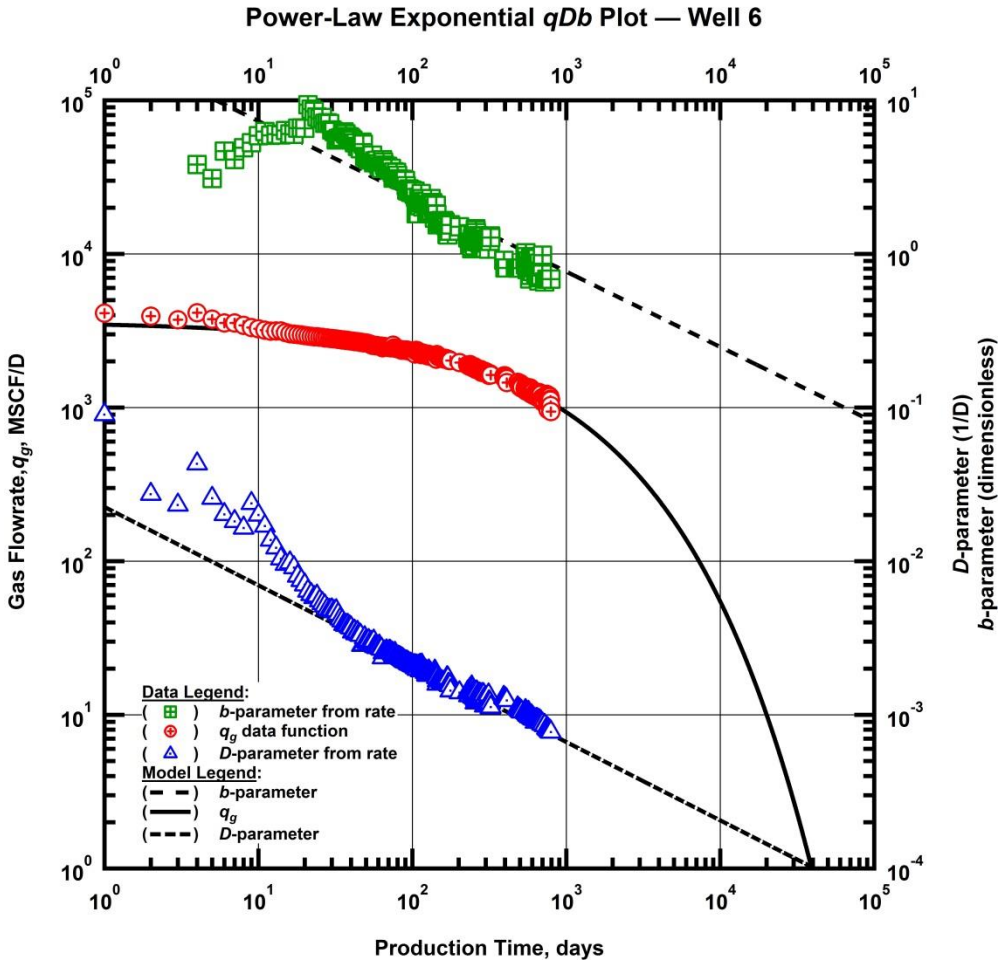

Figure 3.8 — (Log-log Plot): *qDb* plot — gas flow rate (q_g), *D*- and *b*-parameters versus production time and power-law exponential model matches for Well 6.

The model matches for Well 7 are illustrated in **Figs. 3.9** and **3.10**. The behavior of both the *D*- and *b*-parameters is indicative of hyperbolic decline. The *b*-parameter becomes constant after 100 days and the *D*-parameter exhibits curvature resulting from a relatively low D_i value.

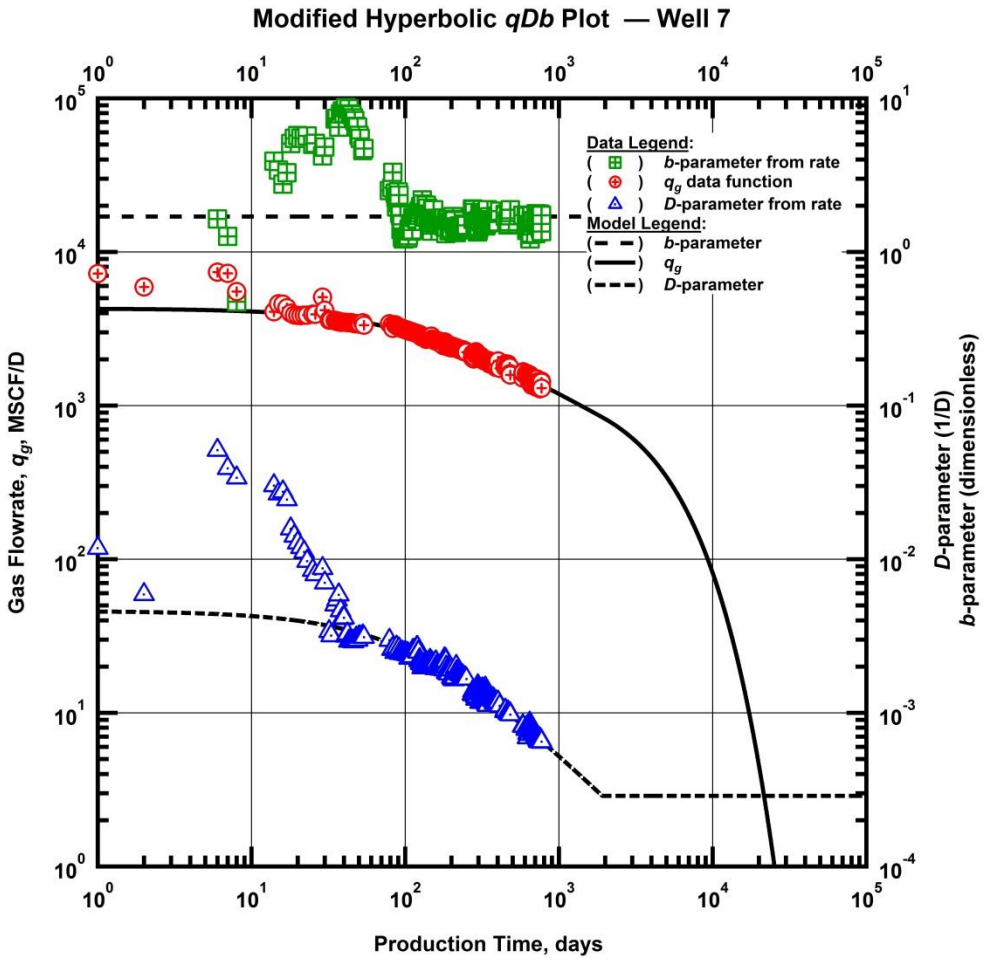

Figure 3.9 — (Log-log Plot): *qDb* plot — gas flow rate (q_g), *D*- and *b*-parameters versus production time and modified hyperbolic model matches for Well 7.

The model parameters used in matching wells 3 through 7 are organized in **Tables 3.2** and **3.3**. For the purposes of this study, when employing the modified hyperbolic model we prescribed a D_{limit} of 10 percent to all wells as a means of consistency as we saw no behavior in the data that suggests using a higher value. We note however that the true value will vary from well to well and that there is potentially a physical phenomenon that governs when such a transition from hyperbolic to exponential type decline would occur.

The power-law exponential model parameter, D_∞, was also zero for all cases in the study. We did not encounter any cases where clear boundary-dominated flow was apparent. Most wells in the study had fewer than three years of production data to analyze. We feel confident that we have reliably evaluated the transient character of these wells with the data available. It is the determination of the onset of boundary-dominated flow that eludes us.

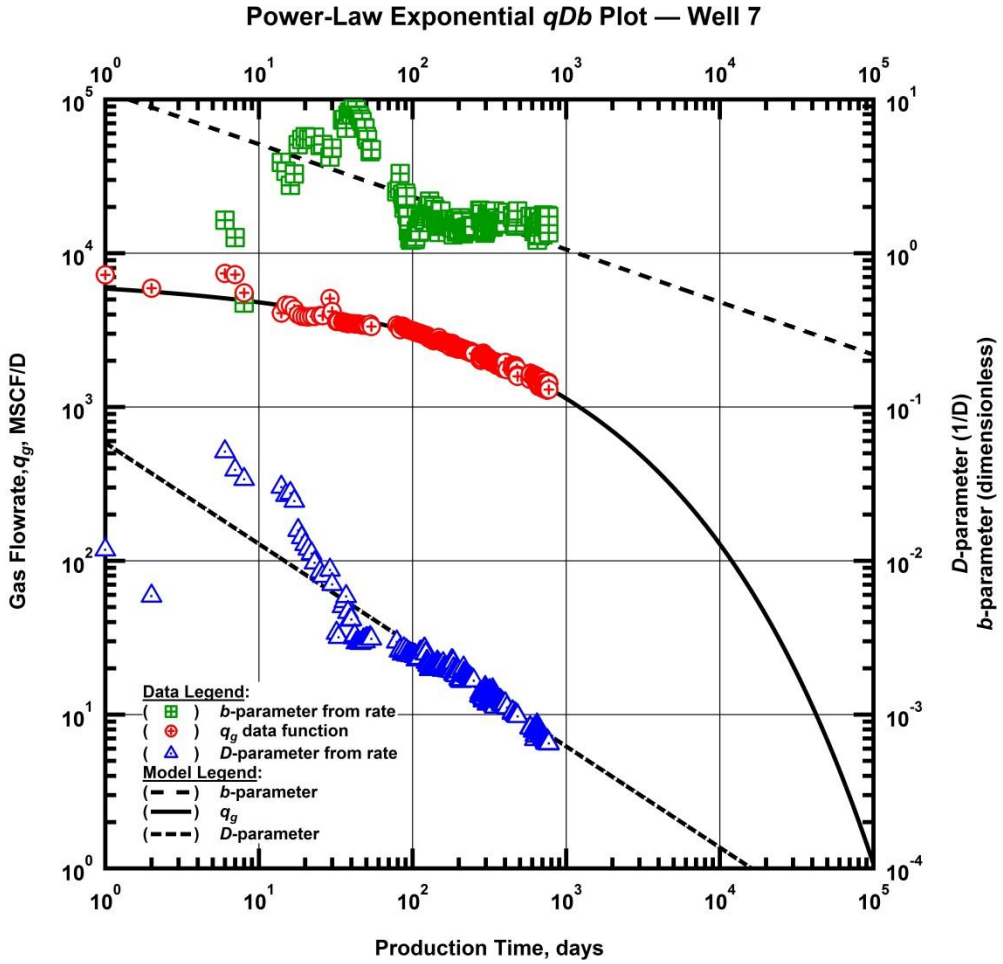

Figure 3.10 — (Log-log Plot): *qDb* plot — gas flow rate (q_g), *D*- and *b*-parameters versus production time and power-law exponential model matches for Well 7.

Table 3.2 — Modified hyperbolic model analysis results from wells 3 through 7.

Well	q_{gi} (MSCF/D)	D_{limit} (percent)	D_i (D^{-1})	b (dimensionless)	EUR_{MH} (BSCF)
3	11,067	10	0.840	2.3	1.93
4	2,029	10	0.00465	1.9	2.88
5	1,684	10	0.00440	1.3	1.86
6	3,080	10	0.00271	1.1	3.91
7	4,282	10	0.00460	1.7	5.44

Table 3.3 — Power-law exponential model analysis results for wells 3 through 7.

Well	q_{gi} (MSCF/D)	n (dimensionless)	$\check{D}_i$ (D^{-1})	D_∞ (D^{-1})	EUR_{PLE} (BSCF)
3	50,541	0.109	2.30	n/a	2.19
4	2,609	0.429	0.0814	n/a	2.31
5	1,715	0.450	0.0675	n/a	1.63
6	3,627	0.490	0.0460	n/a	3.82
7	6,980	0.342	0.1709	n/a	5.17

CHAPTER IV
MODEL-BASED PRODUCTION ANALYSIS

In this chapter we introduce model-based production analysis with illustrative cases of diagnostic flow behavior in the form of rate-normalized pseudopressure plots. We present cases that highlight both the variability of flow characteristics and the aspects common to multi-fractured horizontal wells in shale reservoirs.

We begin with a pair of adjacent wells showing very similar diagnostic behavior. Depicted in **Figs. 4.1** and **4.2** are Wells 1 and 2, respectively. In both cases we see a very strong fracture skin effect in the first forty days material balance time before it diminishes to half-slope behavior. We see the pseudopressure drop and pseudopressure drop derivative trends merge with unit slope at 400 days. This is the signature of boundary influence — where fluid from outside the stimulated reservoir volume (SRV) begins to diffuse along with the SRV fluid and becomes a contributor to the pressure drop of the system.

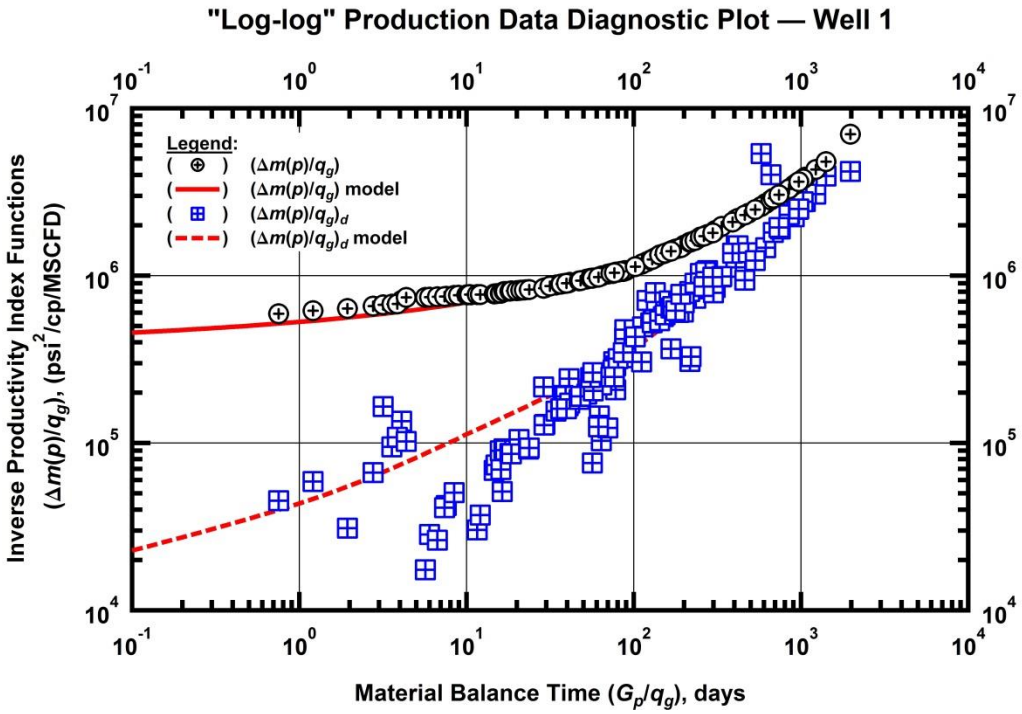

Figure 4.1 — (Log-log Plot): Production data diagnostic plot — inverse productivity index and its Bourdet derivative versus material balance time: data and model matches for Well 1.

While Wells 1 and 2 exhibit very similar character their pseudopressure drop and pseudopressure drop derivative functions are offset on the "log-log" diagnostic plot. The trend for Well 1 is below Well 2, indicating higher productivity. This higher productivity was modeled with a combination of higher permeability, higher fracture half-length, and higher fracture conductivity. The key flow parameters used in matching Wells 1 and 2 are summarized in **Table 4.1**.

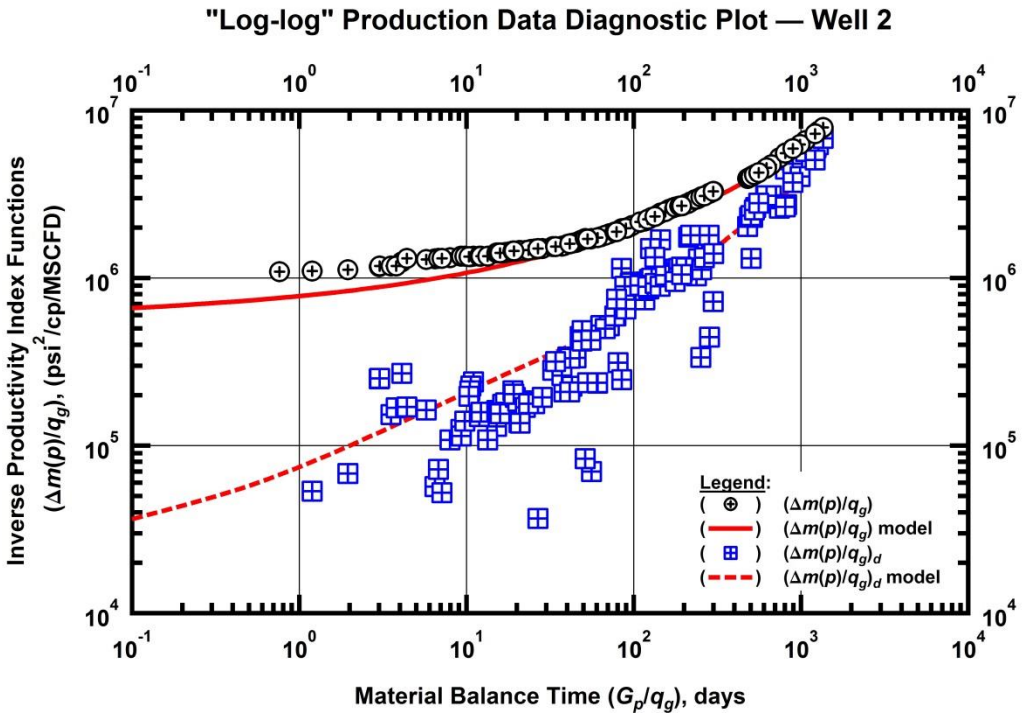

Figure 4.2 — (Log-log Plot): Production data diagnostic plot — inverse productivity index and its Bourdet derivative versus material balance time: data and model matches for Well 2.

Table 4.1 — Key flow parameters from matched models of Wells 1 and 2.

Well	k (nD)	x_f (ft)	F_c (md-ft)	skin (dimensionless)
1	260	180	1.0	0.004
2	230	100	0.42	0.005

To further illustrate the similarity in behavior of Wells 1 and 2 we present the diagnostic production data on the same plot for comparison in **Fig. 4.3**. The likeness of the two is marked in both the pseudopressure drop and the derivative functions. **Fig. 4.4** is the same plot as the one in Fig. 4.3, with the exception of an induced shift of the Well 2 data so that it overlays the data of Well 1. This shift was achieved by dividing the time data and pseudopressure drop and pseudopressure drop derivative data of Well 2 by constant factors until a suitable match was achieved. Particular interest was paid to matching the data beyond 100 days - where the data has stabilized – but the match is excellent over the entire span.

The pseudopressure drop and derivative factor was 1.7 and the time factor was 0.95, meaning a *downward* and *rightward* shift in the Well 2 data. Theoretically, a rightward shift represents an increase in flux area (x_f) and a downward shift means an increase in permeability. Well 1 was modeled with a higher permeability and higher fracture half-length, but not of the same proportions as the shift factors used for matching. In fact, if the factors were reversed they would be an almost an exact ratio match of the respective permeability and fracture half-length values used in the models.

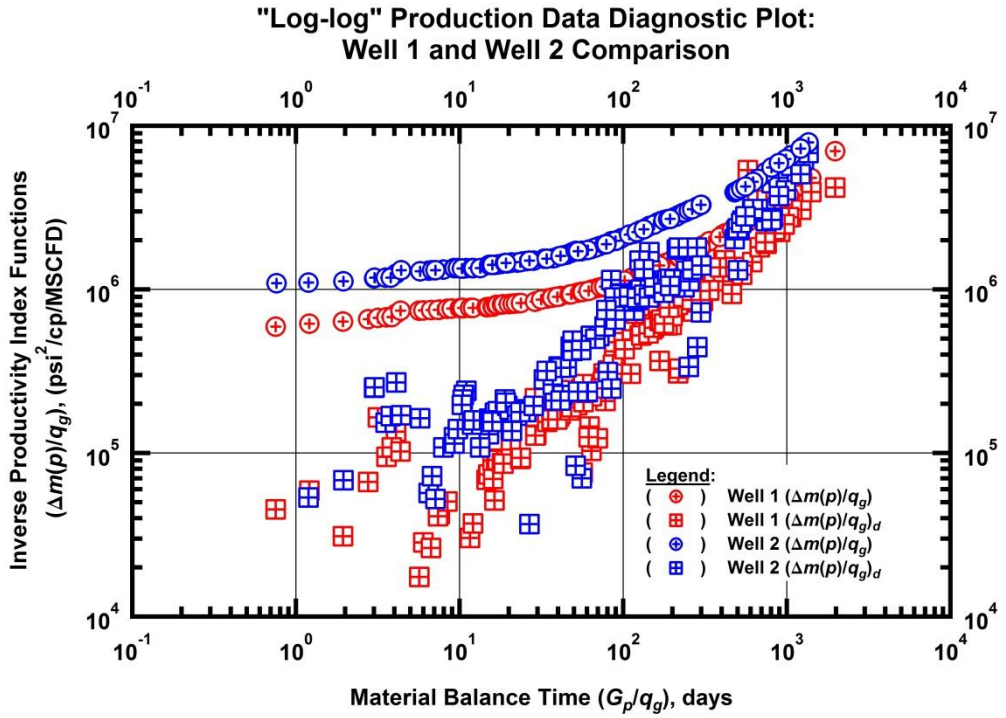

Figure 4.3 — (Log-log Plot): Production data diagnostic plot — inverse productivity index and its Bourdet derivative versus material balance time: Well 1 and Well 2 comparison.

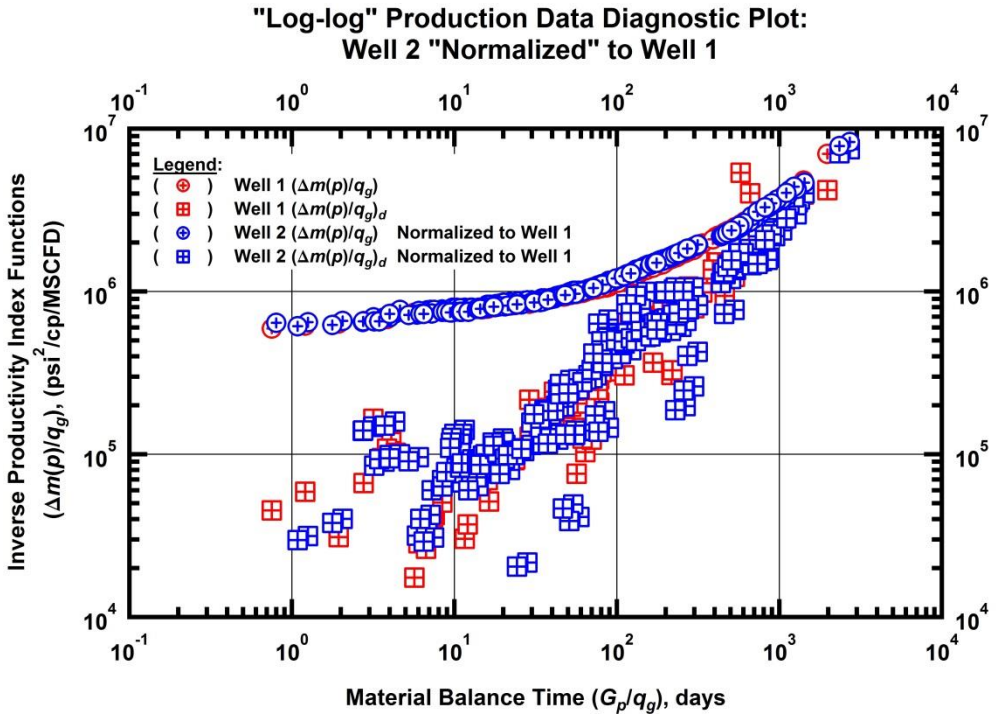

Figure 4.4 — (Log-log Plot): Production data diagnostic plot — inverse productivity index and its Bourdet derivative versus material balance time: Well 2 "normalized" to Well 1.

We now follow this normalizing procedure with another iteration involving two different wells (Wells 15 and 18). The diagnostic plot created using the raw data for Well 15 and Well 18 is shown in **Fig. 4.5**. Like before, we see strikingly similar diagnostic behavior in both the derivative and pseudopressure drop functions. Both wells have a slope of one-third in the pseudopressure drop and derivative trends and are offset by a factor of 3 between 10 and 100 days material balance time. This behavior is not true bilinear flow (¼ slope, factor of 4 offset) nor true formation linear flow (½ slope, factor of 2 offset). We are unsure whether this is an artifact or a distinct flow regime diagnostic that is yet to be classified. We feel it to be worth a mention as we have seen multiple cases of this behavior.

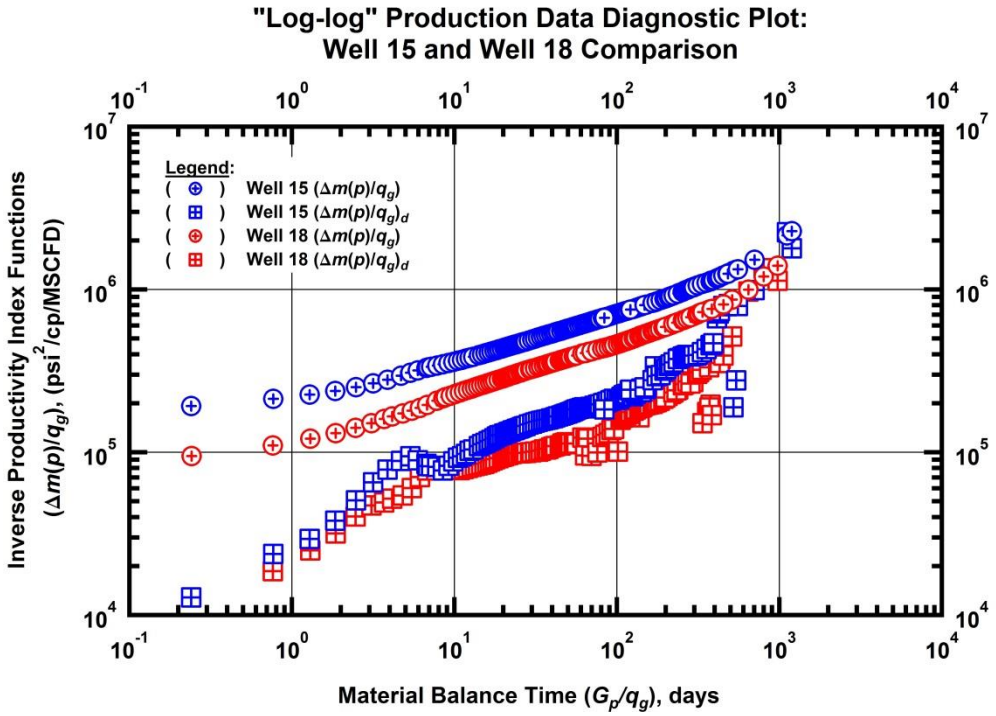

Figure 4.5 — (Log-log Plot): Production data diagnostic plot — inverse productivity index and its Bourdet derivative versus material balance time: Well 15 and Well 18 comparison.

In **Fig. 4.6** we normalize the functions of **Fig. 4.5**. Well 15 is normalized to Well 18 in the same fashion as was done in the first example. The match is excellent beyond ten days as both wells display a transition towards linear flow (½ slope) after 100 days, material balance time. The pseudopressure drop and derivative factor was 1.6 and the time factor was 1.2, meaning a *downward* and *leftward* shift in the Well 15 data. This suggests from theory that Well 15 has a lower permeability, but a greater flux area than Well 18. This exercise is helpful in understanding relative behavior between like wells, but it still leaves us uncertain of the absolute values of the governing flow properties.

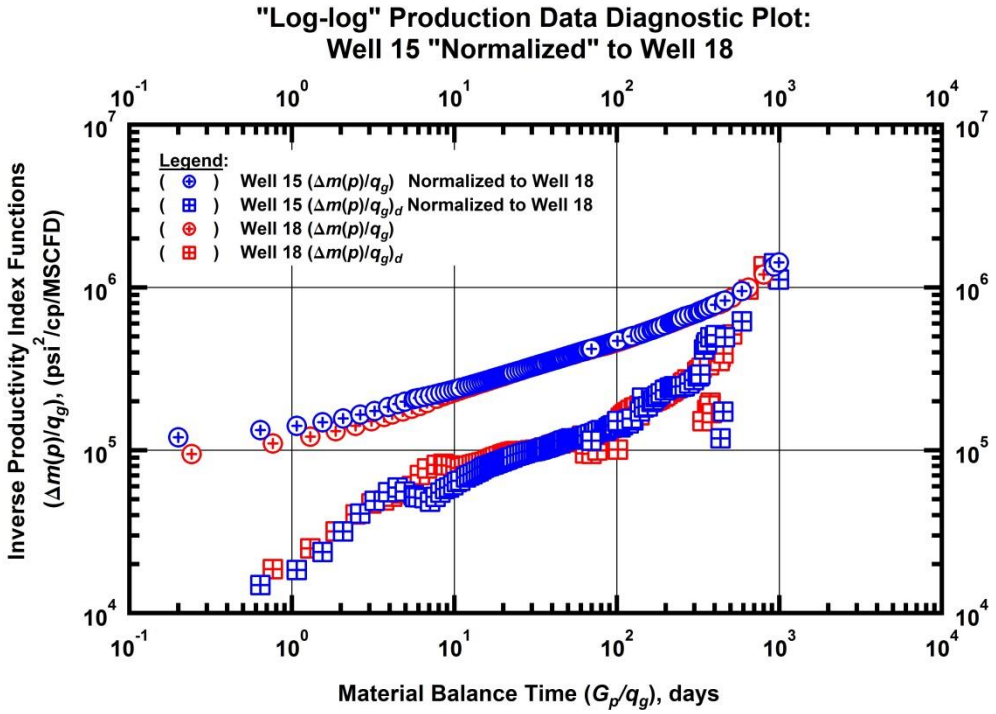

Figure 4.6 — (Log-log Plot): Production data diagnostic plot — inverse productivity index and its Bourdet derivative versus material balance time: Well 15 "normalized" to Well 18.

We extend this "normalizing" exercise to a case of 5 wells from a single pad that exhibit very like behaviors. This can be seen in Fig. 4.7. We "normalize" Wells 39 through 42 to Well 43 (highest productivity well) by shifting them vertically with divisors in the same manner as the previous cases. The divisors (normalizing factors) are enumerated on the plot of **Fig. 4.7**. For this group there was no horizontal shift. We reiterate that horizontal shifts are related to the completion (fracture properties). We expect to see a reasonably small range in fracture property values from these neighbor wells and small variations in fracture half-length (for example) do not yield discernible horizontal offsets. The key flow parameters and EUR values for the Wells 39-43 are displayed in **Table 4.2**.

Table 4.2 — EUR values and key flow parameters from matched models of Wells 39-43.

Well	k (nD)	x_f (ft)	F_c (md-ft)	EUR (BSCF)
39	185	380	0.50	2.11
40	150	320	0.60	1.78
41	180	280	0.25	2.09
42	145	280	0.20	1.80
43	200	350	0.45	2.26

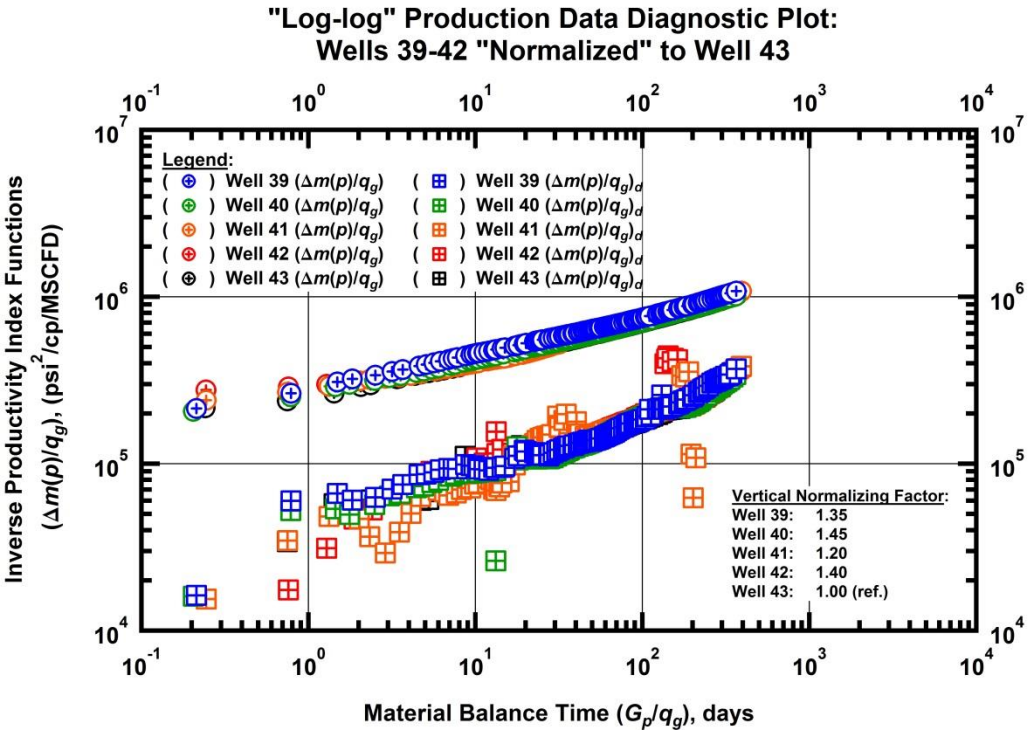

Figure 4.7 — (Log-log Plot): Production data diagnostic plot — inverse productivity index and its Bourdet derivative versus material balance time: Wells 39-42 "normalized" to Well 43.

A quick inspection of the "k" column of **Table 4.2** along with the vertical normalizing factors of **Fig. 4.7** shows an *inverse* proportionality. This is what we expect to see — *i.e.*, the higher on the diagnostic plot the pseudopressure drop derivative function (and thus the greater normalizing factor required), the lower the permeability (all else being equal). We observe a *direct* proportionality between formation permeability and EUR. In fact, it is worth noting that we see a strong linear proportionality for these five wells; however, we advise caution in trying to draw firm conclusions from this small of a sample size.

What we can state qualitatively is that permeability remains the preeminent well/reservoir property influencing well performance and ultimately EUR, even for multi-fractured horizontal wells.

We now introduce an associated set of wells from a deeper, thicker and higher-pressured area and discuss the differences in diagnostic response and well/reservoir properties. The production data diagnostic plots for Wells 35-37 are illustrated **by Figs. 4.8-4.10**, respectively. All three of these wells show half-slope formation linear flow signatures (non-interfering vertical fractures). This is a departure from the commonly observed quarter-slope bilinear flow signature of our set of wells. The inverse productivity index functions of these wells suggest lower permeability and fracture half-length values. The fracture conductivity values are not exceedingly greater than those of the wells showing bilinear flow, but the conductivity contrast resulting from the lower permeability and fracture half-length of these wells yields a near-infinite conductivity response.

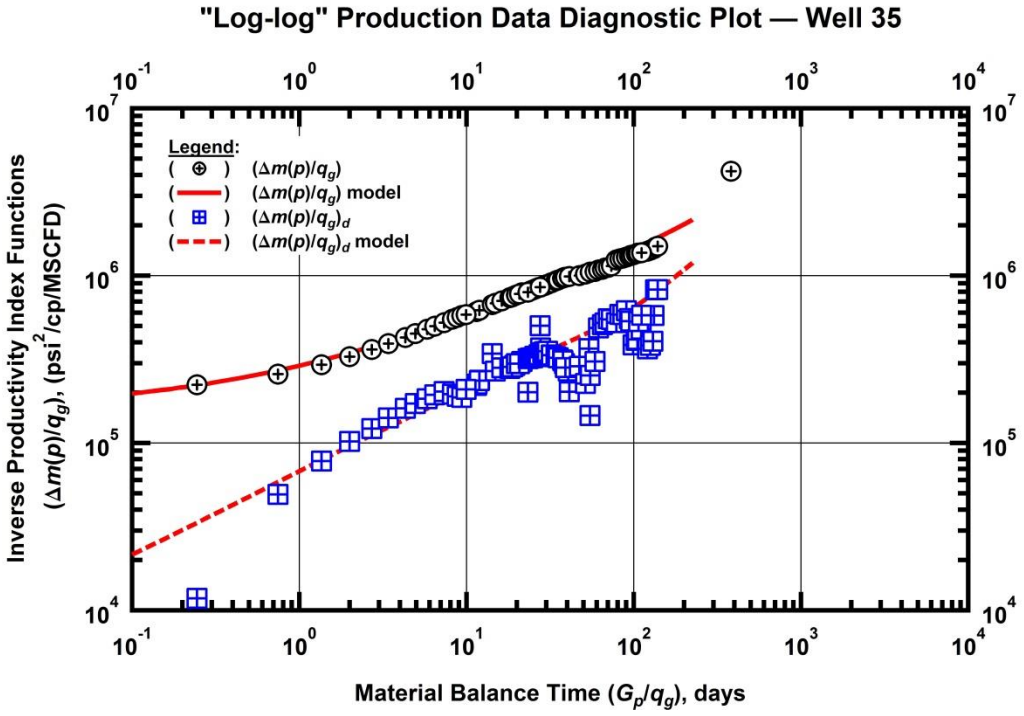

Figure 4.8 — (Log-log Plot): Production data diagnostic plot — inverse productivity index and its Bourdet derivative functions: data and model matches for Well 35.

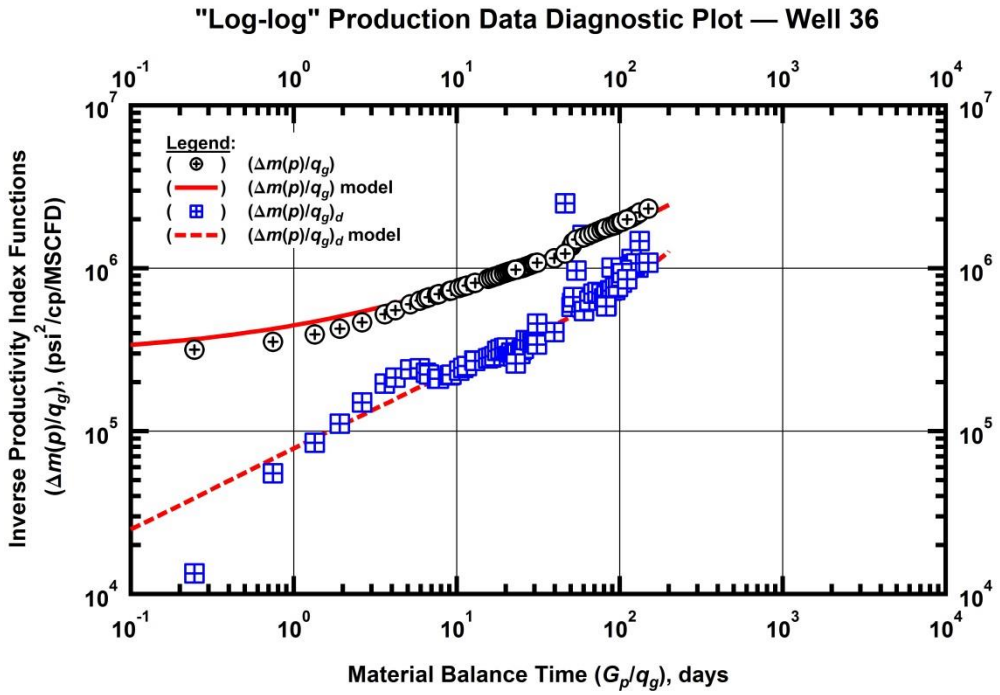

Figure 4.9 — (Log-log Plot): Production data diagnostic plot — inverse productivity index and its Bourdet derivative: data and model matches for Well 36.

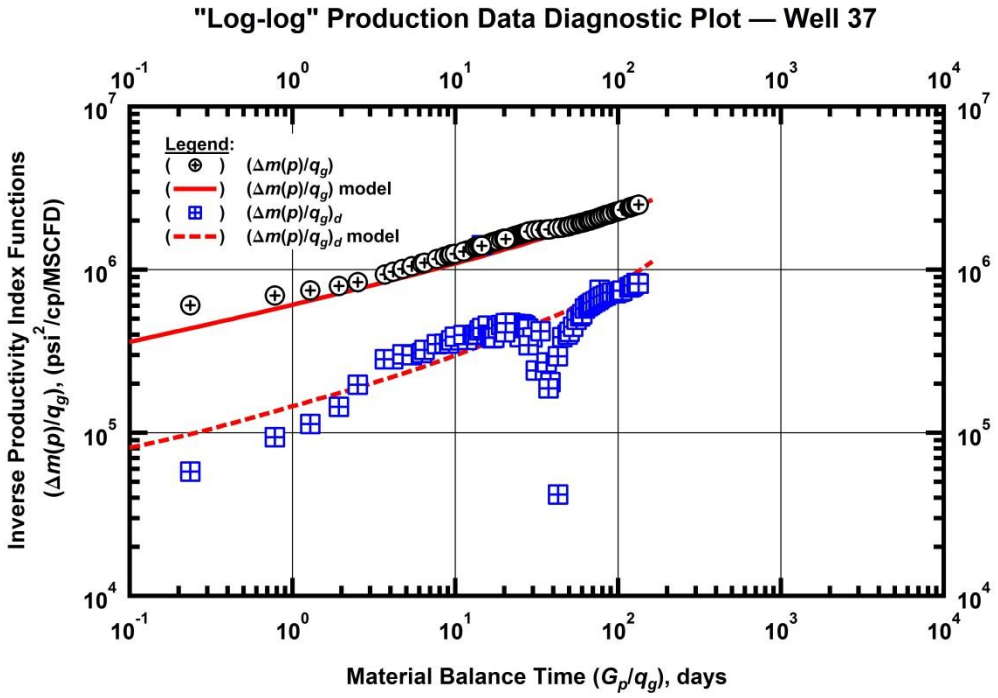

Figure 4.10 — (Log-log Plot): Production data diagnostic plot — inverse productivity index and its Bourdet derivative: data and model matches for Well 37.

Also of interest in these plots is an apparent interference signature between adjacent Wells 36 and 37. The pseudopressure drop and derivative functions of each well demonstrate an opposite behavior at approximately the same point in time. At roughly 50 days (material balance time) Well 36 experiences an instantaneous degradation in productivity as evidenced by the precipitous increase in the pseudopressure drop function. At the same day of measurement Well 37 exhibits an instantaneous increase in productivity as evidenced by a sharp decrease in the pseudopressure drop function.

CHAPTER V
INTEGRATION OF PERFORMANCE AND WELL/RESERVOIR METRICS

The genesis of this chapter's work stems from the idea that the model parameters from modern rate-time relations (i.e. b, D_i, n, etc.) share a fundamental relationship with well/reservoir properties (i.e. k, x_f, F_c, etc.). While it is unlikely that a universal function would ever represent the relationship between any particular rate-time model parameter and a well/reservoir property, our goal is to observe/establish interrelatedness. We do believe that on a small scale (field scale and smaller) of geologically and petrophysically similar flow systems developed with similarly completed wells that there can be a unique relationship between the parameters that describe a well's flowrate decline and the properties that govern a well's flowrate.

The most common challenge faced in analyzing rate-time data is interrupted flow. Monotonicity is necessary in quantifying decline behavior in a reliable manner. Downstream pipeline capacity and other logistical issues can necessitate the shutting-in of wells. Unfortunately this can sometimes render rate-time analysis unreliable, if not completely useless. Well closures (shut-ins) cause the well and fracture system to re-equilibrate which effectively segments the flow periods into separate entities that cannot be analyzed as one. This is particularly the case in the well's early life (within the first year). When attempting to correlate rate-time diagnostic parameters (b and D) with well/reservoir properties it is crucial that the data set is limited to the wells with high-quality rate-time data.

We begin with a "tuning" procedure that was developed from a simple crossplot of the modified hyperbolic b-parameter versus formation permeability value from model-based analysis (k-b plot). (We note that we limited this exercise to 30 wells with higher quality rate-time data so that a high-level confidence can be had in the parameter values). We observed a linear trend with an inverse proportionality and a modest R-squared value of roughly 0.5. Further, we plotted the EUR from the modified hyperbolic rate-time model versus the EUR from the rate-pressure-time model-based analysis. This crossplot yielded a slightly better R^2 value of about 0.6. The idea was to *tune* the model-based analysis permeability values according to the "predicted" values from the k-b correlation.

Once a satisfactory model match was achieved with the new permeability, we re-forecasted the well and obtained a new EUR value. This approach improves the correlation quality for both the k-b plot and the EUR crossplot. The final k-b plot and EUR crossplot are displayed in **Figs. 5.1** and **5.2**. The b-parameter values of the correlated data range from 1.1 to 2.6 while formation permeability values range from 145 nD to 275 nD. These ranges from the 30 tuned wells are a complete representation of the full data set.

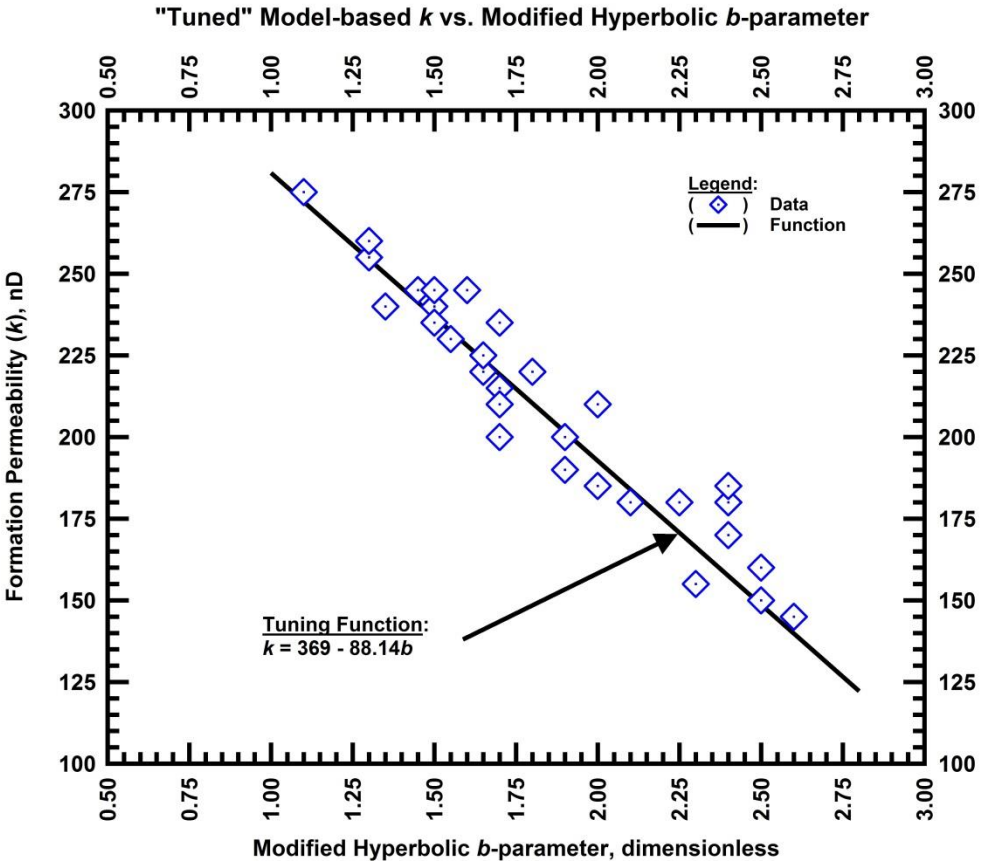

Figure 5.1 — (Cartesian Plot): Formation permeability as a function of modified hyperbolic rate-time model *b*-parameter — a sample of 30 wells.

We stopped short of forcing permeability values to adhere strictly to the tuning function value for a well's *b*-parameter value. Once the tuning function had been established we adjusted the outlier permeability values "by hand" to fall within a bandwidth of the function itself. This was done for several reasons. Foremost was that we recognize the imprecise nature of this concept. We contend that this tuning technique serves more as an additional way to think about the relationships between rate-time parameters and well/reservoir properties than it does as a rigorous prediction tool. We are interested to see how effective imposing a subsurface property value on a physical model according to a rough initial correlating function would be in modeling the diagnostic behavior. Essentially, we were using the non-unique nature of model-based production analysis to force it into an imposed unique character.

Upon obtaining the correlation of **Fig. 5.1** we obtained the correlation of **Fig. 5.2** by extension. To reiterate, **Fig. 5.2** is a crossplot of EUR values of the 30 "tuned" wells with the value on the abscissa being the modified hyperbolic rate-time model and the ordinate being the value from model-based production

analysis. The least-squares linear trendline with forced intercept at the origin indicates a ratio greater than one-to-one.

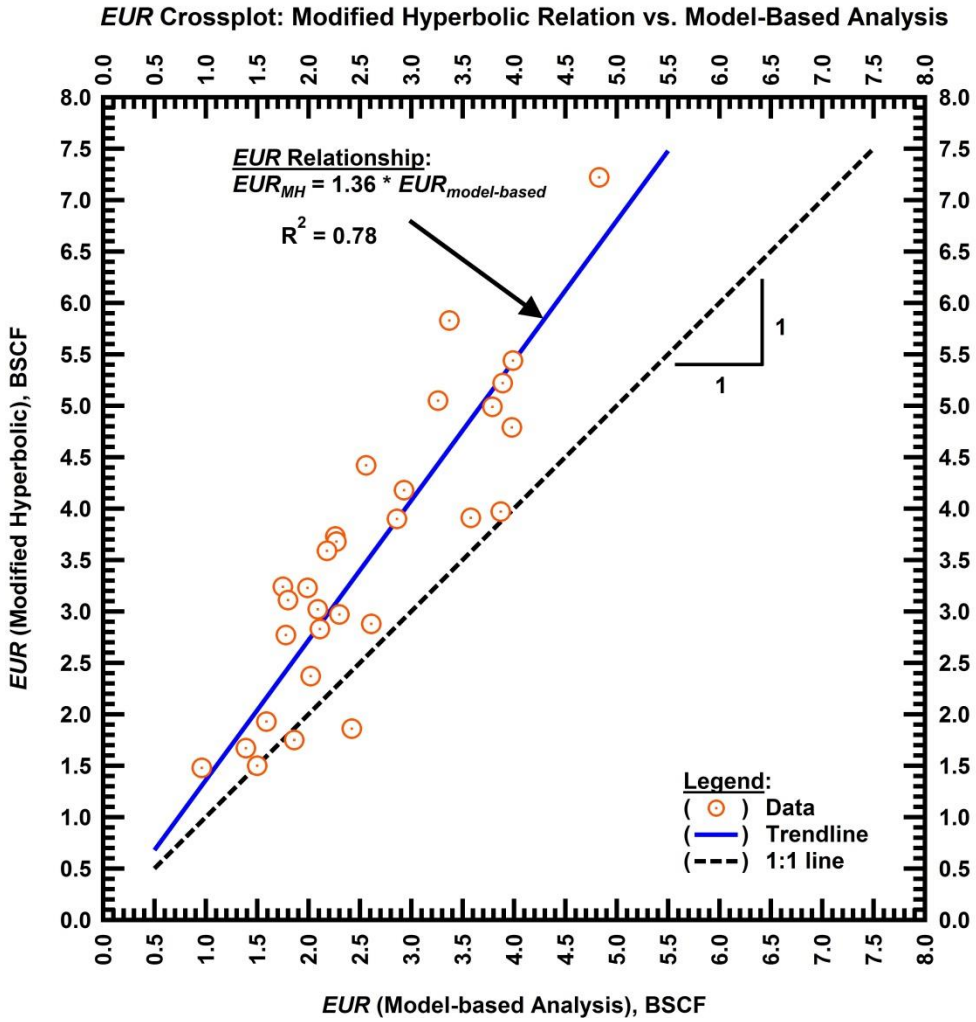

Figure 5.2 — (Cartesian Plot): EUR comparison crossplot — EUR from modified hyperbolic rate-time model versus EUR from model-based production analysis.

The slope of the trendline being 1.36 suggests that, on average, the modified hyperbolic model EUR overestimates model-based analysis EUR by 36 percent.

We include histograms of the *b*-parameter values and permeability values of the "tuned" 30 well set in **Figs. 5.3** and **5.4**. Displayed as below with class interval widths of 0.2 the *b*-parameter distribution is bimodal. Interestingly, if a set of six wells from the same pad and having higher *b*-parameter values are removed from the sample, the second mode disappears. These six wells are geographically apart from the

general location of the bulk of the sample wells. Additionally, these six wells have *b*-parameter values ranging from 1.9 to 2.6, representing the full spectrum of values greater than the lesser mode. Taken in isolation one can deduce that geological differences are contributing to decline character and that combining these data into one set is erroneous.

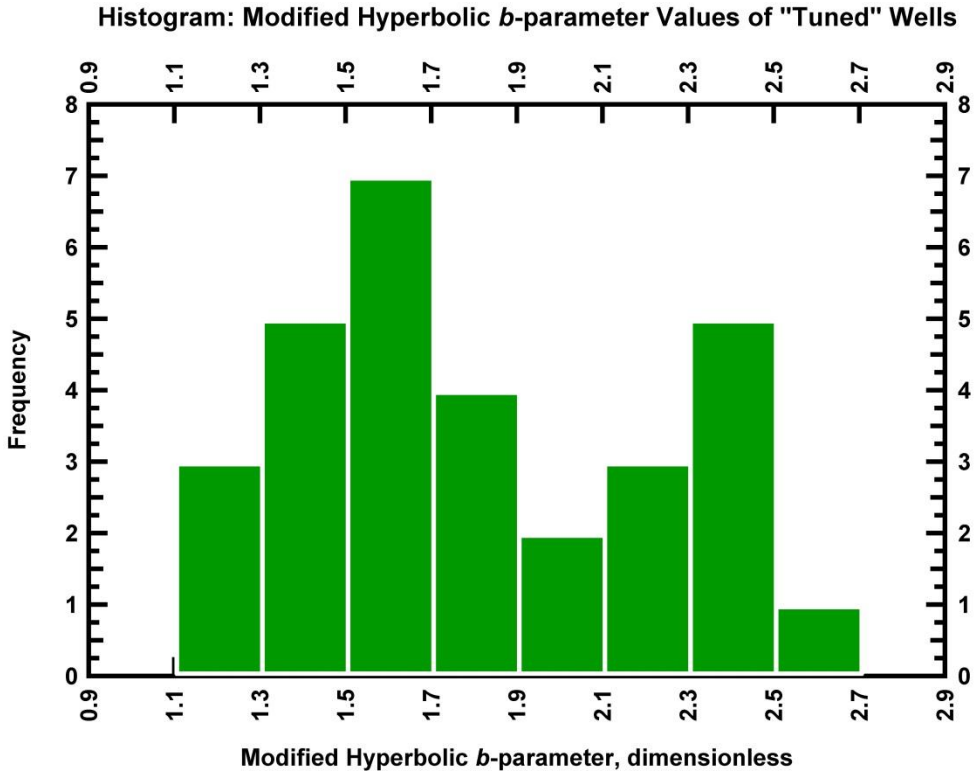

Figure 5.3 — (Histogram): Modified hyperbolic *b*-parameter — Distribution of *b*-parameter values from 30 well sample.

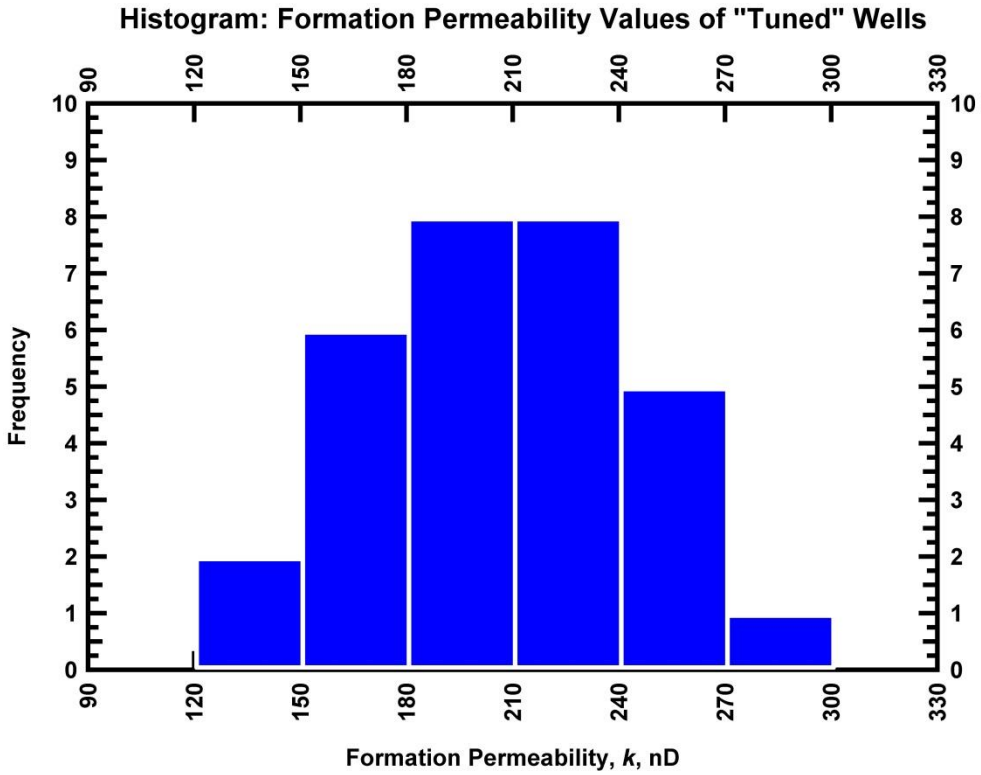

Figure 5.4 — (Histogram): Model-based analysis permeability values — Distribution of permeability values from model-based production analysis of 30 well sample.

We present histograms of EUR distribution from both the modified hyperbolic model and model-based analysis in **Fig. 5.5**. The histograms of **Figs. 5.4 and 5.5** provide alternate illustration to the data plotted in **Fig. 5.2**. The distributions of both histograms are Gaussian with the modified hyperbolic histogram offset to the right and having greater class intervals.

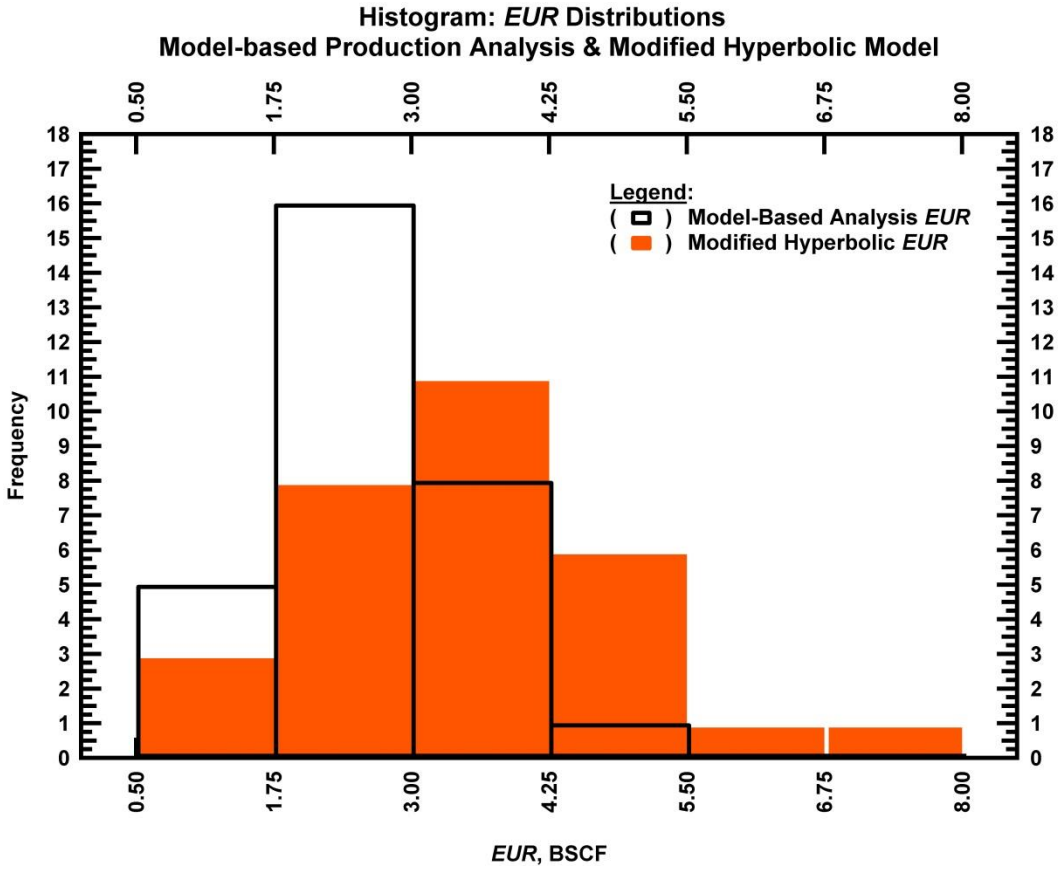

Figure 5.5 — (Histogram): EUR values — Distributions of EUR values from modified hyperbolic model and model-based production analysis: 30 wells.

Thus far we have focused on the integration of the modified hyperbolic relation with model-based production analysis. Now we turn our attention to the relationships we observe between the results of rate-time analysis with the power-law exponential relation and those from model-based analysis. To start we show the 30 well crossplot of power-law exponential EUR and model-based EUR in **Fig. 5.6**. Included on the plot is a least-squares linear trendline that suggests a one-to-one relationship with a positive vertical intercept. It is the nature of rate-time analysis to overestimate EUR when compared to model-based analysis so this intercept is expected. The one-to-one relationship between these independent models is encouraging in spite of the associated error that resulted in an R-squared value of 0.66. This correlation is not as strong as the EUR correlation between the modified hyperbolic relation and model-based analysis, however this data is not tuned as it was in the prior case.

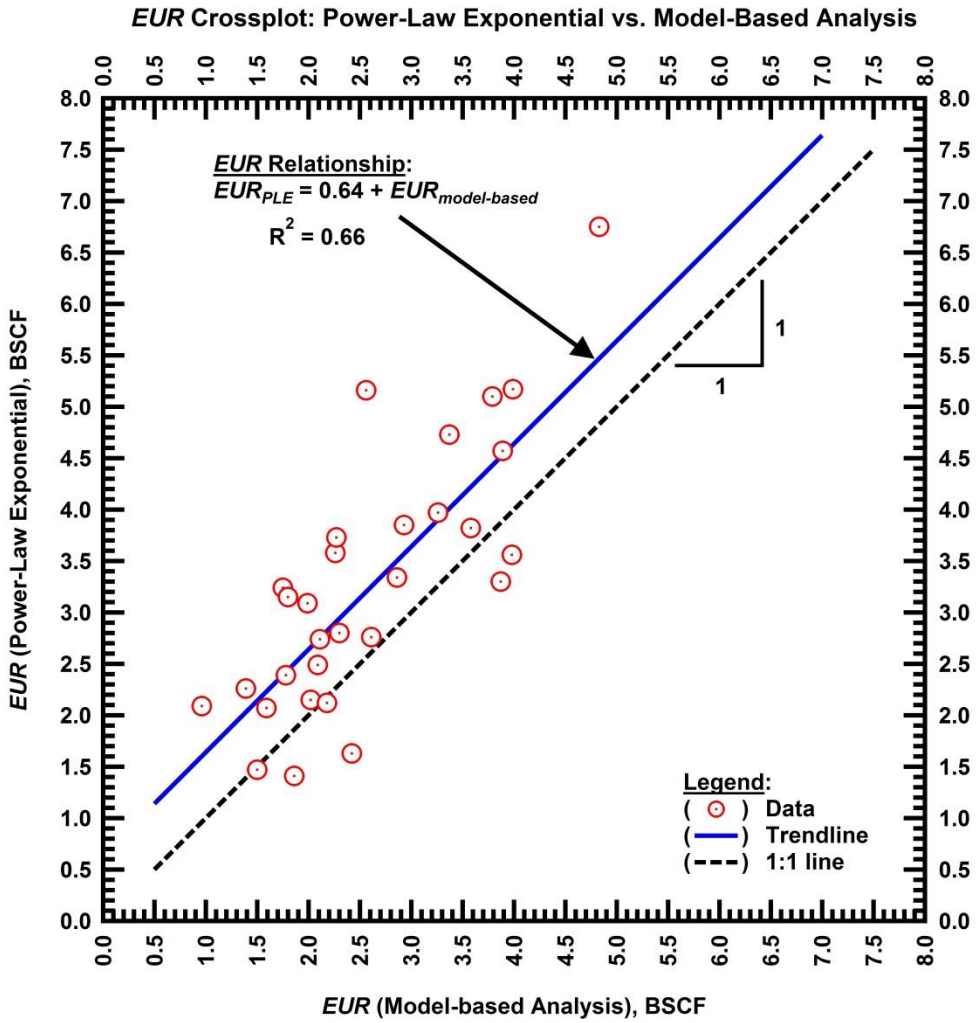

Figure 5.6 — (Cartesian Plot): EUR comparison crossplot — EUR from the power-law exponential rate-time model versus EUR from model-based production analysis.

We now present a pair of histograms of the decline parameters for the power-law exponential relation used in modeling the thirty-well sample. **Fig. 5.7** is a histogram of the PLE *n*-parameter and **Fig. 5.8** is a histogram of the PLE $\check{D}_i$ parameter. Upon inspection of **Figs. 5.7 and 5.8** we notice a "mirrored" relationship between their respective distributions. This is not an artifact as they share an exponential decay relationship – where the wells with lower *n*-parameter values have higher $\check{D}_i$ -parameter values. This relationship is illustrated in **Fig. 5.9** in the form of a semi-log plot.

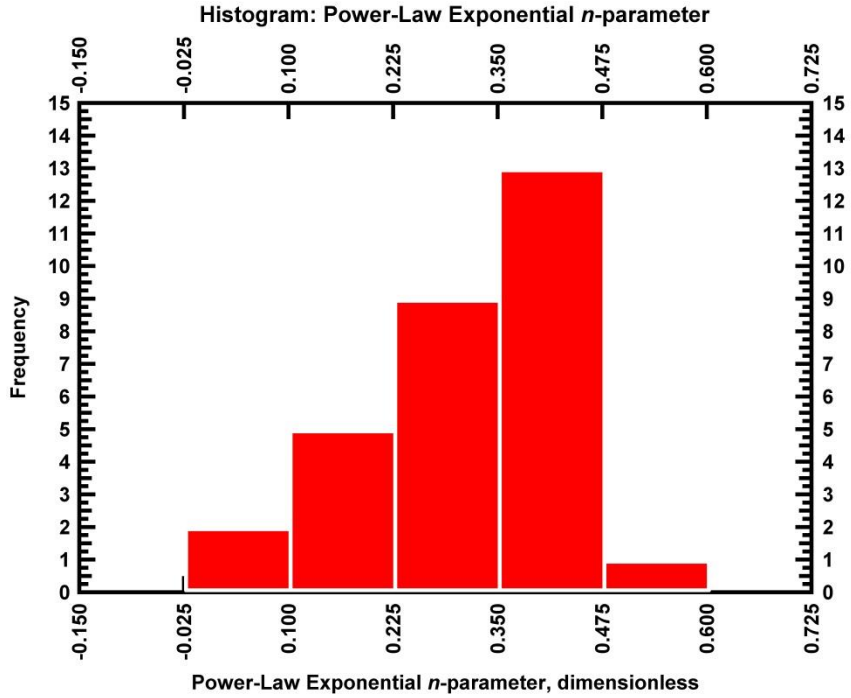

Figure 5.7 — (Histogram): Power-law exponential n-parameter — Distribution of n-parameter values from 30 well sample.

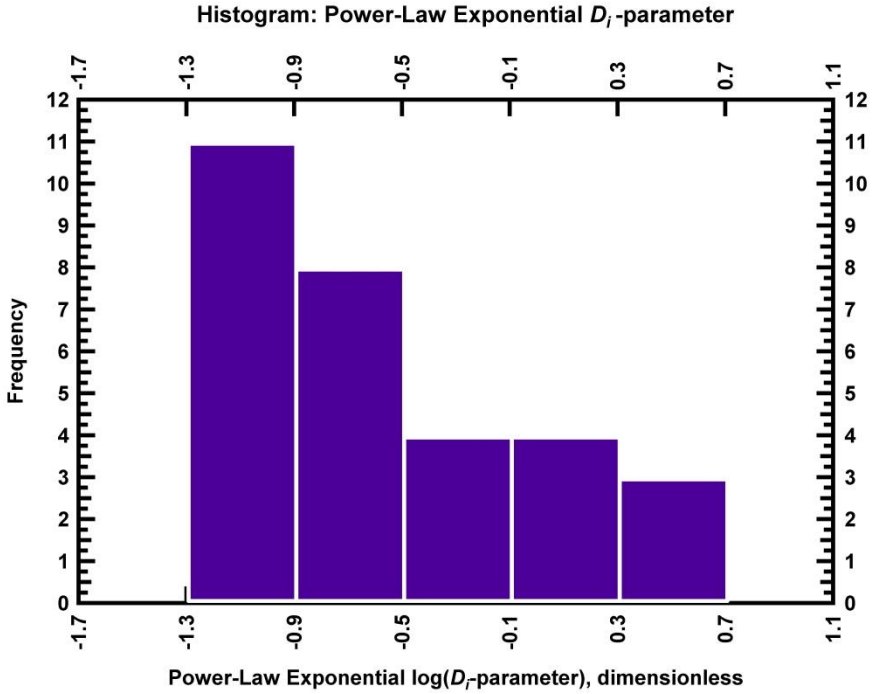

Figure 5.8 — (Histogram): Power-law exponential $\check{D}_i$-parameter — Distribution of the logarithm of the $\check{D}_i$ -parameter values from 30 well sample.

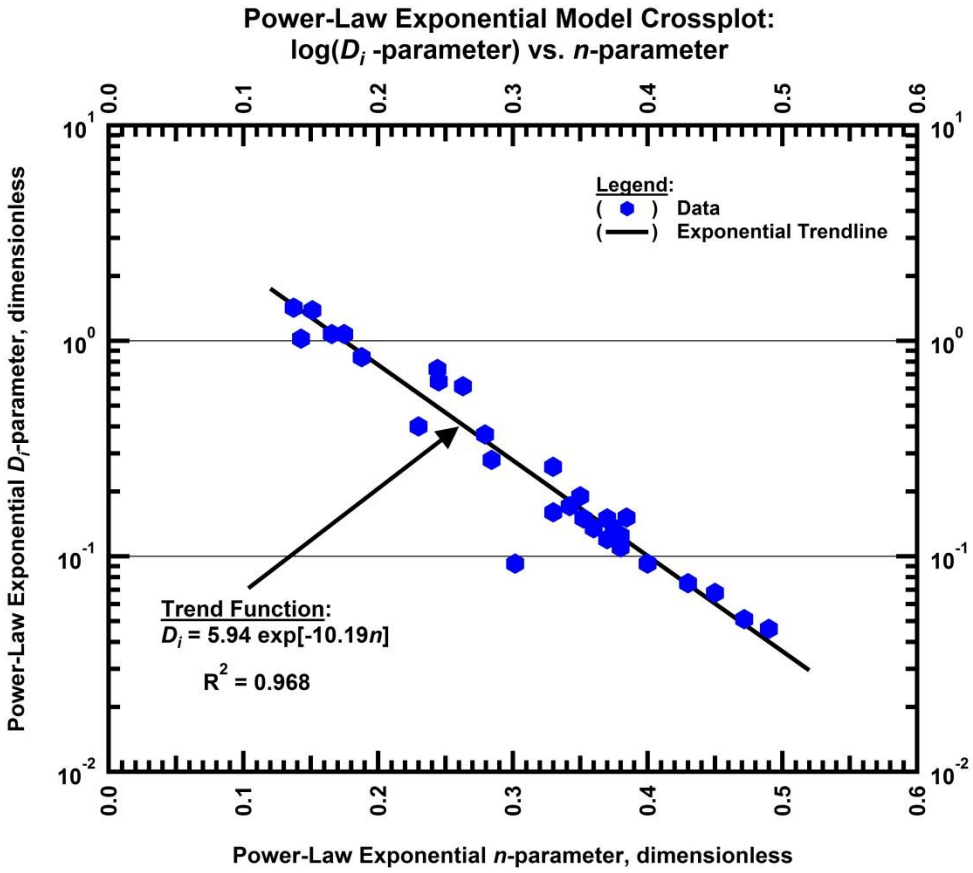

Figure 5.9 — (Semi-log Plot): Power-law exponential model parameters — exponential relationship between the $\check{D}_i$ -parameter and n-parameter: 30 well sample.

Fig. 5.10 is a EUR histogram comparison of model-based production analysis and the power-law exponential model.

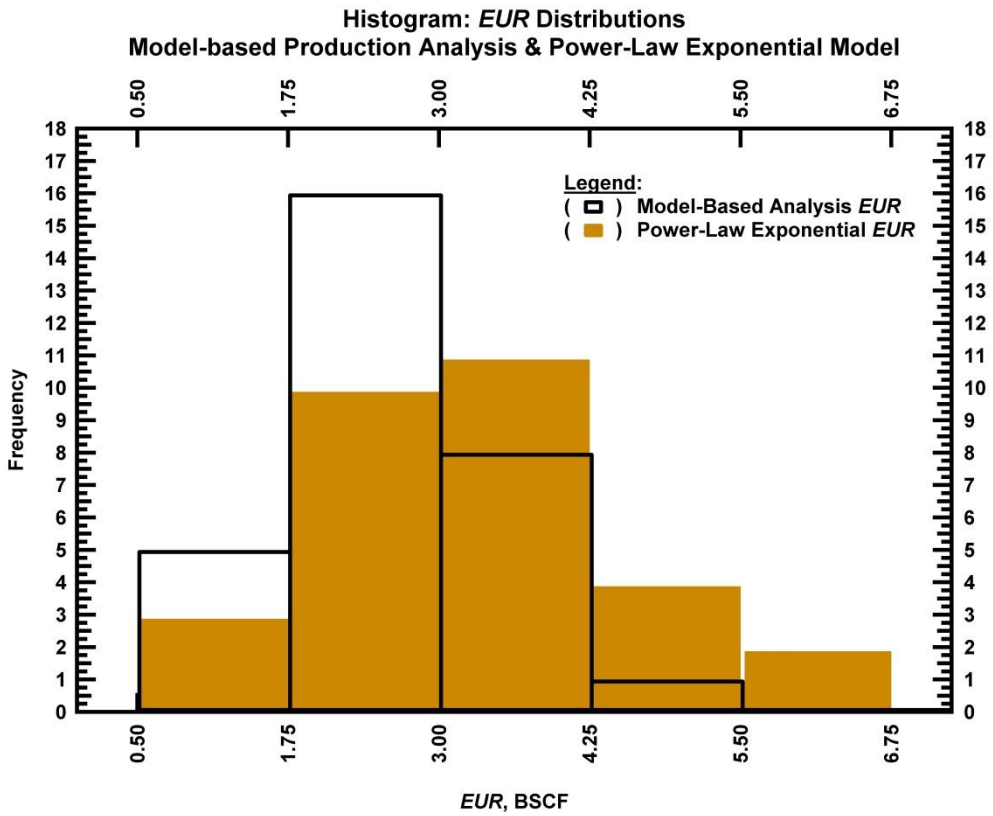

Figure 5.10 — (Histogram): EUR values — Distributions of EUR values from the power-law exponential model and model-based production analysis: 30 wells.

CHAPTER VI
PRESSURE TRANSIENT ANALYSIS

In this chapter we cover pressure transient analysis in the form of pressure buildup tests. Pressure transient analysis (PTA) is a classical reservoir evaluation tool long been used in the industry but has yet to find widespread applicability to shale reservoirs. Shortcomings in PTA application can be attributed largely to the ultra-low formation permeabilities characteristic to unconventional reservoirs and also to the complex architecture of the well/completion system. The low permeabilities create large pressure gradients and thus inhibit deep investigation into the reservoir matrix in a timely manner. The complex fracture network and long horizontal wellbore characteristic of modern wells exert a larger influence in the total measured response and thus present challenges in analyzing pure reservoir behavior.

In spite of the present shortcomings of PTA in shale reservoir systems, we present a collection of illustrative cases complete with diagnostic interpretations, analytical model matches, and discussion on the challenges we encounter – particularly as it pertains to the non-uniqueness in quantitative interpretation. Further, we attempt to conflate model-based production analysis and pressure transient analysis in an effort to better understand their interrelation.

6.1 High-Frequency Bottomhole Gauge Buildup Analysis

We begin by illustrating a pressure buildup test for Well 9; depicted in **Fig. 6.1** with the log-log diagnostic plot of the pseudopressure drop functions. This buildup test is 656 hours (27 days) in duration, which in conventional pressure transient analysis is an exceedingly long time to record pressure transients and it is likely to see a boundary or reflection influence of some kind. As we see from the data character in **Fig. 6.1** this well is exhibiting *infinite-acting* linear flow signified by the two half-slope parallel "forks." This half-slope behavior is particularly interesting when we consider the character of the production drawdown behavior.

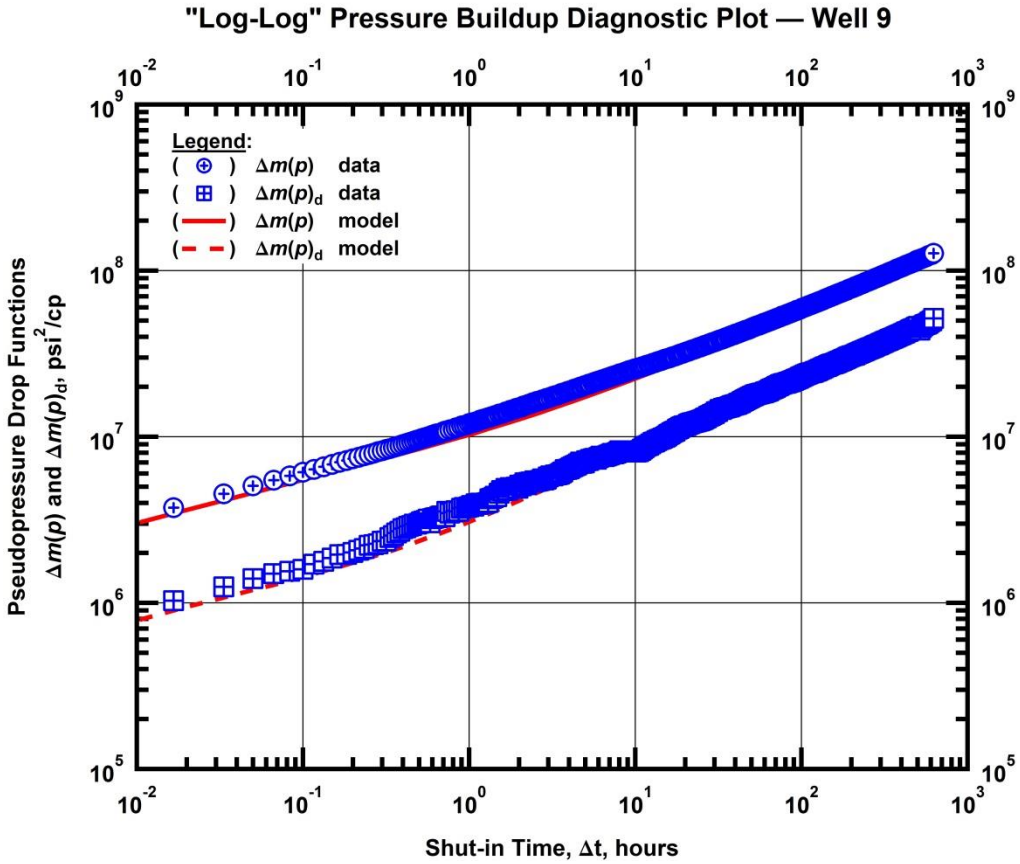

Figure 6.1 — (Log-log Plot): Pressure buildup diagnostic plot — pseudopressure drop and Bourdet derivative of pseudopressure drop functions for Well 9.

In **Fig. 6.2** we recall the production data diagnostic plot of Well 9 for inspection. The early transient diagnostic character of **Fig. 6.2** is quarter-slope which is representative of bilinear flow — governed by

lower fracture conductivity (greater contrast between reservoir and fracture flow capacity). The models of **Figs. 6.1 and 6.2** consist of identical reservoir/well properties with the exception of fracture conductivity (F_c) and fracture half-length (x_f). The fracture conductivity and half-length values for the production data model are 1.3 md-ft and 350 ft, respectively. The fracture conductivity and half-length values for the pressure buildup model are 11.4 md-ft, and 210 ft, respectively. The complete list of relevant model parameters is included in **Table 6.1**.

That we are able to effectively model the dynamic production drawdown data (which uses a constant-rate approximation) and the static pressure buildup data with the same parameters excluding two is encouraging. Further, it is intriguing that the properties of disagreement (F_c and x_f) are ones that could conceivably be sensitive to pressure and/or net stress in the fracture.

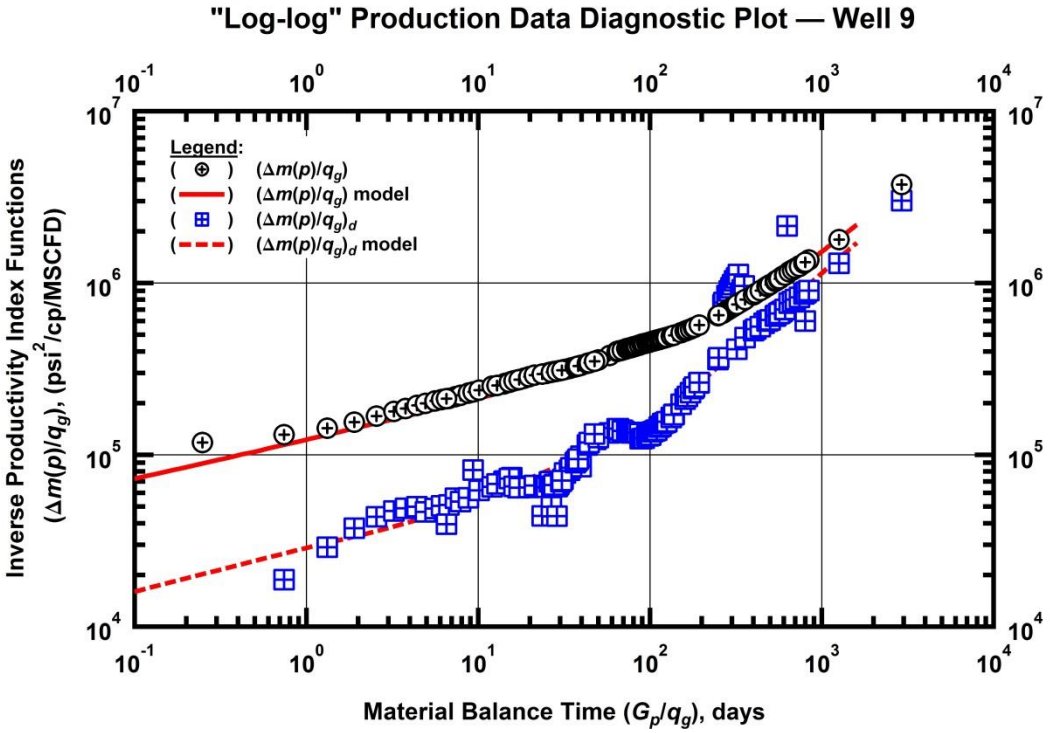

Figure 6.2 — (Log-log Plot): Production data diagnostic plot — inverse productivity index and its Bourdet derivative versus material balance time: data and model matches for Well 9.

Table 6.1 — Key flow parameters in production drawdown and pressure buildup models of Well 9.

Source	k (nD)	x_f (ft)	n_f (dimensionless)	F_c (md-ft)	skin (dimensionless)
Drawdown	260	350	36	1.3	1E-4
Buildup	260	210	36	11.4	0

When we model the drawdown data with the buildup model fracture parameters, and vice versa, we find that they are diagnostically incompatible. It is not merely a disagreement in magnitude of flow capacity but a dichotomy in "form" of flow capacity. The third and fifth columns of **Table 6.1** tabulate the disagreement between model parameters of the two analyses. Drawdown behavior requires a longer and less conductive fracture to satisfy the pressure-flowrate reconciliation while the buildup requires a shorter and more conductive fracture to model the pressure drop. No amount of fracture half-length can be added to the buildup model to make up for a low conductivity value on the order of the drawdown model. Likewise, no amount of fracture conductivity can be added to the drawdown model to make up for a low fracture half-length value on the order of the buildup model.

We now present an additional case from a well within reasonably close proximity to Well 9. Unfortunately the buildup test from this case is of lower quality than that of Well 9 in the sense that the first 9 hours of buildup behavior were not captured by the bottomhole gauge. Regardless, we can still draw from the data that was captured and use it as a reference in analysis. The "log-log" diagnostic buildup plot for Well 49 is presented in **Fig. 6.3**.

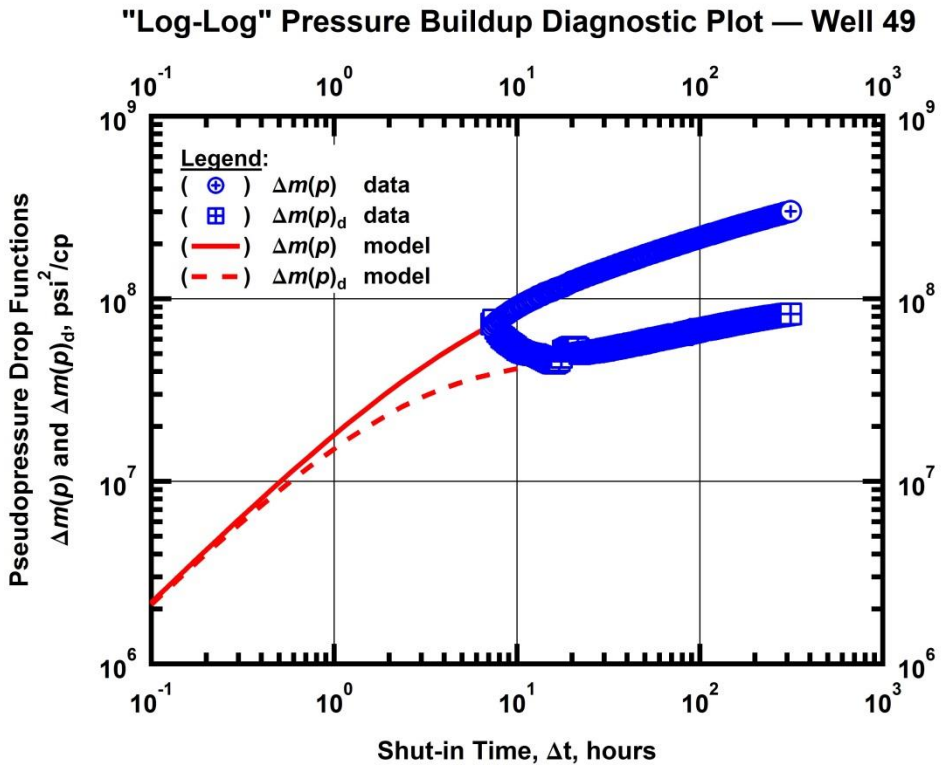

Figure 6.3 — (Log-log Plot): Pressure buildup diagnostic plot — pseudopressure drop and Bourdet derivative of pseudopressure drop functions for Well 49.

For comparison we present the "log-log" production data diagnostic plot in **Fig. 6.4**. As with the case of Well 9, we model both the buildup and drawdown data with identical parameters save for the fracture parameters (F_c and x_f). The complete list of flow parameters used for modeling the data of **Figs. 6.3 and 6.4** are presented in **Table 6.2**.

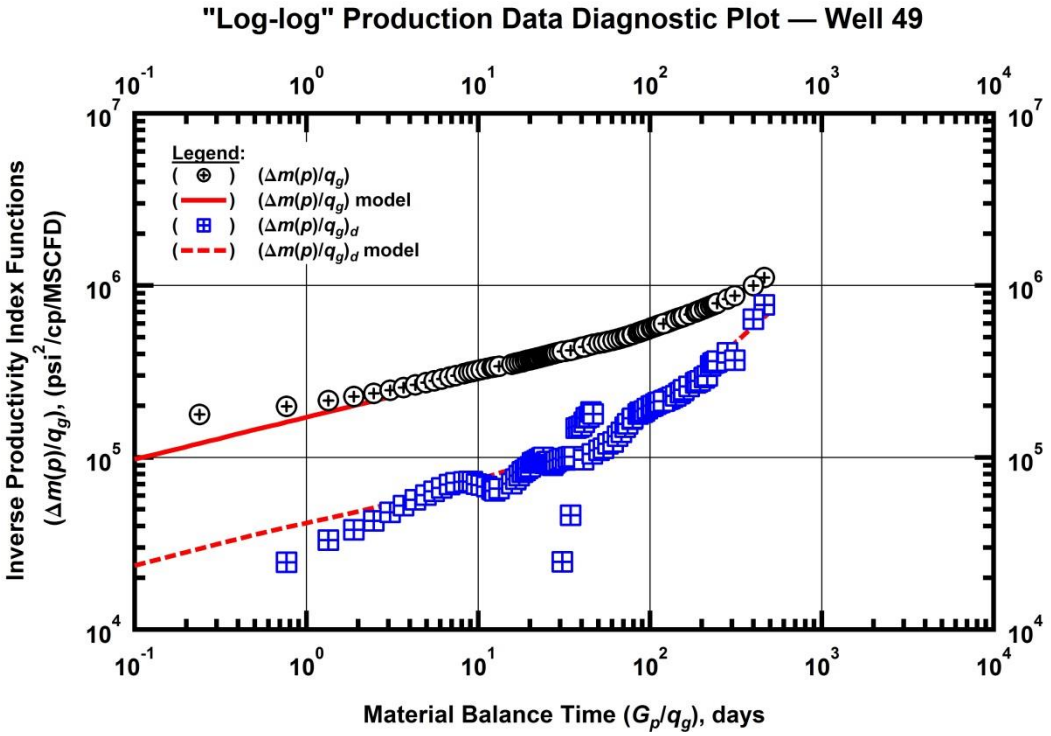

Figure 6.4 — (Log-log Plot): Production data diagnostic plot — inverse productivity index and its Bourdet derivative versus material balance time: data and model matches for Well 49.

Table 6.2 — Key flow parameters in production drawdown and pressure buildup models of Well 49.

Source	k (nD)	x_f (ft)	n_f (dimensionless)	F_c (md-ft)	C (bbl/psi)
Drawdown	220	400	36	0.65	n/a
Buildup	220	230	36	2	4

Being satisfied with the quality of the model matches for the respective analyses and noticing that the difference in fracture properties did not differ as greatly as they did in the previous case we endeavored to find a "middle ground" between the two interpretations. After some iterative matching of both the diagnostic production data and diagnostic pressure buildup data we found a unique model that suited both data sources. The key flow parameters for this model are listed in **Table 6.3**. We display the data and resulting matches together in a single "combination plot" in **Fig. 6.5**. In order to make a single model match both data sets they each had to sacrifice some precision in their respective matches. The difference is slight, but noticeable and it raises some important questions. Are we truly observing two distinct flow behaviors between the dynamic production drawdown and the static pressure buildup periods? Does the fracture actually dilate during shut-in under a reduction in effective stress and behave as a more

conductive fracture? Is the lower conductivity drawdown response actually just a flowrate-dependent skin effect that masks what is otherwise a high conductivity fracture? These are all questions that need answering to gain a better understanding of the nature of flow in multi-fractured horizontal shale wells. Knowledge of the fracture behavior under differing stress conditions might help us better understand the resulting long-term flow implications.

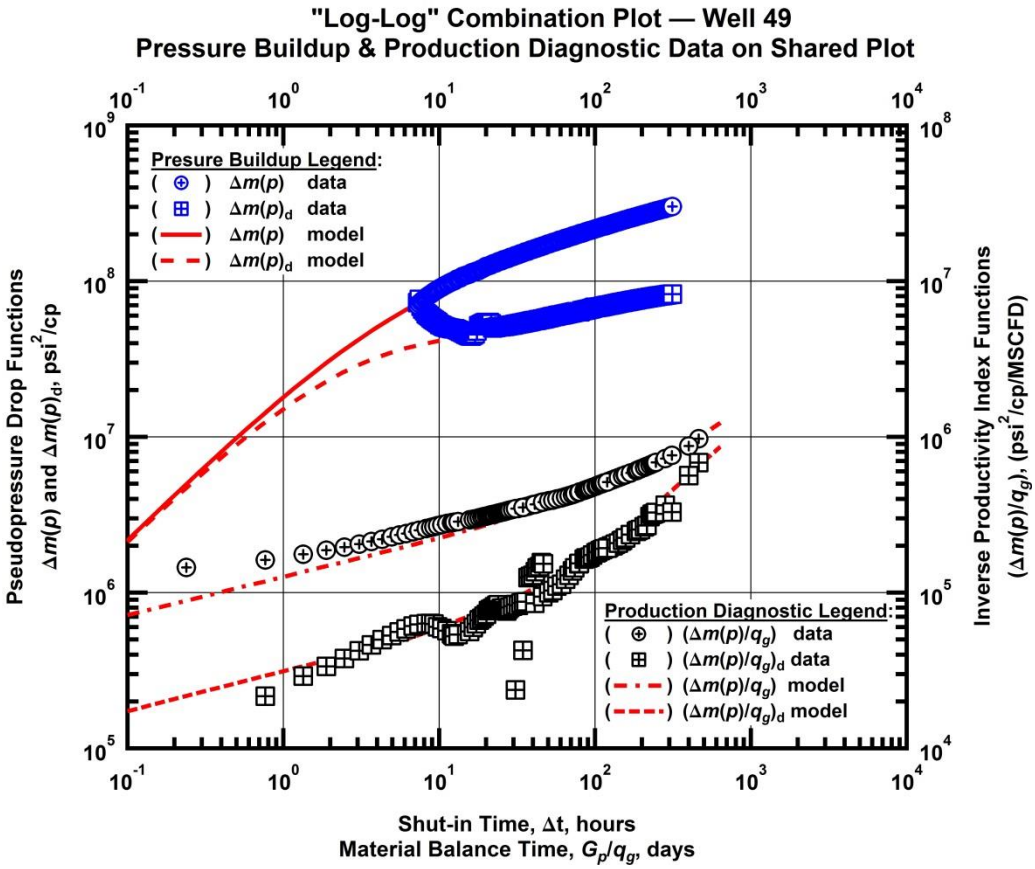

Figure 6.5 — (Log-log Plot): Combination diagnostic plot — pressure buildup and production data diagnostic curves for Well 49 with a unique model.

Table 6.3 — Key flow parameters in the model matching both the pressure buildup and production diagnostic data of Well 49.

Well	k (nD)	x_f (ft)	n_f (dimensionless)	F_c (md-ft)	C (bbl/psi)
49	220	360	36	1.2	5.5

For purposes of discussion we present in **Fig. 6.6** an un-modeled pressure buildup diagnostic plot. This test shows severe wellbore distortion effects in both the Bourdet derivative and the primary pressure derivative (green trend denoted by $dm(p)/dt$). We observe a "rollover" in the Bourdet derivative at 4 hours

which coincides with a spike and subsequently steeper slope in the primary pressure derivative. This is followed by a period of half-slope in the derivative from about 20 hours until 100 hours, suggesting linear flow. We take caution in investing much confidence in the diagnostics of this buildup test as the wellbore effects have distorted the composite signature and rendered the remainder of the test dubious. We felt it worth including this as an example of a faulty test that can occur as a result of numerous causes.

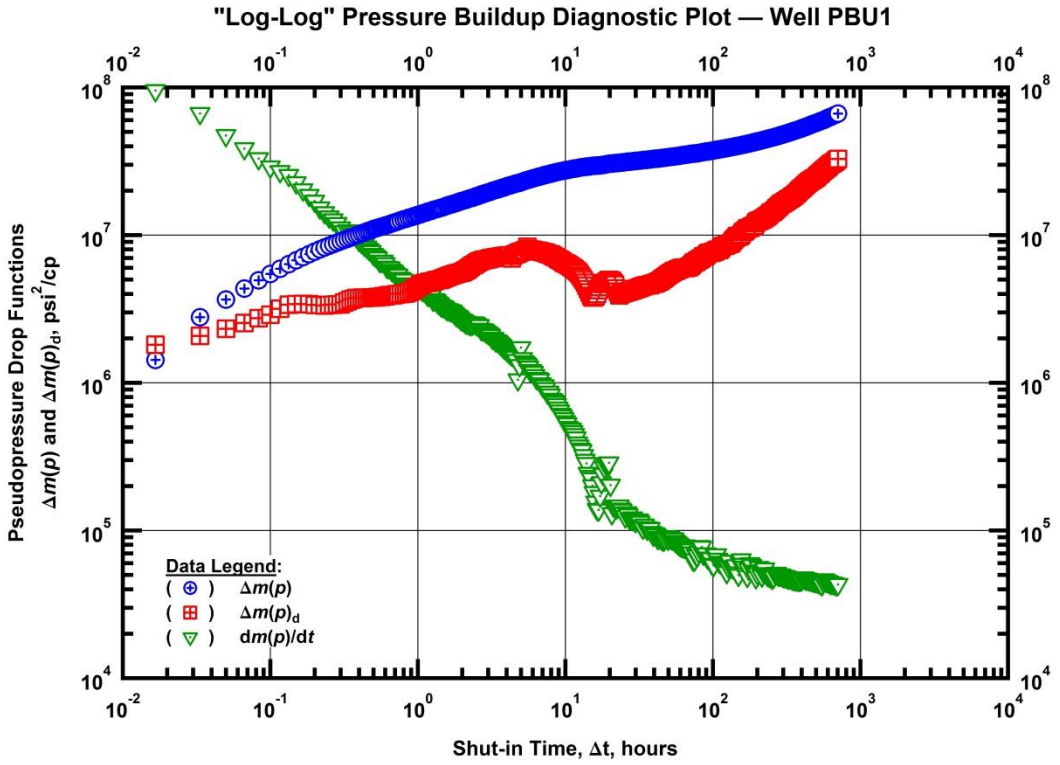

Figure 6.6 — (Log-log Plot): Pressure buildup diagnostic plot — pseudopressure drop, Bourdet derivative of pseudopressure drop and primary pressure derivative functions for Well PBU1.

6.2 Daily-Measured Surface Gauge Buildup Analysis

In this section we present multiple cases of pressure buildup tests performed from daily surface gauge readings. Traditionally, pressure transient analysis requires high-frequency data in order to obtain smooth numerical differentiation and thus to fully capture the minute signatures of the reservoir flow behavior. In the case of the wells in this study, being that they produce a very dry gas, we will demonstrate how plotting daily surface readings in the same manner as high-frequency bottomhole readings can produce clear diagnostic data curves that can also be modeled. We first demonstrate with the three examples of the previous section how closely the surface measurements reflect the bottomhole measurements.

Figs. 6.7 - 6.9 are the pressure buildup diagnostic plots with the daily surface data overlain on the high-frequency bottomhole data of Well 9, Well 49 and Well PBU1, respectively.

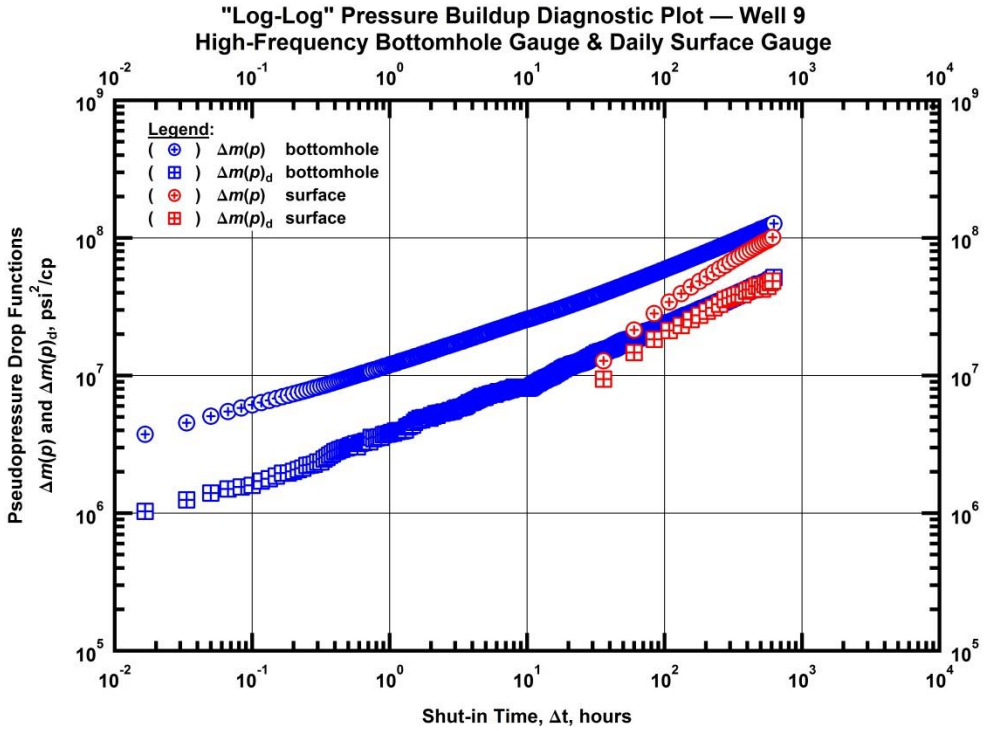

Figure 6.7 — (Log-log Plot): Pressure buildup diagnostic plot — high-frequency bottomhole gauge and daily surface gauge comparison for Well 9.

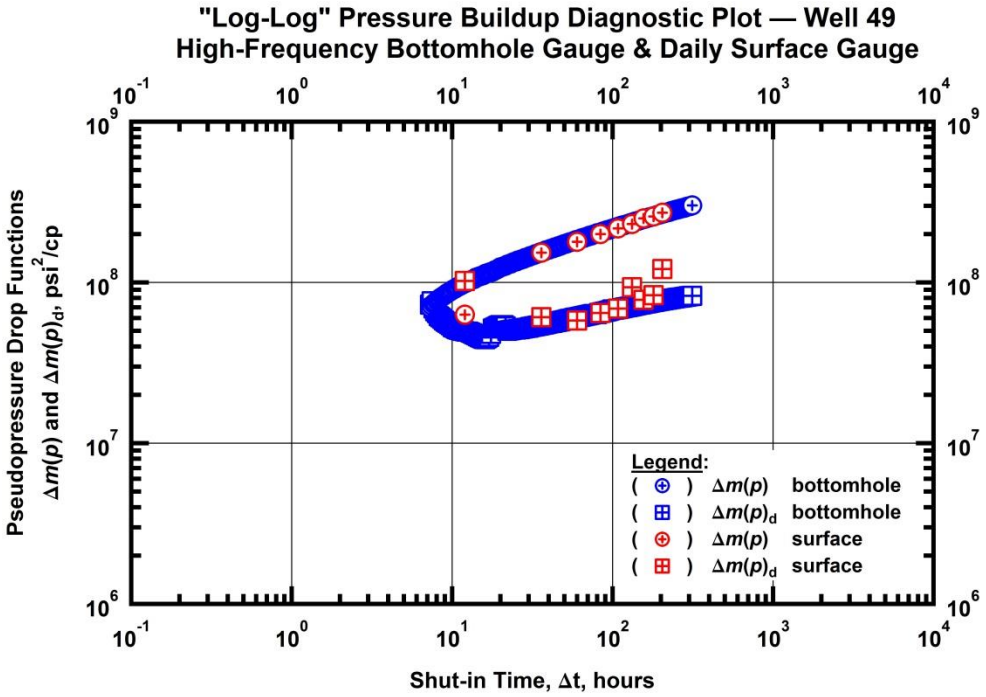

Figure 6.8 — (Log-log Plot): Pressure buildup diagnostic plot — high-frequency bottomhole gauge and daily surface gauge comparison for Well 49.

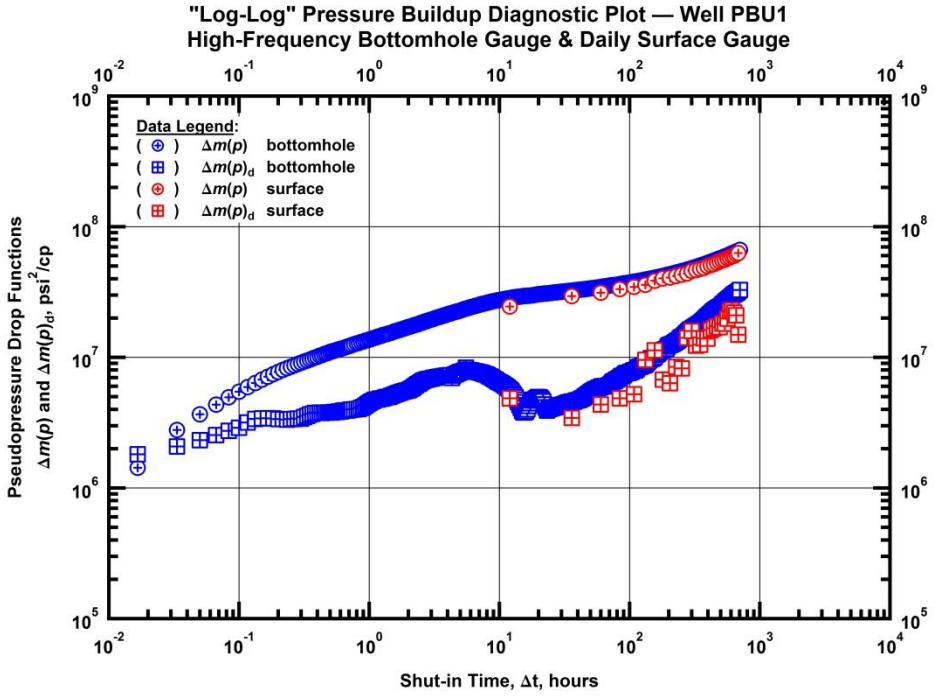

Figure 6.9 — (Log-log Plot): Pressure buildup diagnostic plot — high-frequency bottomhole gauge and daily surface gauge comparison for Well PBU1.

It is readily apparent from inspection of **Figs. 6.6 - 6.9** that the daily surface pressure buildup curves closely mimic the high-frequency bottomhole curves. In all cases the derivative overlay is of high enough quality to serve as a surrogate for the bottomhole data in an attempt to acquire a deliverability value (*k-xf*). In the case of Well 9, the pseudopressure drop curve from surface pressure does not model the bottomhole data, but the derivative confirms the diagnostic behavior of the bottomhole data.

It is with these three cases of surface gauge and bottomhole gauge diagnostic similarity that we proceed with cases of only daily surface buildup data. We plot them as we have done before and model them with analytical multi-fractured well models. We discuss diagnostic flow signatures we observe from the surface data and the parameters used for modeling these data and their interrelation with production data model analysis. We do this noting that we take caution in investing a great deal of confidence in the quantitative results from this exercise, however we maintain the benefit that can be derived from an alternate source of information.

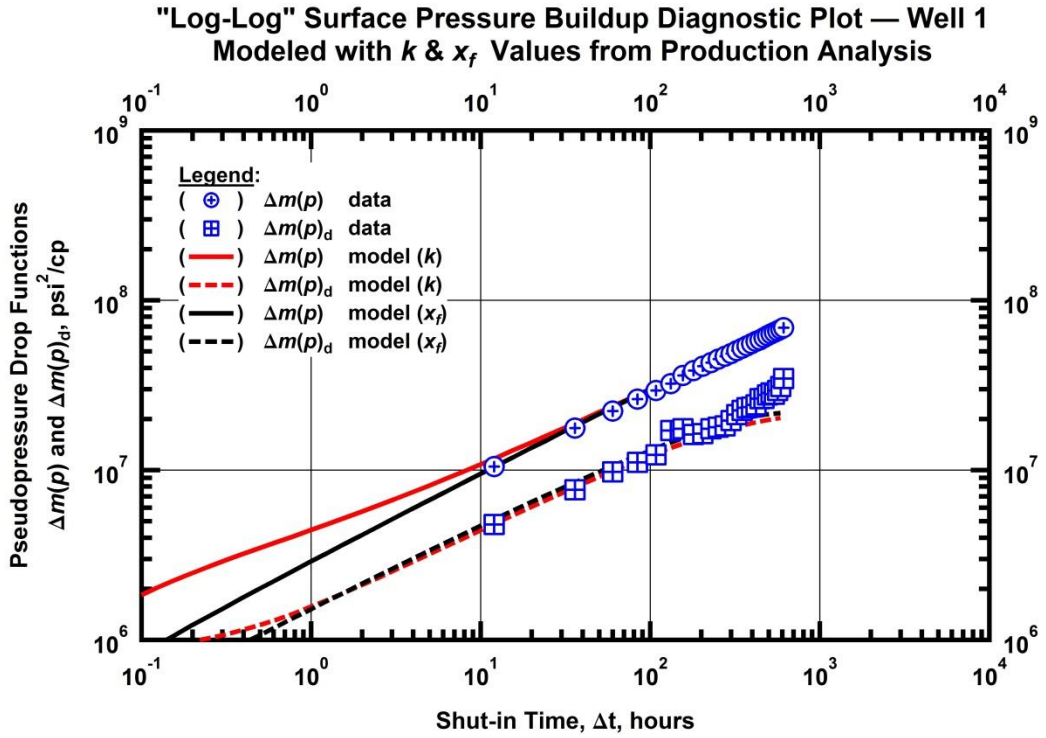

Figure 6.10 — (Log-log Plot): Pressure buildup diagnostic plot — daily surface pressure buildup response and model matches with parameters from production diagnostic analysis for Well 1.

In **Fig. 6.10** we show the daily surface pressure buildup response for Well 1. Diagnostically, the first thing that we observe is two parallel half-slope trends in the data functions. This suggests linear flow and high

conductivity fractures. The two models matching the data are derived from the production diagnostic model, however they are modeled with infinite conductivity fracture models. The red model is the match using the permeability value from production analysis and the black model is the match using the fracture half-length value from production analysis. Following the subtext of this chapter, the pressure buildup diagnostic for Well 1 suggests infinite-conductivity fracture, formation-linear flow while the production data diagnostic suggests lower-conductivity, bilinear flow.

We continue with the same procedure in **Fig. 6.11**, this time presenting Well 2. As with Well 1, we see half-slope behavior indicating that formation linear flow is the dominant regime during the shut-in period for Well 2. We combine the diagnostic buildup data for Wells 1 and 2 onto one plot in **Fig. 6.12** to illustrate the similarity in behavior.

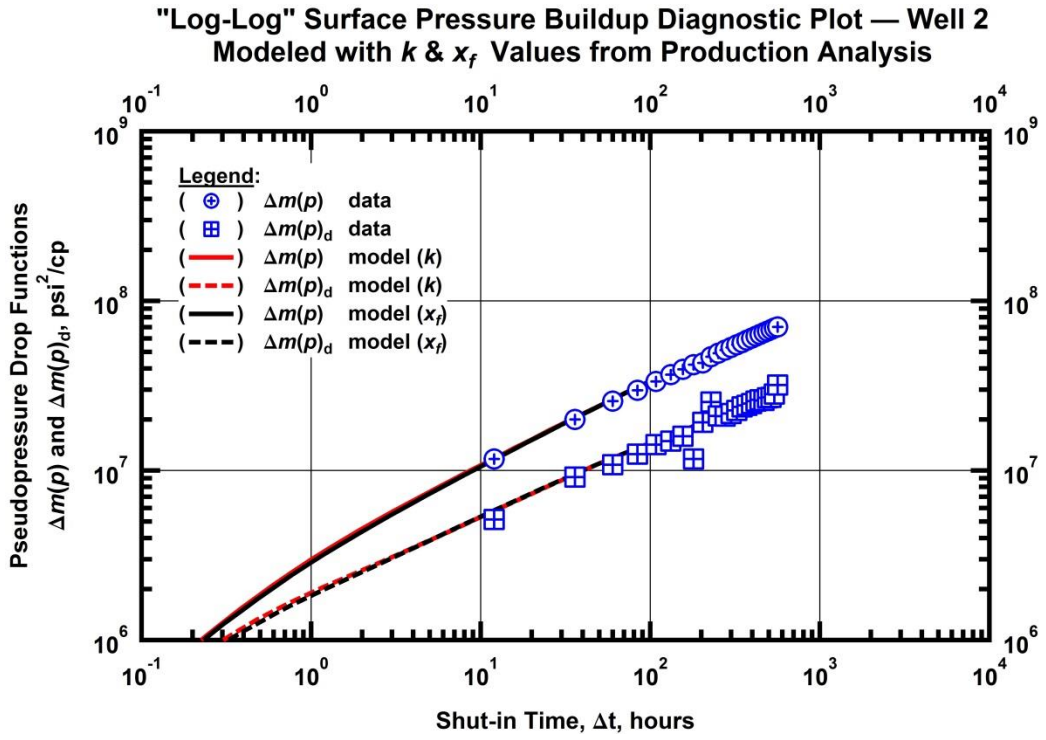

Figure 6.11 — (Log-log Plot): Pressure buildup diagnostic plot — daily surface pressure buildup response and model matches with parameters from production diagnostic analysis for Well 2.

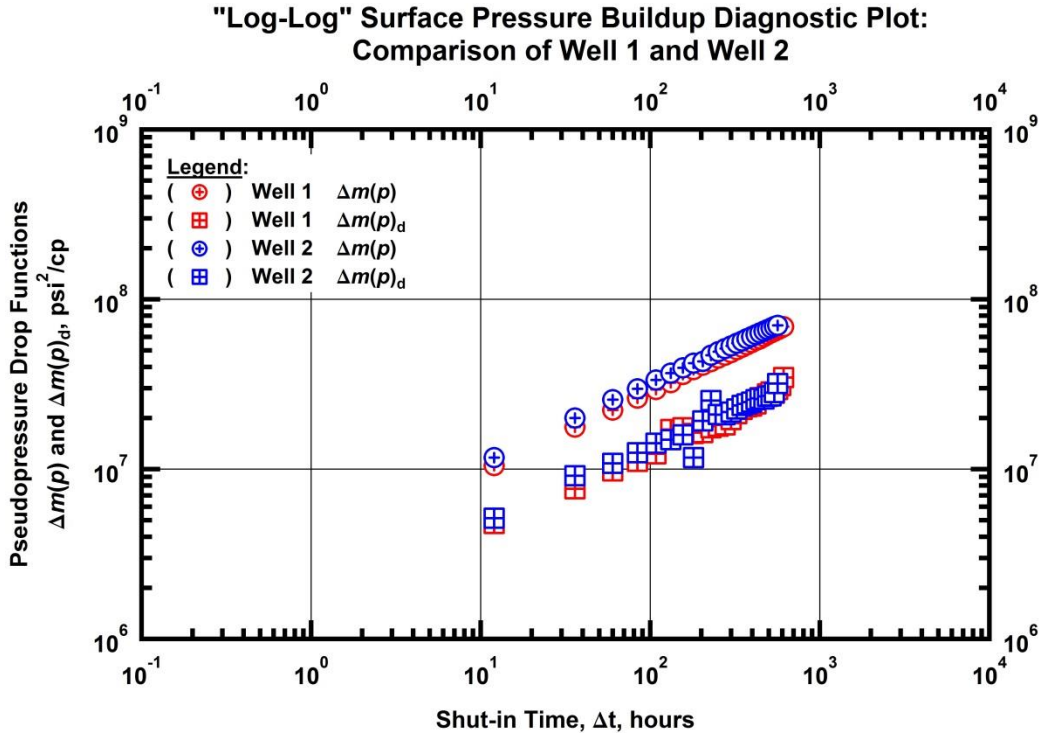

Figure 6.12 — (Log-log Plot): Pressure buildup diagnostic plot — daily surface pressure buildup response: comparison of Well 1 and Well 2.

If we apply a 10 percent downward shift to the Well 2 data in **Fig. 6.12** it will precisely overlay the data of Well 1. We performed a similar "shift" technique with these same two wells in the model-based production analysis chapter. The shift was more pronounced in the production data as the discrepancy between the two wells was greater.

We now introduce Well 10 as an additional illustration in the observed dichotomy of diagnostic flow regimes between drawdown and shut-in periods. **Fig. 6.13** is a "combination plot" in the same vein as **Fig. 6.5** where we've plotted both the pressure buildup response and the production data transient response on the same plot for comparison. The buildup data exhibits half-slope behavior while the production data exhibits quarter-slope behavior for the first 200 material balance days. The period after 200 material balance days that is not overlain by the "quarter-slope lines" corresponds to the flow period after the shut-in period.

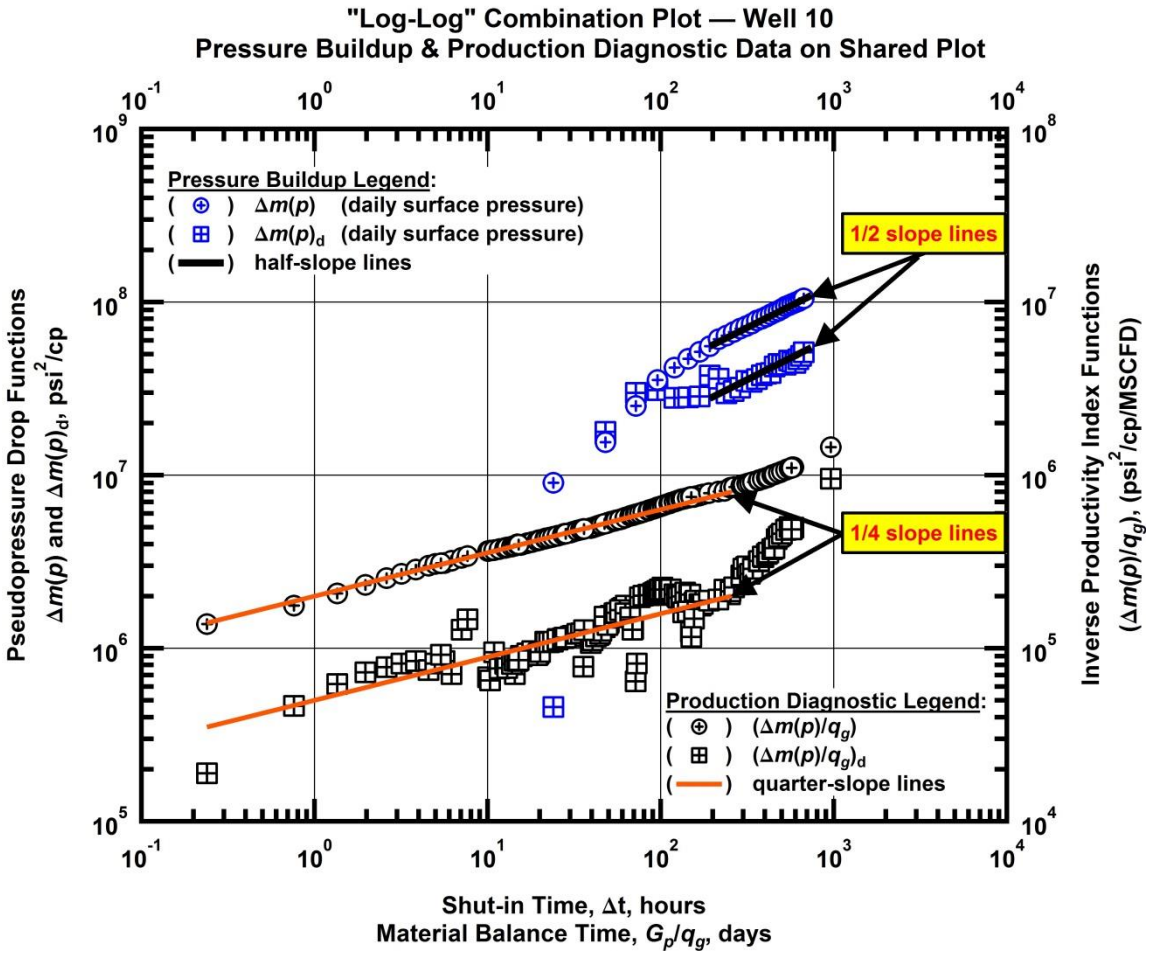

Figure 6.13 — (Log-log Plot): Combination diagnostic plot — pressure buildup and production data diagnostic curves for Well 10 with a diagnostic flow regime lines.

CHAPTER VII
SUMMARY, CONCLUSIONS, AND RECOMMENDATIONS FOR FUTURE WORK

7.1 Summary

In this work we have presented a multi-faceted well performance study on a group of 55 multiply-fractured horizontal shale wells. Included in the study is a comprehensive rate-time analysis using two modern rate-time relations: the modified hyperbolic relation and the power-law exponential model. We independently analyzed pressure-rate-time data in a model-based analysis scheme. Further, we integrated the rate-time analysis and model-based production analysis with a "tuning" technique where we modeled formation permeability to be a function of the modified hyperbolic *b*-parameter. We gained an improved correlation in *EUR* between the two analyses from this technique. Finally, we presented a collection of pressure buildup tests and discussed the diagnostic signatures characteristic of the individual wells and of the set as a whole.

7.2 Conclusions

1. The diagnostic *D*- and *b*- parameters from rate-time analysis exhibit hyperbolic decline character rather than power-law decline character for a majority of wells in this set.
2. The power-law exponential relation EUR values are more conservative than the modified hyperbolic relation EUR values and correlated more strongly with the EUR values from model-based production analysis than the "un-tuned" modified hyperbolic values.
3. An overwhelming majority of the 55 well sample exhibited primarily bilinear production data diagnostic character and thus they were modeled with low-conductivity fractures. Forty-five wells of the 55 well set were modeled with dimensionless fracture conductivity values of 20 or less.
4. The "tuning" technique used to model formation permeability as a function of the modified-hyperbolic *b*-parameter value slightly improved the EUR correlation between model-based production analysis and rate-time analysis.
5. We have observed multiple cases where diagnostic character of pressure buildup data differs from the diagnostic character of production drawdown data. Half-slope, infinite conductivity fracture behavior was the theme of pressure buildup analysis while quarter-slope, low-conductivity fracture flow was the theme of model-based production analysis.
6. Model-based production analysis is an effective tool even in cases of erratic production data.

7.3 Recommendations for Future Work

We recommend the following as worthy pursuits in the analysis of shale reservoir systems:

- Further investigation of the dichotomy of diagnostic flow behavior between a static shut-in period and a dynamic drawdown period. A permanent downhole pressure gauge would be an ideal scenario; however we have shown that for the case of dray gas wells, we can obtain reliable diagnostics from surface measurement.
- A more involved study of integrating rate-time parameters and well/reservoir properties. This is a challenging endeavor and its difficulty is a testament to the issue of non-uniqueness of model-based production analysis. High-quality data is imperative for this task.

NOMENCLATURE

b	Derivative of the loss ratio, dimensionless
C	Wellbore storage coefficient, bbl/psi
D	Loss ratio, D^{-1}
D_i	Initial decline constant for modified hyperbolic rate relation, D^{-1}
D_∞	Decline constant at "infinite time" for power-law exponential relation, D^{-1}
$\check{D}_i$	Decline constant for power-law exponential relation, D^{-1}
D_{limit}	Minimum D value where modified hyperbolic relation transitions to exponential decline, D^{-1}
EUR	Estimated Ultimate Recovery, BSCF
EUR_{MH}	Modified hyperbolic relation estimated ultimate recovery, BSCF
EUR_{PLE}	Power-law exponential relation estimated ultimate recovery, BSCF
F_c	Fracture conductivity, md-ft
F_{cD}	Dimensionless fracture conductivity, dimensionless
G_p	Cumulative gas production, BSCF
k	Formation permeability, nD
$m(p)$	Real gas pseudopressure, psi^2/cp
n	Time exponent for power-law exponential relation, dimensionless
n_f	Number of fractures, dimensionless
p	Pressure, psi
p_{wf}	Bottomhole flowing pressure, psi
p_{wfc}	Calculated bottomhole flowing pressure, psi
q_g	Gas flowrate, MSCF/D
q_{gi}	Initial gas flowrate, MSCF/D
t	Production time, days
t_e	Material balance time [i.e., $G_p(t)/q_g(t)$], days
τ	Integration variable of substitution for t, days
x_f	Fracture half-length, ft

REFERENCES

Aboaba, A. and Cheng, Y. 2010. Estimation of Fracture Properties for a Horizontal Well with Multiple Hydraulic Fractures in Gas Shale. Paper presented at the SPE Eastern Regional Meeting, Morgantown, West Virginia. SPE 138524.

Al-Ahmadi, H.A., Almarzooq, A.M., and Wattenbarger, R.A. 2010. Application of Linear Flow Analysis to Shale Gas Wells — Field Cases. Paper presented at the SPE Unconventional Gas Conference, Pittsburgh, Pennsylvania. SPE 130370.

Arps, J.J. 1944. Analysis of Decline Curves. Trans. AIME 160: 228-247.

Cheng, Y. 2011. Pressure Transient Characteristics of Hydraulically Fractured Horizontal Shale Gas Wells. Paper presented at the SPE Eastern Regional Meeting, Columbus, Ohio. SPE 149311.

Cinco-Ley, H., Samaniego, F.V., and Dominguez, N.A. 1978. Transient Pressure Behavior for a Well with a Finite-Conductivity Vertical Fracture. Society of Petroleum Engineers Journal. (August 1978) 253-264. SPE 6014.

Cinco-Ley, H. and Samaniego, F.V. 1981. Transient Pressure Analysis for Fractured Wells. Journal of Petroleum Technology. (September 1981) 1749-1766. SPE 7490-PA.

Gentry, R.W. and McCray A.W. 1978. The Effect of Reservoir and Fluid Properties on Production Decline Curves. Paper presented at the SPE-AIME Economics and Evaluation Symposium, Dallas, Texas. SPE 6341-PA.

Ilk, D. Okouma, V., and Blasingame, T.A. 2011a. Characterization of Well Performance in Unconventional Reservoirs using Production Data Diagnostics. Paper presented at the SPE Annual Technical Conference and Exhibition, Denver, Colorado. SPE 147604.

Ilk, D., Rushing, J.A., and Blasingame, T.A. 2011b. Integration of Production Analysis and Rate-time Analysis via Parametric Correlations — Theoretical Considerations and Practical Applications. Paper presented at the SPE Hydraulic Fracturing Technology Conference, The Woodlands, Texas. SPE 140556.

Ilk, D., Jenkins, C.D., and Blasingame, T.A. 2011c. Production Analysis in Unconventional Reservoirs — Diagnostics, Challenges, and Methodologies. Paper presented at the SPE North American Unconventional Gas Conference and Exhibition, The Woodlands, Texas. SPE 144376.

Johnson R.H. and Bollens, A.L. 1927. The Loss Ratio Method of Extrapolating Oil Well Decline Curves. Trans. AIME 77:771-778.

Larson, L. and Hegre, T.M. 1994. Pressure Transient Analysis of Multifractured Horizontal Wells. Paper presented at the SPE 69th Annual Technical Conference and Exhibition, New Orleans, Louisiana. SPE 28389.

Lewis, J.O. and Beal, C.H. 1918. Some New Methods for Estimating the Future Production of Oil Wells. Trans. AIME 59: 492-525.

Maley, S. 1985. The Use of Conventional Decline Curve Analysis in Tight Gas Well Applications. Paper presented at the SPE/DOE Low Permeability Gas Reservoirs Symposium, Denver, Colorado. SPE 13898-MS.

Mayerhofer, M.J., Stegent, N.A., Barth, J.O., and Ryan, K.M. 2011. Integrating Fracture Diagnostics and Engineering Data in the Marcellus Shale. Paper presented at the SPE Annual Technical Conference and Exhibition, Denver, Colorado. SPE 145463.

APPENDIX A

INVENTORY OF WELL AND RESERVOIR DATA

We include an inventory of the parameters used in modeling the rate-time data and the pressure-rate-time data. **Table A1** is a summary of the model parameter values from the modified hyperbolic decline relation. **Table A2** is the collection of the power-law exponential model parameter values. **Table A3** consists of the model-based production analysis parameters.

Table A1 — Modified hyperbolic rate-time relation match parameters.

Well	q_{gi} (MSCF/D)	D_{limit} (%)	D_i (D^{-1})	b (dimensionless)	EUR_{MH} (BSCF)
1	8,760	55	0.12	2.2	1.03
2	2,125	10	0.01	0.7	0.91
3	11,067	10	0.84	2.3	1.93
4	2,029	10	0.00	1.9	2.88
5	1,615	10	0.00	1.3	1.79
6	3,080	10	0.00	1.1	3.91
7	4,282	10	0.00	1.7	5.44
8	2,235	10	0.00	0.9	2.63
9	8,031	10	0.01	1.3	4.79
10	4,292	10	0.04	3.8	6.36
11	3,072	10	0.01	1.3	2.36
12	2,567	10	0.03	2.0	1.50
13	4,098	10	0.18	2.5	1.72
14	2,591	10	0.08	2.5	1.48
15	4,849	10	0.01	1.7	4.99
16	5,646	10	0.01	1.6	3.97
17	5,981	10	0.01	1.5	5.22
18	5,161	10	0.00	1.7	7.40
19	9,786	10	0.03	1.9	6.70
20	8,663	10	0.45	3.5	6.87
21	12,094	10	0.03	1.4	1.85
22	4,739	10	0.01	1.3	2.35
23	7,480	10	0.26	3.9	5.78

A1 Continued

Well	q_{gi} (MSCF/D)	D_{limit} (%)	D_i (D^{-1})	b (dimensionless)	EUR_{MH} (BSCF)
24	8,808	10	0.37	4.0	6.63
25	8,871	10	0.20	3.3	5.75
26	2,854	10	0.00	1.3	2.89
27	2,597	10	0.01	1.5	2.37
28	2,907	10	0.00	1.0	2.77
29	2,298	10	0.00	1.8	3.90
30	5,885	10	0.07	2.8	4.84
31	3,772	10	0.01	1.7	4.18
32	4,783	63	0.33	4.0	0.97
33	4,402	10	0.00	1.5	5.82
34	3,536	10	0.01	1.5	3.23
35	13,256	10	0.37	2.6	4.51
36	8,342	10	0.11	1.7	1.94
37	5,738	10	0.50	3.6	3.30
38	5,954	10	0.10	2.4	3.24
39	1,960	10	0.01	2.0	2.83
40	1,825	10	0.01	2.5	2.77
41	1,916	10	0.00	2.1	3.02
42	2,346	10	0.01	2.6	3.11
43	2,591	10	0.00	1.9	3.73
44	5,607	10	0.06	2.9	4.37
45	3,525	10	0.00	1.4	4.46
46	3,691	10	0.02	3.0	4.65
47	7,061	10	0.08	4.0	10.50
48	2,874	10	0.00	2.4	6.66
49	9,976	10	0.02	1.9	7.16
50	4,302	10	0.01	2.5	6.94
51	3,472	10	0.07	2.8	2.53
52	7,275	10	0.01	1.1	5.62
53	10,460	10	0.01	1.3	6.32
54	10,480	10	0.15	2.3	3.81
55	7,394	10	0.03	1.7	3.64

Table A2 — Power-law exponential rate-time relation match parameters.

Well	q_{gi} (MSCF/D)	n (dimensionless)	$\check{D}_i$ (D^{-1})	D_∞ (D^{-1})	EUR_{PLE} (BSCF)
1	139,693	0.093	2.70	1.4E-03	1.04
2	4,567	0.310	0.35	1.0E-14	1.00
3	11,301	0.166	1.08	1.0E-14	2.07
4	2,921	0.360	0.14	1.0E-14	2.76
5	1,715	0.450	0.07	1.0E-14	1.63
6	3,627	0.490	0.05	1.0E-14	3.82
7	6,980	0.342	0.17	1.0E-14	5.17
8	4,042	0.370	0.13	1.0E-14	3.32
9	9,116	0.440	0.11	1.0E-14	3.56
10	4,330	0.300	0.18	1.0E-14	7.04
11	4,270	0.384	0.15	1.0E-14	1.98
12	10,952	0.175	1.07	1.0E-14	1.47
13	8,619	0.140	1.20	1.0E-14	2.26
14	5,899	0.140	1.10	1.0E-14	2.09
15	6,057	0.352	0.15	1.0E-14	5.10
16	8,990	0.326	0.25	1.0E-14	3.30
17	9,083	0.350	0.19	1.0E-14	4.57
18	6,513	0.430	0.08	1.0E-14	6.75
19	14,223	0.330	0.26	1.0E-14	4.73
20	16,383	0.200	0.68	1.0E-14	5.96
21	16,227	0.244	0.74	1.0E-14	1.41
22	4,525	0.338	0.20	1.0E-14	2.41
23	5,151	0.300	0.20	1.0E-14	5.64
24	14,789	0.110	0.96	1.0E-14	15.08
25	5,935	0.215	0.31	1.0E-14	10.24
26	7,778	0.279	0.37	1.0E-14	2.80
27	3,472	0.370	0.15	1.0E-14	2.15
28	3,393	0.480	0.06	1.0E-14	2.56
29	2,861	0.451	0.06	1.0E-14	3.34
30	7,035	0.232	0.43	1.0E-14	5.16
31	4,849	0.380	0.13	1.0E-14	3.85
32	3,308	0.550	0.05	1.0E-14	1.42
33	4,940	0.460	0.06	1.0E-14	5.49
34	4,474	0.375	0.14	1.0E-14	3.09
35	5,938	0.215	0.45	1.0E-14	5.13
36	64,238	0.138	2.05	1.0E-14	1.74

A2 Continued

Well	q_{gi} (MSCF/D)	n (dimensionless)	$\check{D}_i$ (D^{-1})	D_∞ (D^{-1})	EUR_{PLE} (BSCF)
37	21,696	0.120	1.58	1.0E-14	3.65
38	4,278	0.284	0.28	1.0E-14	3.24
39	2,579	0.370	0.12	1.0E-14	2.74
40	2,215	0.400	0.09	1.0E-14	2.39
41	2,174	0.472	0.05	1.0E-14	2.49
42	2,941	0.330	0.16	1.0E-14	3.15
43	3,496	0.380	0.11	1.0E-14	3.58
44	7,599	0.240	0.43	1.0E-14	4.21
45	4,422	0.366	0.08	1.2E-04	6.30
46	4,157	0.287	0.18	1.0E-14	6.60
47	195,454	0.051	3.28	2.8E-04	5.51
48	24,350	0.067	1.76	3.3E-04	3.97
49	37,325	0.071	1.70	5.0E-04	5.48
50	7,225	0.276	0.25	1.0E-14	7.69
51	5,556	0.219	0.56	1.0E-14	2.36
52	7,311	0.540	0.04	1.0E-14	5.53
53	11,637	0.540	0.05	1.0E-14	4.52
54	43,496	0.144	1.54	1.0E-14	3.73
55	9,769	0.350	0.27	1.0E-14	2.12

Table A3 — Well/reservoir model properties from model-based production analysis.

Well	k (nD)	x_f (ft)	F_c (md-ft)	F_{cD} (dimensionless)	EUR (BSCF)
1	260	180	1.00	21	1.92
2	230	100	0.42	18	1.41
3	155	115	0.36	20	1.59
4	190	215	0.19	5	2.61
5	255	220	0.67	12	2.42
6	275	300	0.25	3	3.58
7	235	600	0.35	3	3.99
8	78	325	0.23	9	2.58
9	260	350	1.30	14	3.98
10	250	245	0.60	10	3.93
11	210	310	0.50	8	1.79
12	210	130	0.80	29	1.5
13	180	300	0.27	5	1.39
14	160	240	0.21	6	0.96
15	220	340	0.50	7	3.79
16	230	300	0.81	12	3.7
17	240	340	0.75	9	3.85
18	225	250	0.70	13	4.83
19	210	230	0.76	16	3.18
20	210	165	0.20	6	2.67
21	240	109	0.18	7	1.87
22	175	275	0.50	10	1.88
23	100	205	0.12	6	2.41
24	80	175	0.08	6	2.9
25	90	180	0.06	4	2.98
26	245	190	1.50	32	2.3
27	235	325	0.40	5	2.02
28	240	335	0.70	9	2.52
29	220	235	1.20	23	2.84
30	200	350	4.00	57	2.56
31	215	255	1.10	20	2.93
32	260	215	0.34	6	2.91
33	240	370	1.33	15	4.35
34	245	275	0.75	11	1.99
35	70	95	1.20	180	1.86

A3 Continued

Well	k (nD)	x_f (ft)	F_c (md-ft)	F_{cD} (dimensionless)	EUR (BSCF)
36	80	75	1.80	300	1.85
37	60	95	0.04	7	1.58
38	170	300	2.62	51	1.75
39	185	380	0.50	7	2.11
40	150	320	0.60	4	1.78
41	180	280	0.25	5	2.09
42	145	280	0.20	5	1.8
43	200	350	0.45	6	2.26
44	100	200	0.15	8	2.32
45	205	450	0.97	11	2.87
46	195	490	0.65	7	2.81
47	200	410	0.75	9	4.25
48	185	450	0.49	6	3.26
49	220	400	0.65	7	4.1
50	200	325	0.98	15	4.09
51	60	58	0.02	6	1.83
52	200	255	9.18	180	3.3
53	150	560	2.50	30	4.52
54	180	140	1.25	50	2.27
55	210	230	0.35	7	2.18

APPENDIX B
RATE-TIME ANALYSIS

We present the *qDb* analysis plots for the modified hyperbolic and power-law exponential rate-decline models.

Modified Hyperbolic Models

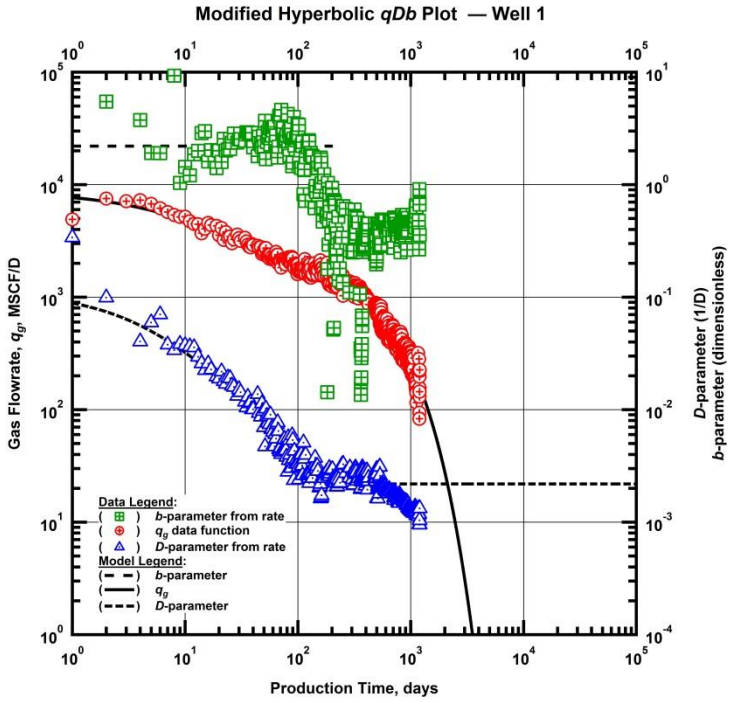

Figure B1 — (Log-log Plot): *qDb* plot — gas flow rate (q_{gi}), *D*- and *b*-parameters versus production time and modified hyperbolic model matches for Well 1.

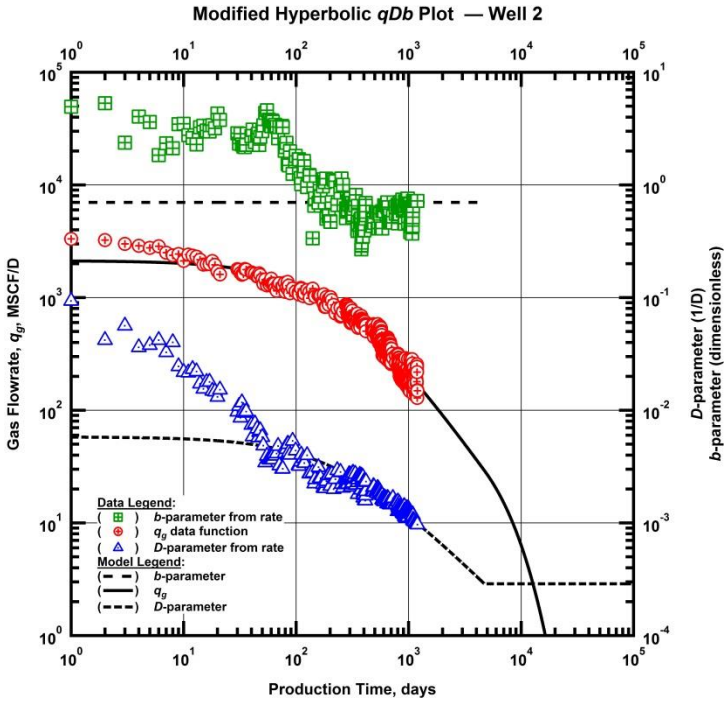

Figure B2 — (Log-log Plot): *qDb* plot — gas flow rate (q_{gi}), *D*- and *b*-parameters versus production time and modified hyperbolic model matches for Well 2.

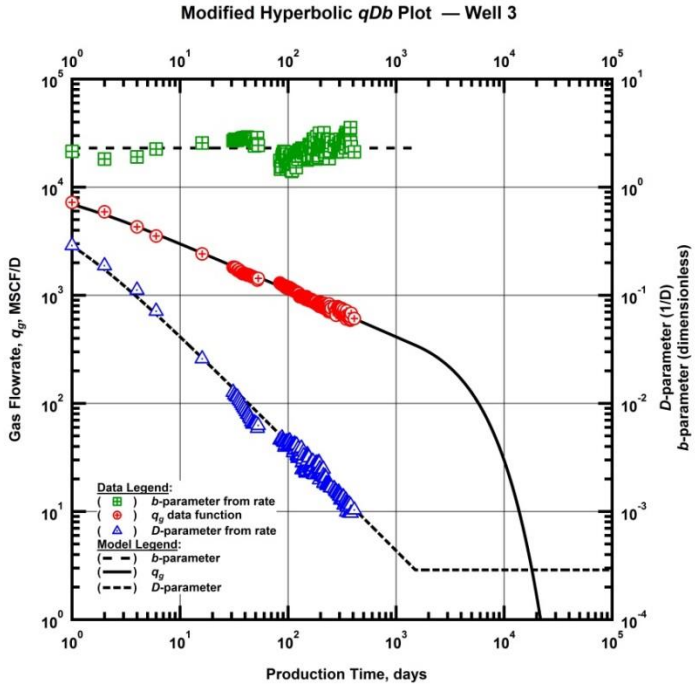

Figure B3 — (Log-log Plot): *qDb* plot — gas flow rate (q_{gi}), *D*- and *b*-parameters versus production time and modified hyperbolic model matches for Well 3.

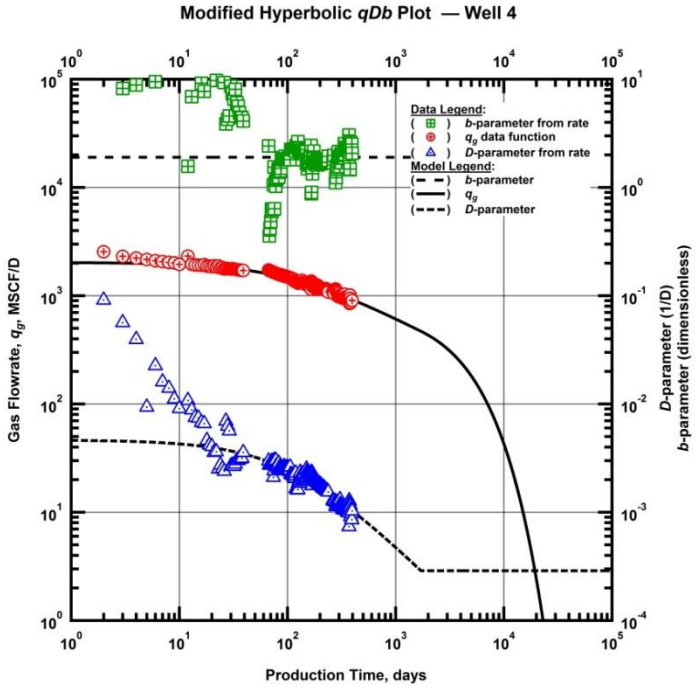

Figure B4 — (Log-log Plot): *qDb* plot — gas flow rate (q_{gi}), *D*- and *b*-parameters versus production time and modified hyperbolic model matches for Well 4.

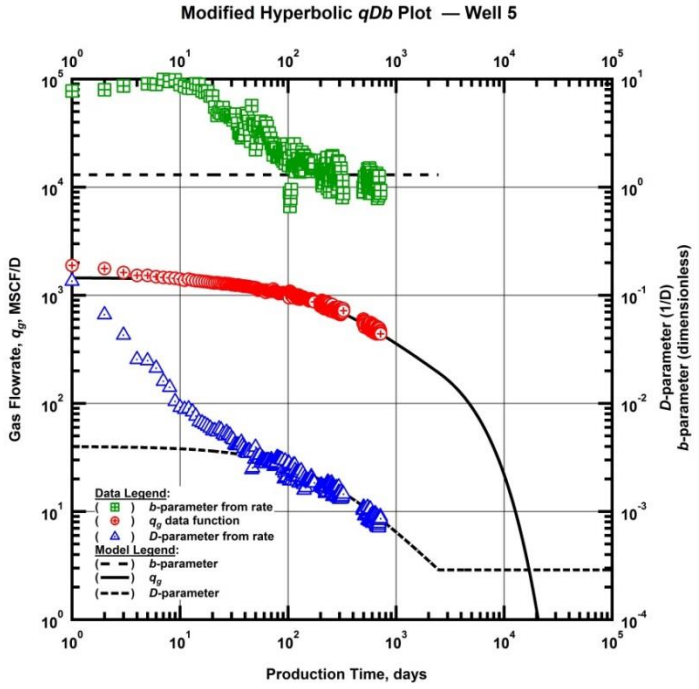

Figure B5 — (Log-log Plot): *qDb* plot — gas flow rate (q_{gi}), *D*- and *b*-parameters versus production time and modified hyperbolic model matches for Well 5.

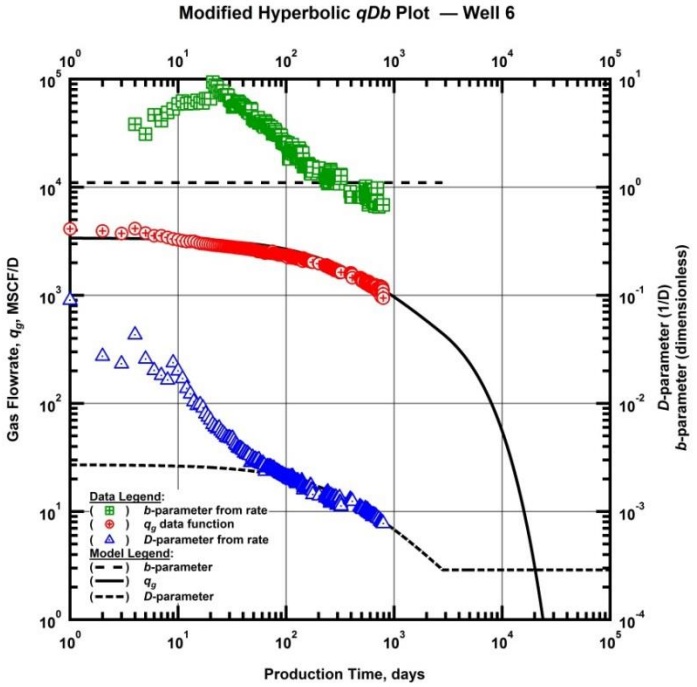

Figure B6 — (Log-log Plot): *qDb* plot — gas flow rate (q_{gi}), *D*- and *b*-parameters versus production time and modified hyperbolic model matches for Well 6.

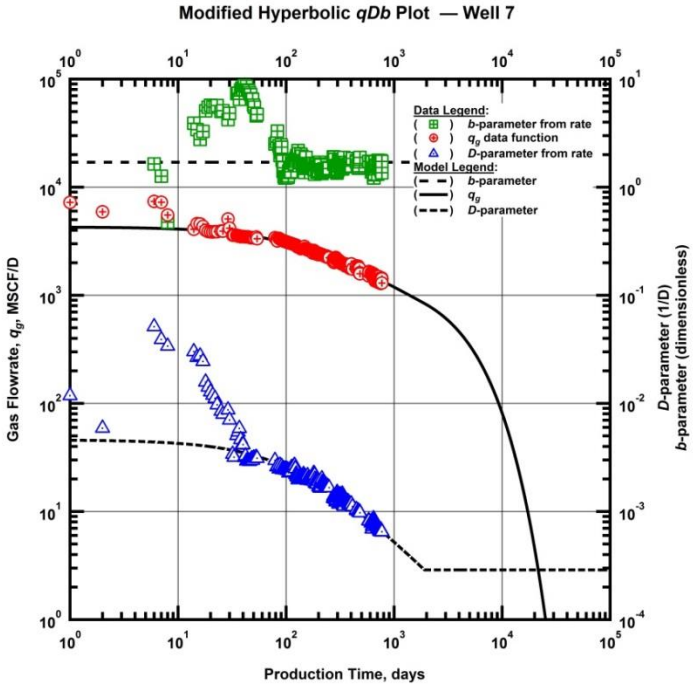

Figure B7 — (Log-log Plot): *qDb* plot — gas flow rate (q_{gi}), *D*- and *b*-parameters versus production time and modified hyperbolic model matches for Well 7.

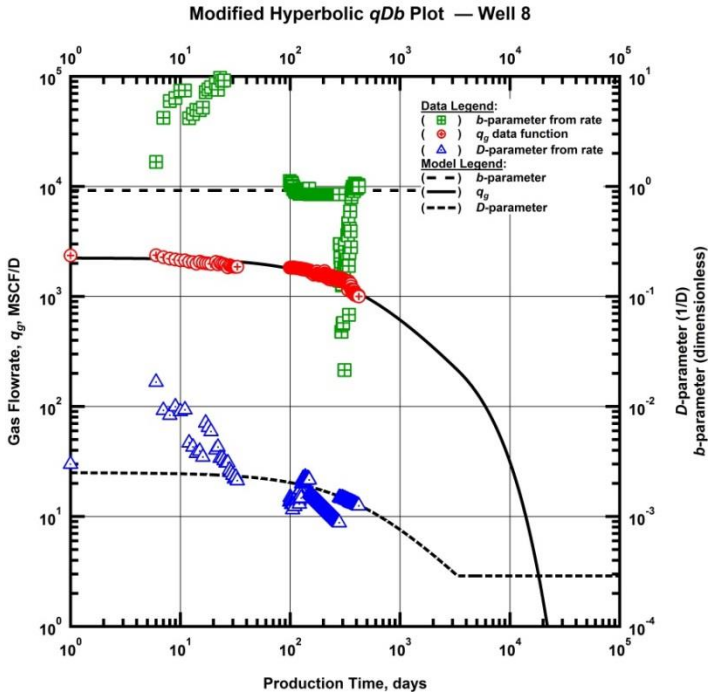

Figure B8 — (Log-log Plot): *qDb* plot — gas flow rate (q_{gi}), *D*- and *b*-parameters versus production time and modified hyperbolic model matches for Well 8.

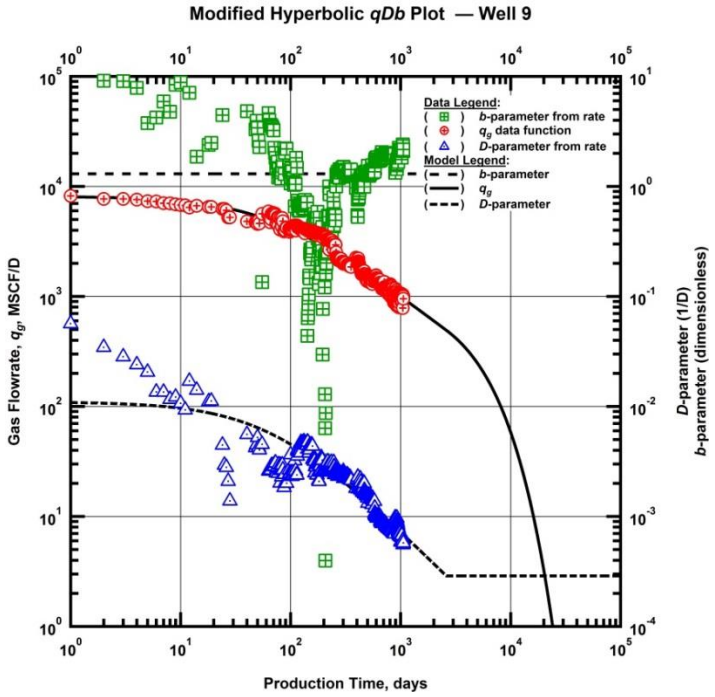

Figure B9 — (Log-log Plot): *qDb* plot — gas flow rate (q_{gi}), *D*- and *b*-parameters versus production time and modified hyperbolic model matches for Well 9.

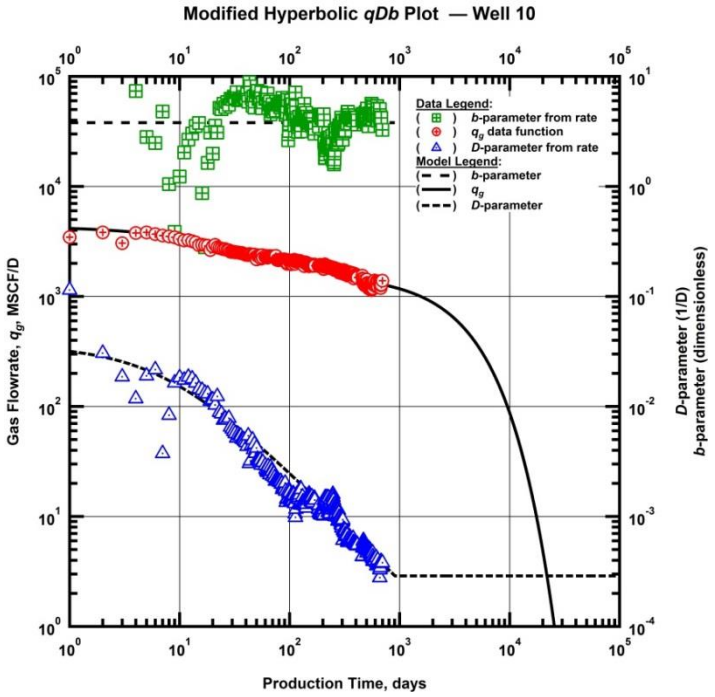

Figure B10 — (Log-log Plot): *qDb* plot — gas flow rate (q_{gi}), *D*- and *b*-parameters versus production time and modified hyperbolic model matches for Well 10.

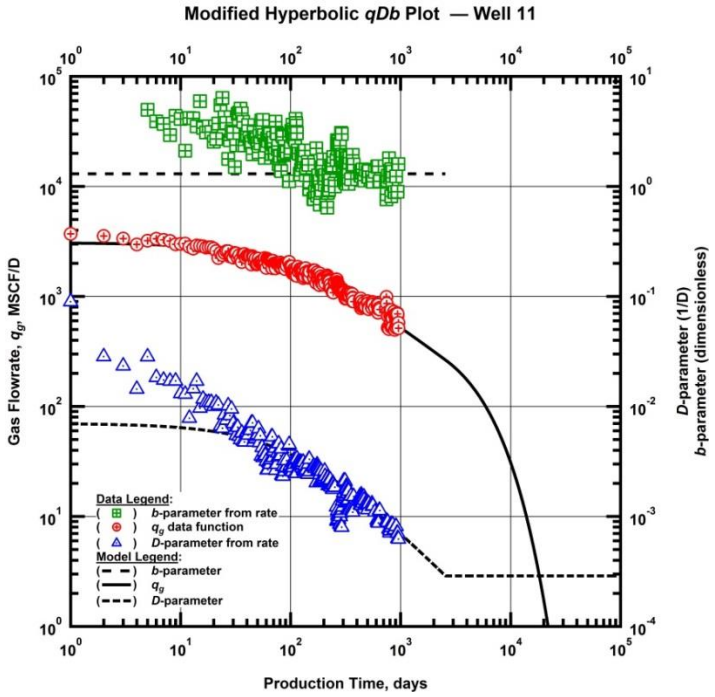

Figure B11 — (Log-log Plot): *qDb* plot — gas flow rate (q_{gi}), *D*- and *b*-parameters versus production time and modified hyperbolic model matches for Well 11.

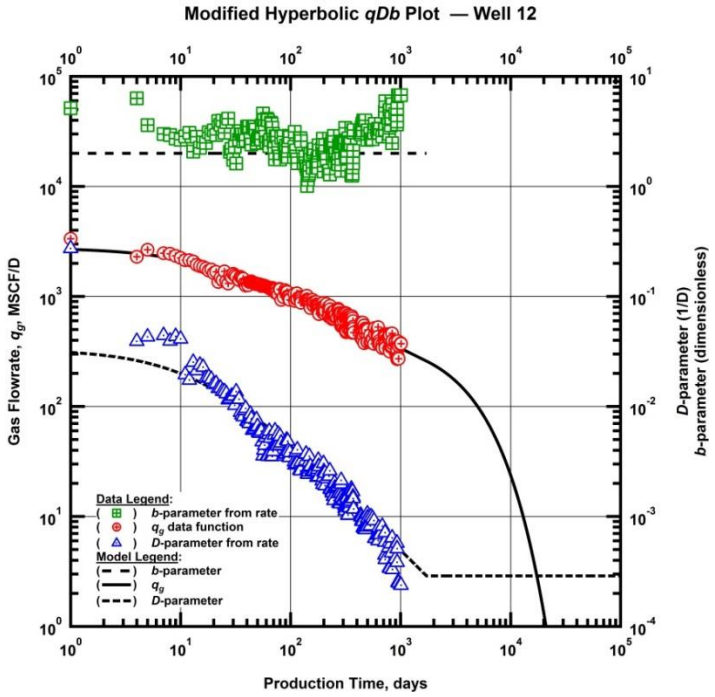

Figure B12 — (Log-log Plot): *qDb* plot — gas flow rate (q_{gi}), *D*- and *b*-parameters versus production time and modified hyperbolic model matches for Well 12.

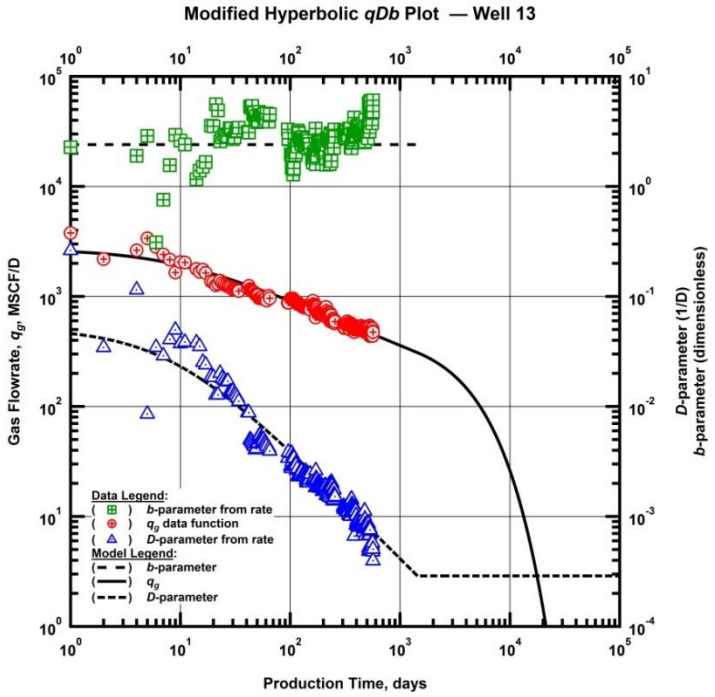

Figure B13 — (Log-log Plot): *qDb* plot — gas flow rate (q_{gi}), *D*- and *b*-parameters versus production time and modified hyperbolic model matches for Well 13.

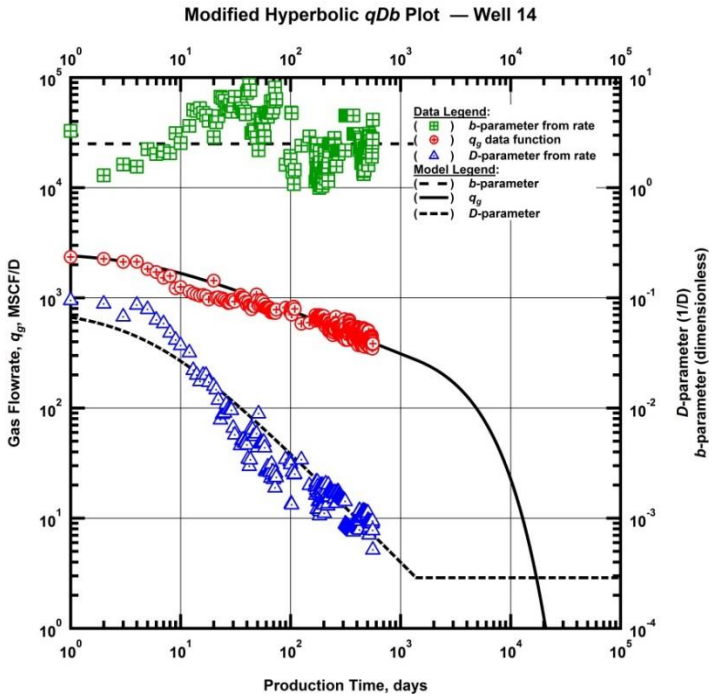

Figure B14 — (Log-log Plot): *qDb* plot — gas flow rate (q_{gi}), *D*- and *b*-parameters versus production time and modified hyperbolic model matches for Well 14.

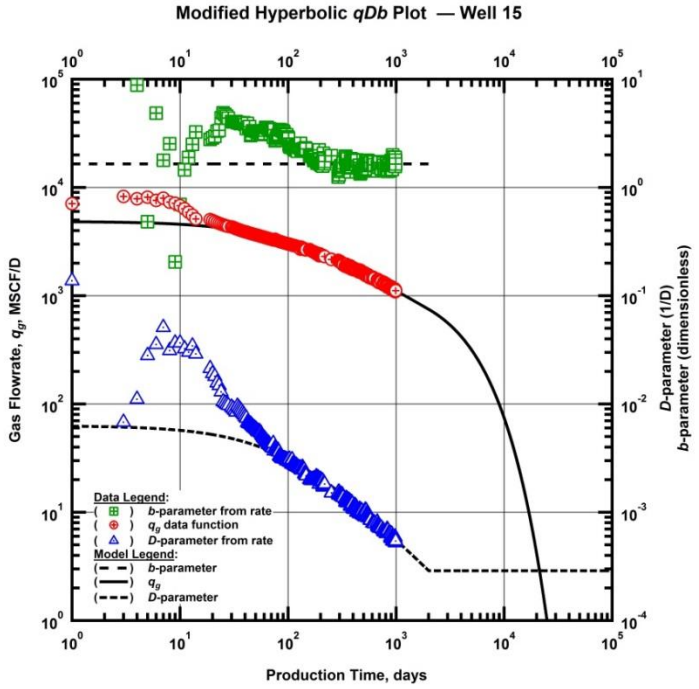

Figure B15 — (Log-log Plot): *qDb* plot — gas flow rate (q_{gi}), *D*- and *b*-parameters versus production time and modified hyperbolic model matches for Well 15.

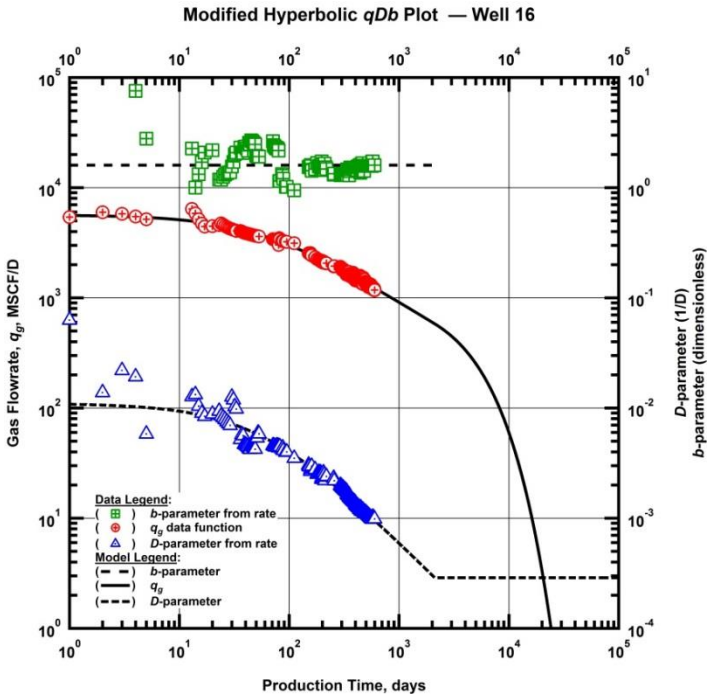

Figure B16 — (Log-log Plot): *qDb* plot — gas flow rate (q_{gi}), *D*- and *b*-parameters versus production time and modified hyperbolic model matches for Well 16.

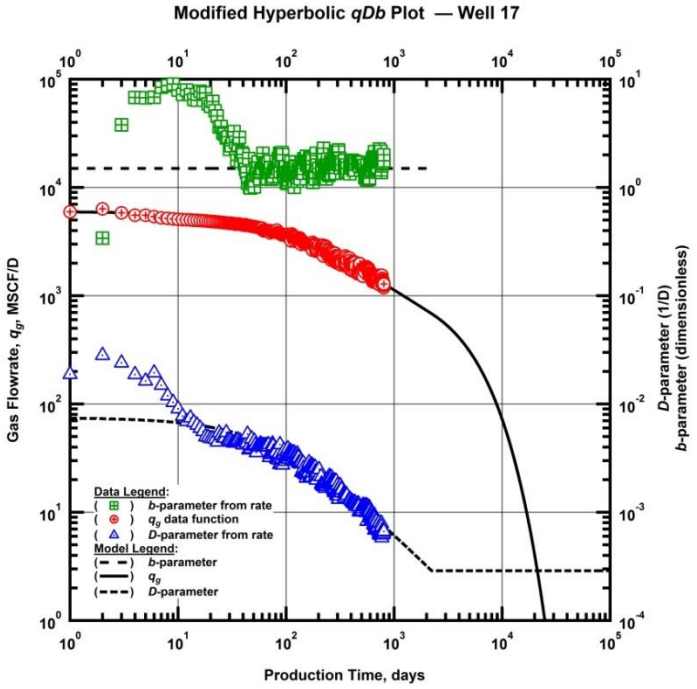

Figure B17 — (Log-log Plot): *qDb* plot — gas flow rate (q_{gi}), *D*- and *b*-parameters versus production time and modified hyperbolic model matches for Well 17.

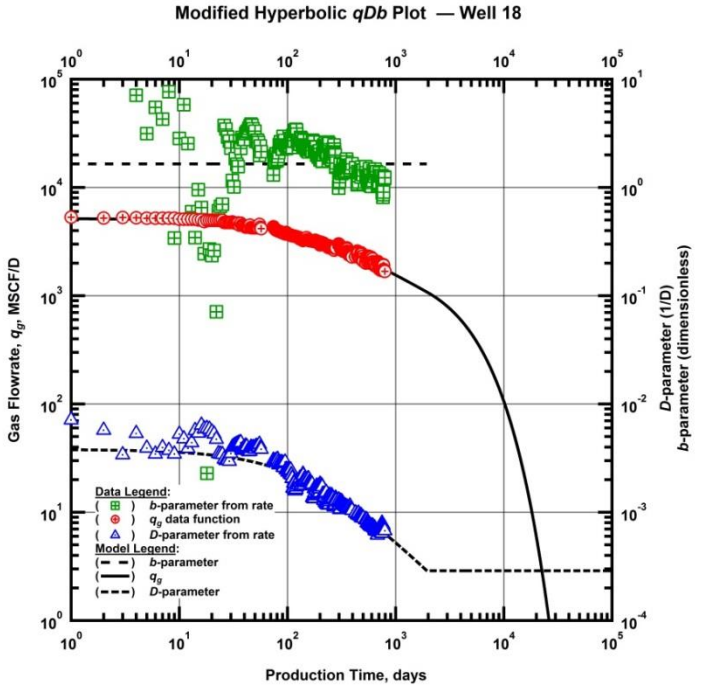

Figure B18 — (Log-log Plot): *qDb* plot — gas flow rate (q_{gi}), *D*- and *b*-parameters versus production time and modified hyperbolic model matches for Well 18.

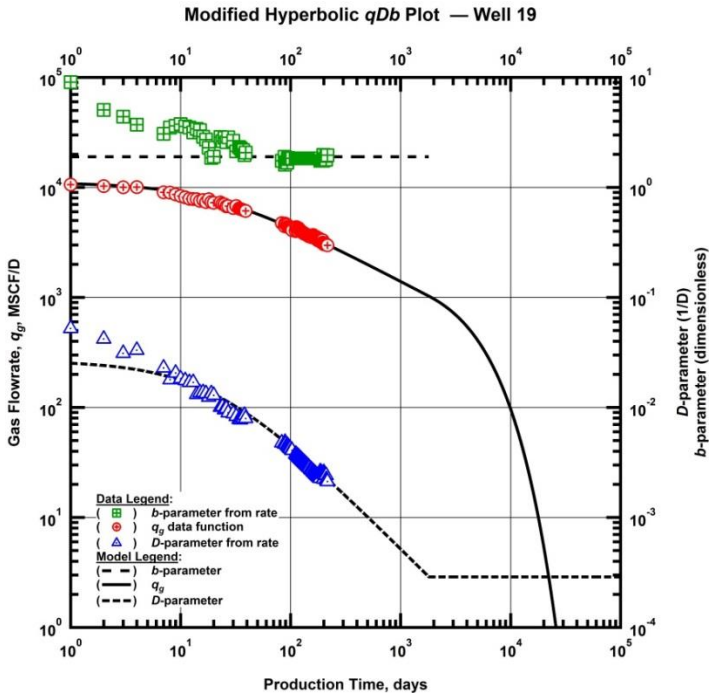

Figure B19 — (Log-log Plot): *qDb* plot — gas flow rate (q_{gi}), *D*- and *b*-parameters versus production time and modified hyperbolic model matches for Well 19.

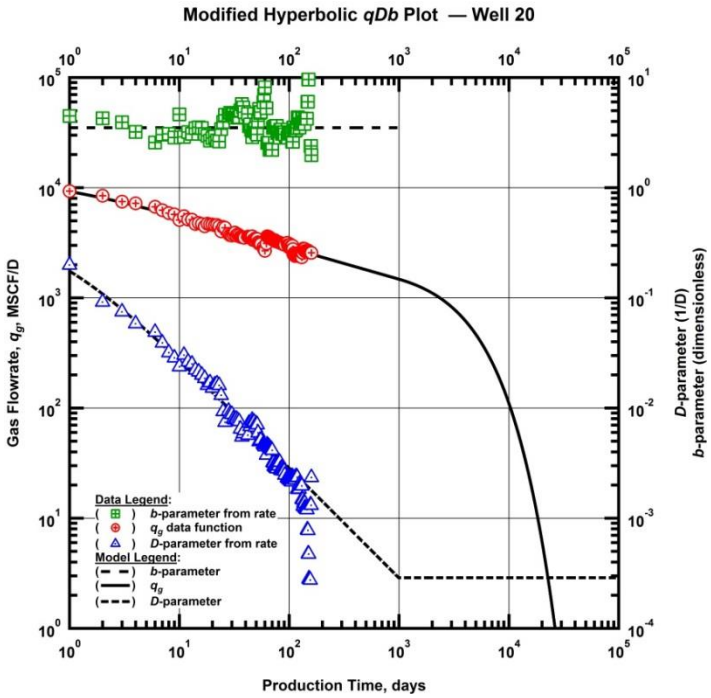

Figure B20 — (Log-log Plot): *qDb* plot — gas flow rate (q_{gi}), *D*- and *b*-parameters versus production time and modified hyperbolic model matches for Well 20.

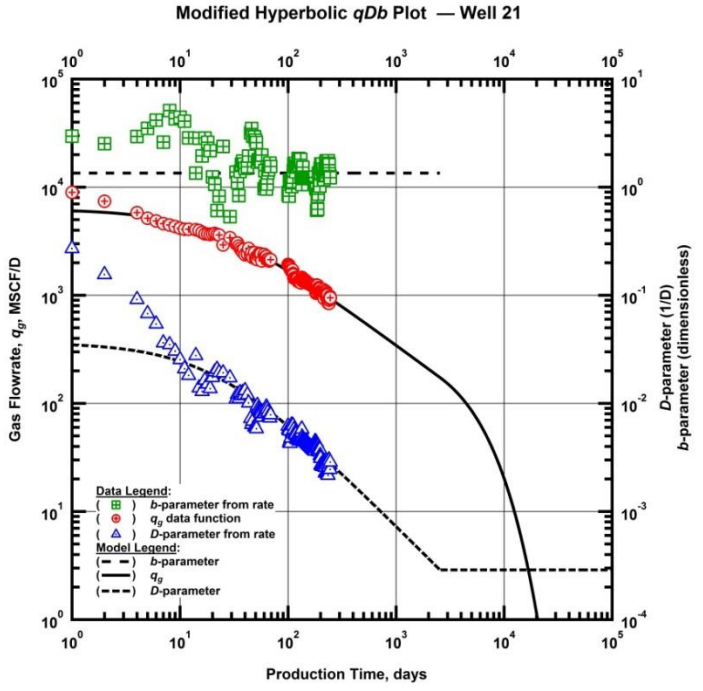

Figure B21 — (Log-log Plot): *qDb* plot — gas flow rate (q_{gi}), *D*- and *b*-parameters versus production time and modified hyperbolic model matches for Well 21.

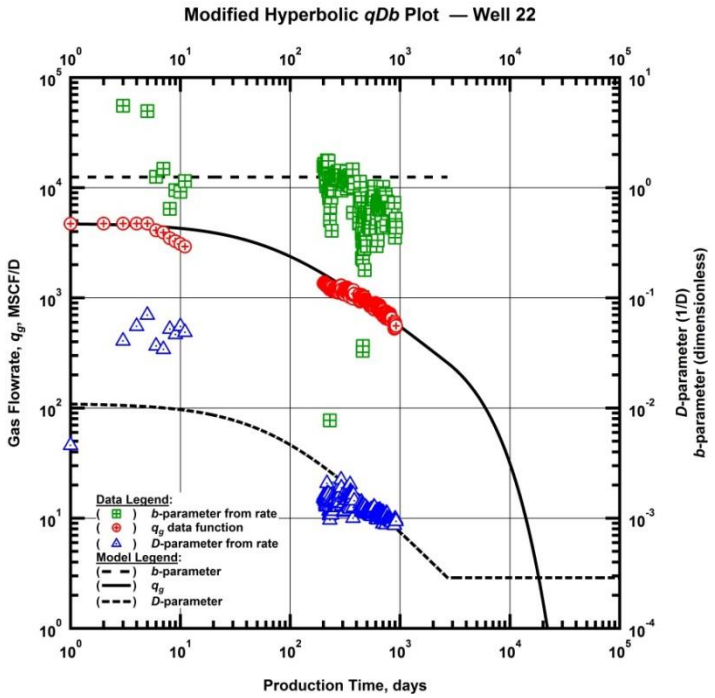

Figure B22 — (Log-log Plot): *qDb* plot — gas flow rate (q_{gi}), *D*- and *b*-parameters versus production time and modified hyperbolic model matches for Well 22.

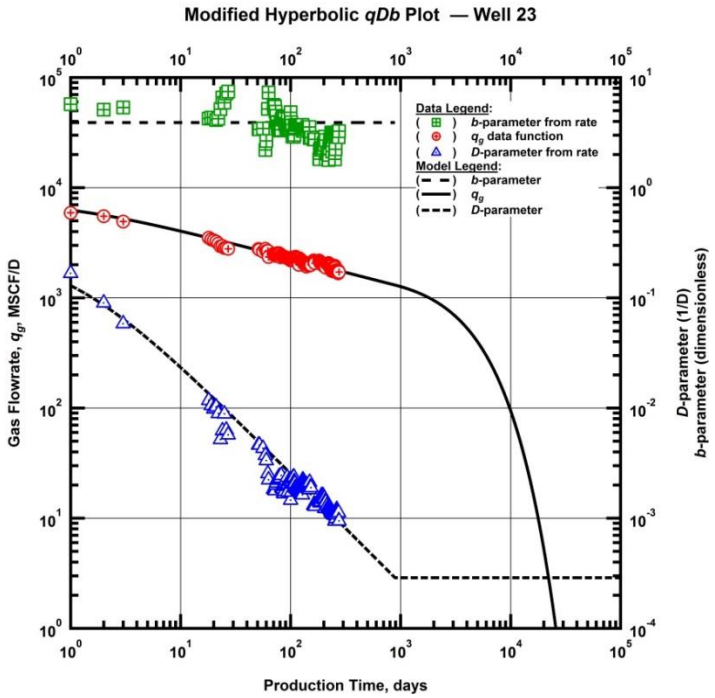

Figure B23 — (Log-log Plot): *qDb* plot — gas flow rate (q_{gi}), *D*- and *b*-parameters versus production time and modified hyperbolic model matches for Well 23.

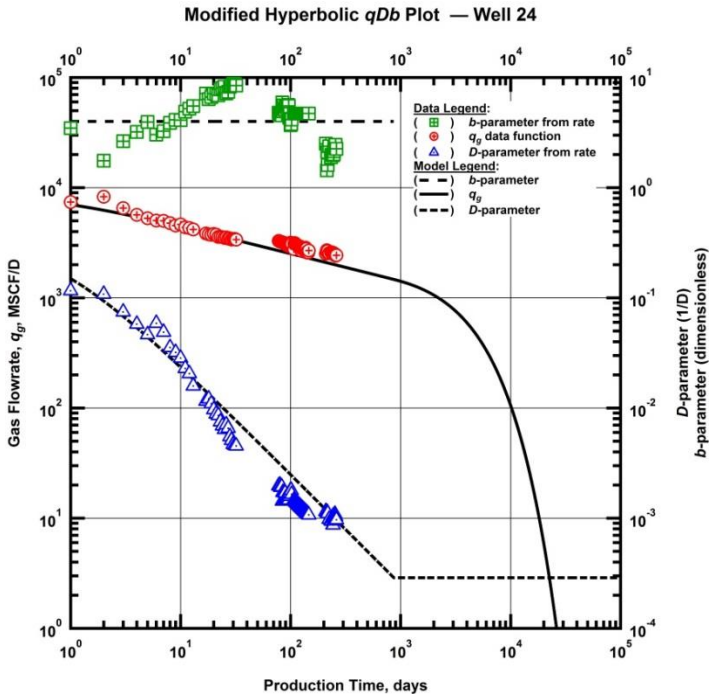

Figure B24 — (Log-log Plot): *qDb* plot — gas flow rate (q_{gi}), *D*- and *b*-parameters versus production time and modified hyperbolic model matches for Well 24.

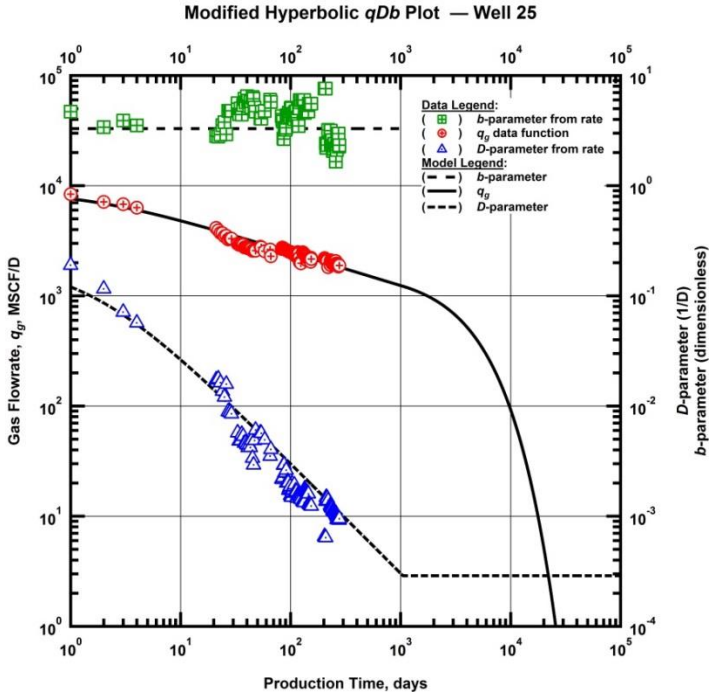

Figure B25 — (Log-log Plot): *qDb* plot — gas flow rate (q_{gi}), *D*- and *b*-parameters versus production time and modified hyperbolic model matches for Well 25.

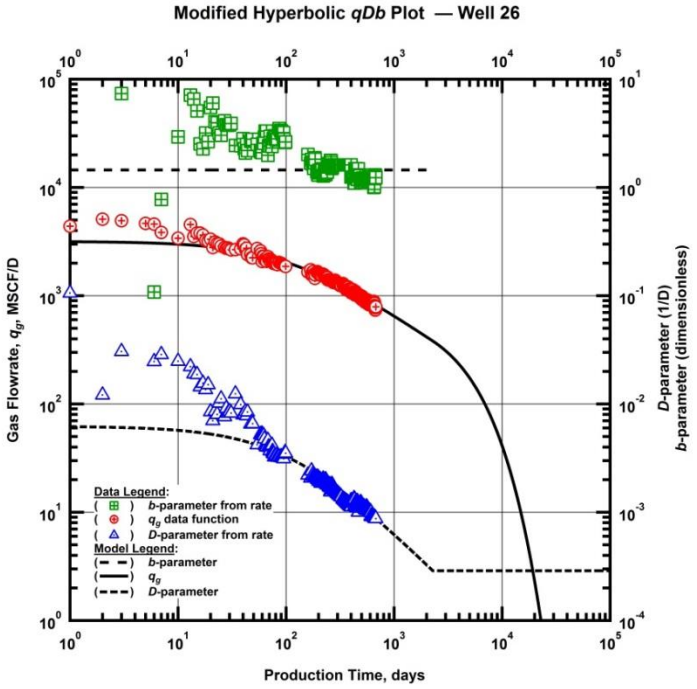

Figure B26 — (Log-log Plot): *qDb* plot — gas flow rate (q_{gi}), *D*- and *b*-parameters versus production time and modified hyperbolic model matches for Well 26.

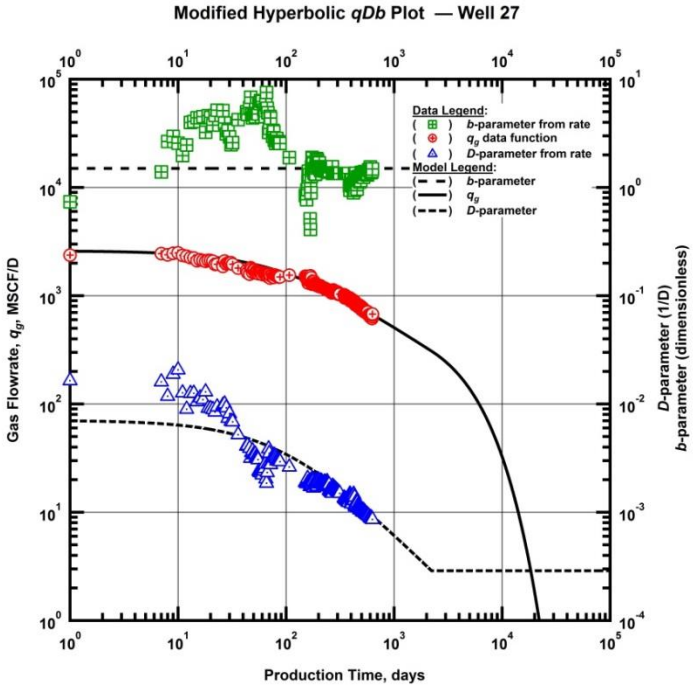

Figure B27 — (Log-log Plot): *qDb* plot — gas flow rate (q_{gi}), *D*- and *b*-parameters versus production time and modified hyperbolic model matches for Well 27.

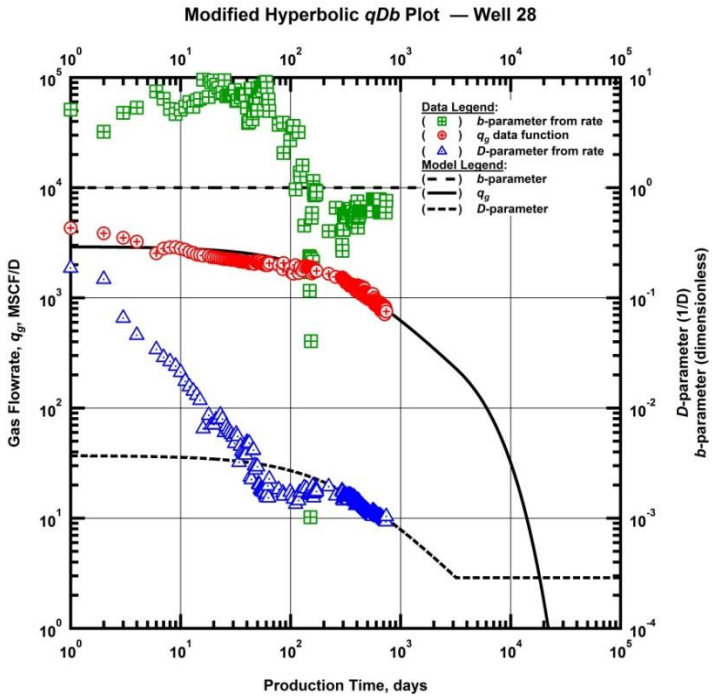

Figure B28 — (Log-log Plot): *qDb* plot — gas flow rate (q_{gi}), *D*- and *b*-parameters versus production time and modified hyperbolic model matches for Well 28.

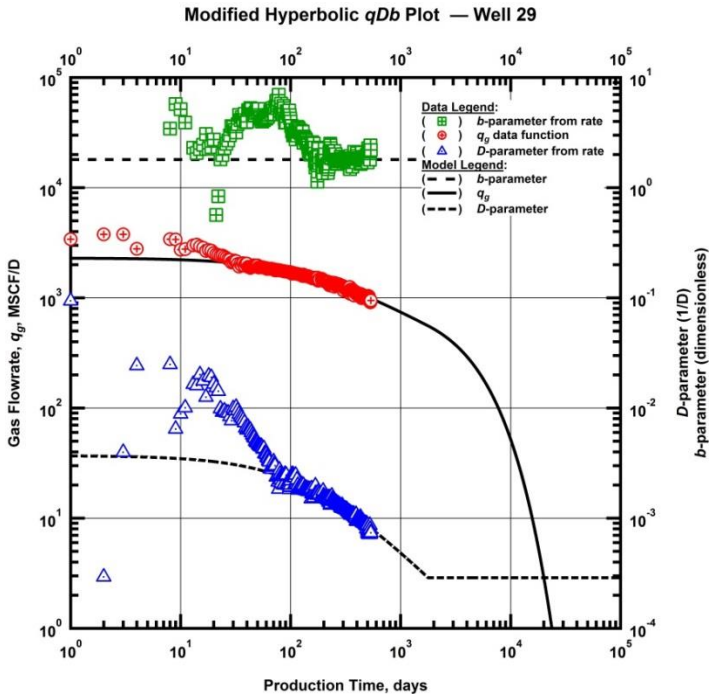

Figure B29 — (Log-log Plot): *qDb* plot — gas flow rate (q_{gi}), *D*- and *b*-parameters versus production time and modified hyperbolic model matches for Well 29.

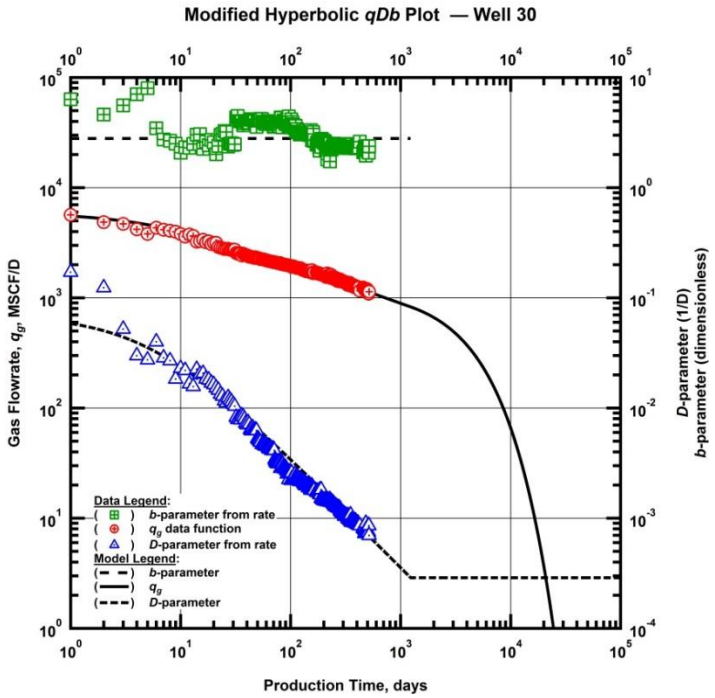

Figure B30 — (Log-log Plot): *qDb* plot — gas flow rate (q_{gi}), *D*- and *b*-parameters versus production time and modified hyperbolic model matches for Well 30.

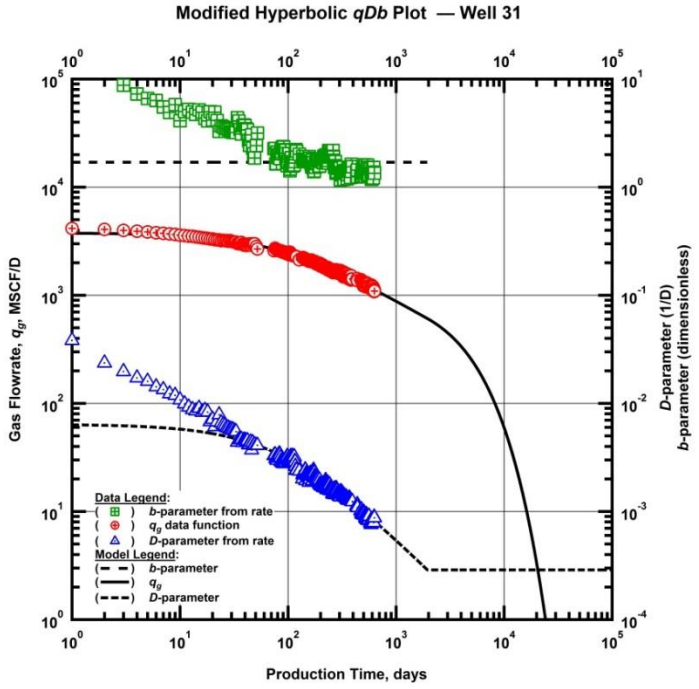

Figure B31 — (Log-log Plot): *qDb* plot — gas flow rate (q_{gi}), *D*- and *b*-parameters versus production time and modified hyperbolic model matches for Well 31.

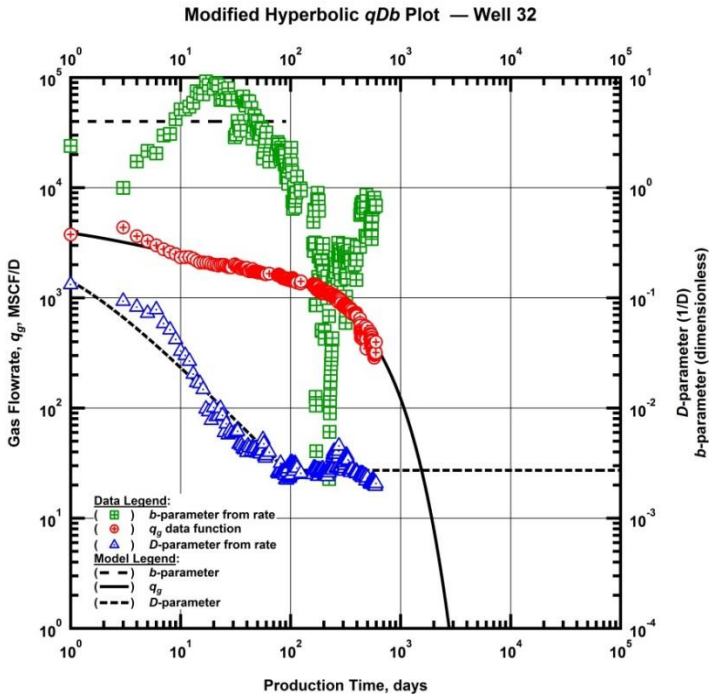

Figure B32 — (Log-log Plot): *qDb* plot — gas flow rate (q_{gi}), *D*- and *b*-parameters versus production time and modified hyperbolic model matches for Well 32.

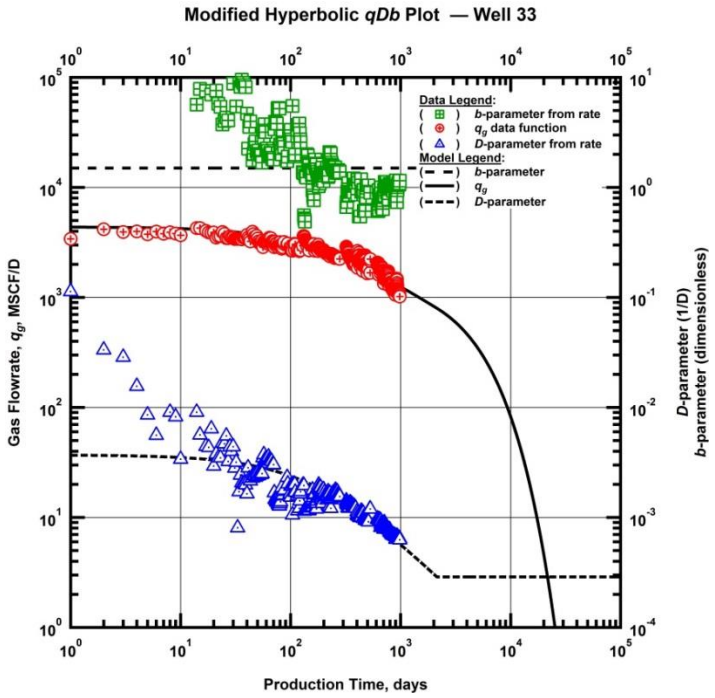

Figure B33 — (Log-log Plot): *qDb* plot — gas flow rate (q_{gi}), *D*- and *b*-parameters versus production time and modified hyperbolic model matches for Well 33.

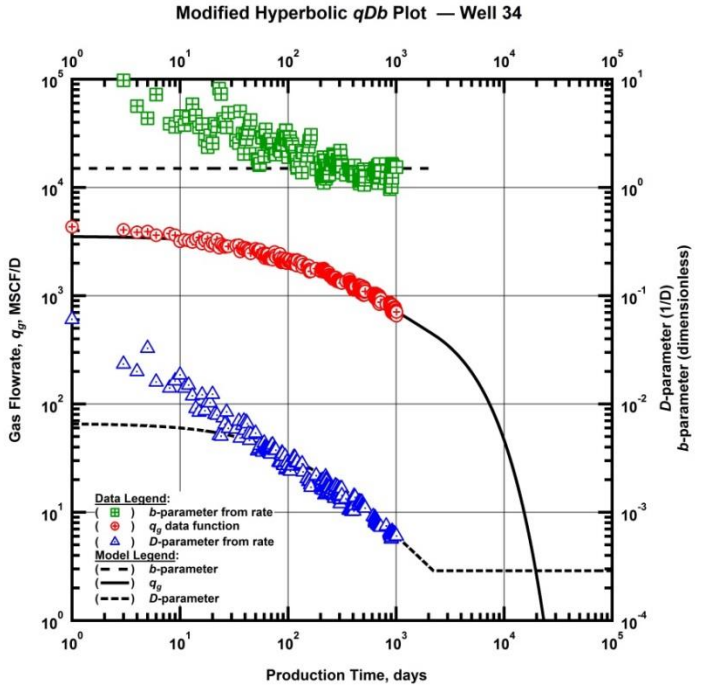

Figure B34 — (Log-log Plot): *qDb* plot — gas flow rate (q_{gi}), *D*- and *b*-parameters versus production time and modified hyperbolic model matches for Well 34.

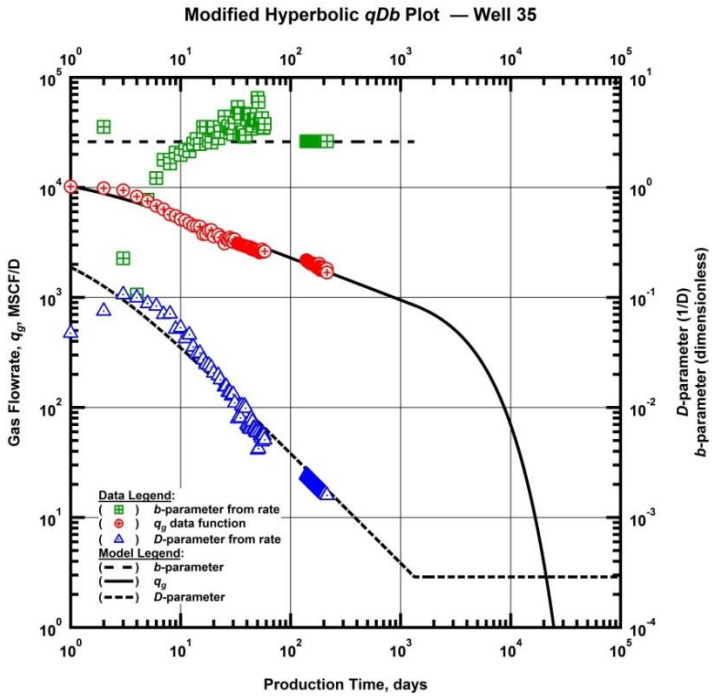

Figure B35 — (Log-log Plot): *qDb* plot — gas flow rate (q_{gi}), *D*- and *b*-parameters versus production time and modified hyperbolic model matches for Well 35.

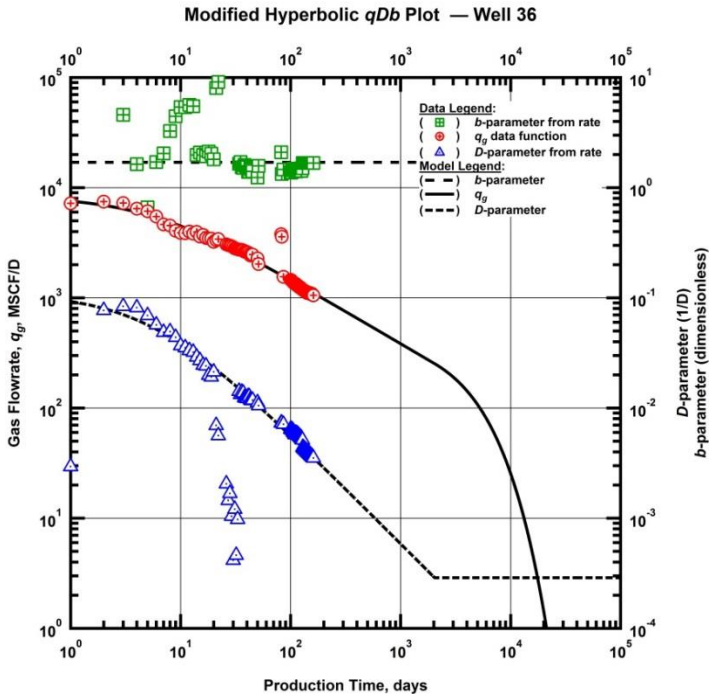

Figure B36 — (Log-log Plot): *qDb* plot — gas flow rate (q_{gi}), *D*- and *b*-parameters versus production time and modified hyperbolic model matches for Well 36.

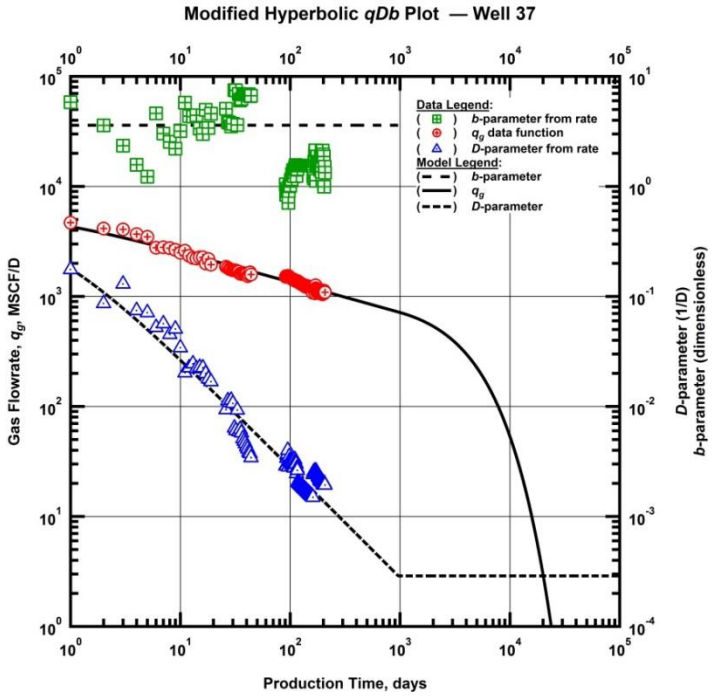

Figure B37 — (Log-log Plot): *qDb* plot — gas flow rate (q_{gi}), *D*- and *b*-parameters versus production time and modified hyperbolic model matches for Well 37.

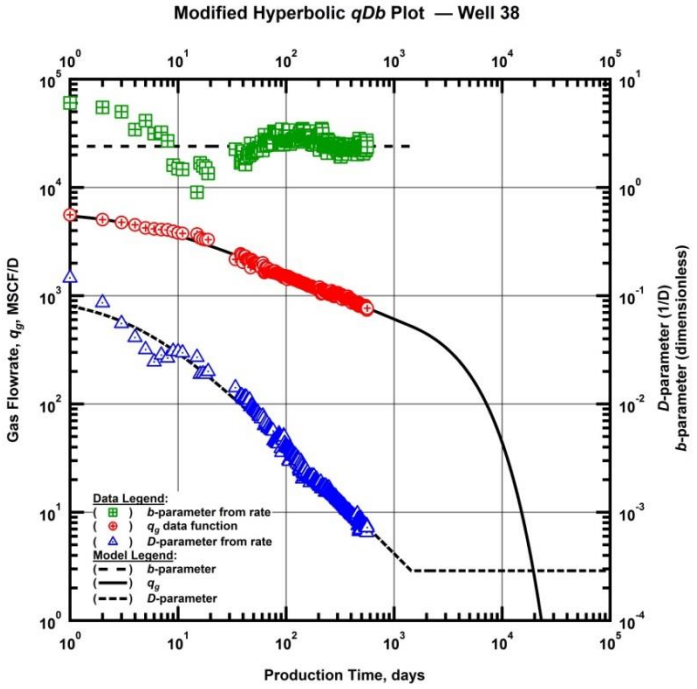

Figure B38 — (Log-log Plot): *qDb* plot — gas flow rate (q_{gi}), *D*- and *b*-parameters versus production time and modified hyperbolic model matches for Well 38.

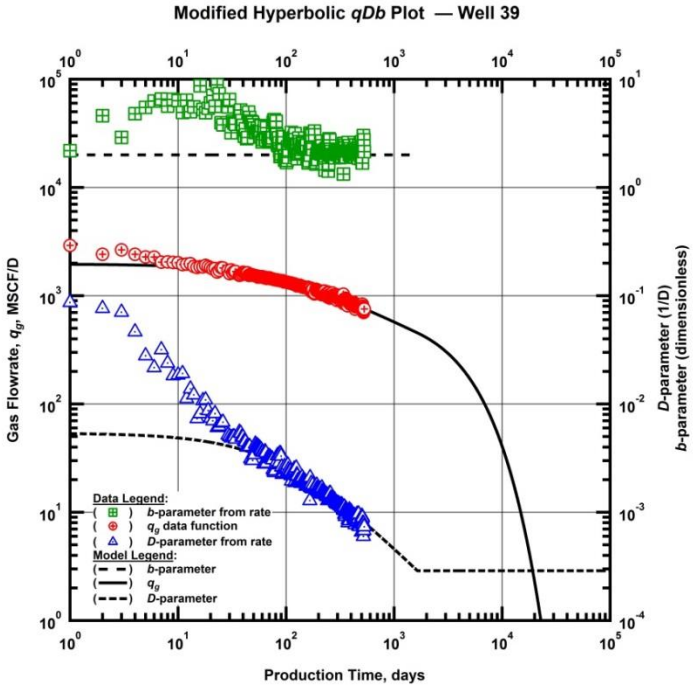

Figure B39 — (Log-log Plot): *qDb* plot — gas flow rate (q_{gi}), *D*- and *b*-parameters versus production time and modified hyperbolic model matches for Well 39.

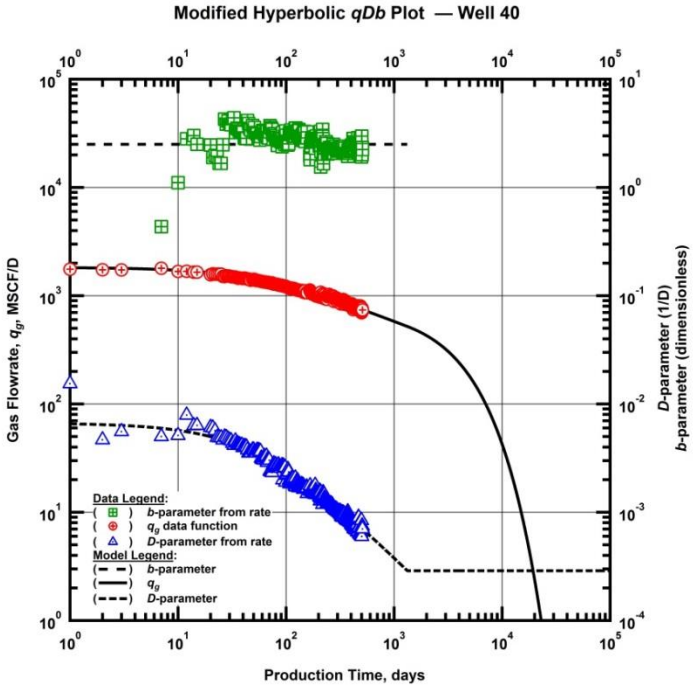

Figure B40 — (Log-log Plot): *qDb* plot — gas flow rate (q_{gi}), *D*- and *b*-parameters versus production time and modified hyperbolic model matches for Well 40.

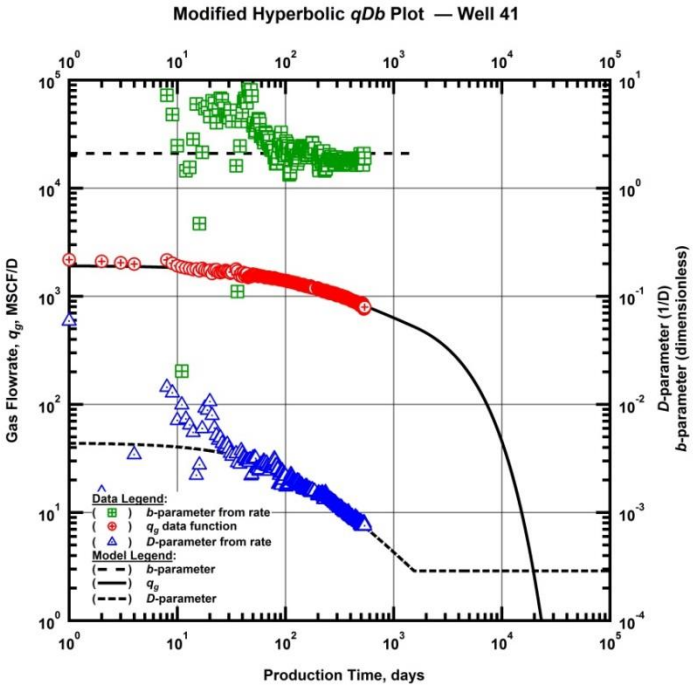

Figure B41 — (Log-log Plot): *qDb* plot — gas flow rate (q_{gi}), *D*- and *b*-parameters versus production time and modified hyperbolic model matches for Well 41.

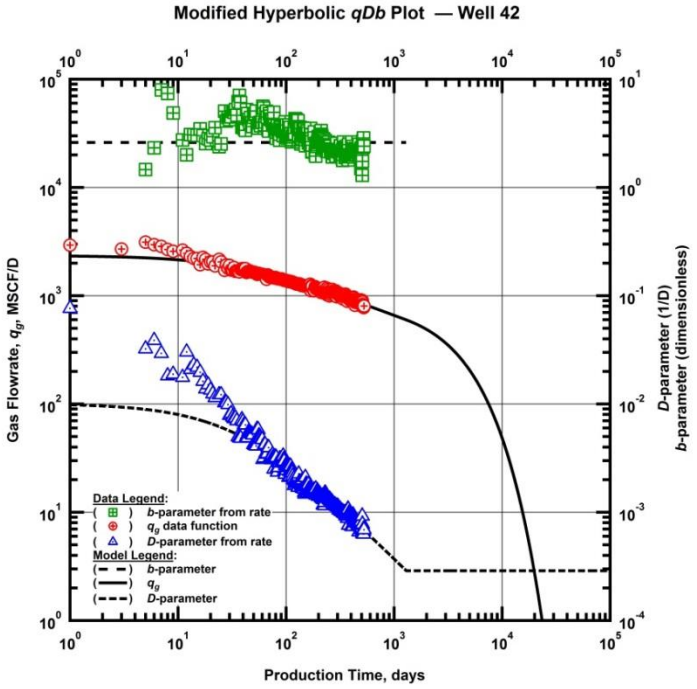

Figure B42 — (Log-log Plot): *qDb* plot — gas flow rate (q_{gi}), *D*- and *b*-parameters versus production time and modified hyperbolic model matches for Well 42.

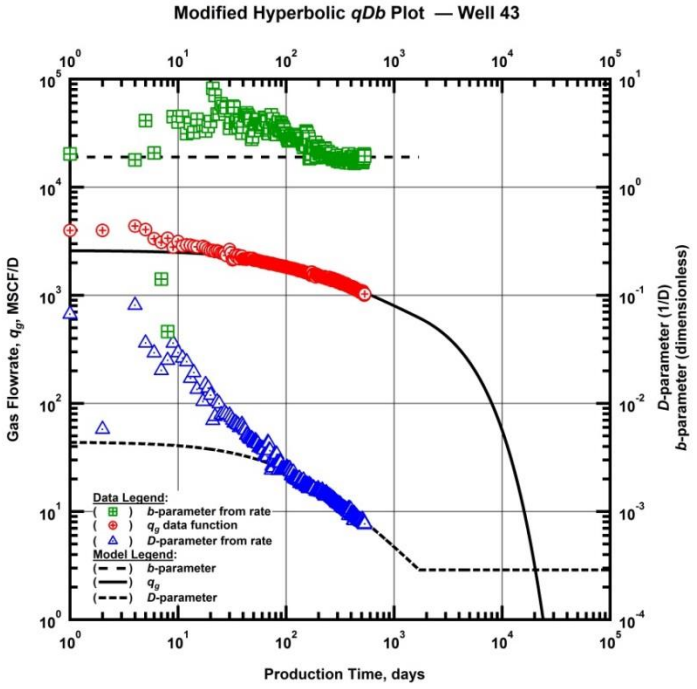

Figure B43 — (Log-log Plot): *qDb* plot — gas flow rate (q_{gi}), *D*- and *b*-parameters versus production time and modified hyperbolic model matches for Well 43.

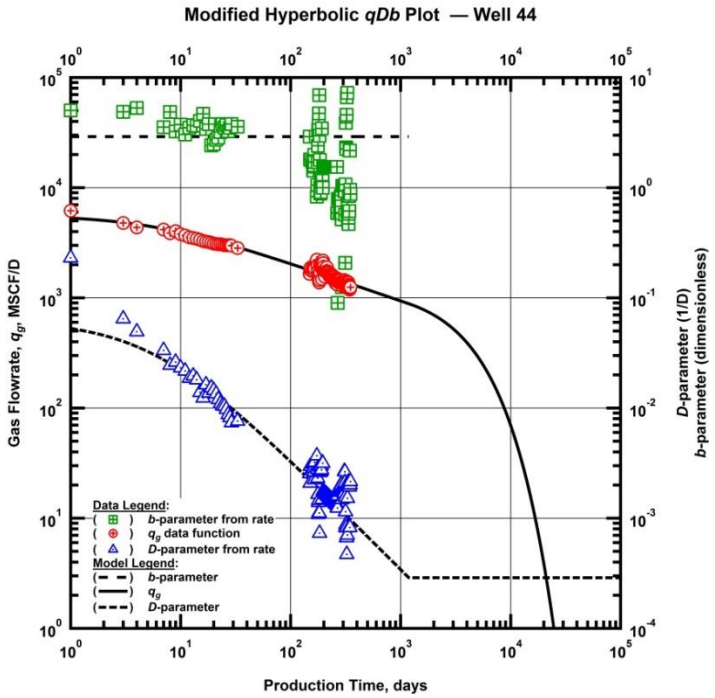

Figure B44 — (Log-log Plot): *qDb* plot — gas flow rate (q_{gi}), *D*- and *b*-parameters versus production time and modified hyperbolic model matches for Well 44.

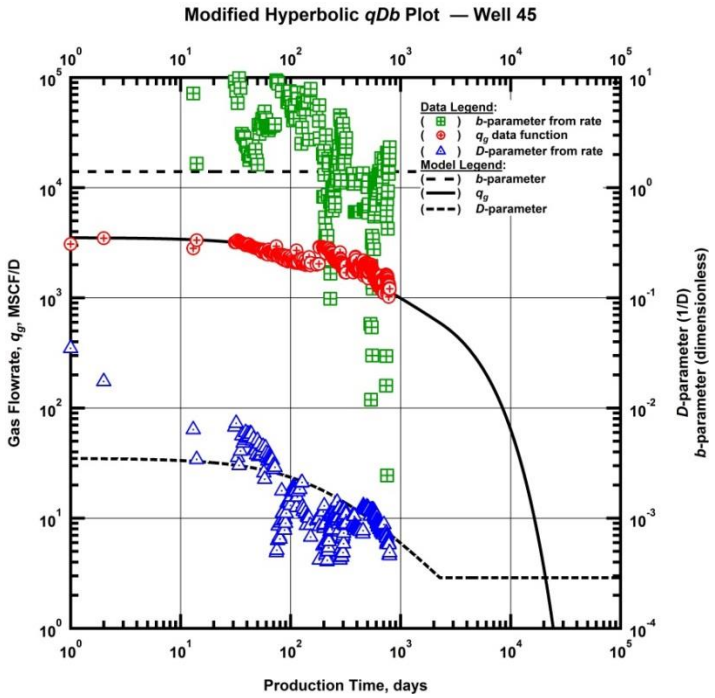

Figure B45 — (Log-log Plot): *qDb* plot — gas flow rate (q_{gi}), *D*- and *b*-parameters versus production time and modified hyperbolic model matches for Well 45.

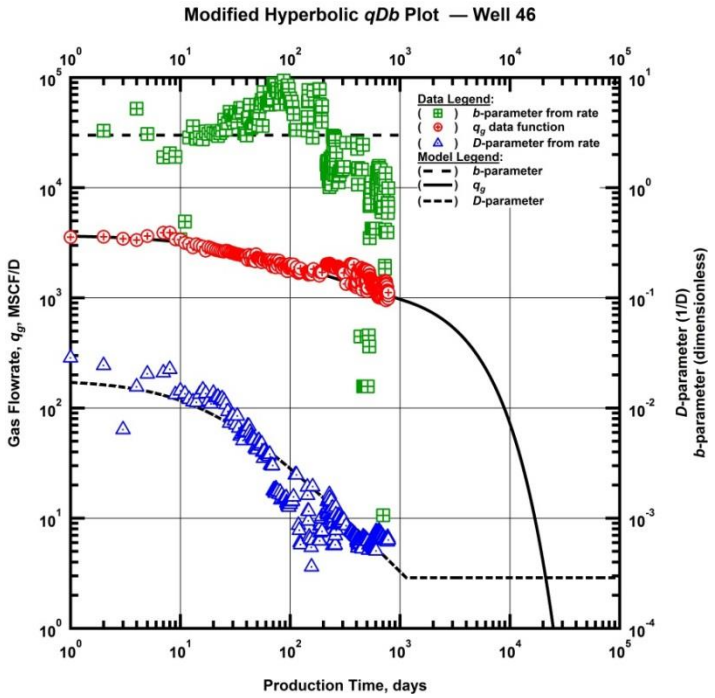

Figure B46 — (Log-log Plot): *qDb* plot — gas flow rate (q_{gi}), *D*- and *b*-parameters versus production time and modified hyperbolic model matches for Well 46.

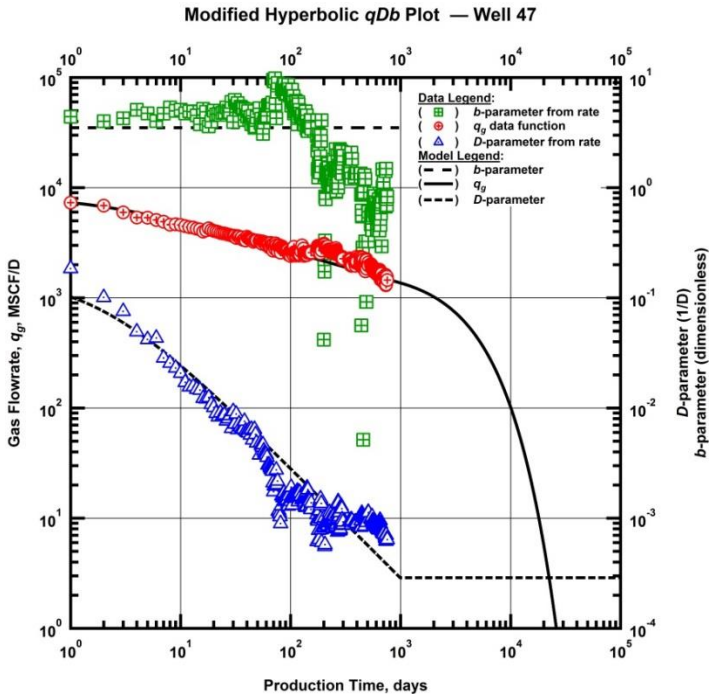

Figure B47 — (Log-log Plot): *qDb* plot — gas flow rate (q_{gi}), *D*- and *b*-parameters versus production time and modified hyperbolic model matches for Well 47.

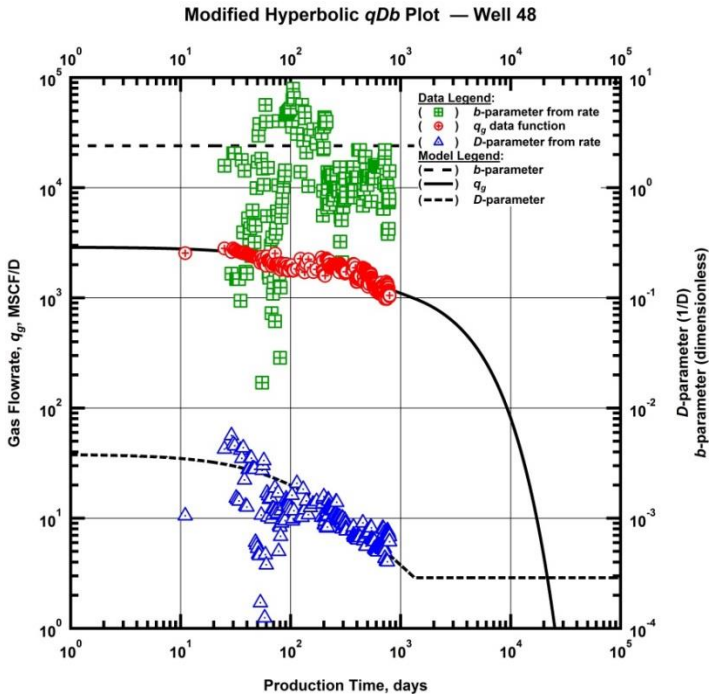

Figure B48 — (Log-log Plot): *qDb* plot — gas flow rate (q_{gi}), *D*- and *b*-parameters versus production time and modified hyperbolic model matches for Well 48.

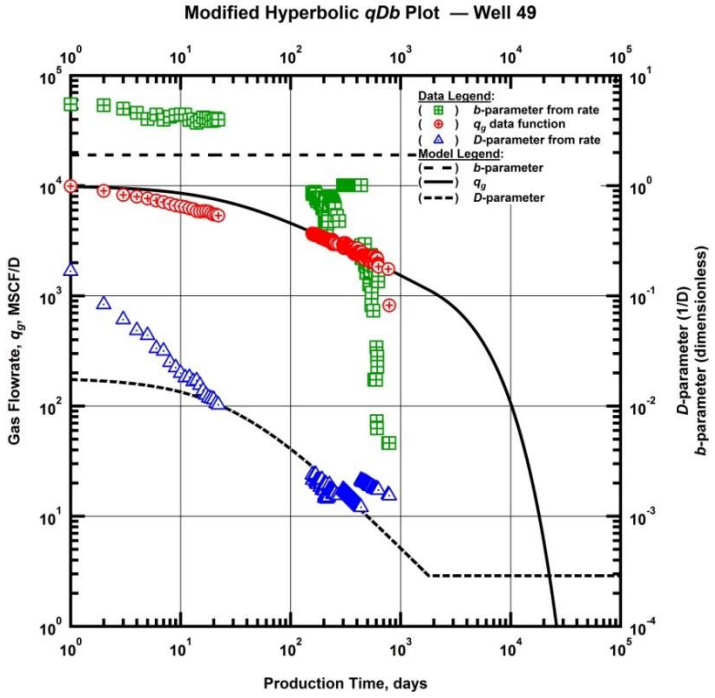

Figure B49 — (Log-log Plot): *qDb* plot — gas flow rate (q_{gi}), *D*- and *b*-parameters versus production time and modified hyperbolic model matches for Well 49.

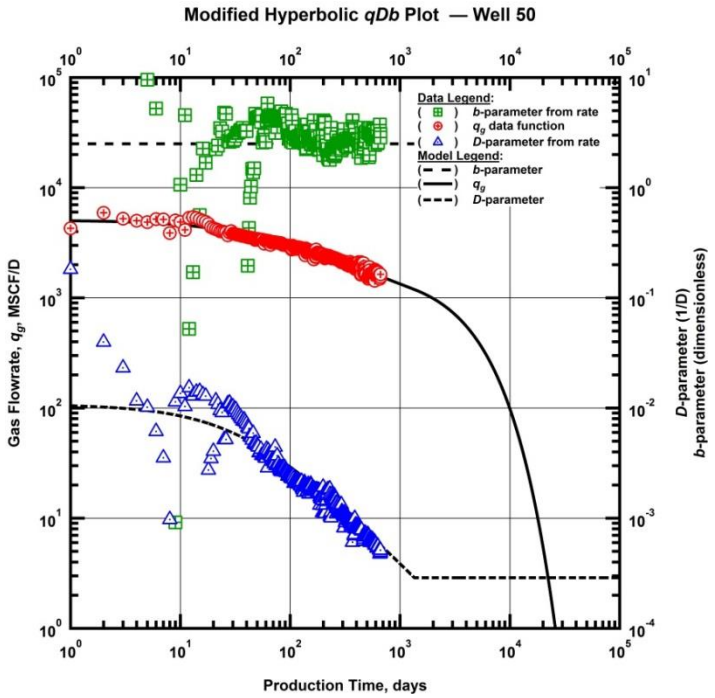

Figure B50 — (Log-log Plot): *qDb* plot — gas flow rate (q_{gi}), *D*- and *b*-parameters versus production time and modified hyperbolic model matches for Well 50.

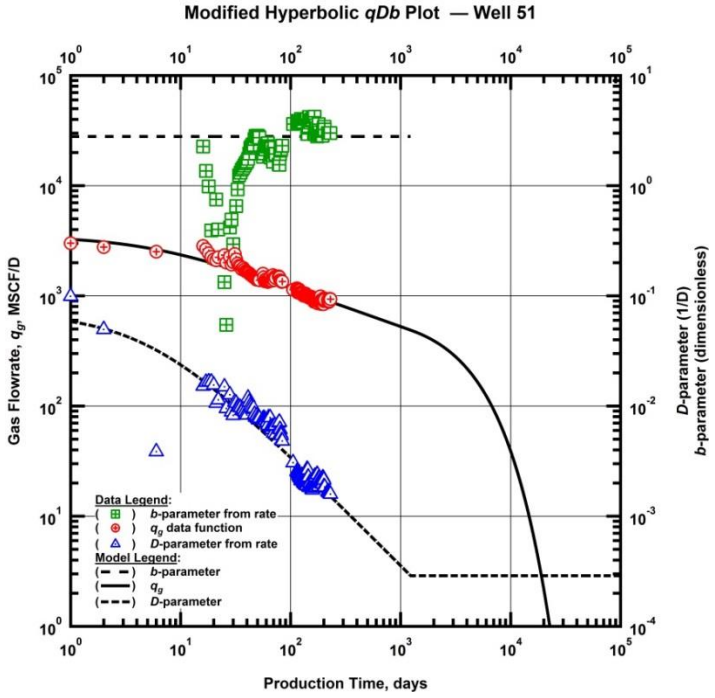

Figure B51 — (Log-log Plot): *qDb* plot — gas flow rate (q_{gi}), *D*- and *b*-parameters versus production time and modified hyperbolic model matches for Well 51.

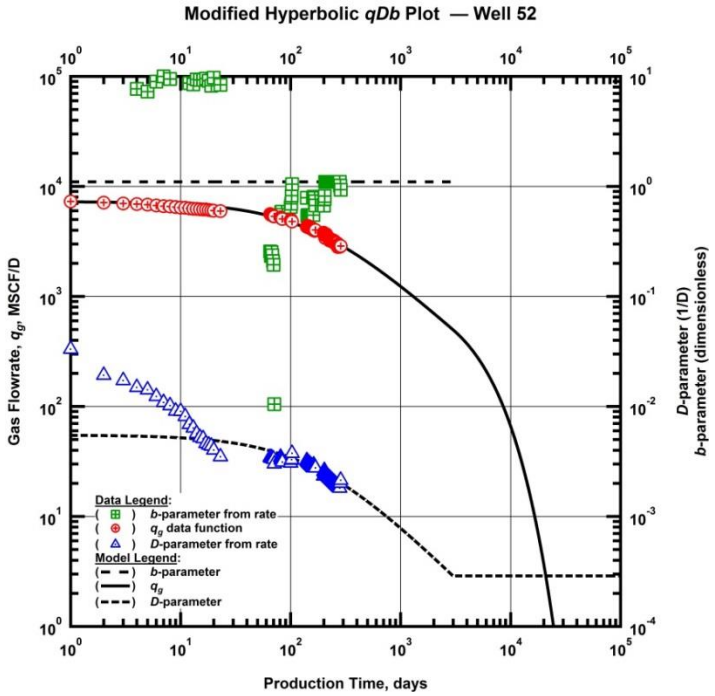

Figure B52 — (Log-log Plot): *qDb* plot — gas flow rate (q_{gi}), *D*- and *b*-parameters versus production time and modified hyperbolic model matches for Well 52.

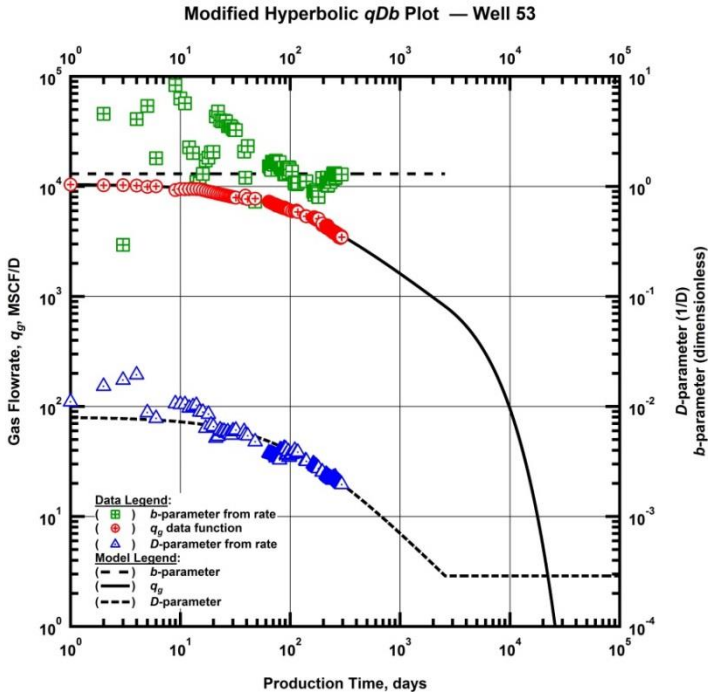

Figure B53 — (Log-log Plot): *qDb* plot — gas flow rate (q_{gi}), *D*- and *b*-parameters versus production time and modified hyperbolic model matches for Well 53.

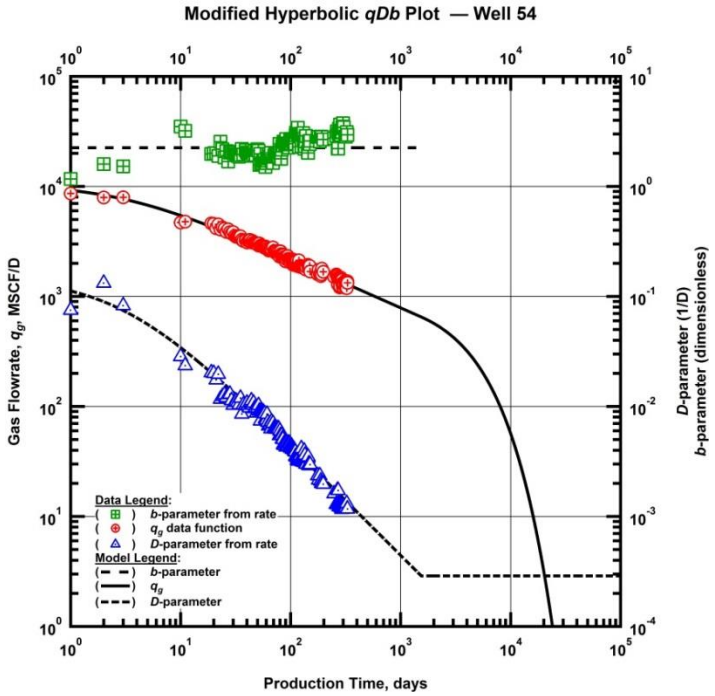

Figure B54 — (Log-log Plot): *qDb* plot — gas flow rate (q_{gi}), *D*- and *b*-parameters versus production time and modified hyperbolic model matches for Well 54.

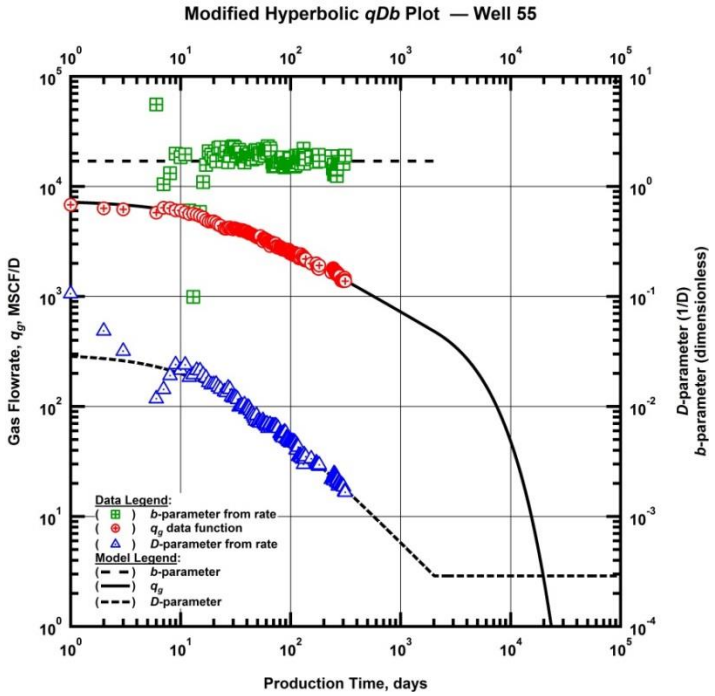

Figure B55 — (Log-log Plot): *qDb* plot — gas flow rate (q_{gi}), *D*- and *b*-parameters versus production time and modified hyperbolic model matches for Well 55

Power-Law Exponential Models

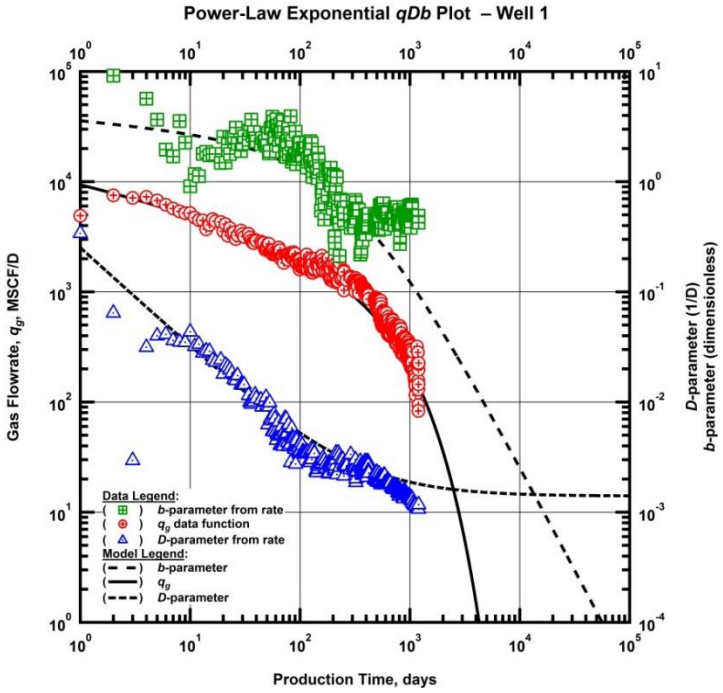

Figure B56 — (Log-log Plot): *qDb* plot — gas flow rate (q_{gi}), *D*- and *b*-parameters versus production time and modified hyperbolic model matches for Well 1.

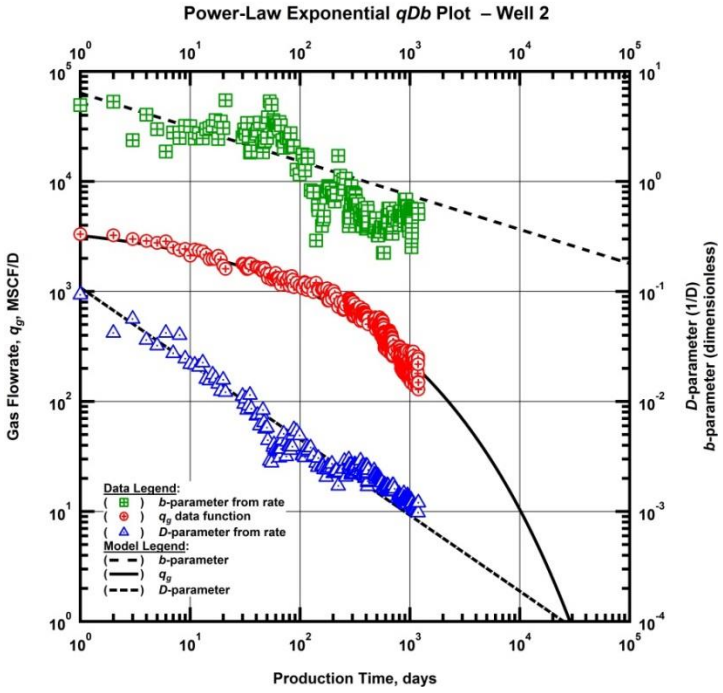

Figure B57 — (Log-log Plot): *qDb* plot — gas flow rate (q_{gi}), *D*- and *b*-parameters versus production time and modified hyperbolic model matches for Well 2.

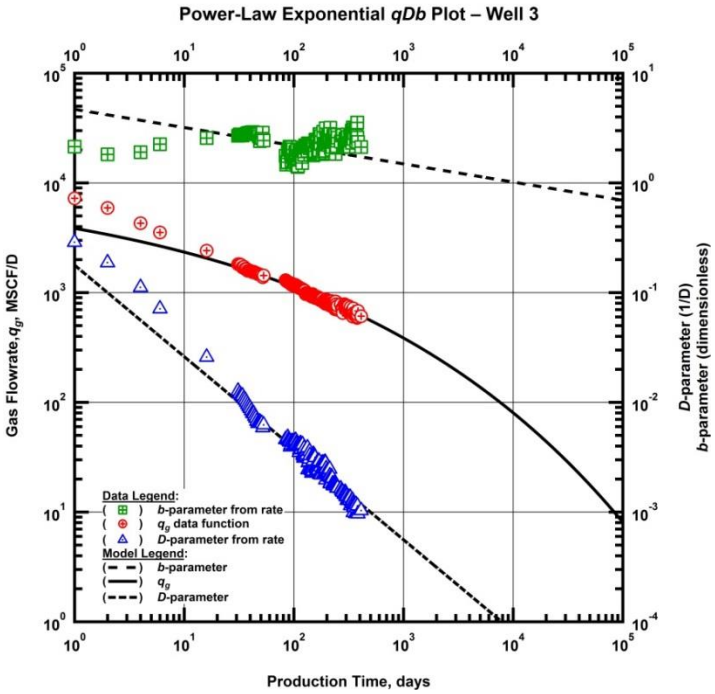

Figure B58 — (Log-log Plot): *qDb* plot — gas flow rate (q_{gi}), *D*- and *b*-parameters versus production time and modified hyperbolic model matches for Well 3.

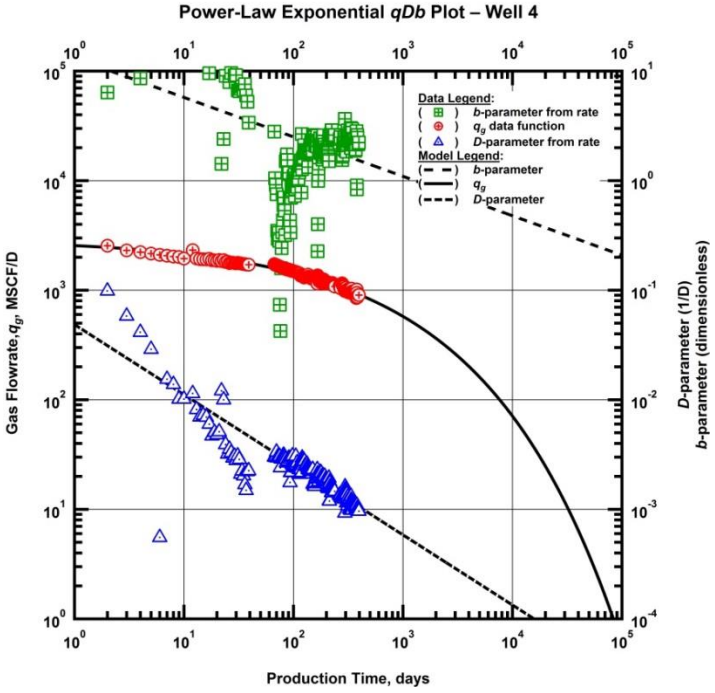

Figure B59 — (Log-log Plot): *qDb* plot — gas flow rate (q_{gi}), *D*- and *b*-parameters versus production time and modified hyperbolic model matches for Well 4.

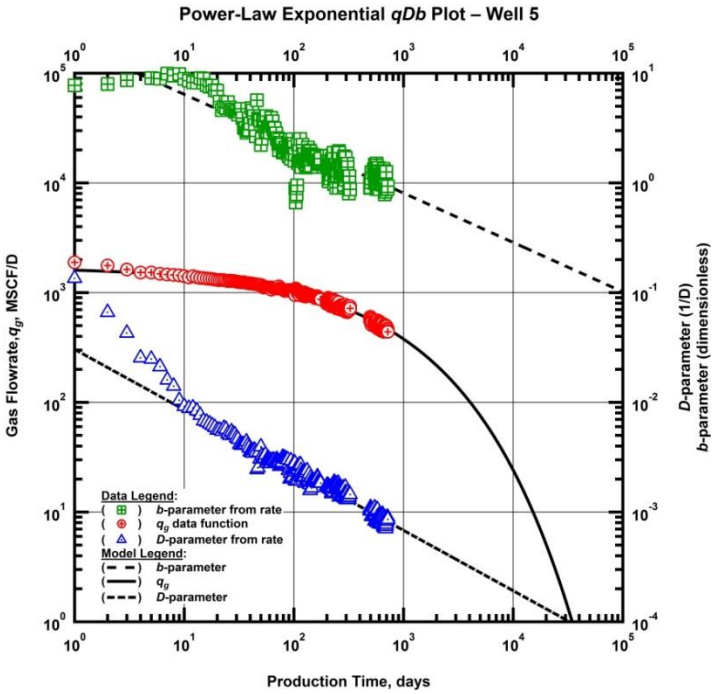

Figure B60 — (Log-log Plot): *qDb* plot — gas flow rate (q_{gi}), *D*- and *b*-parameters versus production time and modified hyperbolic model matches for Well 5.

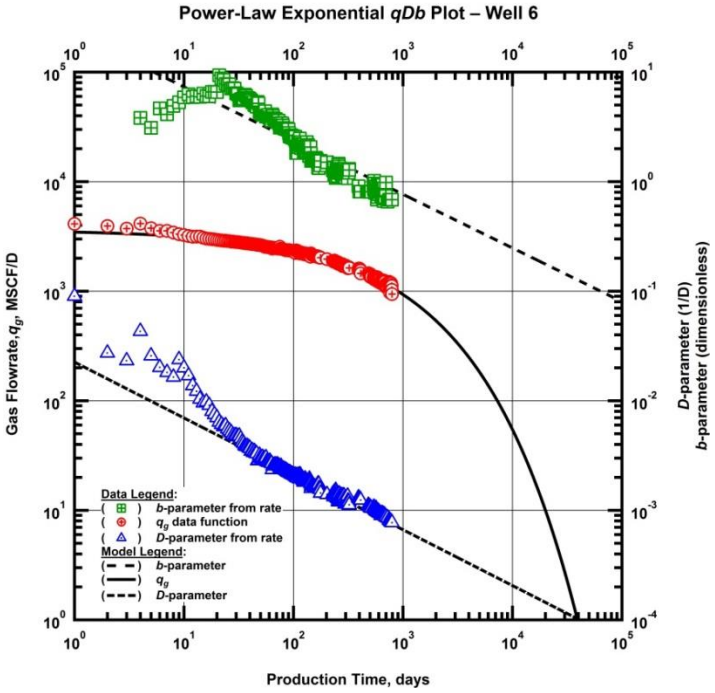

Figure B61 — (Log-log Plot): *qDb* plot — gas flow rate (q_{gi}), *D*- and *b*-parameters versus production time and modified hyperbolic model matches for Well 6.

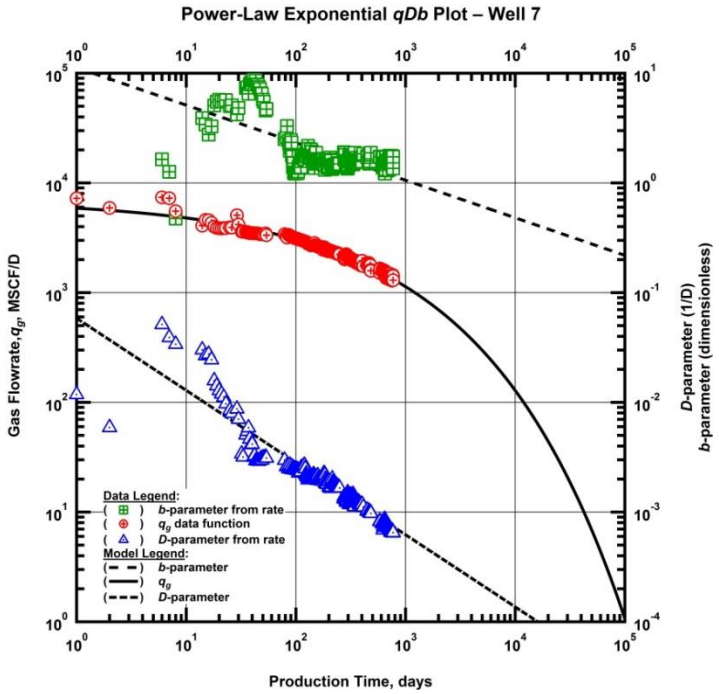

Figure B62 — (Log-log Plot): *qDb* plot — gas flow rate (q_{gi}), *D*- and *b*-parameters versus production time and modified hyperbolic model matches for Well 7.

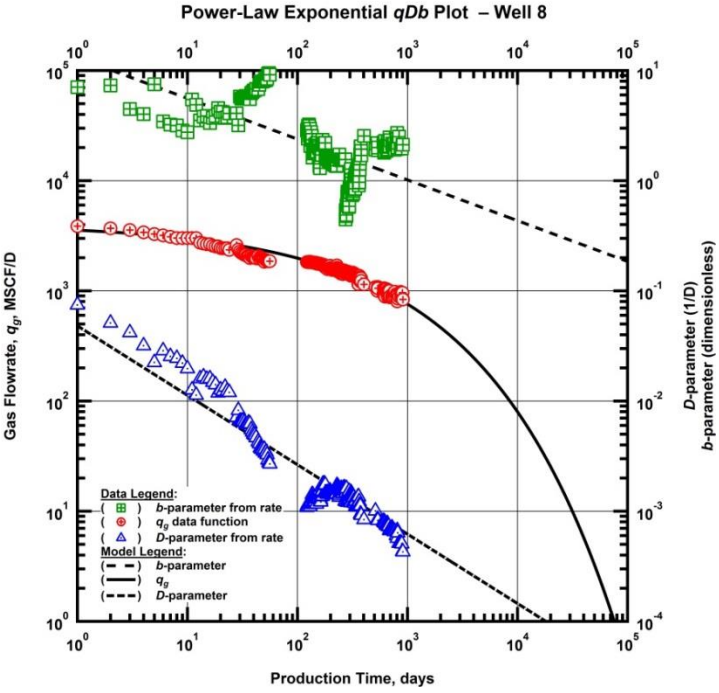

Figure B63 — (Log-log Plot): *qDb* plot — gas flow rate (q_{gi}), *D*- and *b*-parameters versus production time and modified hyperbolic model matches for Well 8.

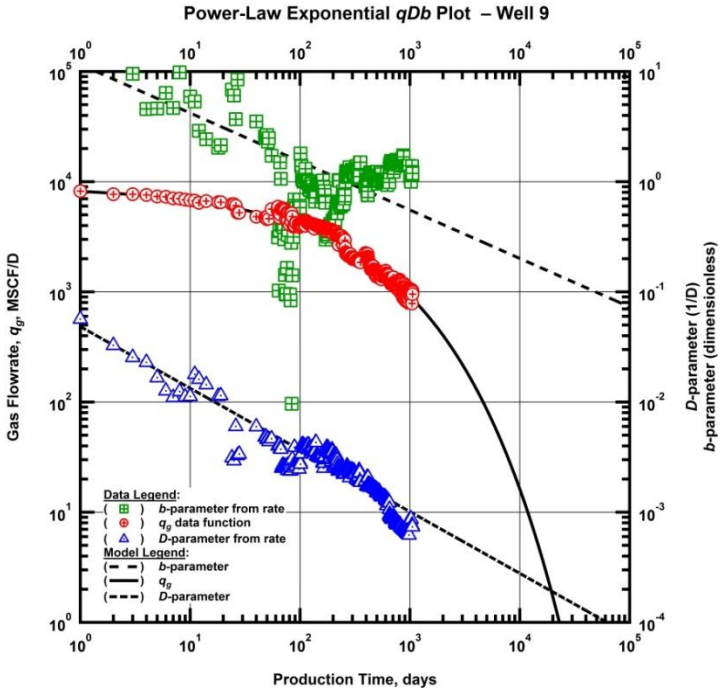

Figure B64 — (Log-log Plot): *qDb* plot — gas flow rate (q_{gi}), *D*- and *b*-parameters versus production time and modified hyperbolic model matches for Well 9.

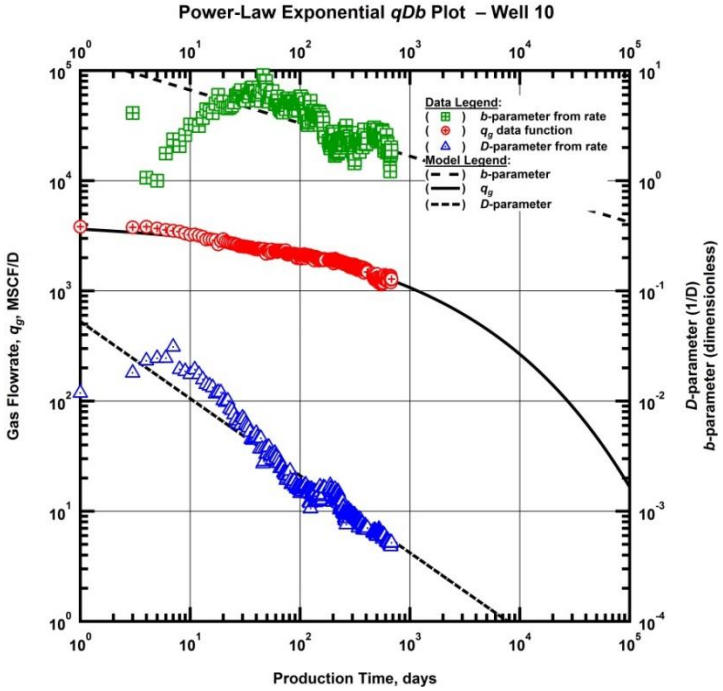

Figure B65 — (Log-log Plot): *qDb* plot — gas flow rate (q_{gi}), *D*- and *b*-parameters versus production time and modified hyperbolic model matches for Well 10.

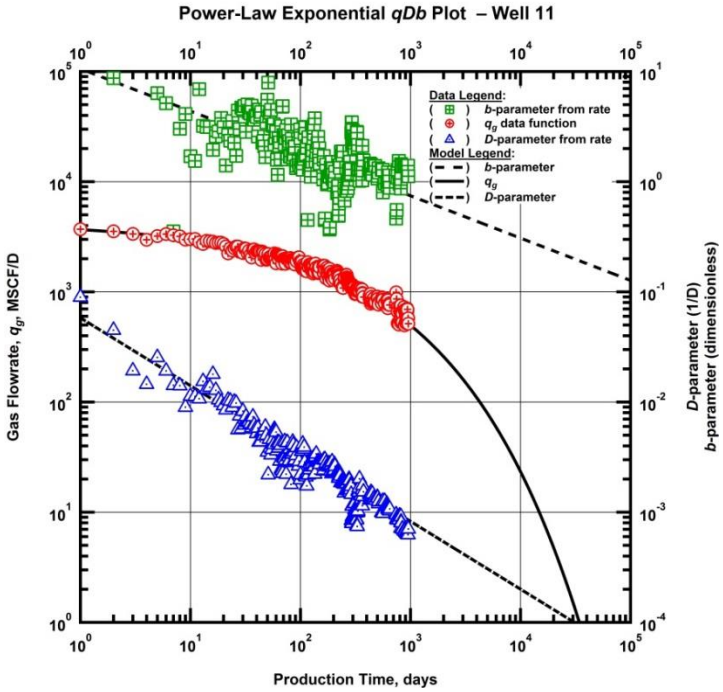

Figure B66 — (Log-log Plot): *qDb* plot — gas flow rate (q_{gi}), *D*- and *b*-parameters versus production time and modified hyperbolic model matches for Well 11.

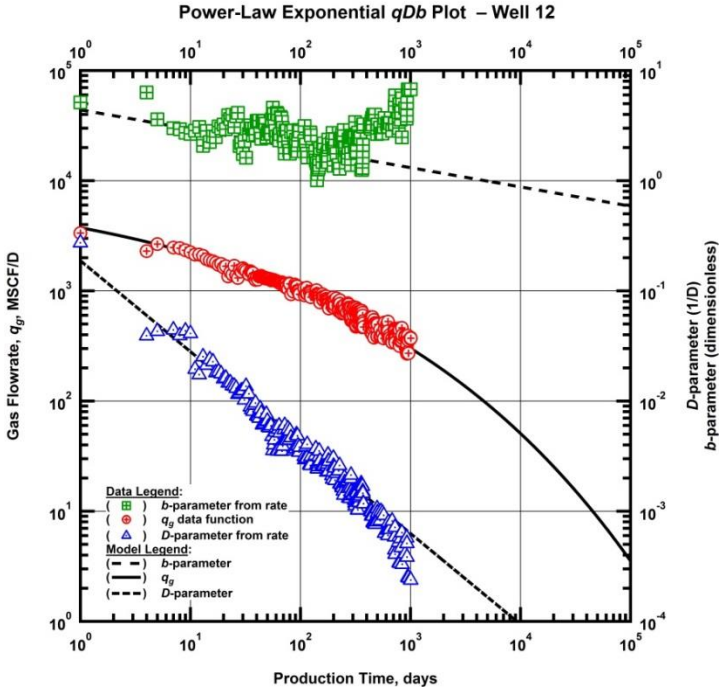

Figure B67 — (Log-log Plot): *qDb* plot — gas flow rate (q_{gi}), *D*- and *b*-parameters versus production time and modified hyperbolic model matches for Well 12.

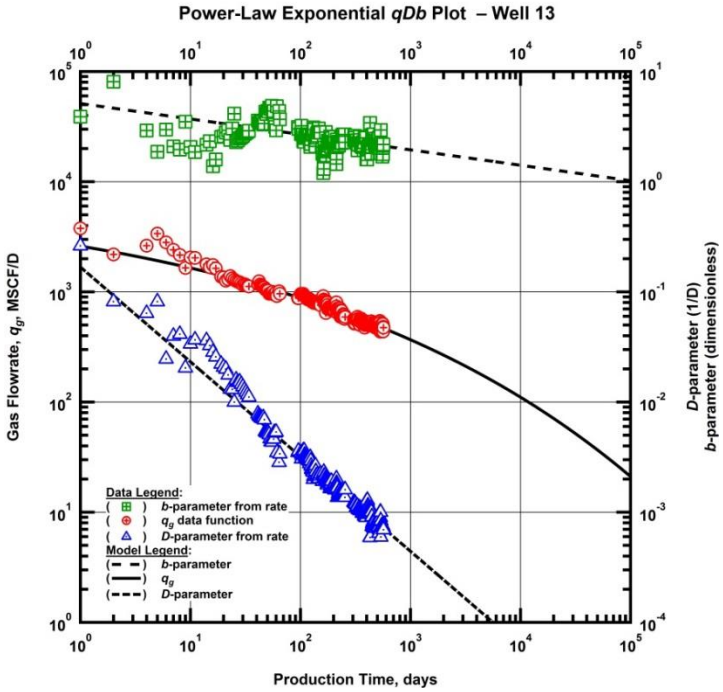

Figure B68 — (Log-log Plot): *qDb* plot — gas flow rate (q_{gi}), *D*- and *b*-parameters versus production time and modified hyperbolic model matches for Well 13.

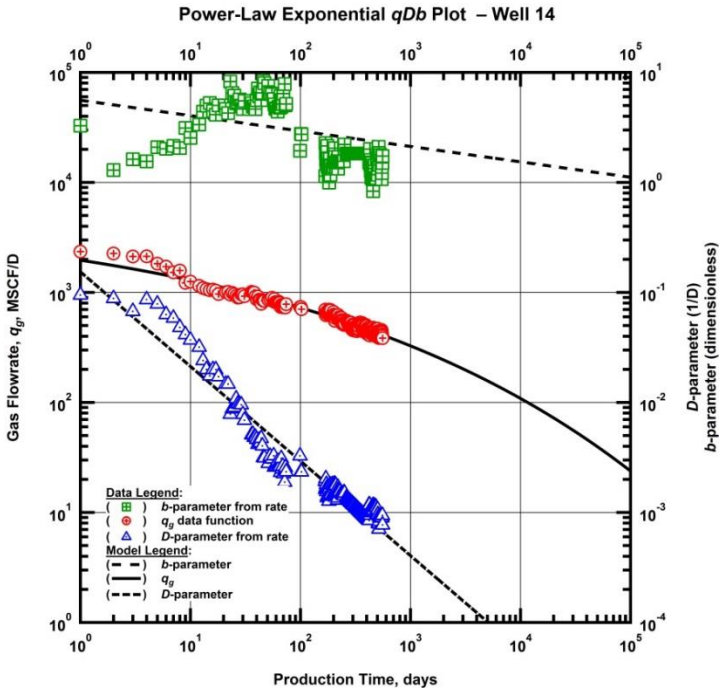

Figure B69 — (Log-log Plot): *qDb* plot — gas flow rate (q_{gi}), *D*- and *b*-parameters versus production time and modified hyperbolic model matches for Well 14.

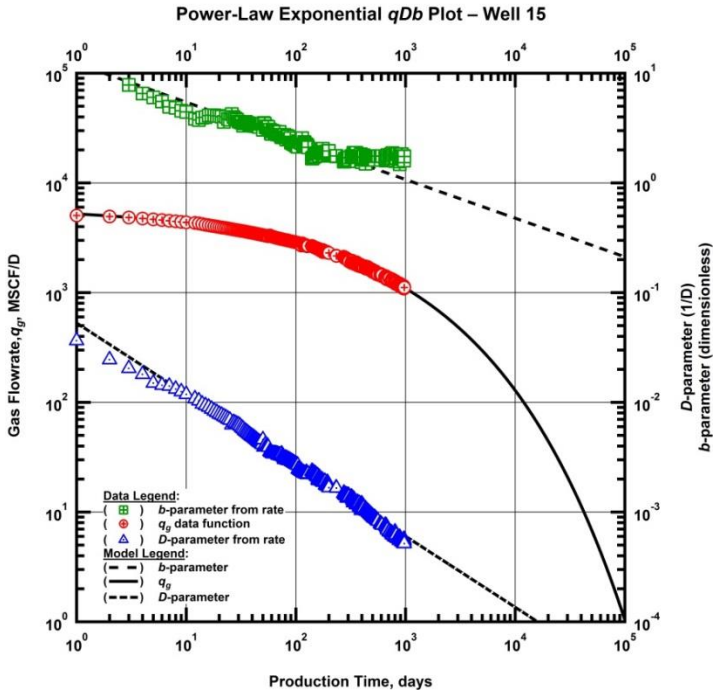

Figure B70 — (Log-log Plot): *qDb* plot — gas flow rate (q_{gi}), *D*- and *b*-parameters versus production time and modified hyperbolic model matches for Well 15.

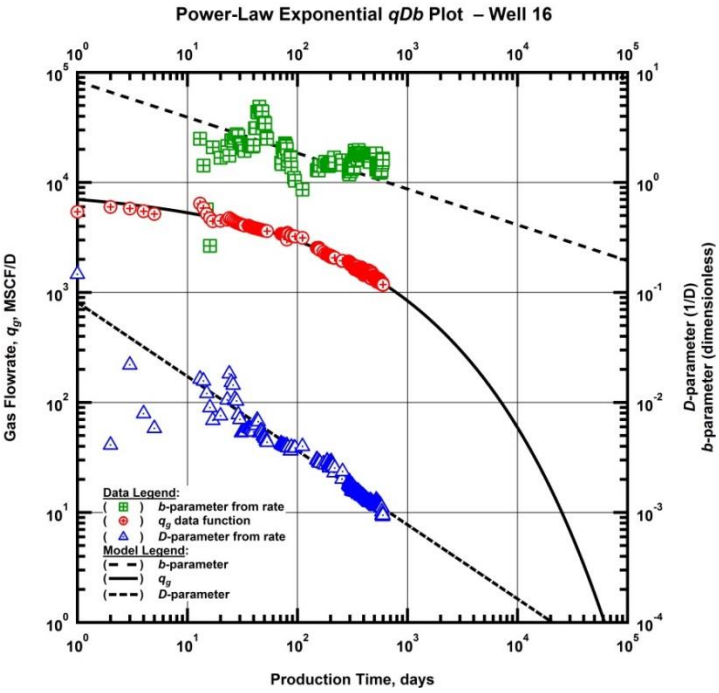

Figure B71 — (Log-log Plot): *qDb* plot — gas flow rate (q_{gi}), *D*- and *b*-parameters versus production time and modified hyperbolic model matches for Well 16.

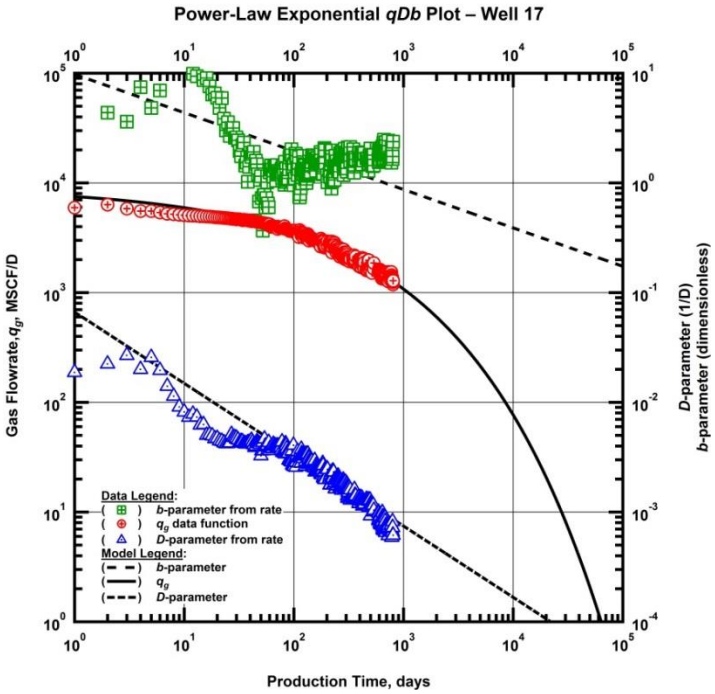

Figure B72 — (Log-log Plot): *qDb* plot — gas flow rate (q_{gi}), *D*- and *b*-parameters versus production time and modified hyperbolic model matches for Well 17.

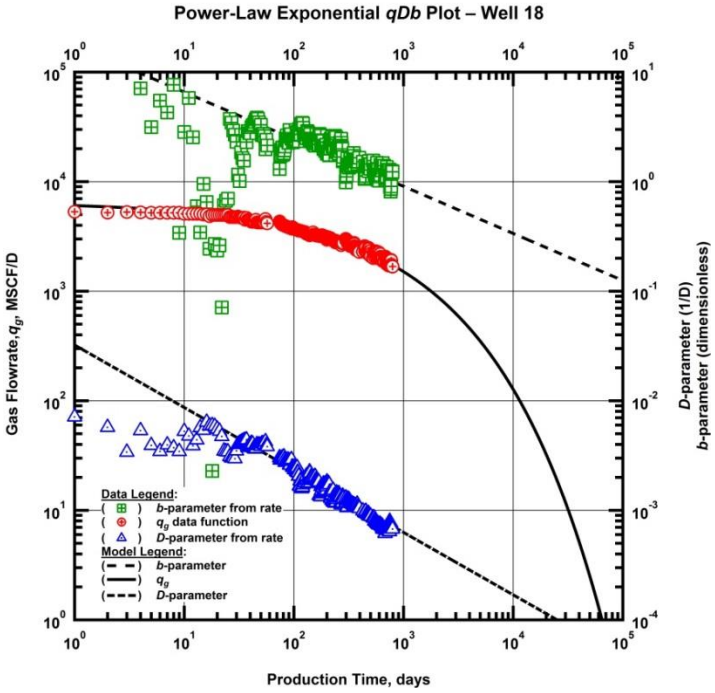

Figure B73 — (Log-log Plot): *qDb* plot — gas flow rate (q_{gi}), *D*- and *b*-parameters versus production time and modified hyperbolic model matches for Well 18.

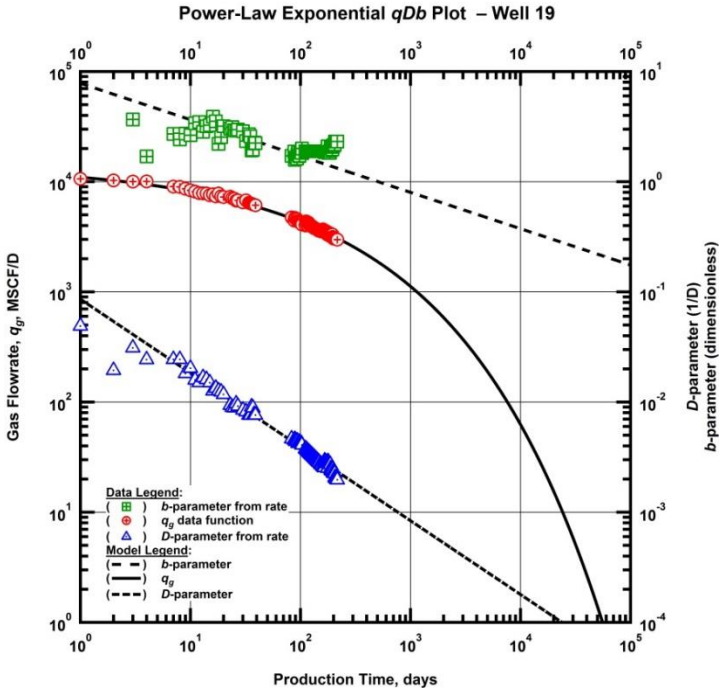

Figure B74 — (Log-log Plot): *qDb* plot — gas flow rate (q_{gi}), *D*- and *b*-parameters versus production time and modified hyperbolic model matches for Well 19.

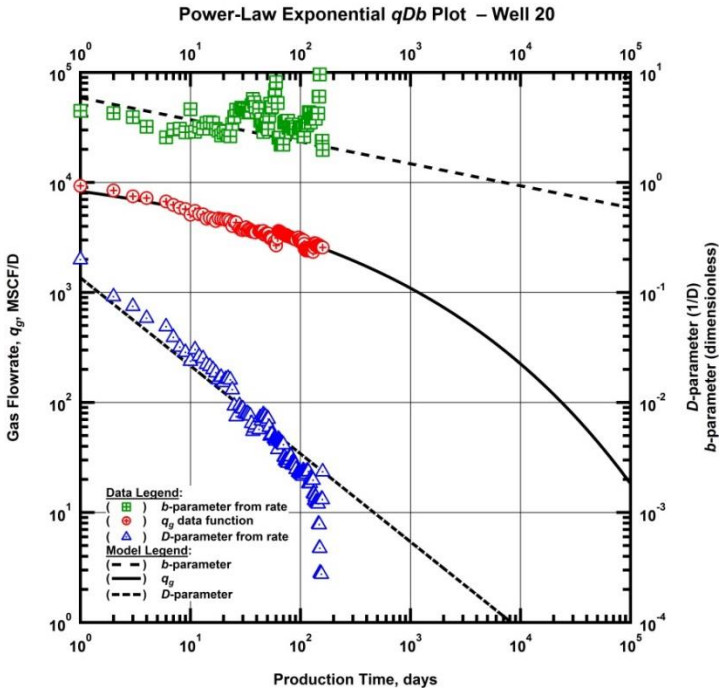

Figure B75 — (Log-log Plot): *qDb* plot — gas flow rate (q_{gi}), *D*- and *b*-parameters versus production time and modified hyperbolic model matches for Well 20.

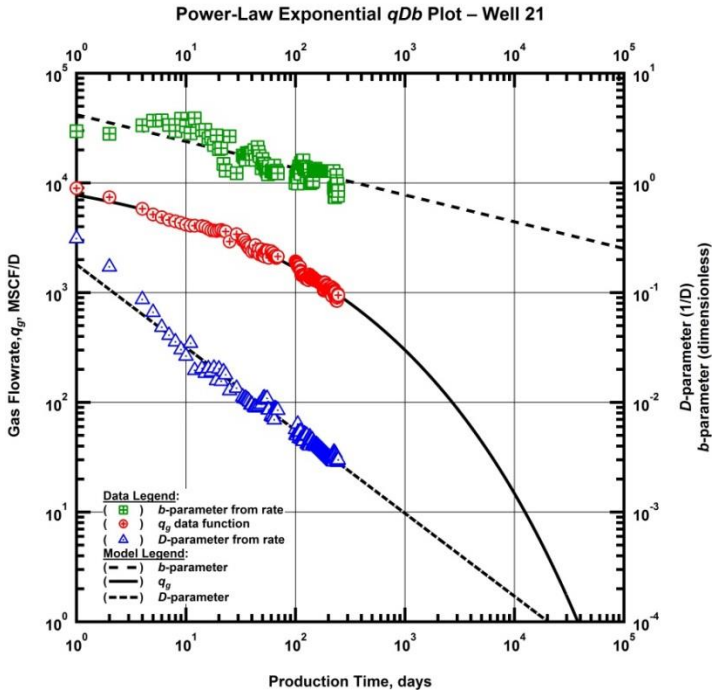

Figure B76 — (Log-log Plot): *qDb* plot — gas flow rate (q_{gi}), *D*- and *b*-parameters versus production time and modified hyperbolic model matches for Well 21.

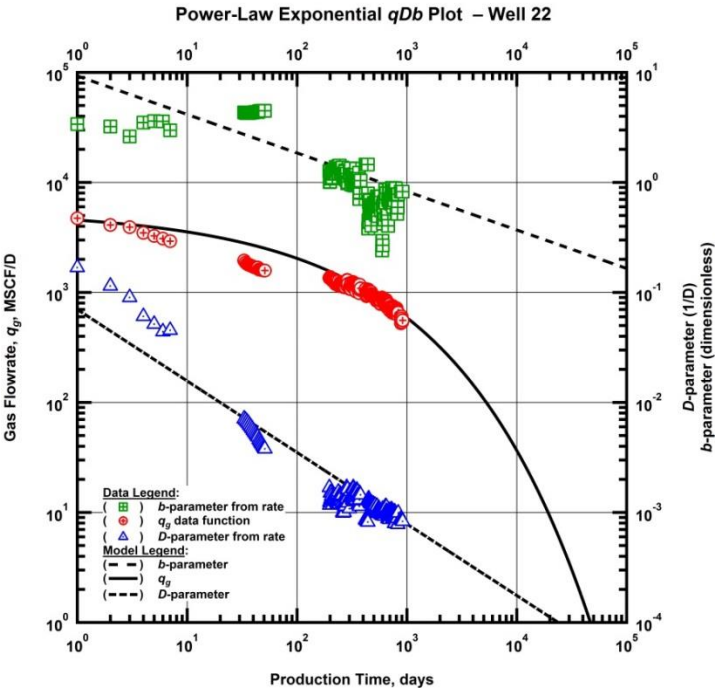

Figure B77 — (Log-log Plot): *qDb* plot — gas flow rate (q_{gi}), *D*- and *b*-parameters versus production time and modified hyperbolic model matches for Well 22.

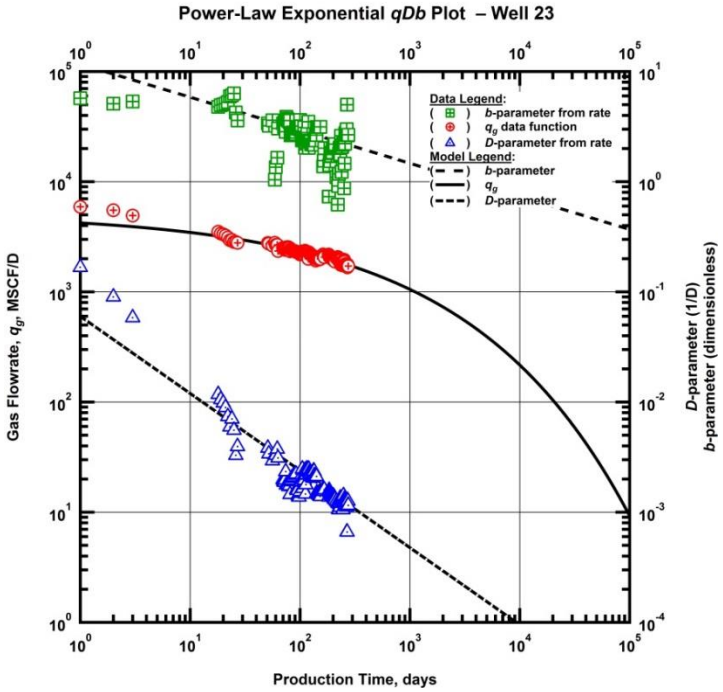

Figure B78 — (Log-log Plot): *qDb* plot — gas flow rate (q_{gi}), *D*- and *b*-parameters versus production time and modified hyperbolic model matches for Well 23.

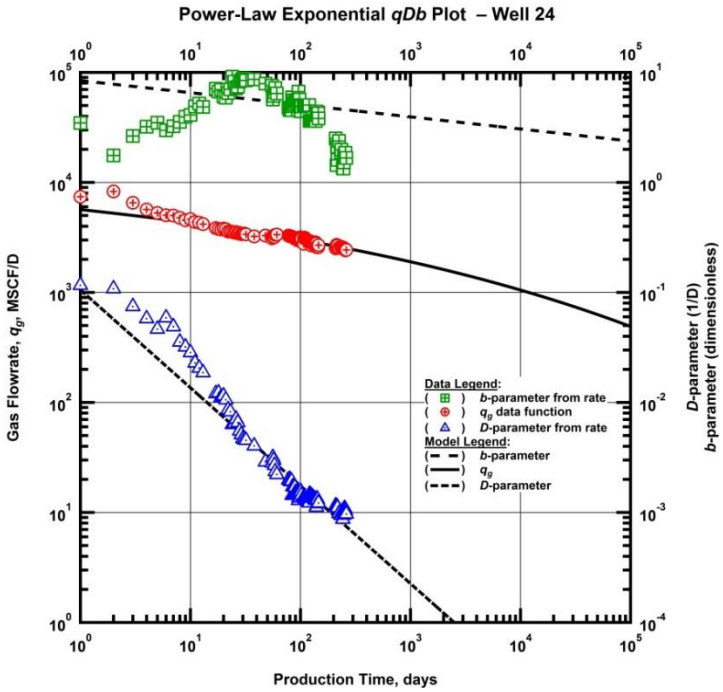

Figure B79 — (Log-log Plot): *qDb* plot — gas flow rate (q_{gi}), *D*- and *b*-parameters versus production time and modified hyperbolic model matches for Well 24.

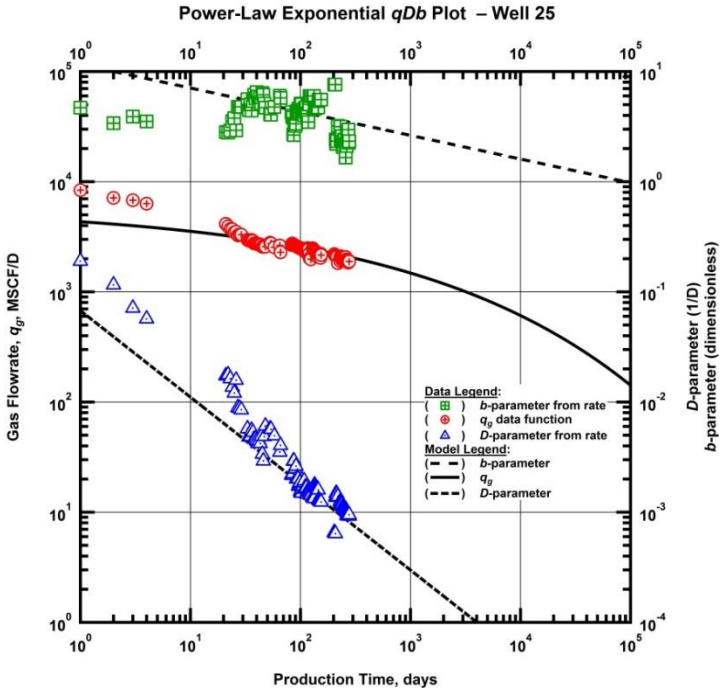

Figure B80 — (Log-log Plot): *qDb* plot — gas flow rate (q_{gi}), *D*- and *b*-parameters versus production time and modified hyperbolic model matches for Well 25.

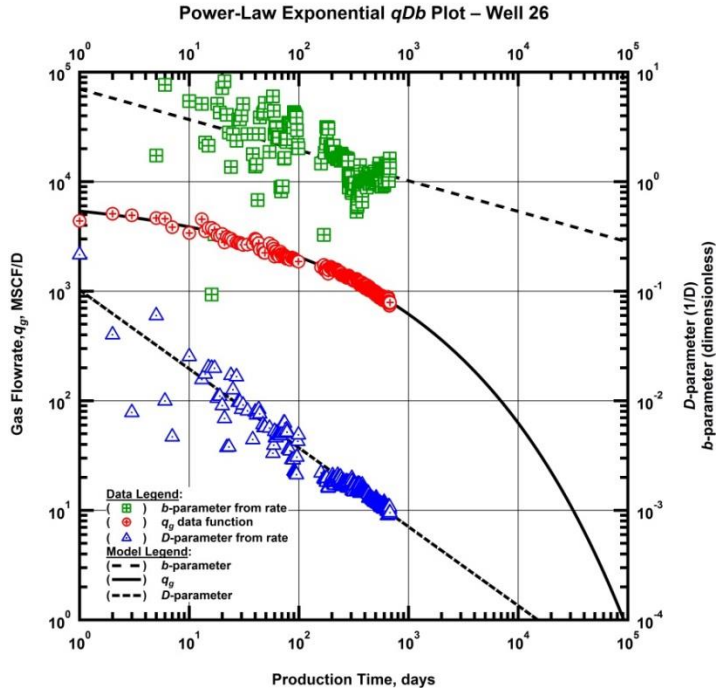

Figure B81 — (Log-log Plot): *qDb* plot — gas flow rate (q_{gi}), *D*- and *b*-parameters versus production time and modified hyperbolic model matches for Well 26.

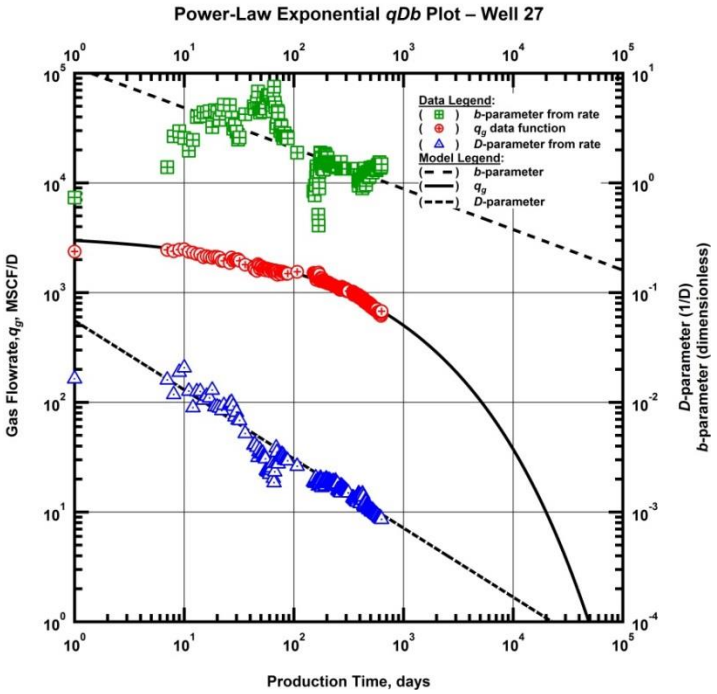

Figure B82 — (Log-log Plot): *qDb* plot — gas flow rate (q_{gi}), *D*- and *b*-parameters versus production time and modified hyperbolic model matches for Well 27.

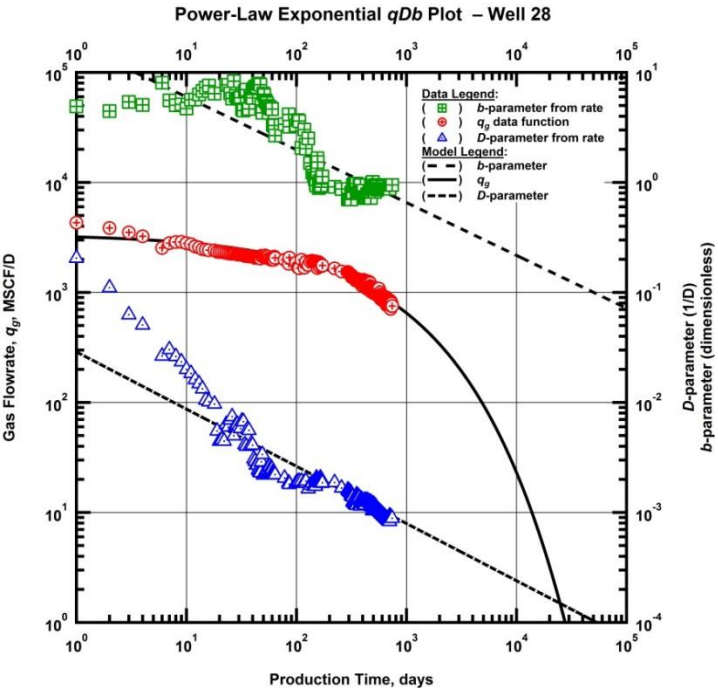

Figure B83 — (Log-log Plot): *qDb* plot — gas flow rate (q_{gi}), *D*- and *b*-parameters versus production time and modified hyperbolic model matches for Well 28.

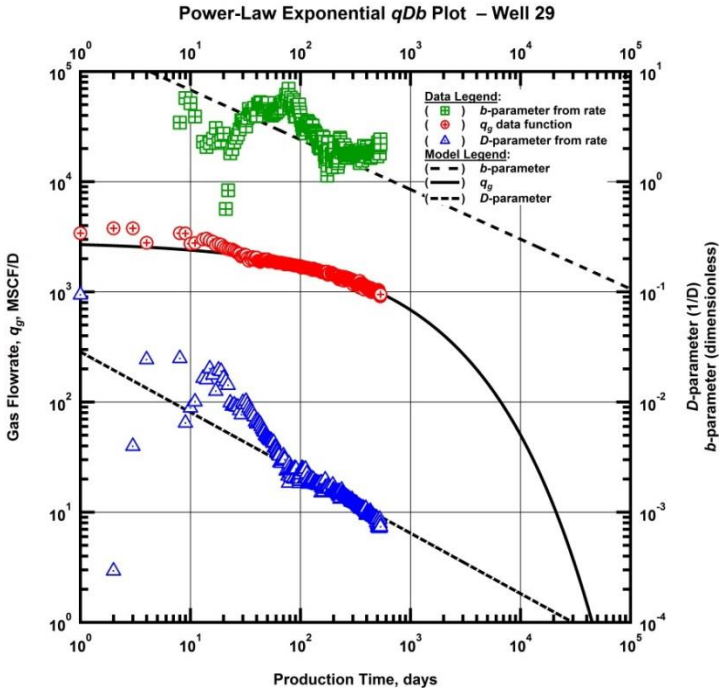

Figure B84 — (Log-log Plot): *qDb* plot — gas flow rate (q_{gi}), *D*- and *b*-parameters versus production time and modified hyperbolic model matches for Well 29.

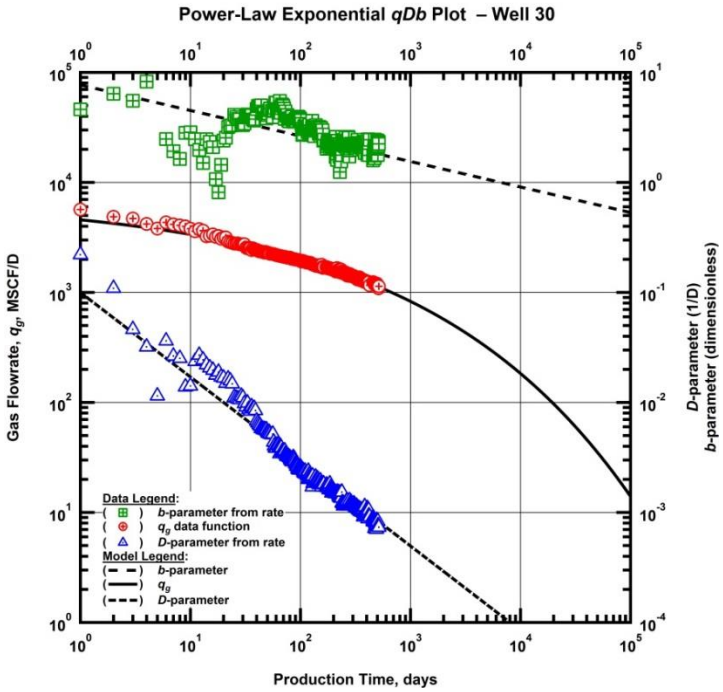

Figure B85 — (Log-log Plot): *qDb* plot — gas flow rate (q_{gi}), *D*- and *b*-parameters versus production time and modified hyperbolic model matches for Well 30.

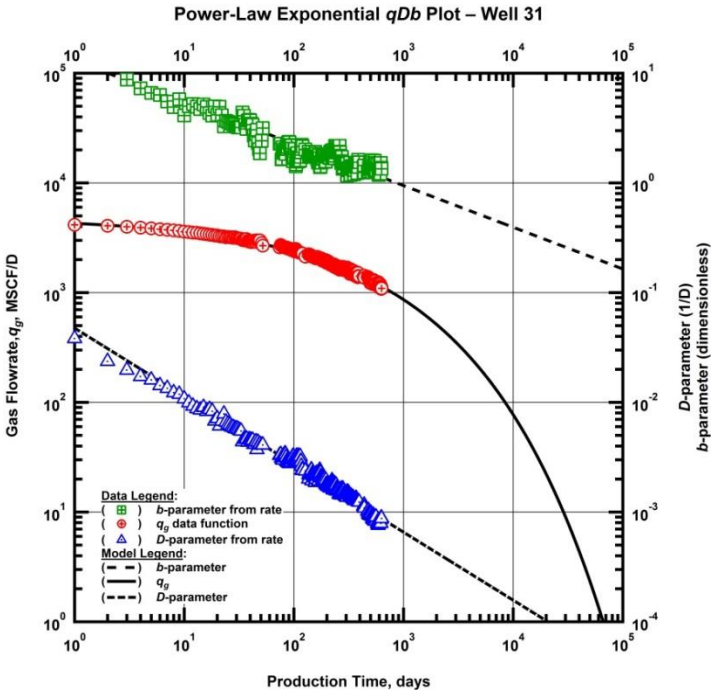

Figure B86 — (Log-log Plot): *qDb* plot — gas flow rate (q_{gi}), *D*- and *b*-parameters versus production time and modified hyperbolic model matches for Well 31.

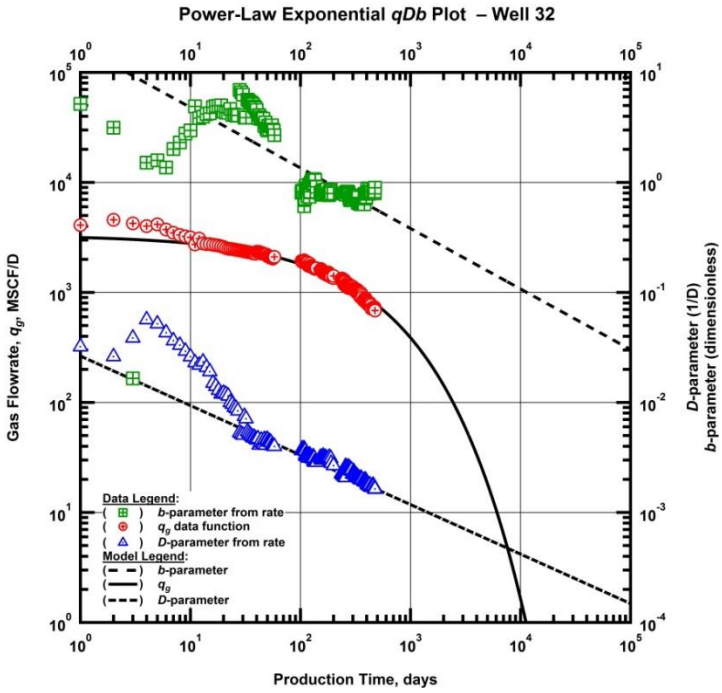

Figure B87 — (Log-log Plot): *qDb* plot — gas flow rate (q_{gi}), *D*- and *b*-parameters versus production time and modified hyperbolic model matches for Well 32.

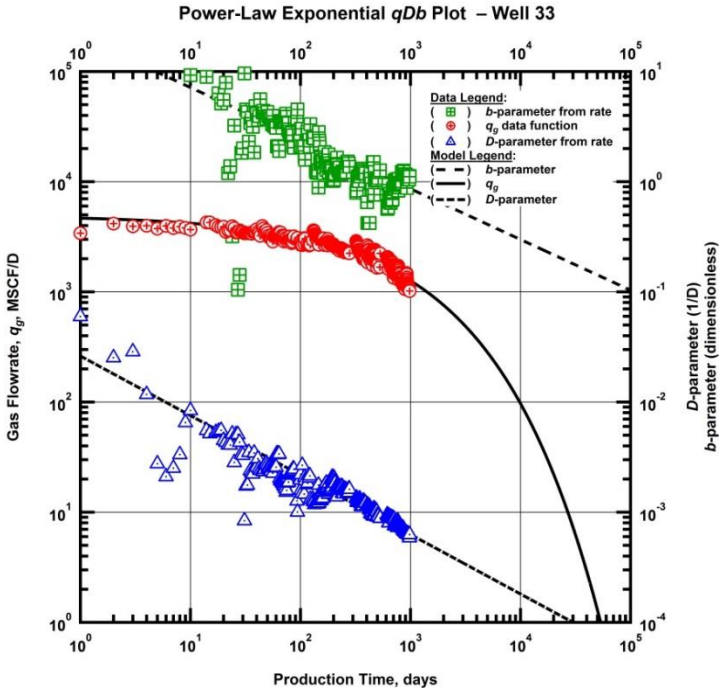

Figure B88 — (Log-log Plot): *qDb* plot — gas flow rate (q_{gi}), *D*- and *b*-parameters versus production time and modified hyperbolic model matches for Well 33.

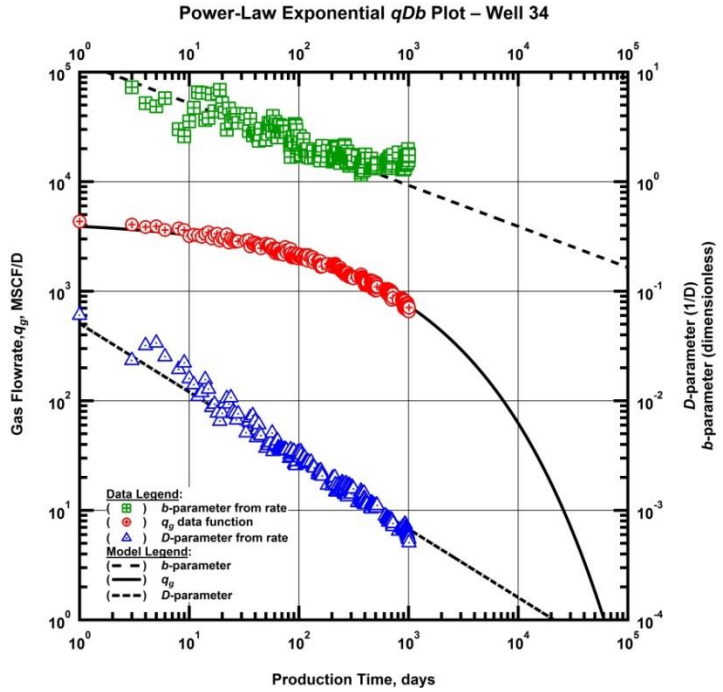

Figure B89 — (Log-log Plot): *qDb* plot — gas flow rate (q_{gi}), *D*- and *b*-parameters versus production time and modified hyperbolic model matches for Well 34.

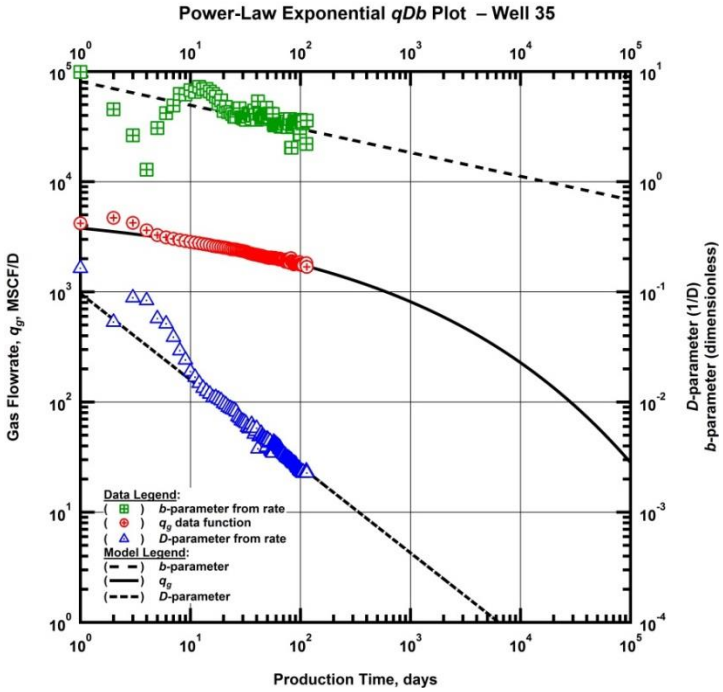

Figure B90 — (Log-log Plot): *qDb* plot — gas flow rate (q_{gi}), *D*- and *b*-parameters versus production time and modified hyperbolic model matches for Well 35.

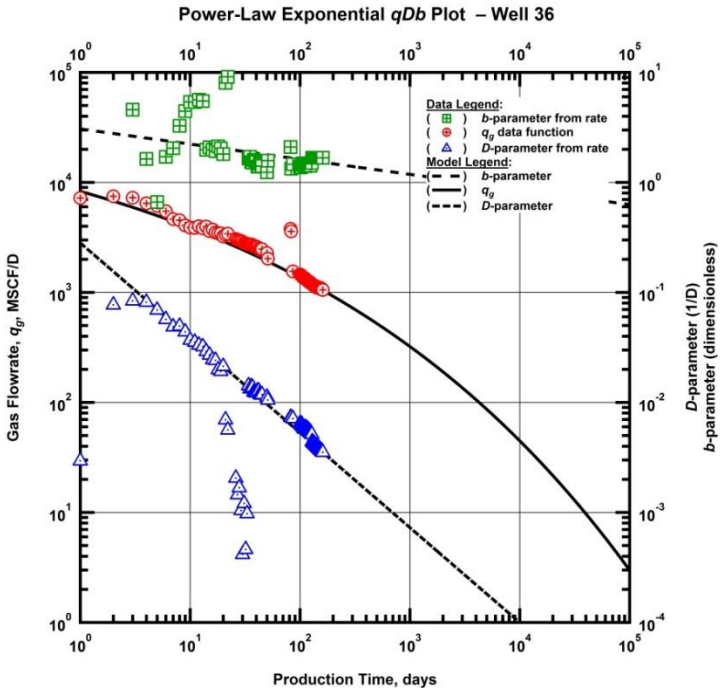

Figure B91 — (Log-log Plot): *qDb* plot — gas flow rate (q_{gi}), *D*- and *b*-parameters versus production time and modified hyperbolic model matches for Well 36.

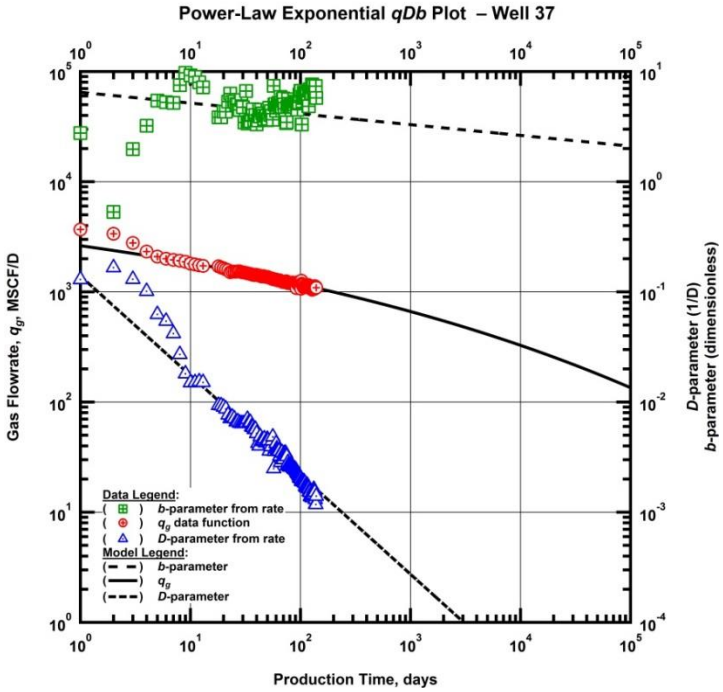

Figure B92 — (Log-log Plot): *qDb* plot — gas flow rate (q_{gi}), *D*- and *b*-parameters versus production time and modified hyperbolic model matches for Well 37.

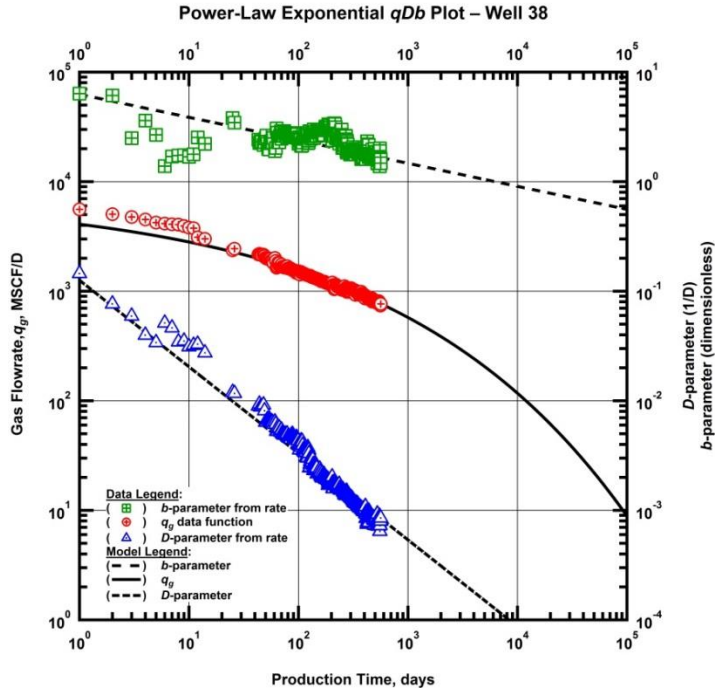

Figure B93 — (Log-log Plot): *qDb* plot — gas flow rate (q_{gi}), *D*- and *b*-parameters versus production time and modified hyperbolic model matches for Well 38.

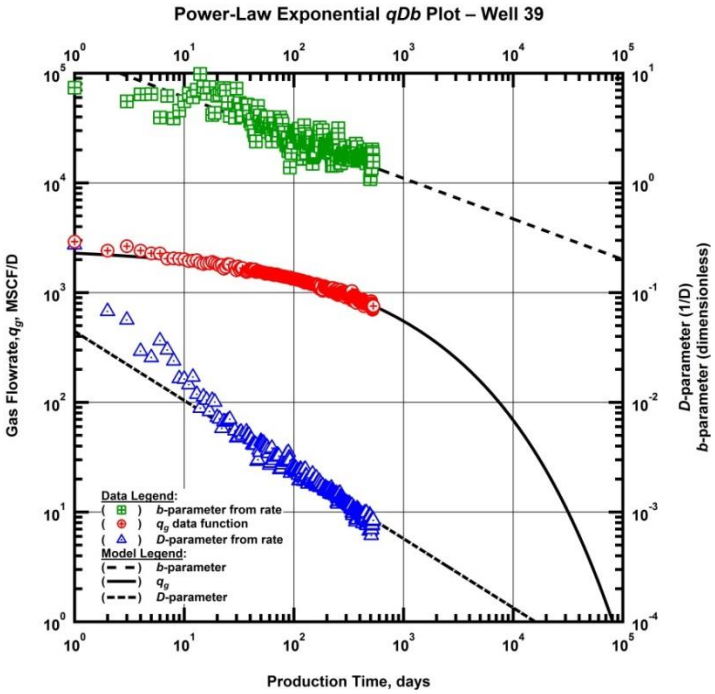

Figure B94 — (Log-log Plot): *qDb* plot — gas flow rate (q_{gi}), *D*- and *b*-parameters versus production time and modified hyperbolic model matches for Well 39.

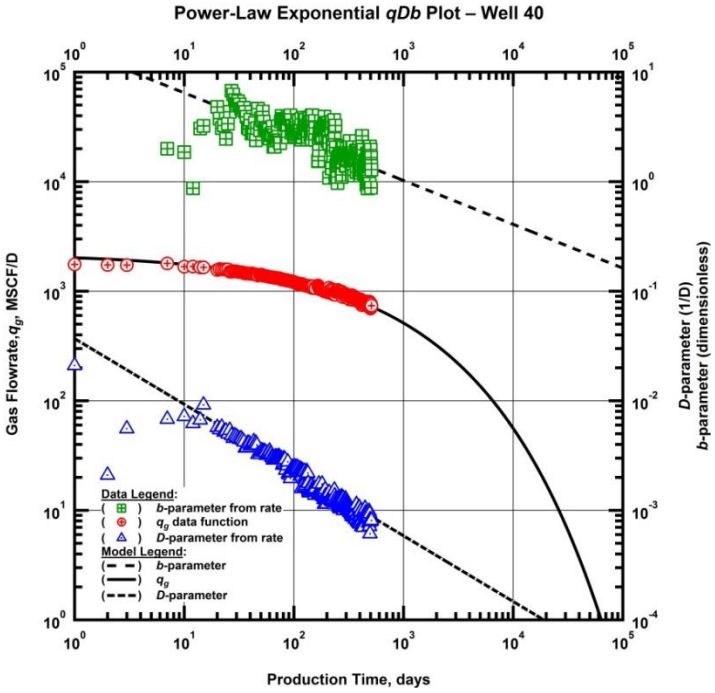

Figure B95 — (Log-log Plot): *qDb* plot — gas flow rate (q_{gi}), *D*- and *b*-parameters versus production time and modified hyperbolic model matches for Well 40.

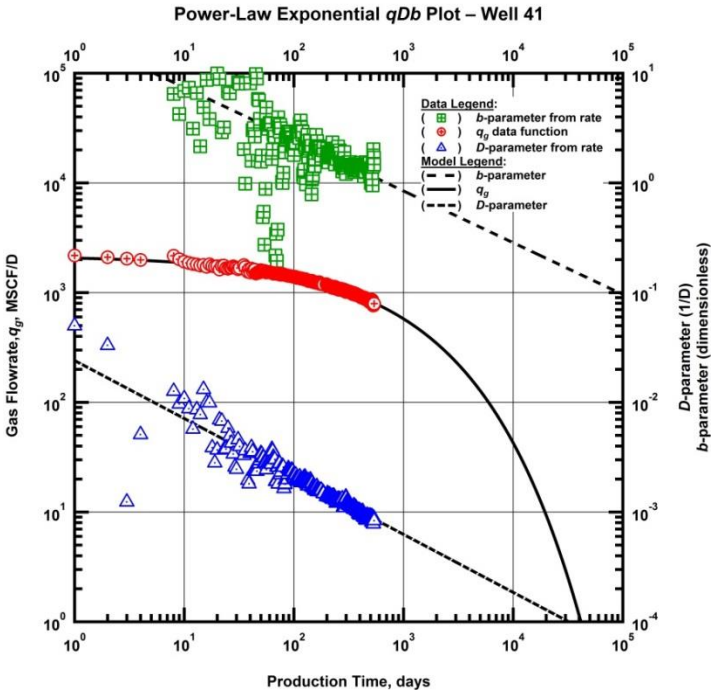

Figure B96 — (Log-log Plot): *qDb* plot — gas flow rate (q_{gi}), *D*- and *b*-parameters versus production time and modified hyperbolic model matches for Well 41.

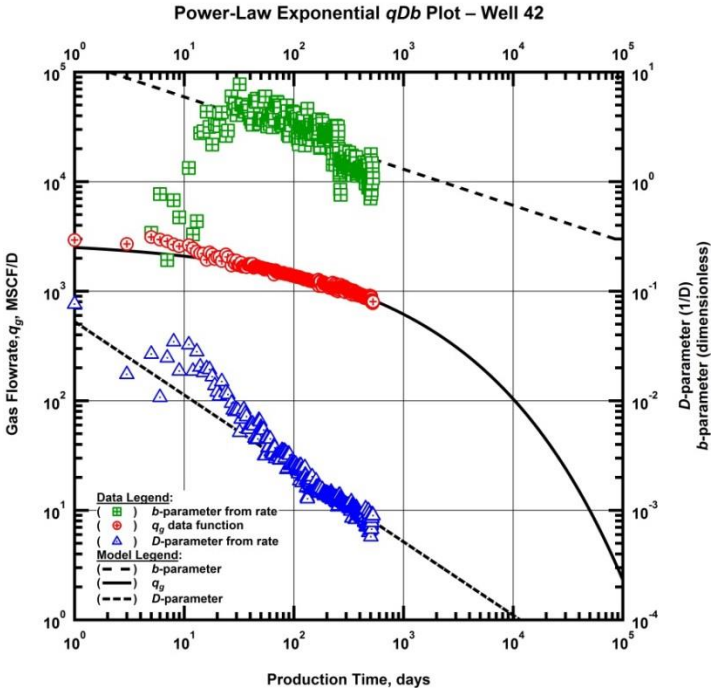

Figure B97 — (Log-log Plot): *qDb* plot — gas flow rate (q_{gi}), *D*- and *b*-parameters versus production time and modified hyperbolic model matches for Well 42.

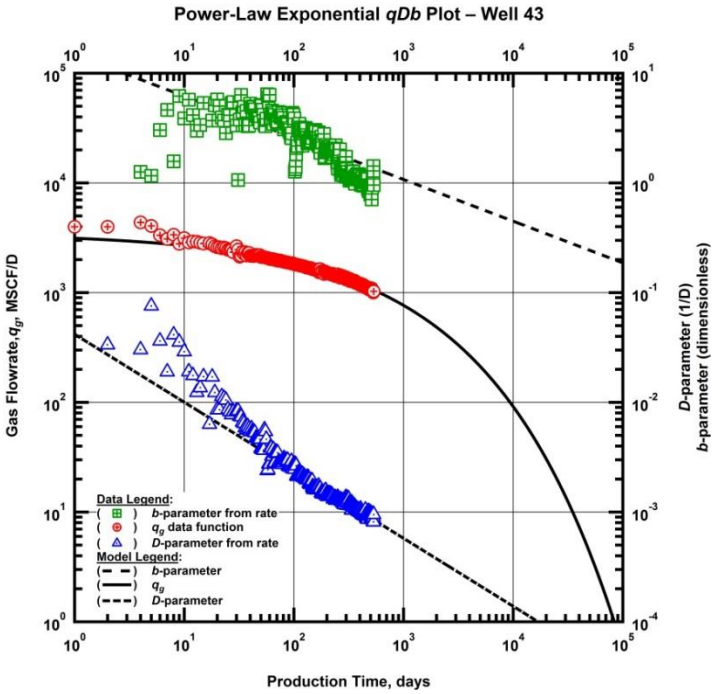

Figure B98 — (Log-log Plot): *qDb* plot — gas flow rate (q_{gi}), *D*- and *b*-parameters versus production time and modified hyperbolic model matches for Well 43.

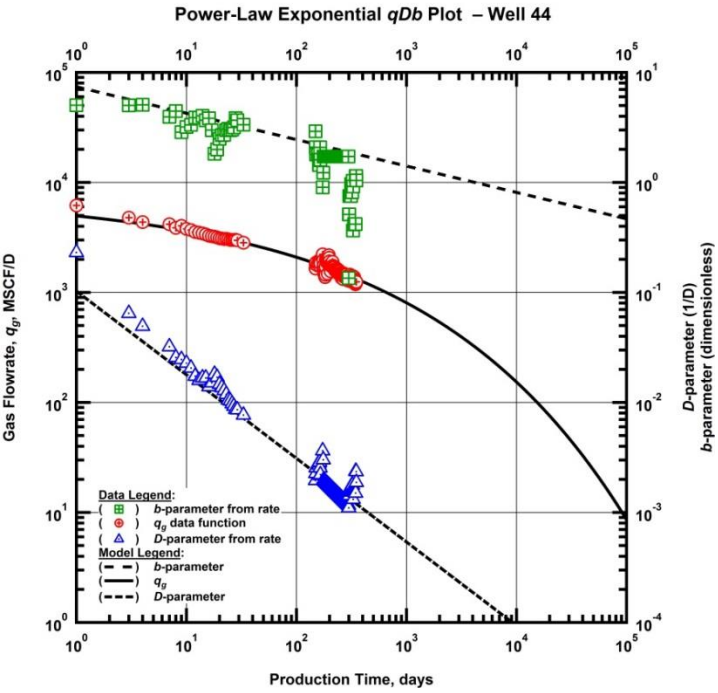

Figure B99 — (Log-log Plot): *qDb* plot — gas flow rate (q_{gi}), *D*- and *b*-parameters versus production time and modified hyperbolic model matches for Well 44.

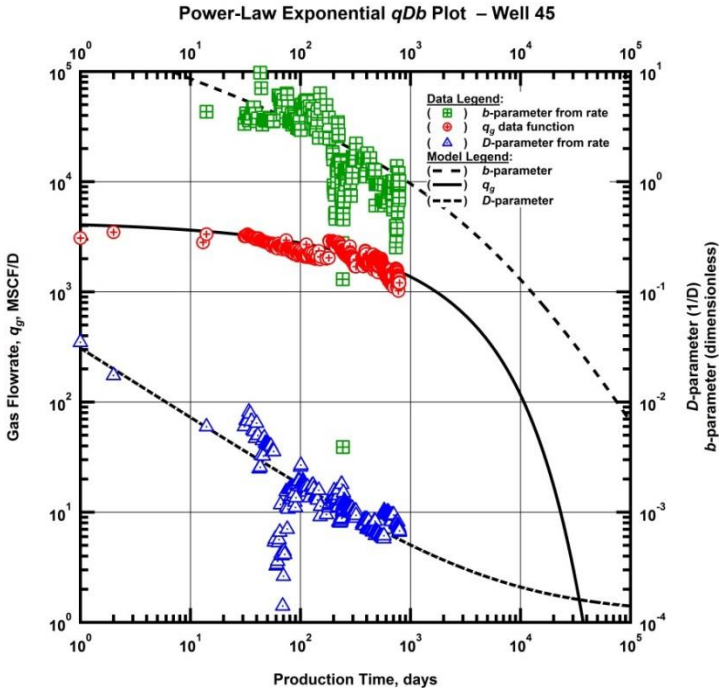

Figure B100 — (Log-log Plot): *qDb* plot — gas flow rate (q_{gi}), *D*- and *b*-parameters versus production time and modified hyperbolic model matches for Well 45.

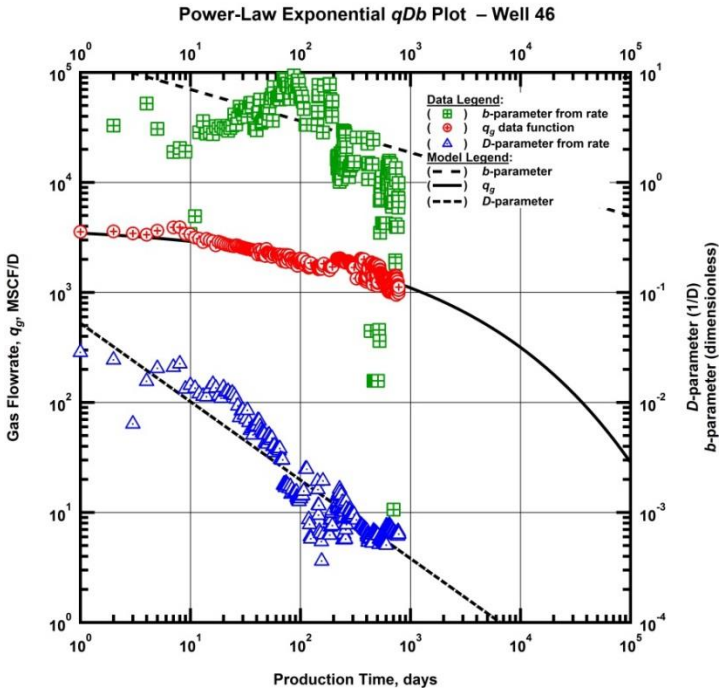

Figure B101 — (Log-log Plot): *qDb* plot — gas flow rate (q_{gi}), *D*- and *b*-parameters versus production time and modified hyperbolic model matches for Well 46.

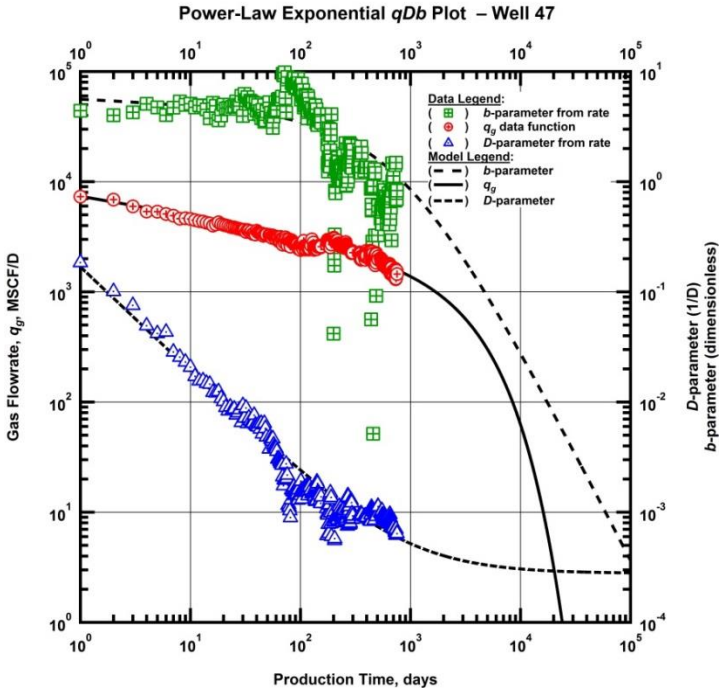

Figure B102 — (Log-log Plot): *qDb* plot — gas flow rate (q_{gi}), *D*- and *b*-parameters versus production time and modified hyperbolic model matches for Well 47.

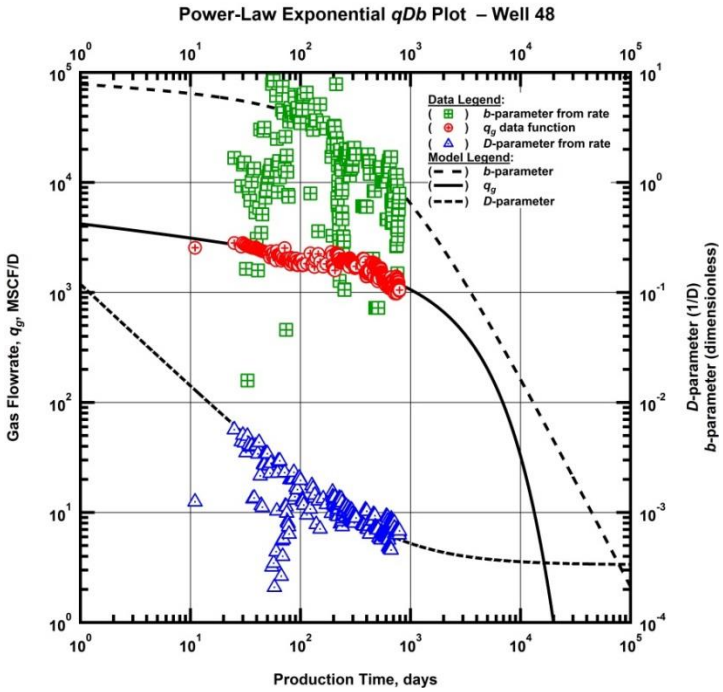

Figure B103 — (Log-log Plot): *qDb* plot — gas flow rate (q_{gi}), *D*- and *b*-parameters versus production time and modified hyperbolic model matches for Well 48.

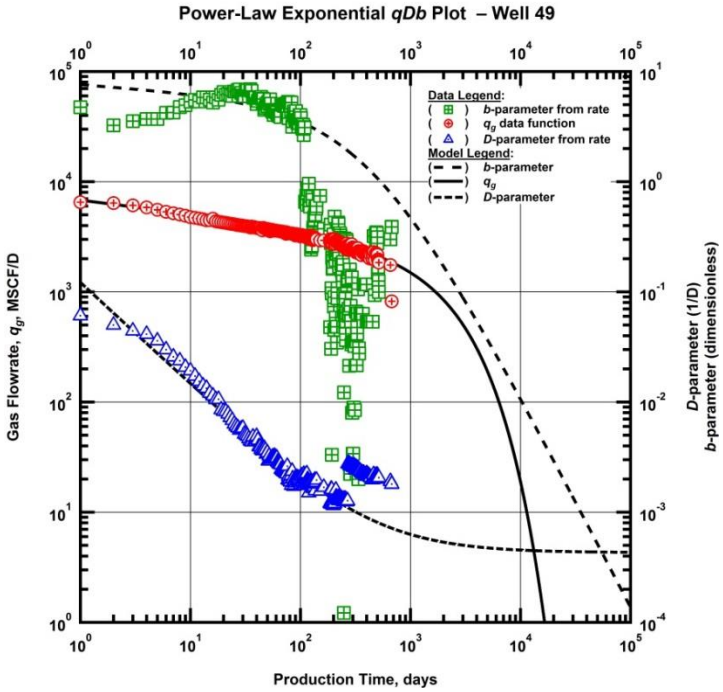

Figure B104 — (Log-log Plot): *qDb* plot — gas flow rate (q_{gi}), *D*- and *b*-parameters versus production time and modified hyperbolic model matches for Well 49.

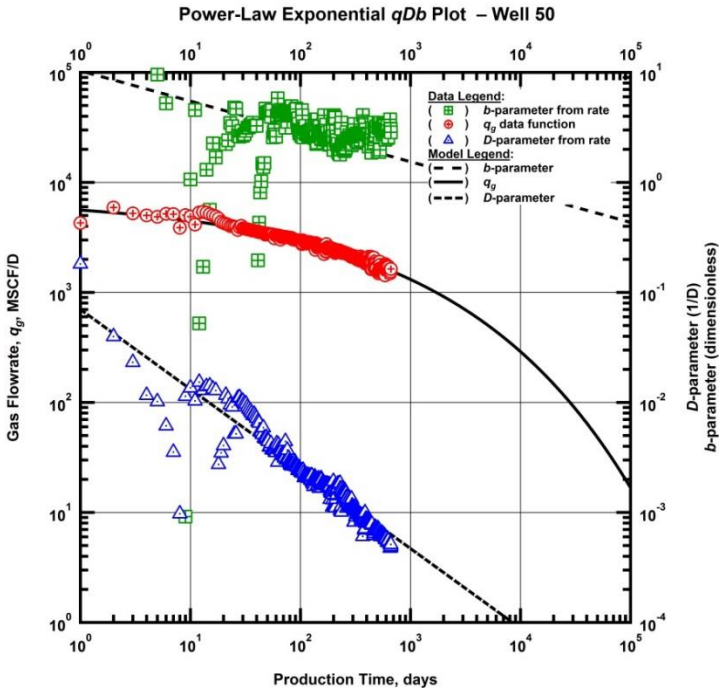

Figure B105 — (Log-log Plot): *qDb* plot — gas flow rate (q_{gi}), *D*- and *b*-parameters versus production time and modified hyperbolic model matches for Well 50.

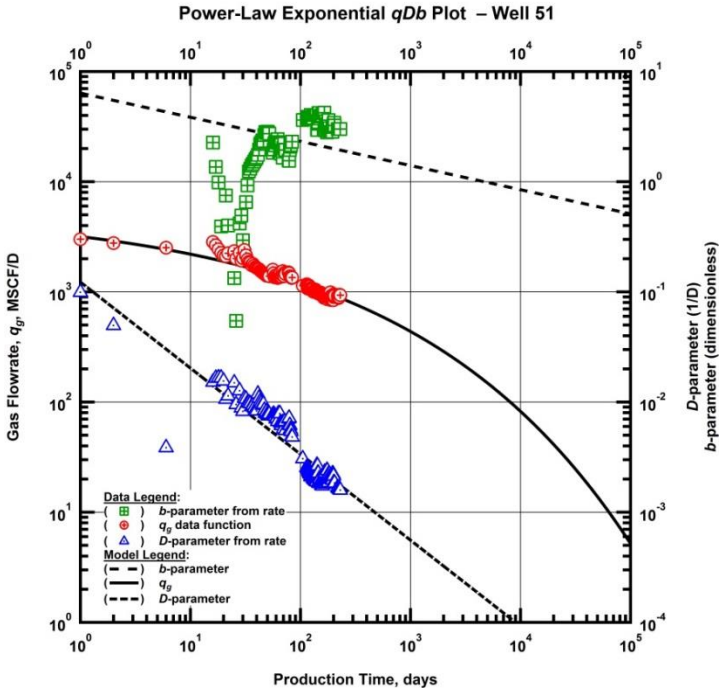

Figure B106 — (Log-log Plot): *qDb* plot — gas flow rate (q_{gi}), *D*- and *b*-parameters versus production time and modified hyperbolic model matches for Well 51.

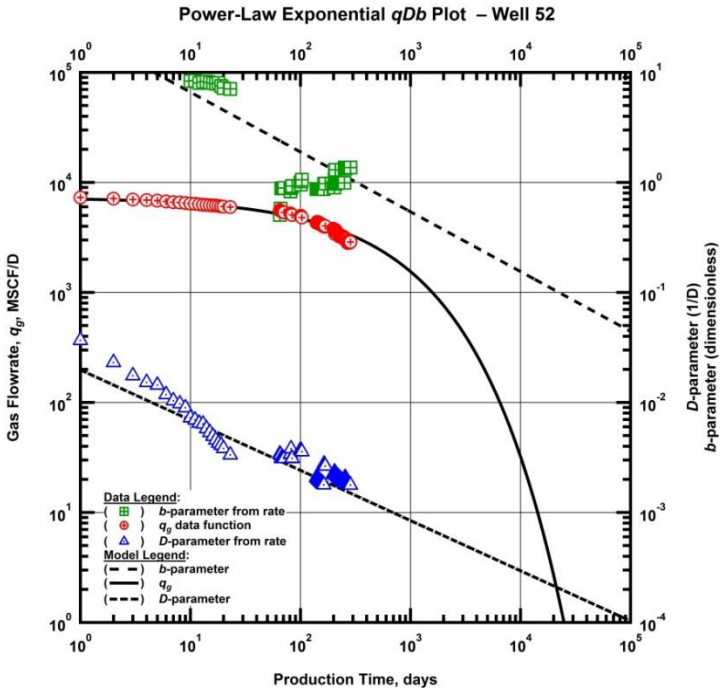

Figure B107 — (Log-log Plot): *qDb* plot — gas flow rate (q_{gi}), *D*- and *b*-parameters versus production time and modified hyperbolic model matches for Well 52.

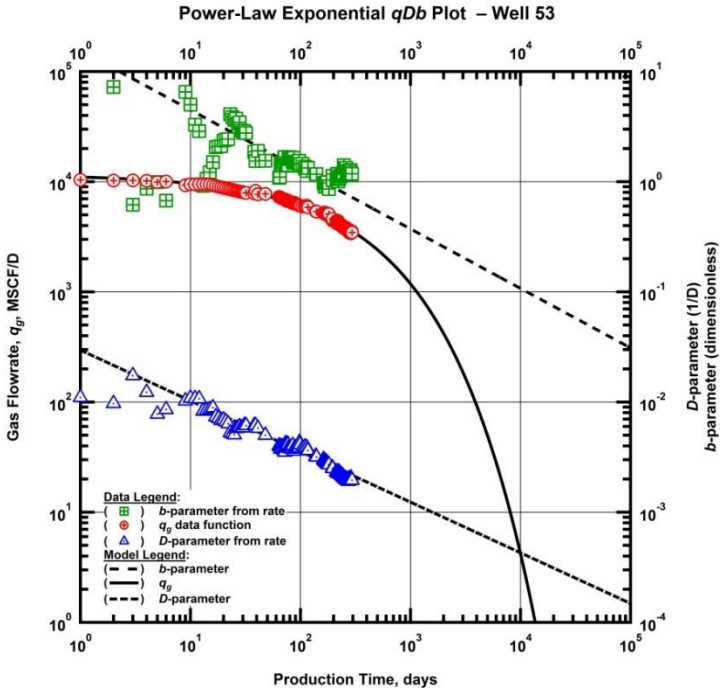

Figure B108 — (Log-log Plot): *qDb* plot — gas flow rate (q_{gi}), *D*- and *b*-parameters versus production time and modified hyperbolic model matches for Well 53.

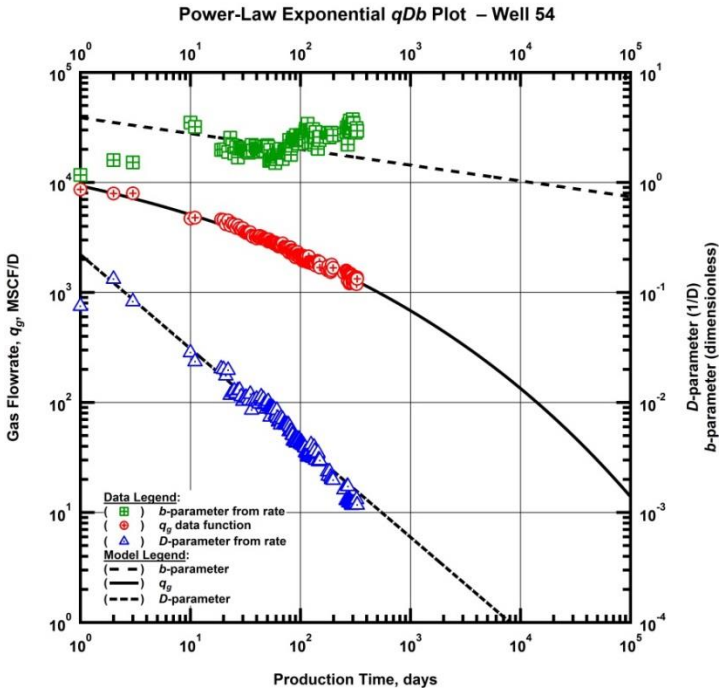

Figure B109 — (Log-log Plot): *qDb* plot — gas flow rate (q_{gi}), *D*- and *b*-parameters versus production time and modified hyperbolic model matches for Well 54.

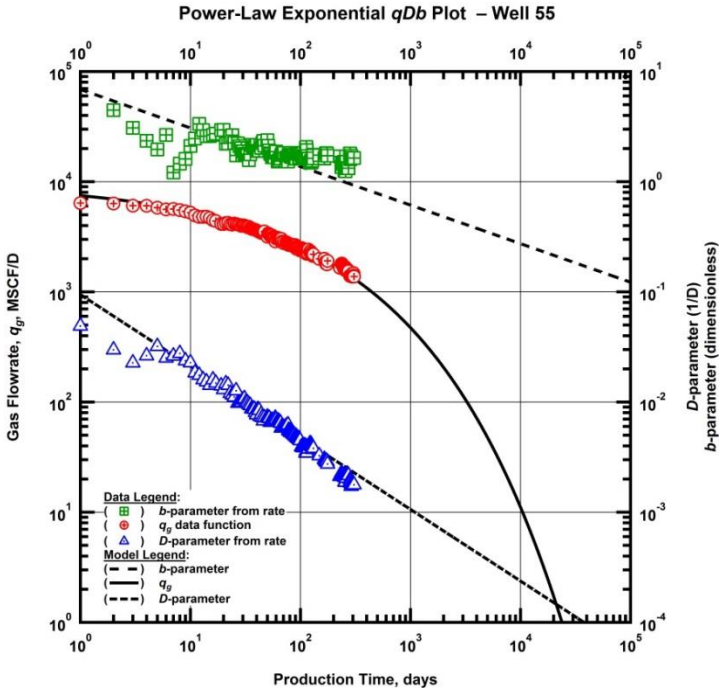

Figure B110 — (Log-log Plot): *qDb* plot — gas flow rate (q_{gi}), *D*- and *b*-parameters versus production time and modified hyperbolic model matches for Well 55.

APPENDIX C
MODEL-BASED PRODUCTION ANALYSIS

We present the full 55-well catalog of model-based production data diagnostic plots in **Figs. C1 - C55**. The two functions plotted are given below.

- $I(t_e) = \frac{1}{t_e}\int_0^{t_e} \frac{m(p_i)-m(p_w(\tau))}{q_g(\tau)}\, d\tau$ ..... Integral of rate-normalized pseudopressure
- $I'(t_e) = \frac{\partial I(t_e)}{\partial ln(t_e)}$ ..... Bourdet derivative of the integral of rate-normalized pseudopressure

These curves can be thought of as the inverse of the productivity index (*J*) plotted continuously versus material balance time, which is the ratio of cumulative production to the flow rate. Normalizing the variable pseudopressure to rate and plotting versus material balance time allows for interpretation as a constant-rate solution. Diagnostic flow regime signatures are preserved in this plot: bilinear flow shows as two curves with quarter-slope offset by a factor of 4 and formation linear flow shows as two half-slope curves offset by a factor of two. Unit slope lines are indicative of boundary-dominated flow.

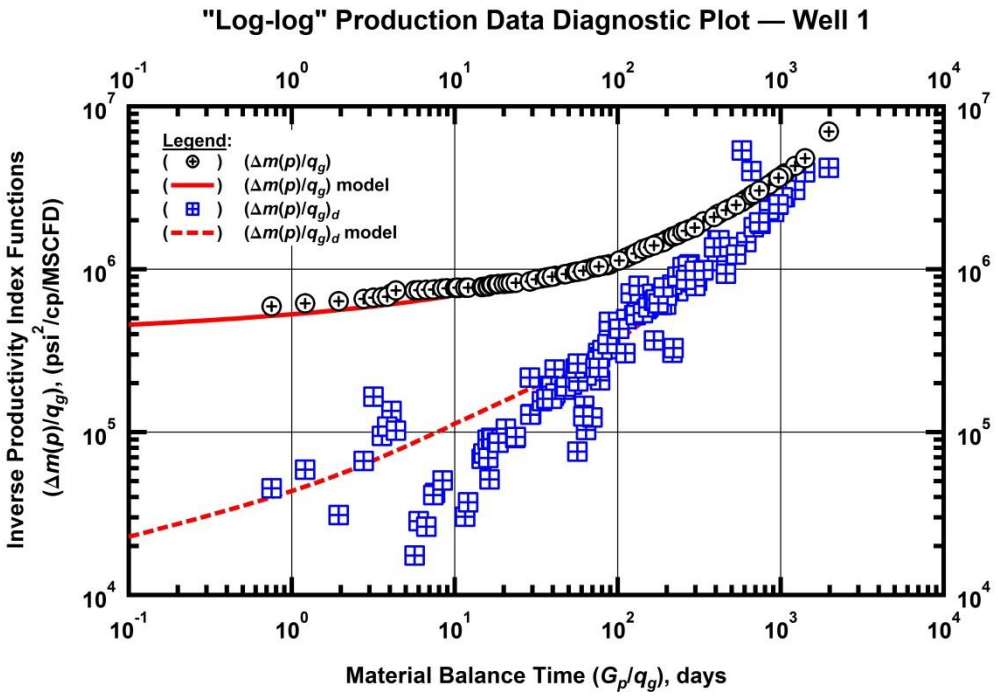

Figure C1 — (Log-log Plot): Production data diagnostic plot — inverse productivity index and its Bourdet derivative functions: data and model matches for Well 1.

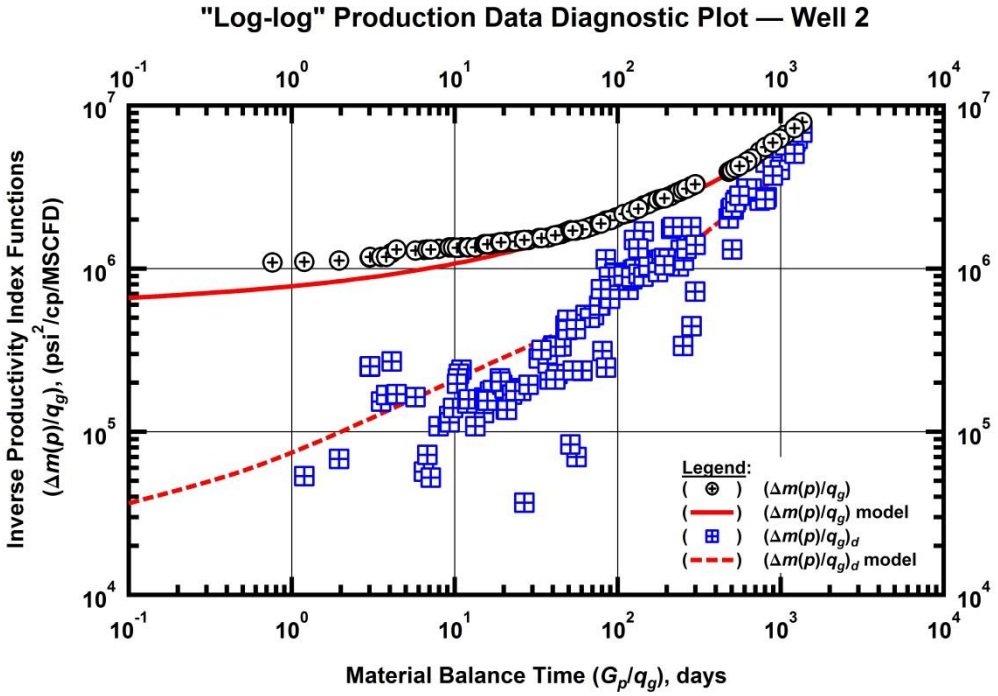

Figure C2 — (Log-log Plot): Production data diagnostic plot — inverse productivity index and its Bourdet derivative functions: data and model matches for Well 2.

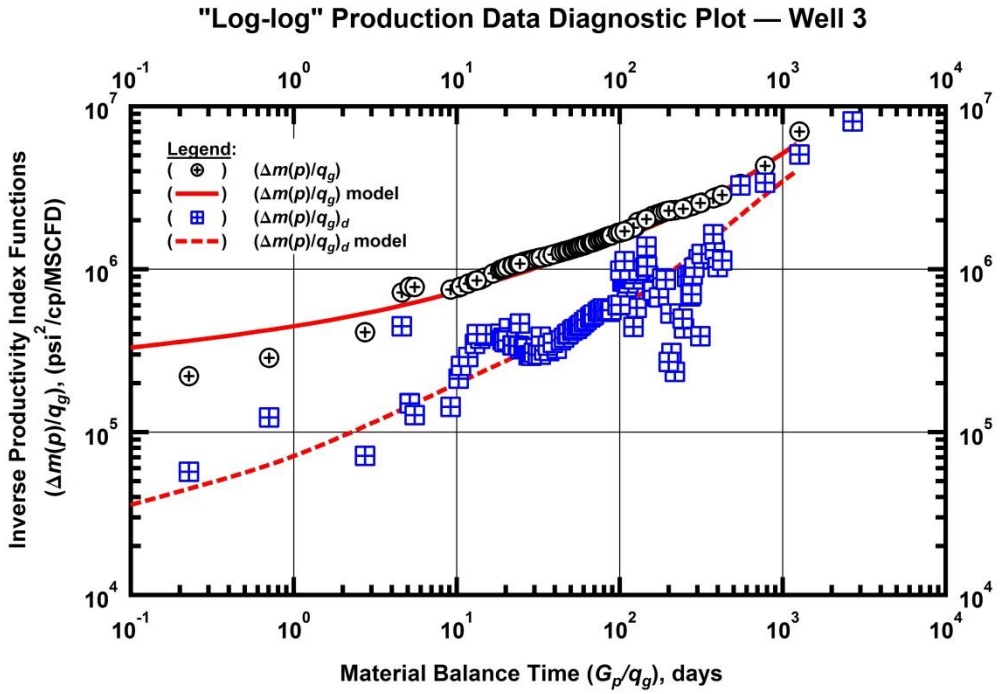

Figure C3 — (Log-log Plot): Production data diagnostic plot — inverse productivity index and its Bourdet derivative functions: data and model matches for Well 3.

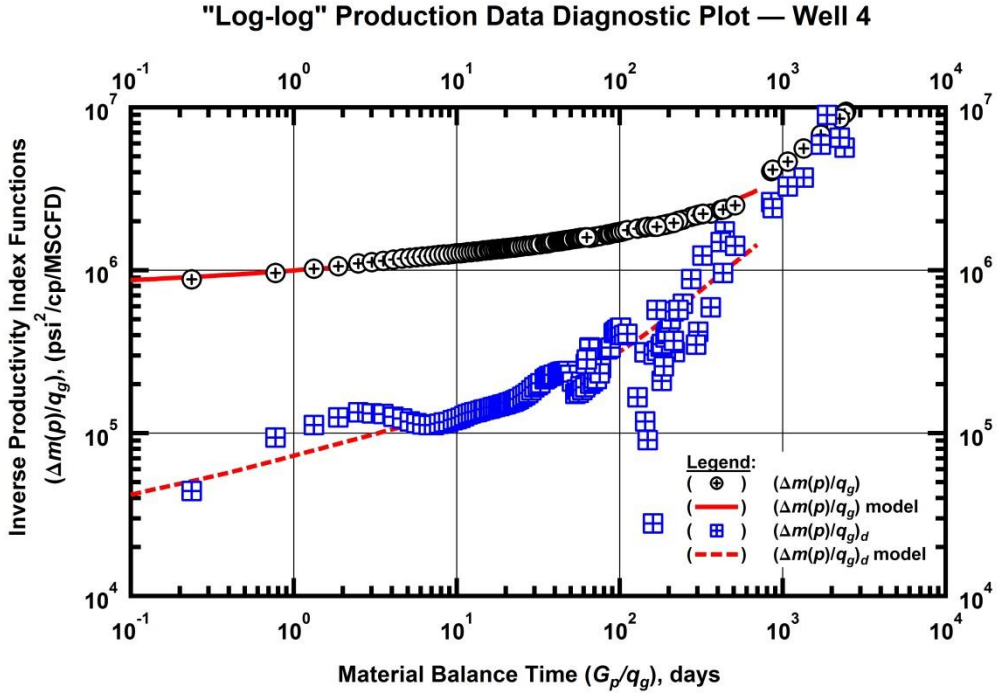

Figure C4 — (Log-log Plot): Production data diagnostic plot — inverse productivity index and its Bourdet derivative functions: data and model matches for Well 4.

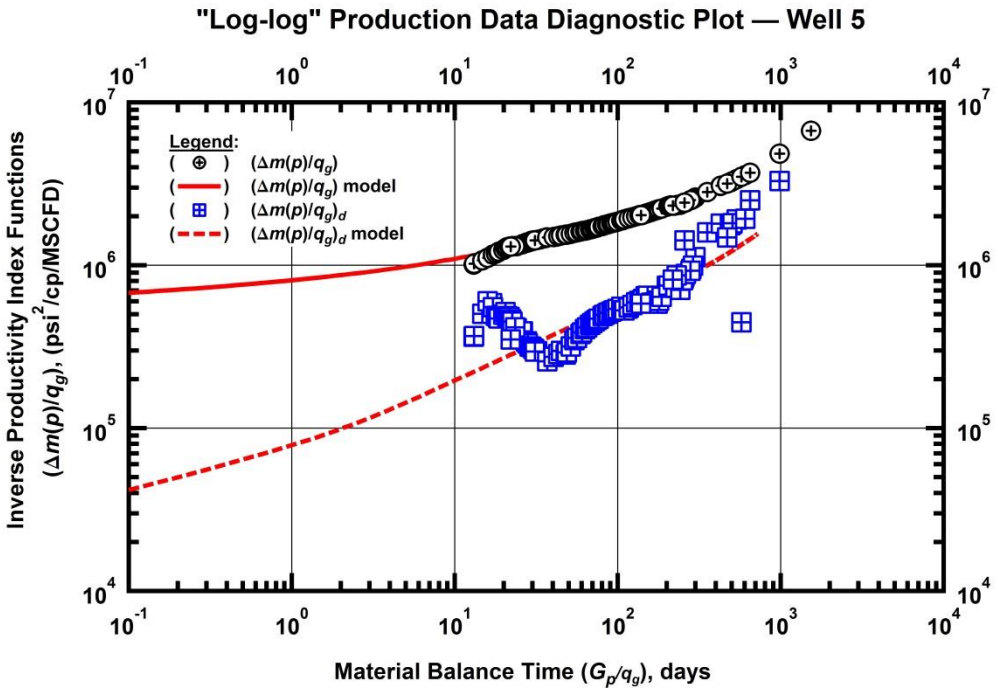

Figure C5 — (Log-log Plot): Production data diagnostic plot — inverse productivity index and its Bourdet derivative functions: data and model matches for Well 5.

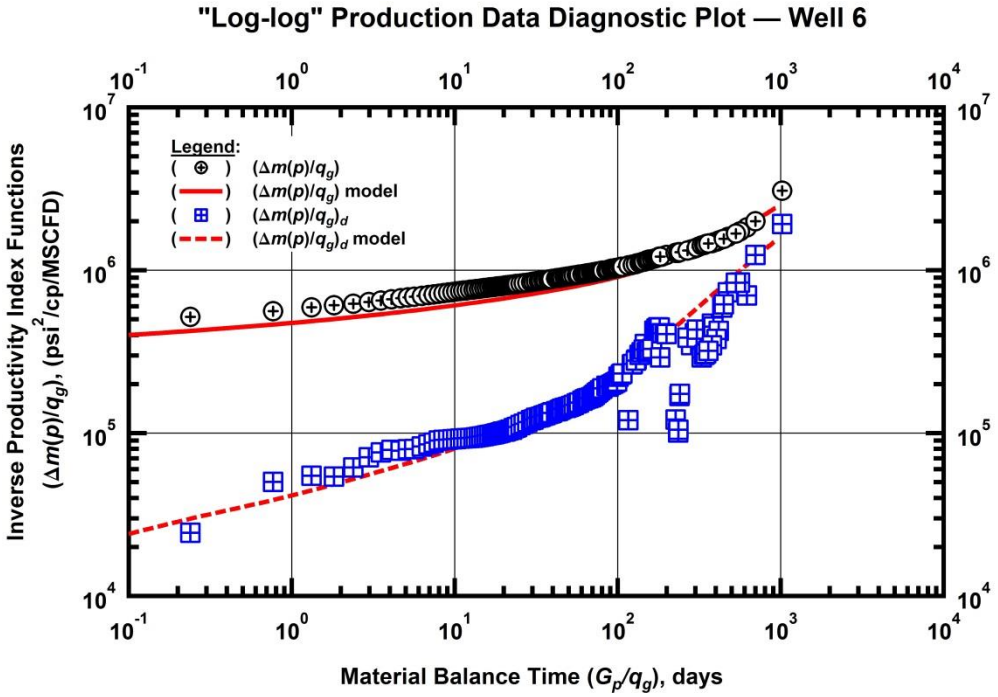

Figure C6 — (Log-log Plot): Production data diagnostic plot — inverse productivity index and its Bourdet derivative functions: data and model matches for Well 6.

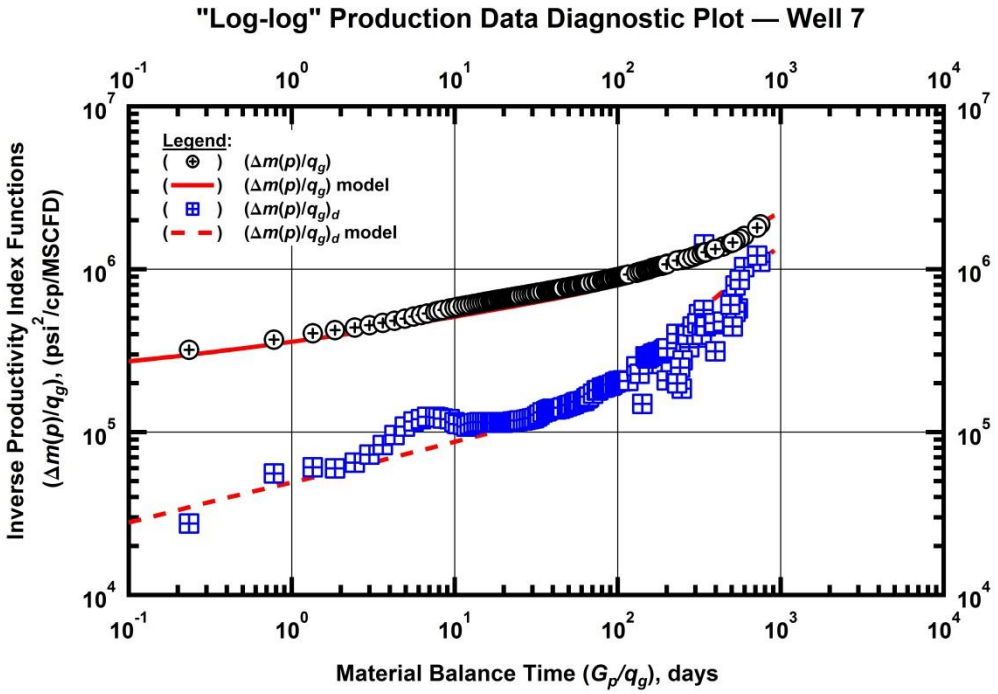

Figure C7 — (Log-log Plot): Production data diagnostic plot — inverse productivity index and its Bourdet derivative functions: data and model matches for Well 7.

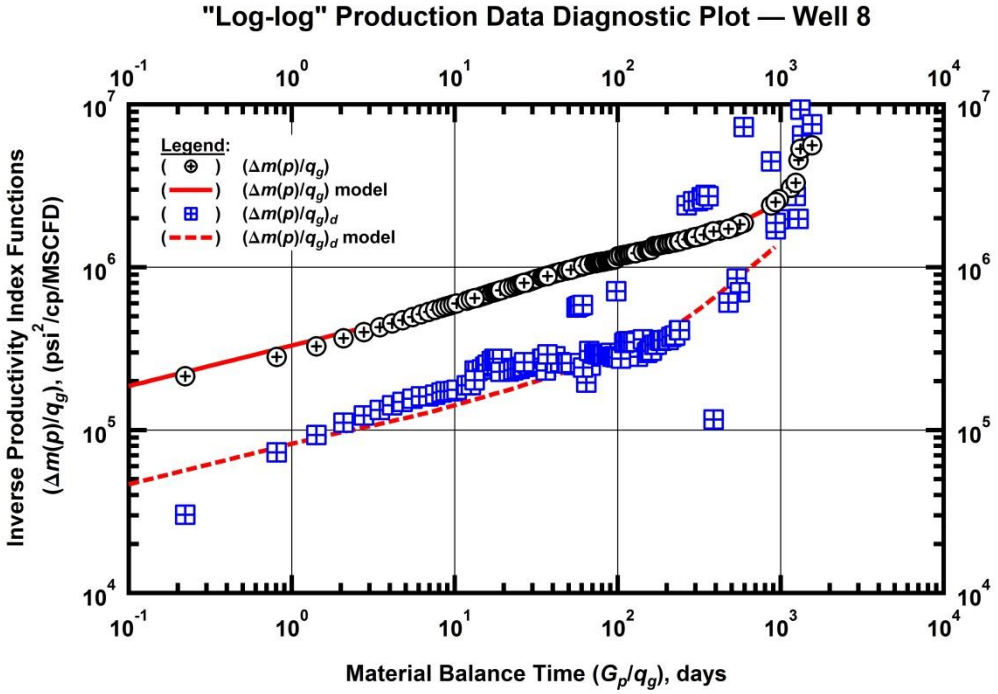

Figure C8 — (Log-log Plot): Production data diagnostic plot — inverse productivity index and its Bourdet derivative functions: data and model matches for Well 8.

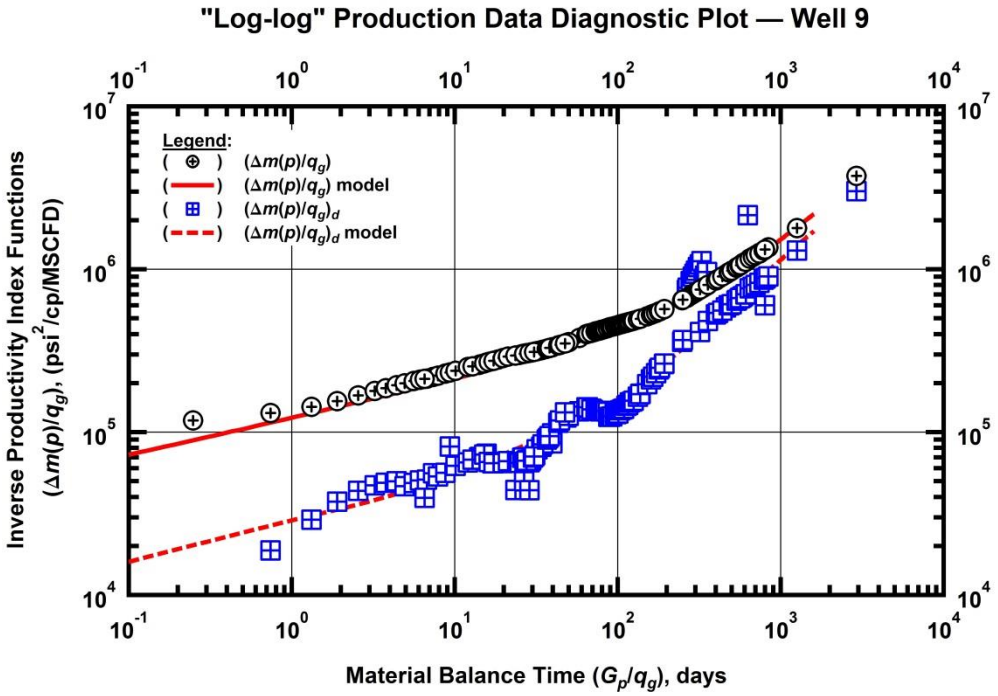

Figure C9 — (Log-log Plot): Production data diagnostic plot — inverse productivity index and its Bourdet derivative functions: data and model matches for Well 9.

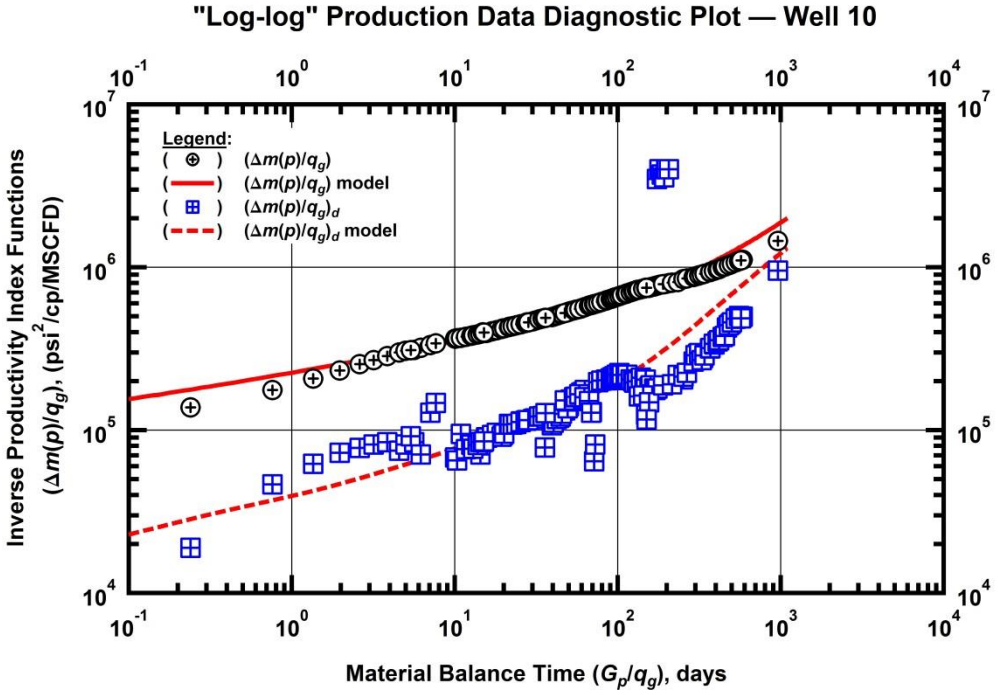

Figure C10 — (Log-log Plot): Production data diagnostic plot — inverse productivity index and its Bourdet derivative functions: data and model matches for Well 10.

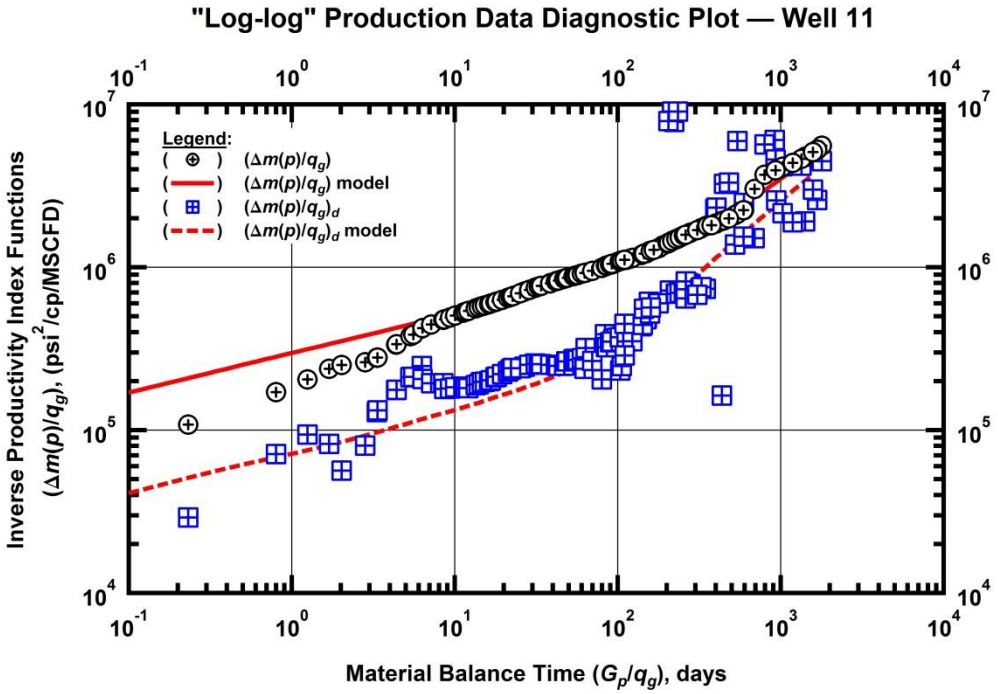

Figure C11 — (Log-log Plot): Production data diagnostic plot — inverse productivity index and its Bourdet derivative functions: data and model matches for Well 11.

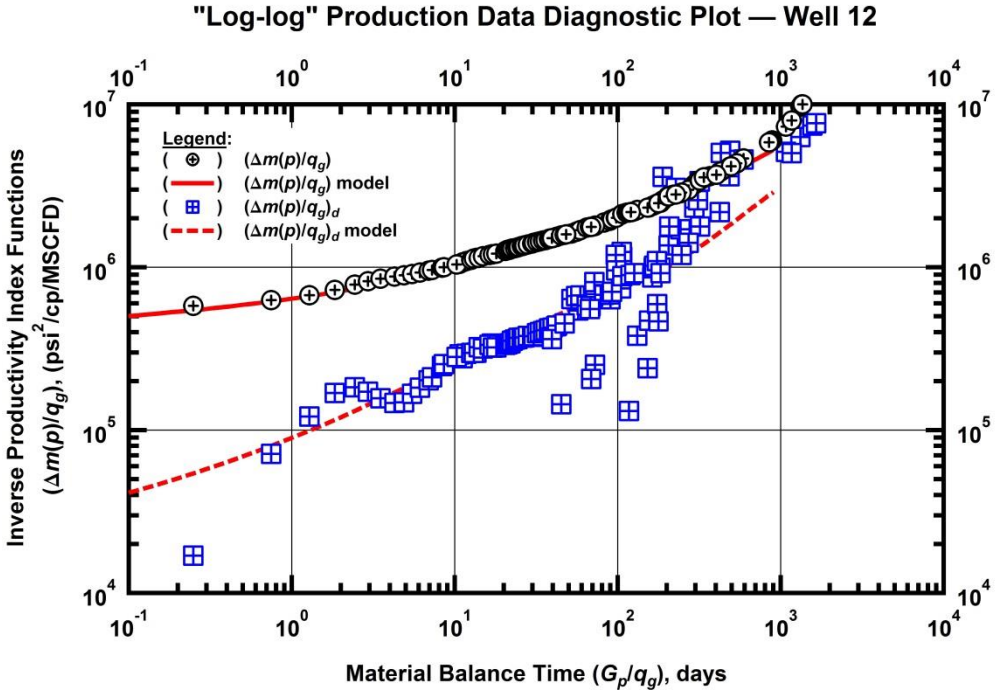

Figure C12 — (Log-log Plot): Production data diagnostic plot — inverse productivity index and its Bourdet derivative functions: data and model matches for Well 12.

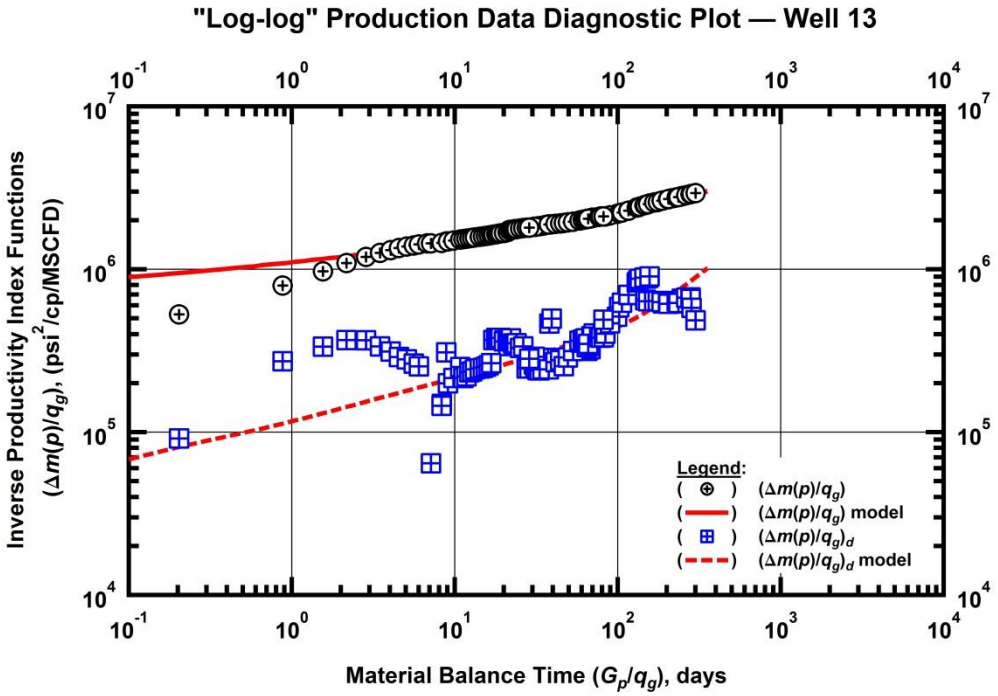

Figure C13 — (Log-log Plot): Production data diagnostic plot — inverse productivity index and its Bourdet derivative functions: data and model matches for Well 13.

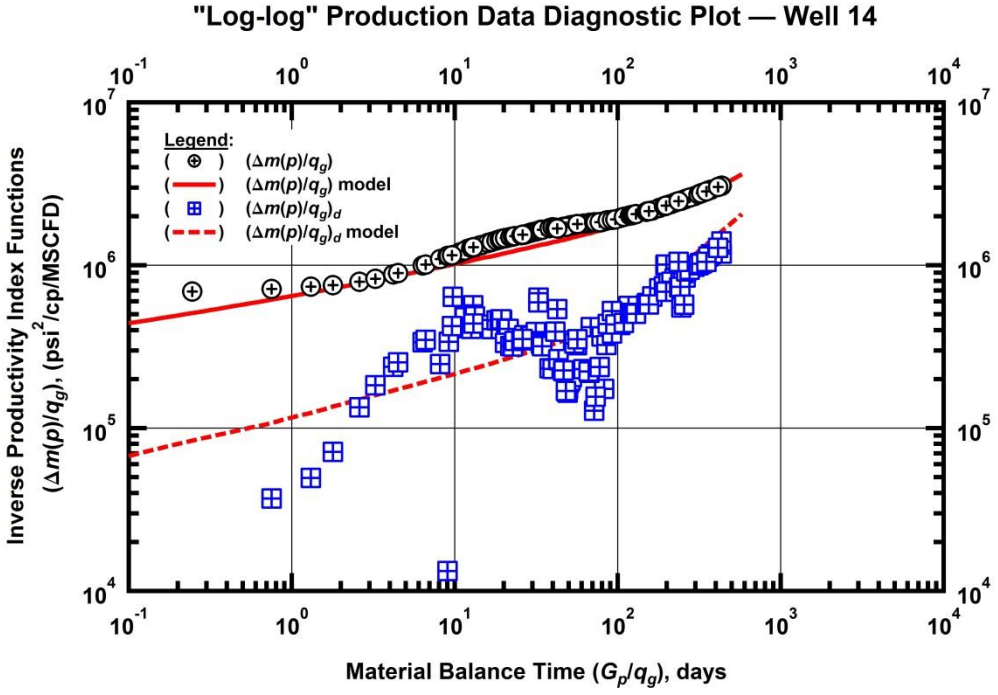

Figure C14 — (Log-log Plot): Production data diagnostic plot — inverse productivity index and its Bourdet derivative functions: data and model matches for Well 14.

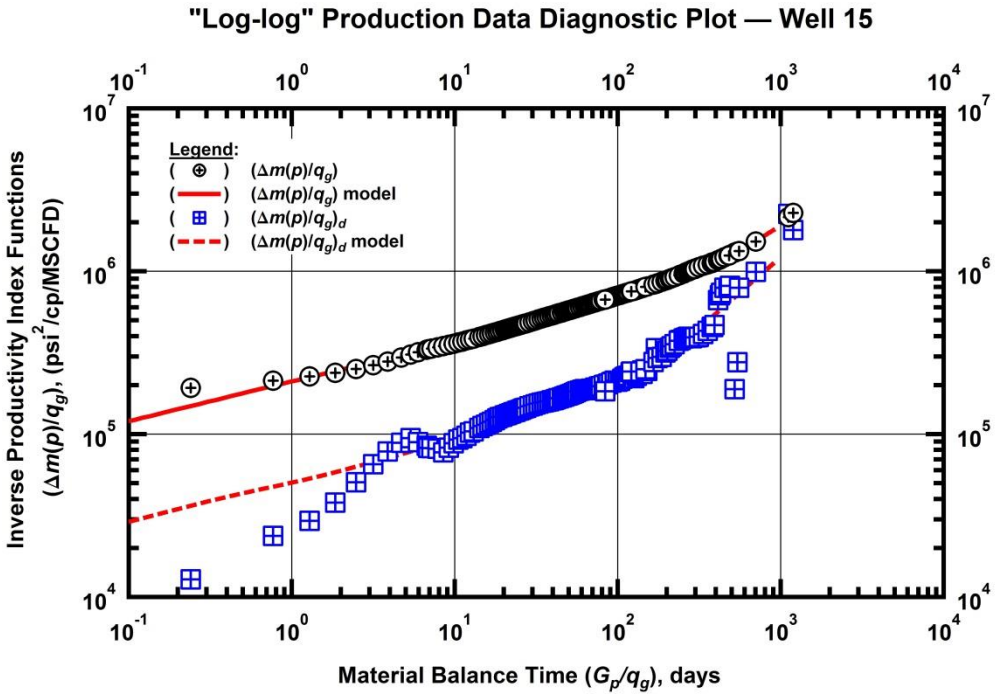

Figure C15 — (Log-log Plot): Production data diagnostic plot — inverse productivity index and its Bourdet derivative functions: data and model matches for Well 15.

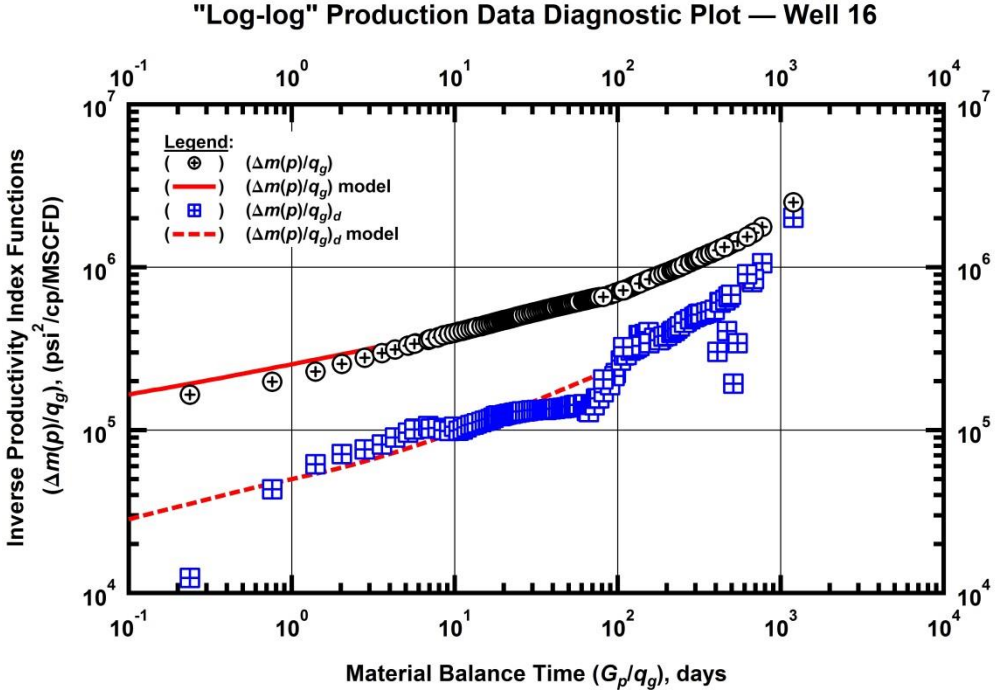

Figure C16 — (Log-log Plot): Production data diagnostic plot — inverse productivity index and its Bourdet derivative functions: data and model matches for Well 16.

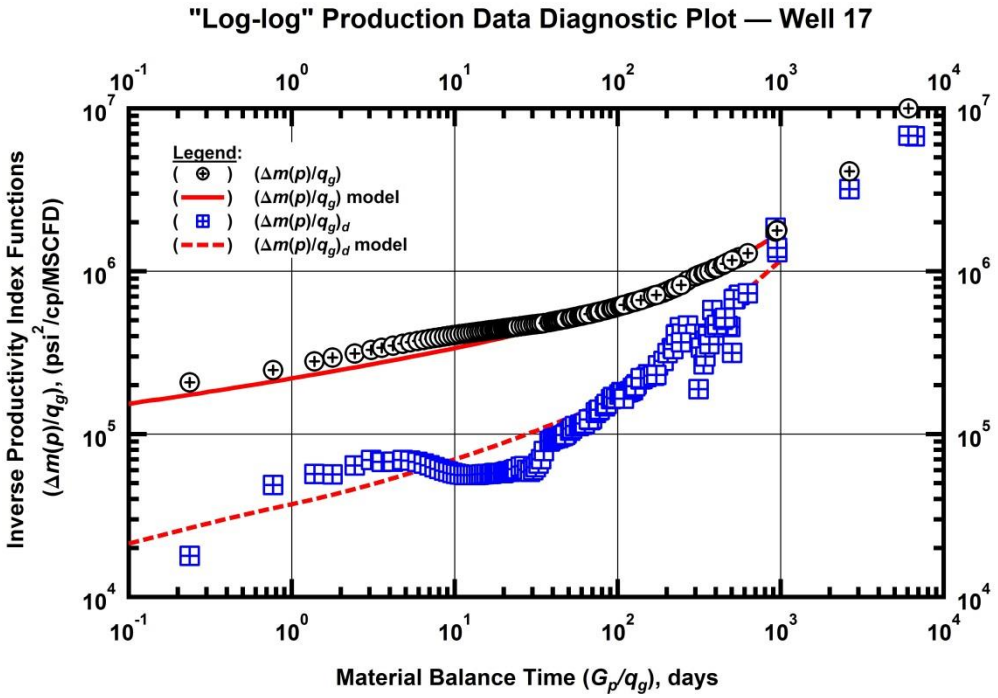

Figure C17 — (Log-log Plot): Production data diagnostic plot — inverse productivity index and its Bourdet derivative functions: data and model matches for Well 17.

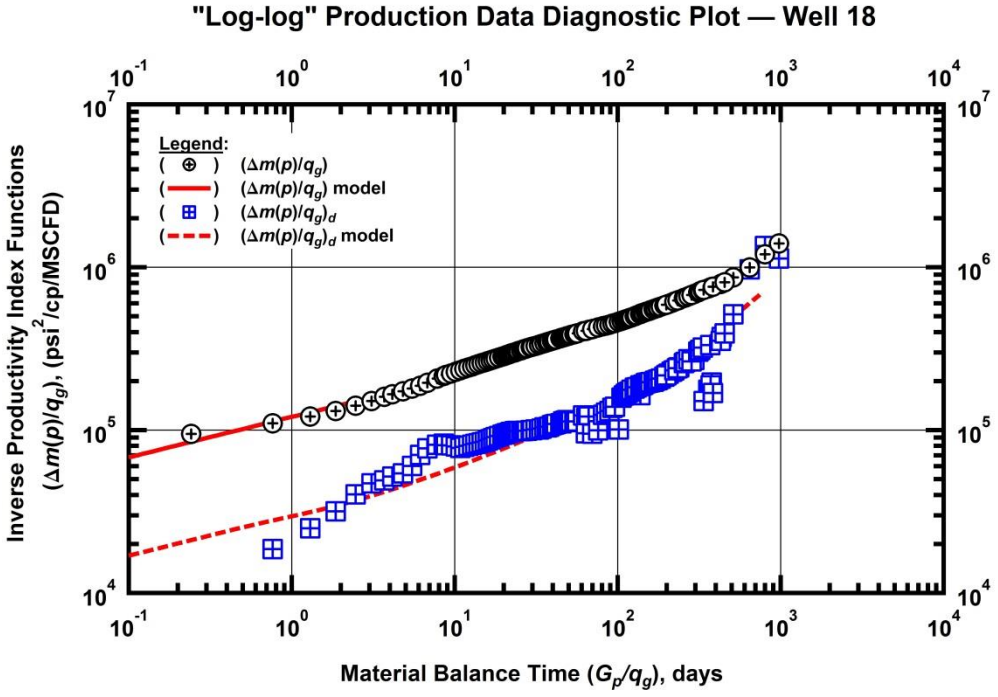

Figure C18 — (Log-log Plot): Production data diagnostic plot — inverse productivity index and its Bourdet derivative functions: data and model matches for Well 18.

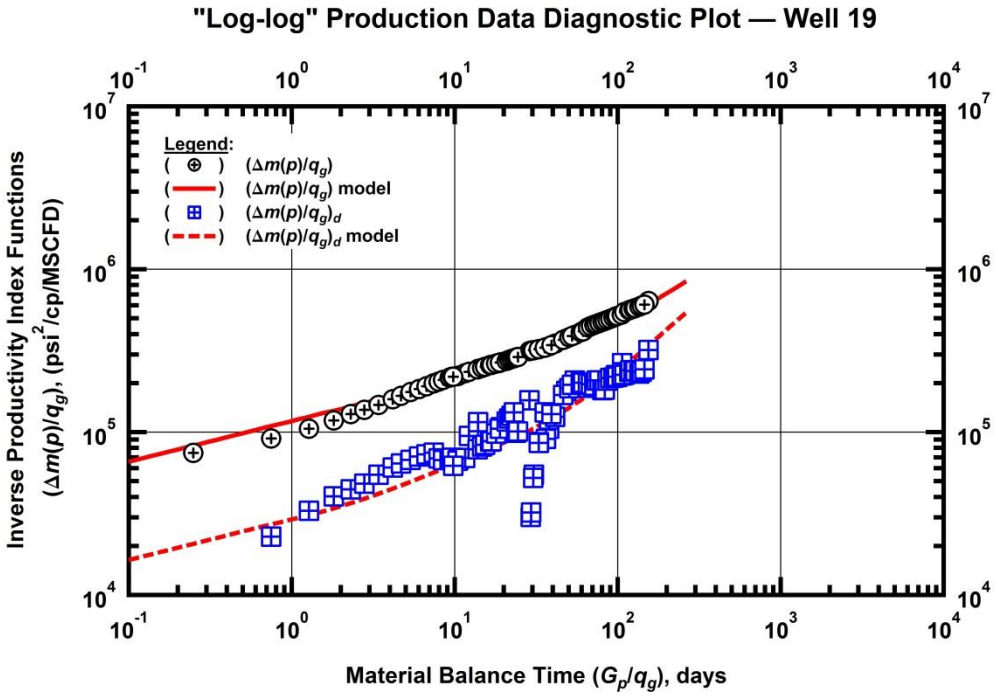

Figure C19 — (Log-log Plot): Production data diagnostic plot — inverse productivity index and its Bourdet derivative functions: data and model matches for Well 19.

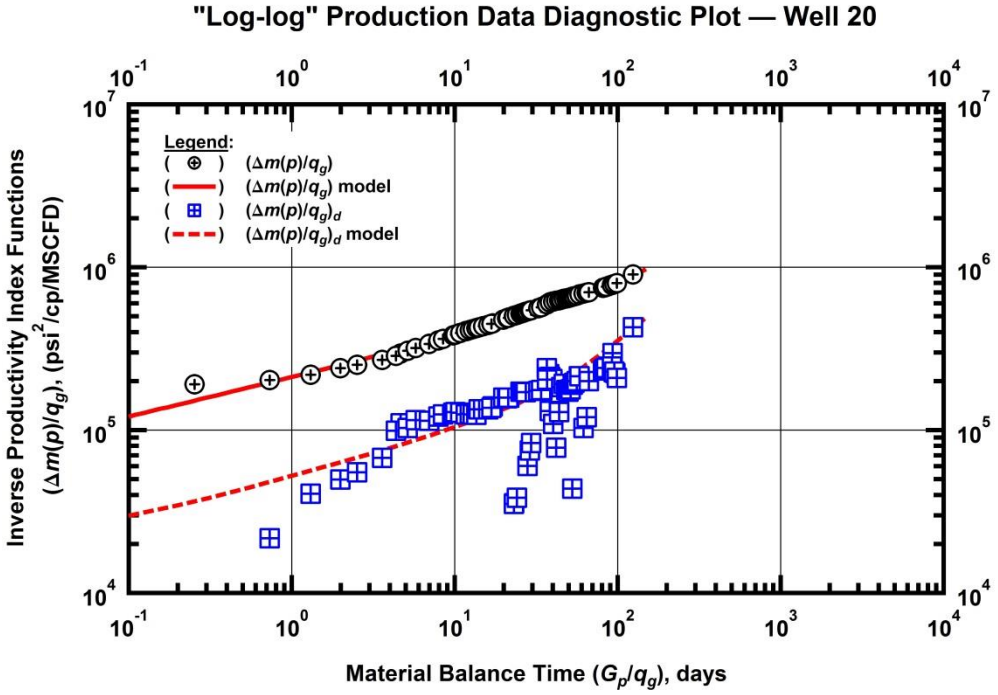

Figure C20 — (Log-log Plot): Production data diagnostic plot — inverse productivity index and its Bourdet derivative functions: data and model matches for Well 20.

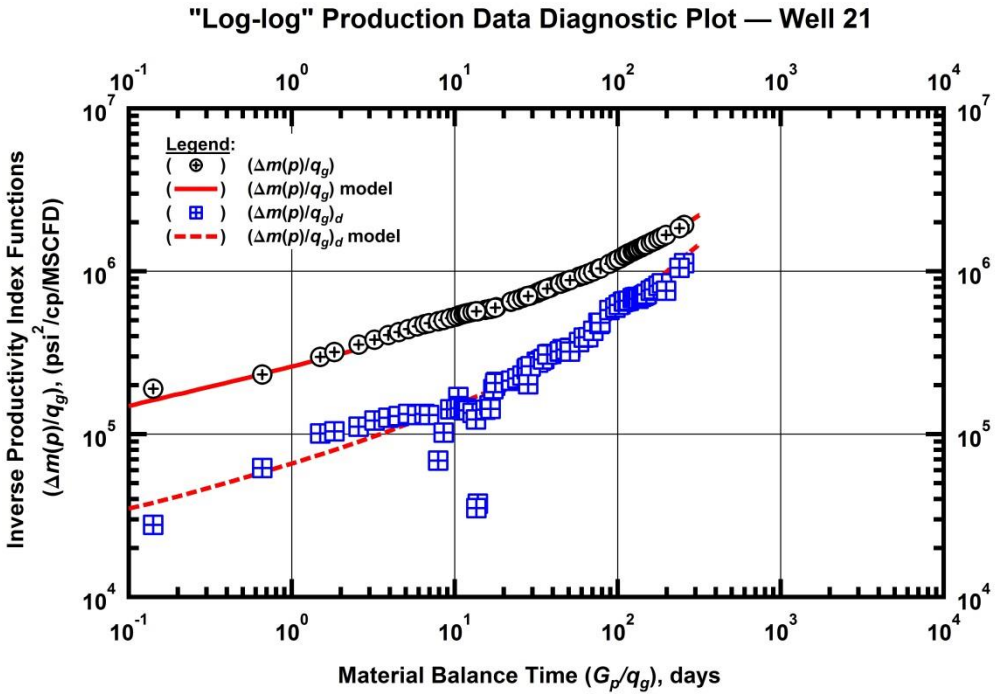

Figure C21 — (Log-log Plot): Production data diagnostic plot — inverse productivity index and its Bourdet derivative functions: data and model matches for Well 21.

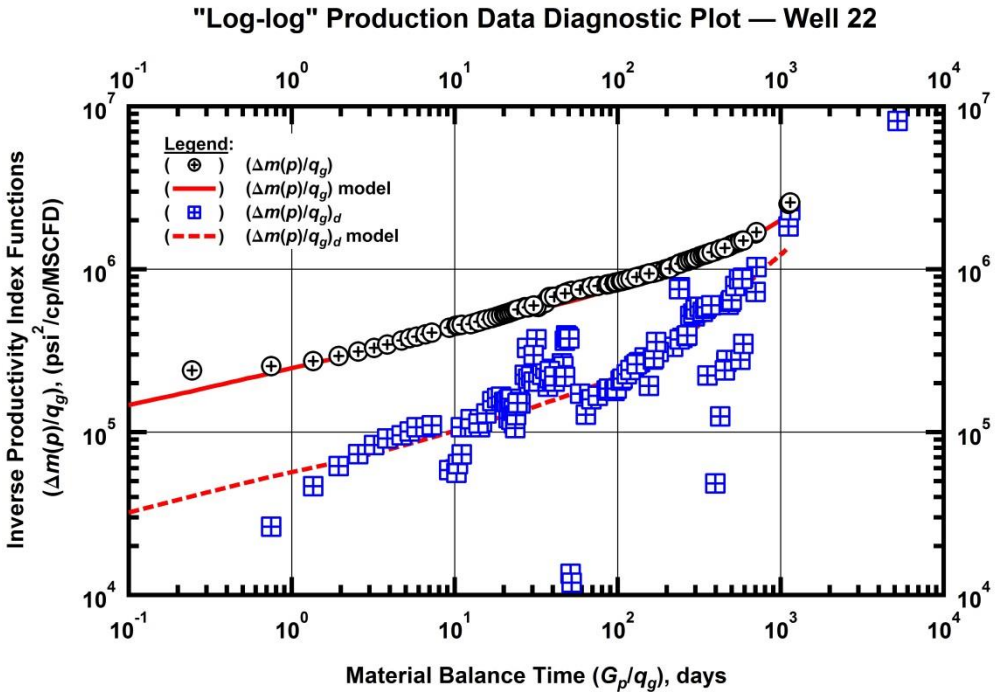

Figure C22 — (Log-log Plot): Production data diagnostic plot — inverse productivity index and its Bourdet derivative functions: data and model matches for Well 22.

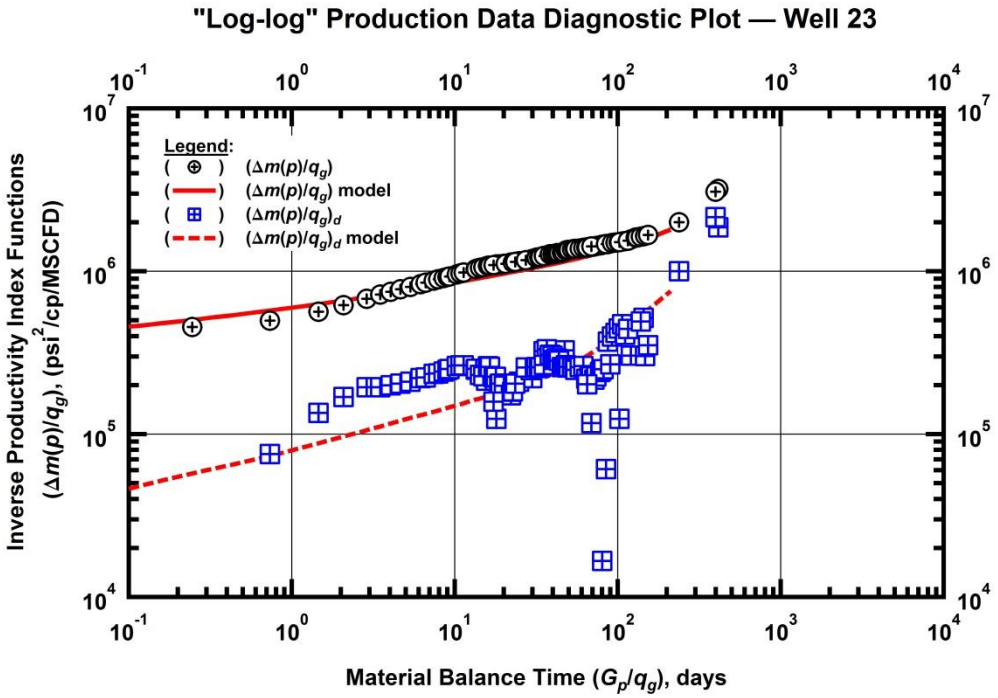

Figure C23 — (Log-log Plot): Production data diagnostic plot — inverse productivity index and its Bourdet derivative functions: data and model matches for Well 23.

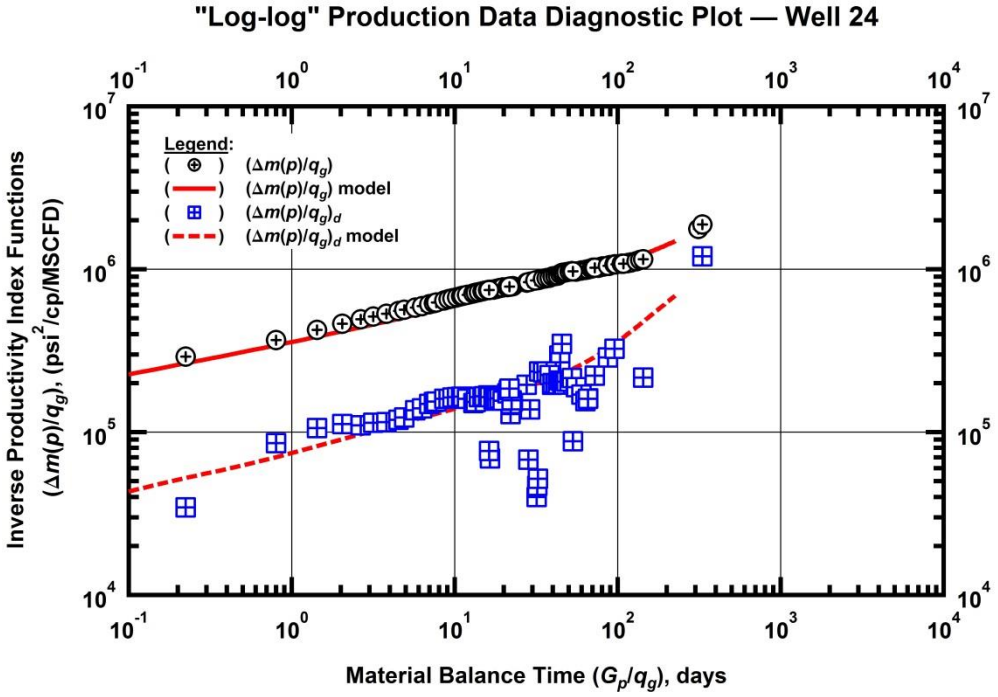

Figure C24 — (Log-log Plot): Production data diagnostic plot — inverse productivity index and its Bourdet derivative functions: data and model matches for Well 24.

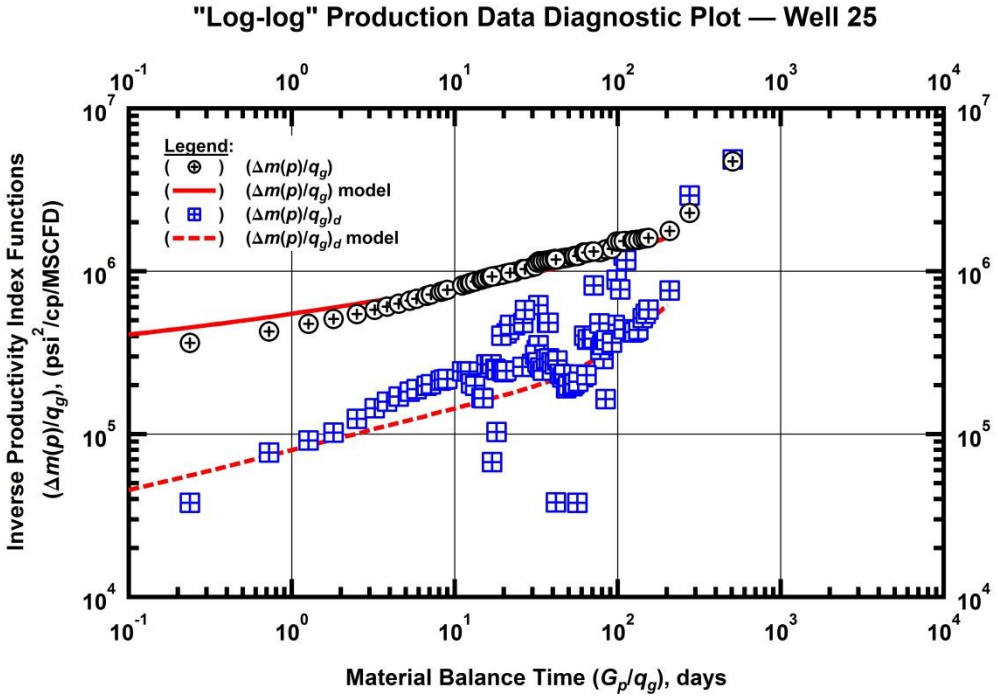

Figure C25 — (Log-log Plot): Production data diagnostic plot — inverse productivity index and its Bourdet derivative functions: data and model matches for Well 25.

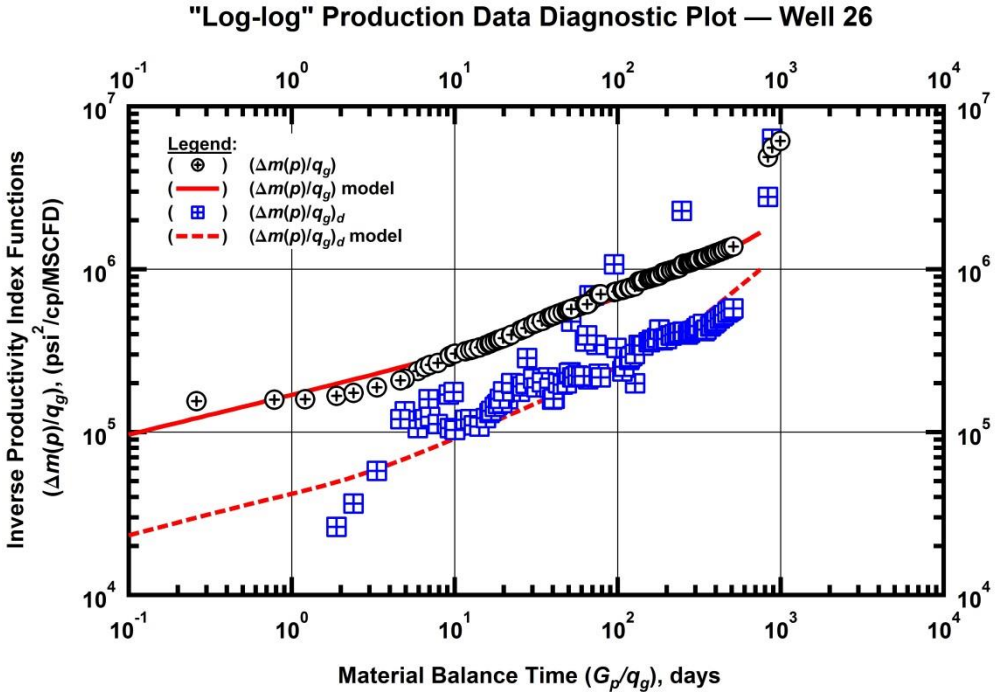

Figure C26 — (Log-log Plot): Production data diagnostic plot — inverse productivity index and its Bourdet derivative functions: data and model matches for Well 26.

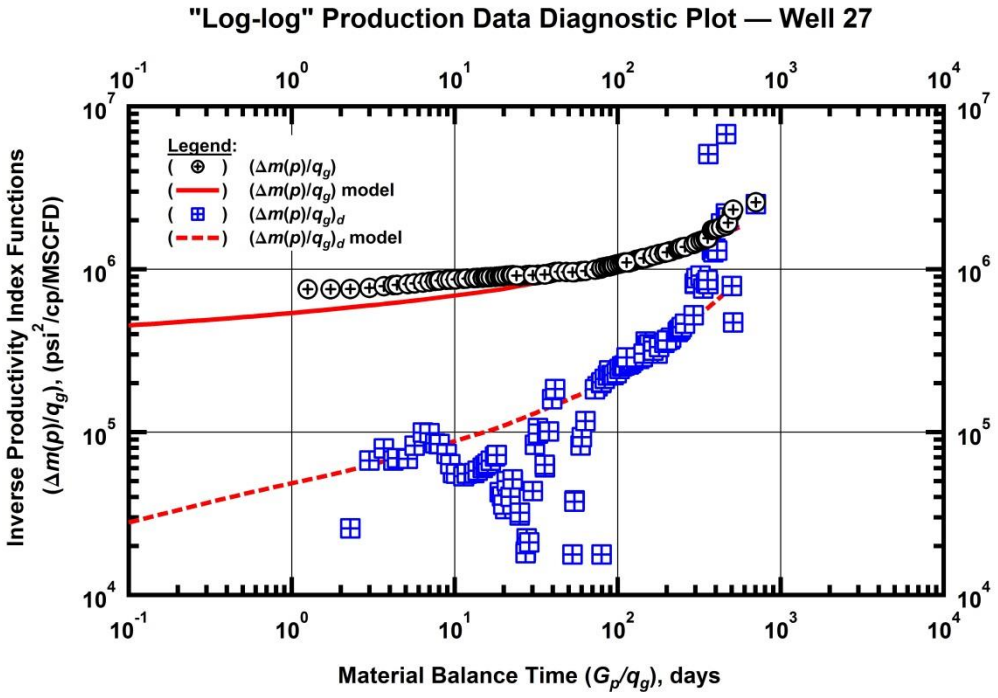

Figure C27 — (Log-log Plot): Production data diagnostic plot — inverse productivity index and its Bourdet derivative functions: data and model matches for Well 27.

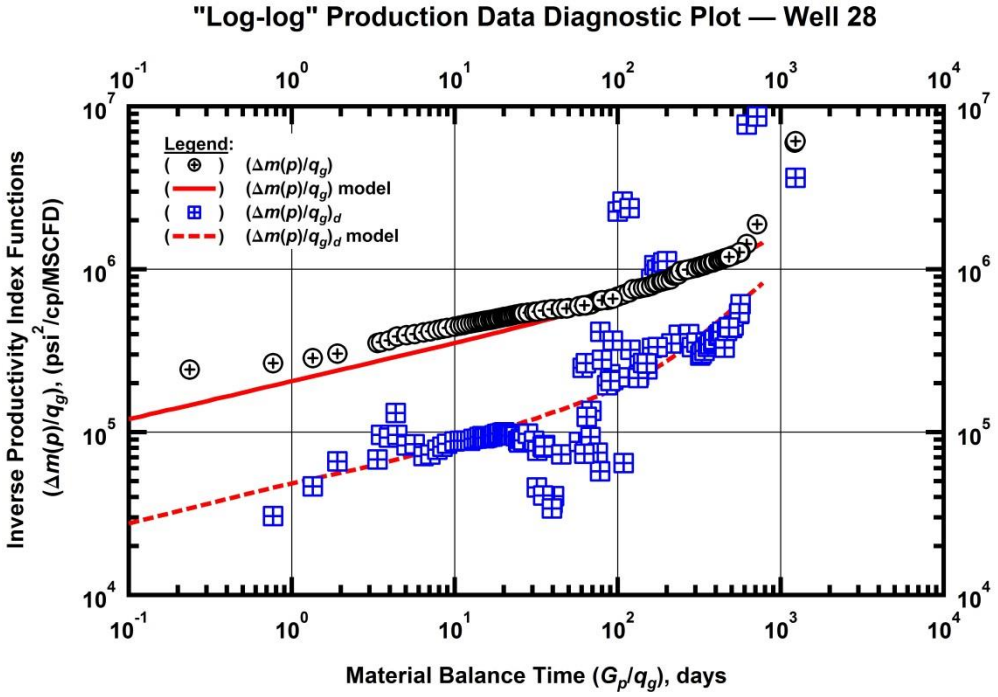

Figure C28 — (Log-log Plot): Production data diagnostic plot — inverse productivity index and its Bourdet derivative functions: data and model matches for Well 28.

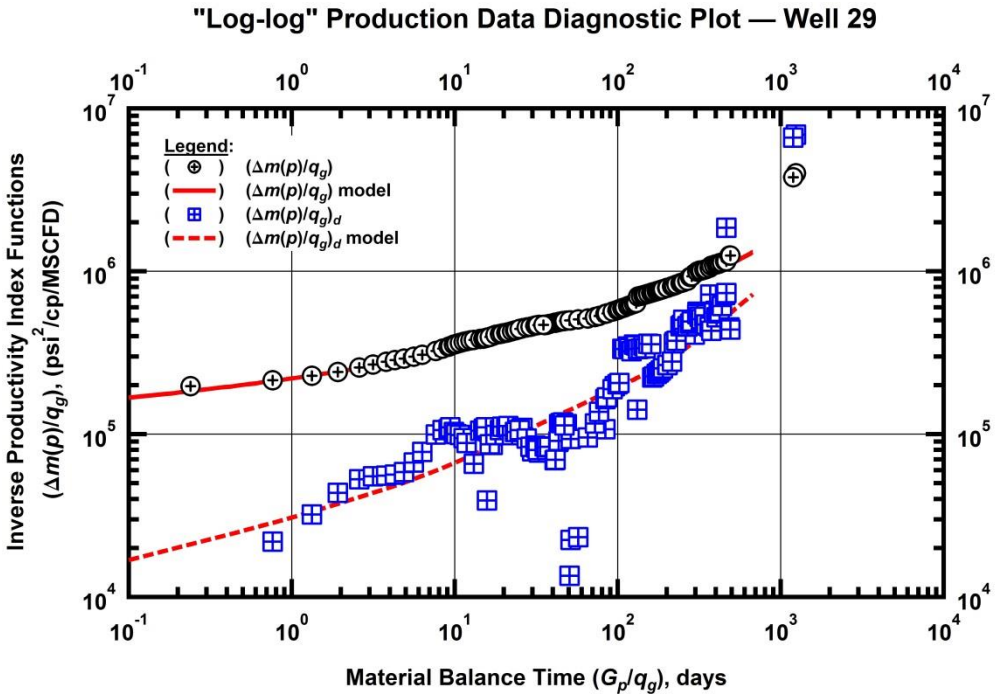

Figure C29 — (Log-log Plot): Production data diagnostic plot — inverse productivity index and its Bourdet derivative functions: data and model matches for Well 29.

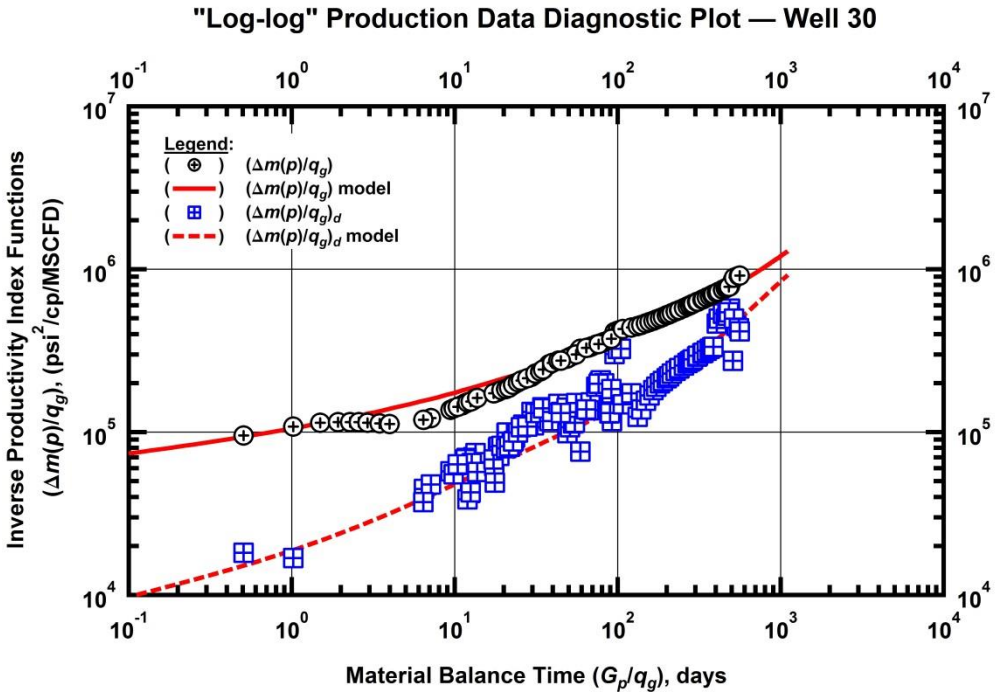

Figure C30 — (Log-log Plot): Production data diagnostic plot — inverse productivity index and its Bourdet derivative functions: data and model matches for Well 30.

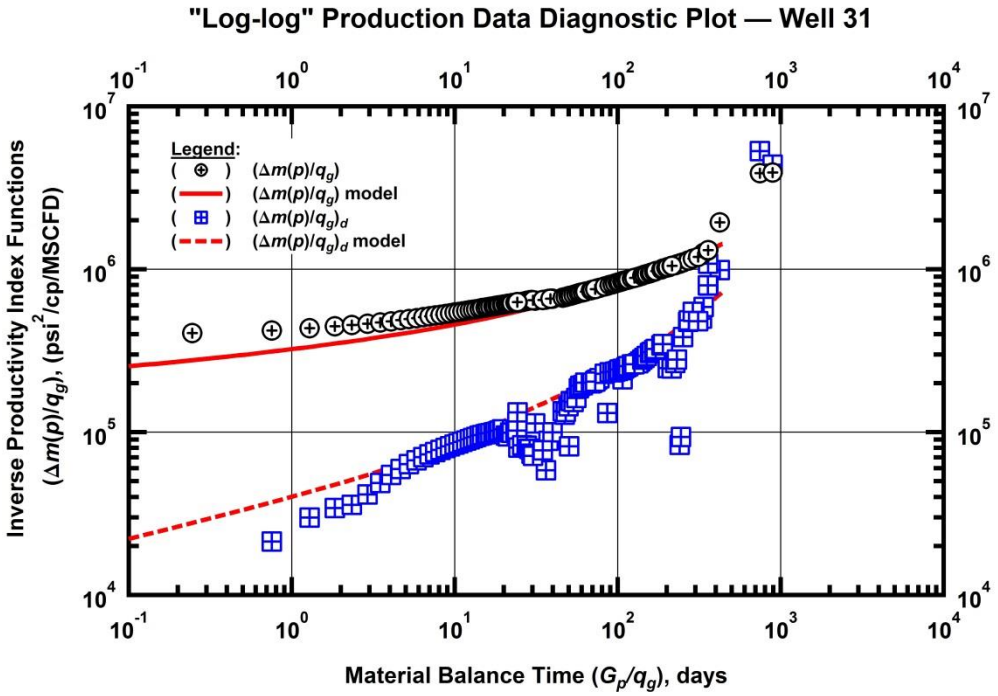

Figure C31 — (Log-log Plot): Production data diagnostic plot — inverse productivity index and its Bourdet derivative functions: data and model matches for Well 31.

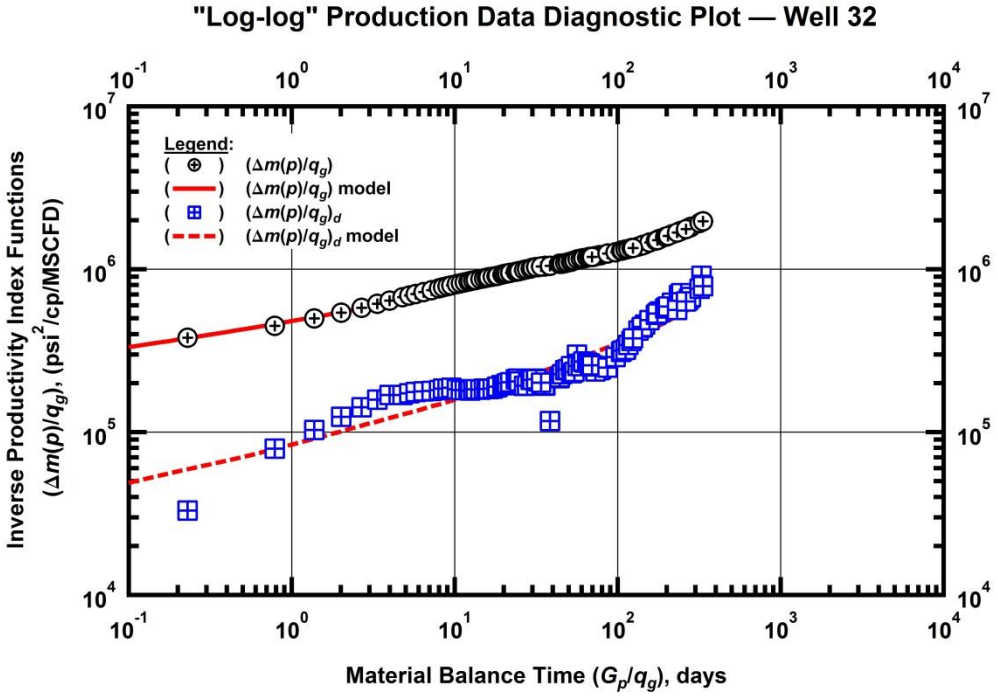

Figure C32 — (Log-log Plot): Production data diagnostic plot — inverse productivity index and its Bourdet derivative functions: data and model matches for Well 32.

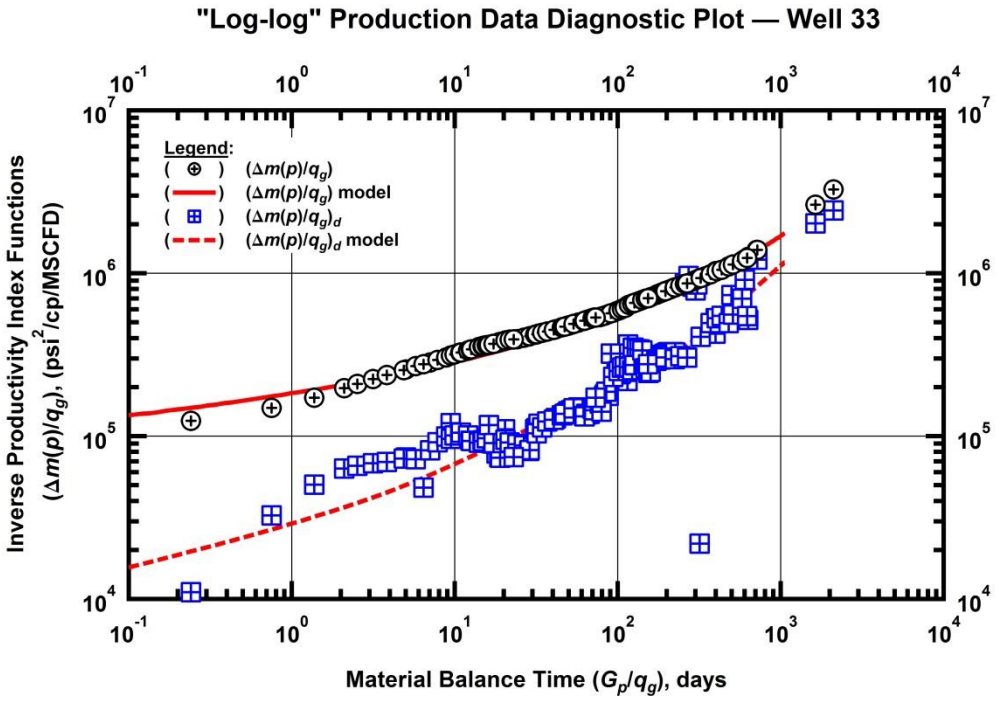

Figure C33 — (Log-log Plot): Production data diagnostic plot — inverse productivity index and its Bourdet derivative functions: data and model matches for Well 33.

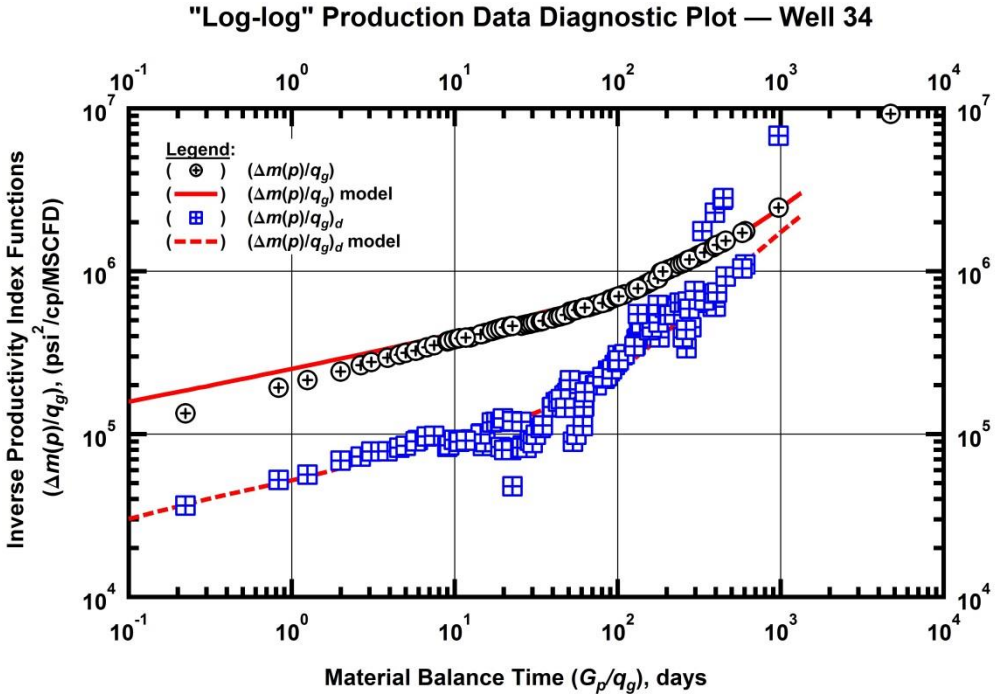

Figure C34 — (Log-log Plot): Production data diagnostic plot — inverse productivity index and its Bourdet derivative functions: data and model matches for Well 34.

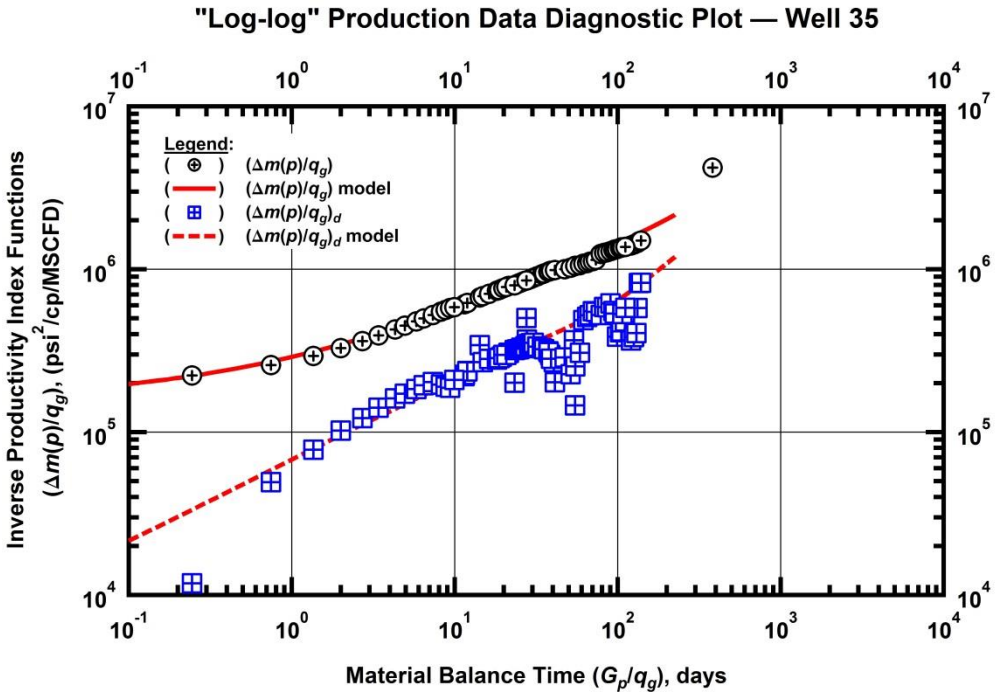

Figure C35 — (Log-log Plot): Production data diagnostic plot — inverse productivity index and its Bourdet derivative functions: data and model matches for Well 35.

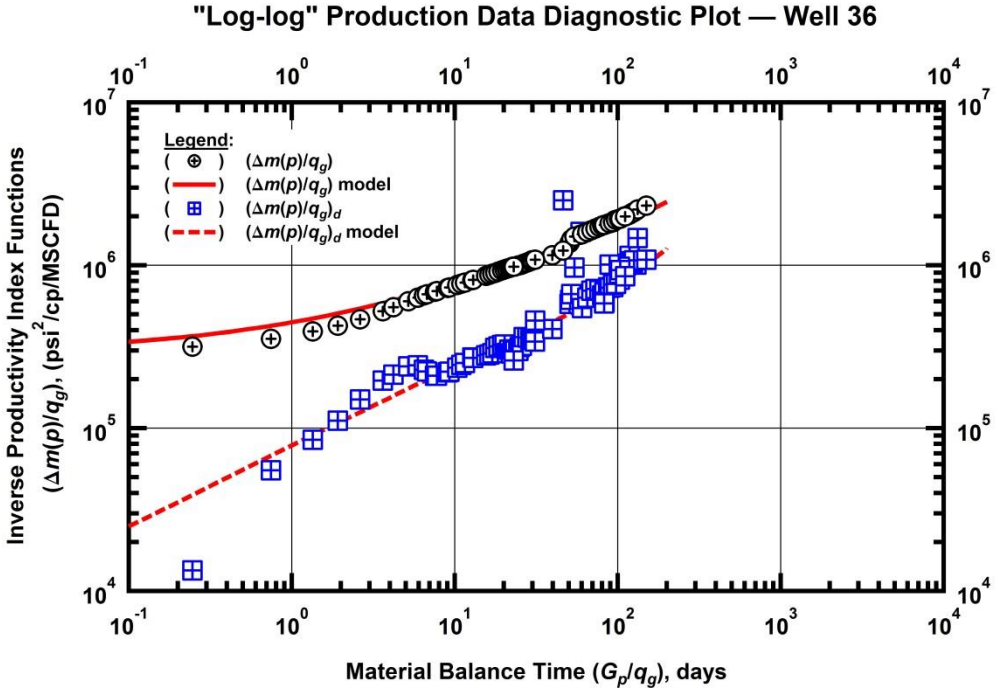

Figure C36 — (Log-log Plot): Production data diagnostic plot — inverse productivity index and its Bourdet derivative functions: data and model matches for Well 36.

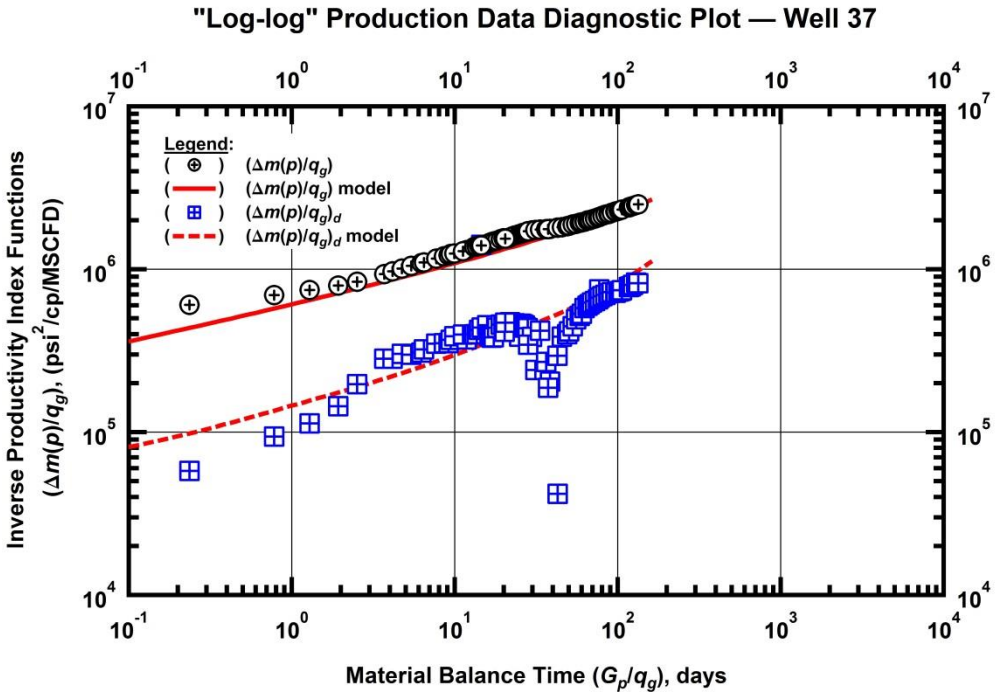

Figure C37 — (Log-log Plot): Production data diagnostic plot — inverse productivity index and its Bourdet derivative functions: data and model matches for Well 37.

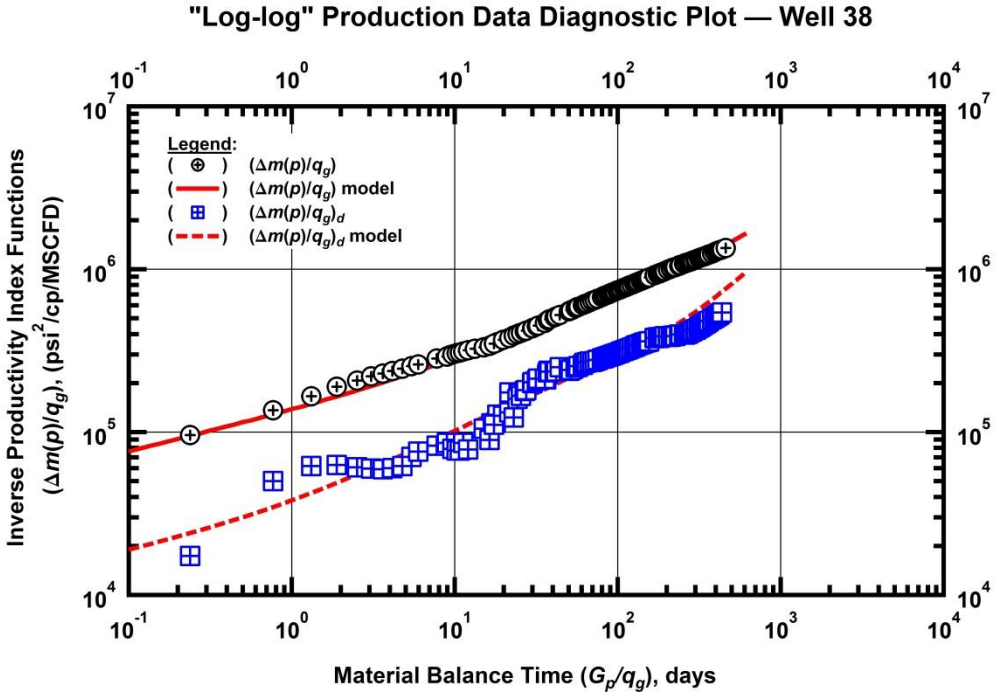

Figure C38 — (Log-log Plot): Production data diagnostic plot — inverse productivity index and its Bourdet derivative functions: data and model matches for Well 38.

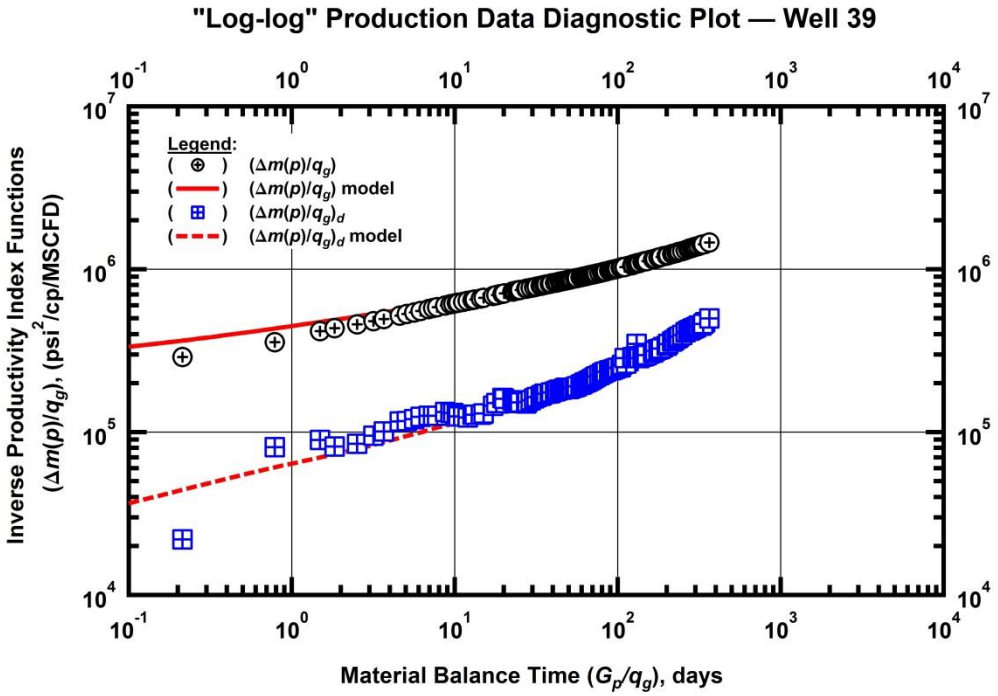

Figure C39 — (Log-log Plot): Production data diagnostic plot — inverse productivity index and its Bourdet derivative functions: data and model matches for Well 39.

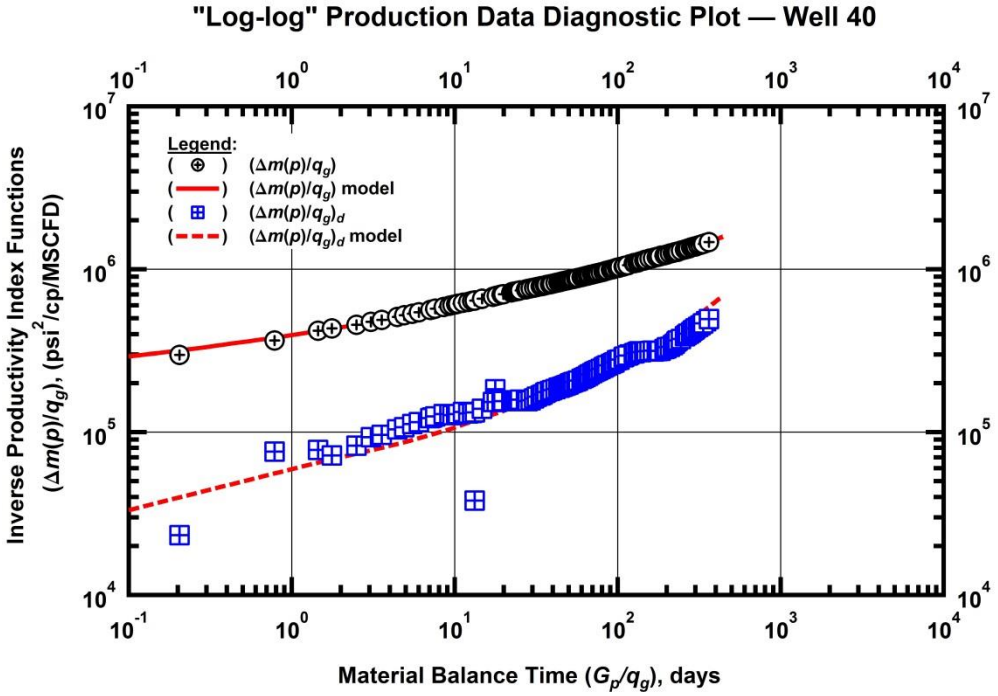

Figure C40 — (Log-log Plot): Production data diagnostic plot — inverse productivity index and its Bourdet derivative functions: data and model matches for Well 40.

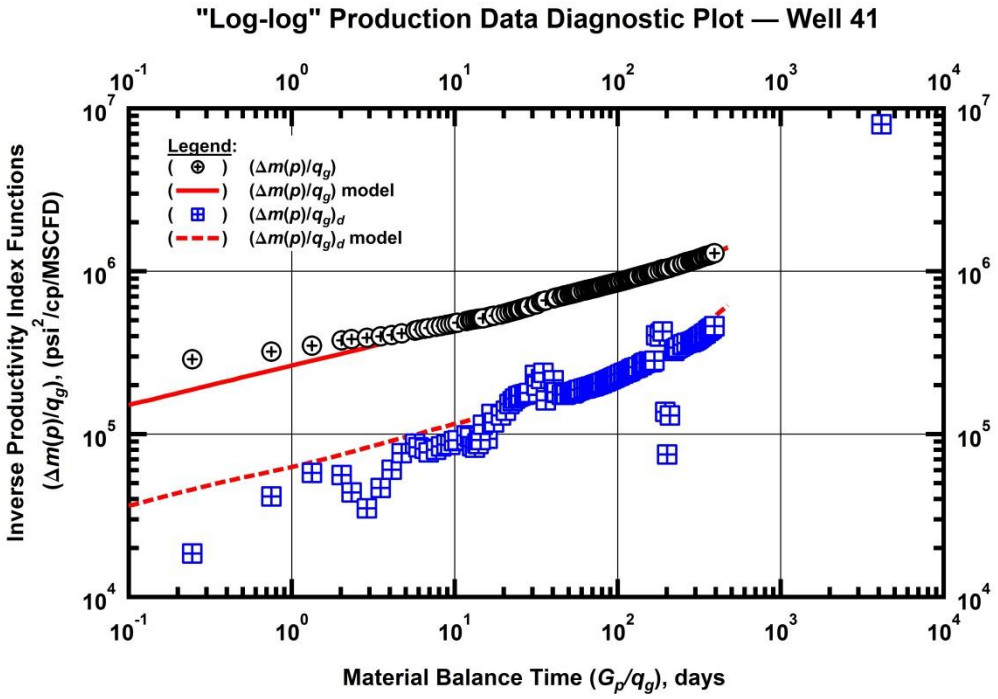

Figure C41 — (Log-log Plot): Production data diagnostic plot — inverse productivity index and its Bourdet derivative functions: data and model matches for Well 41.

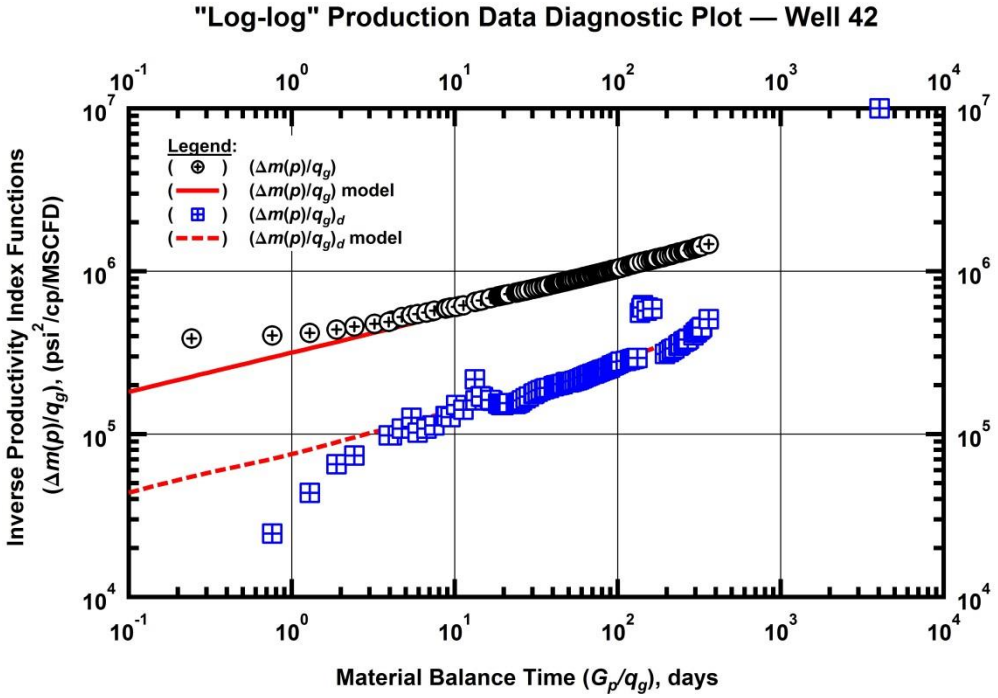

Figure C42 — (Log-log Plot): Production data diagnostic plot — inverse productivity index and its Bourdet derivative functions: data and model matches for Well 42

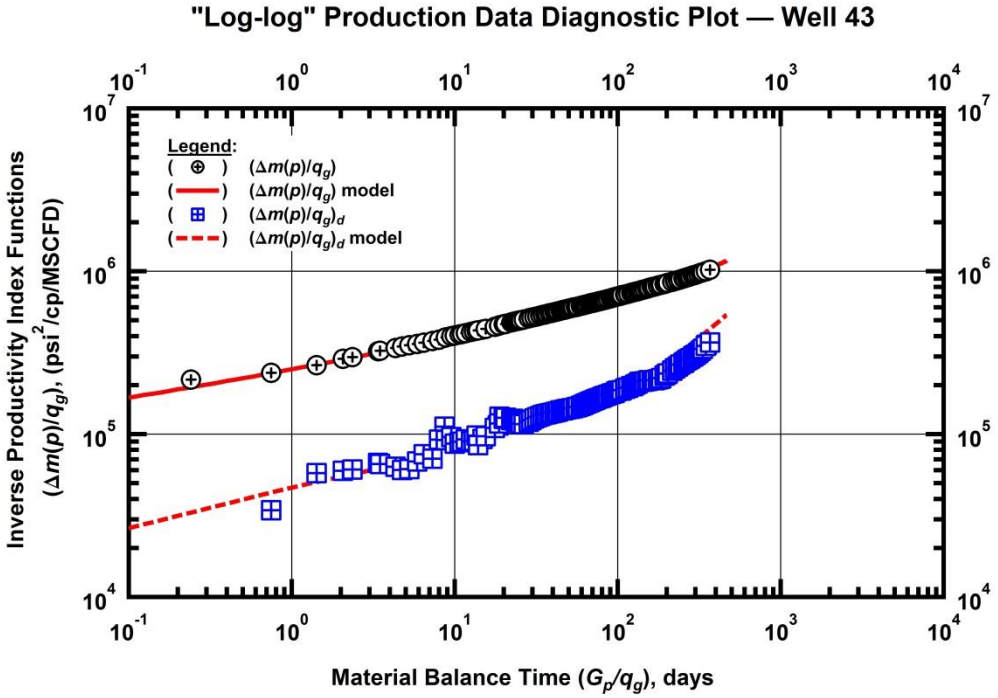

Figure C43 — (Log-log Plot): Production data diagnostic plot — inverse productivity index and its Bourdet derivative functions: data and model matches for Well 43.

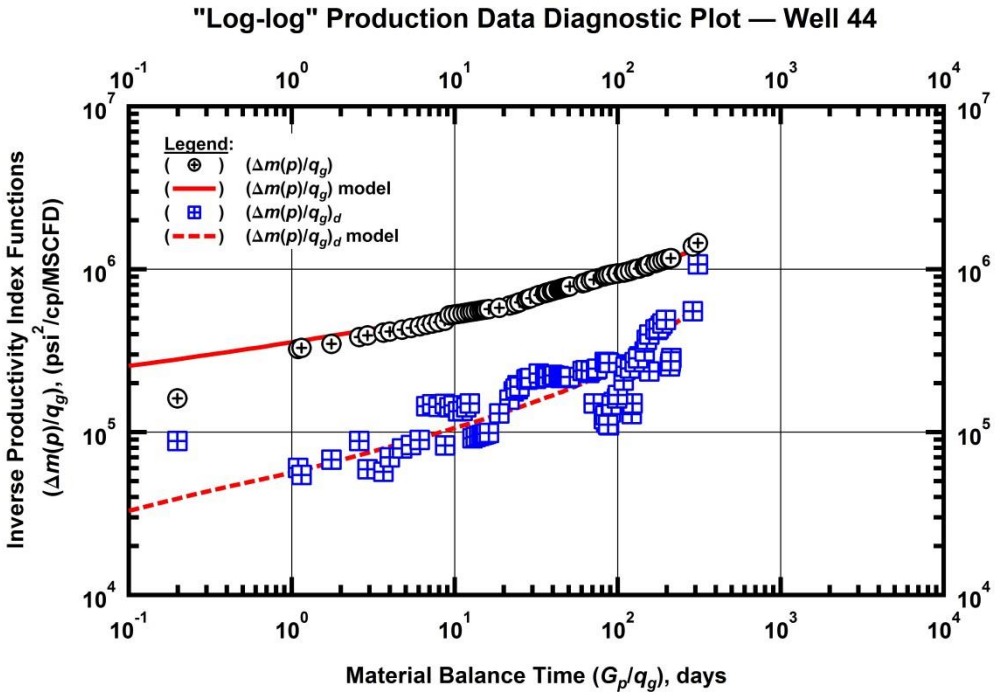

Figure C44 — (Log-log Plot): Production data diagnostic plot — inverse productivity index and its Bourdet derivative functions: data and model matches for Well 44.

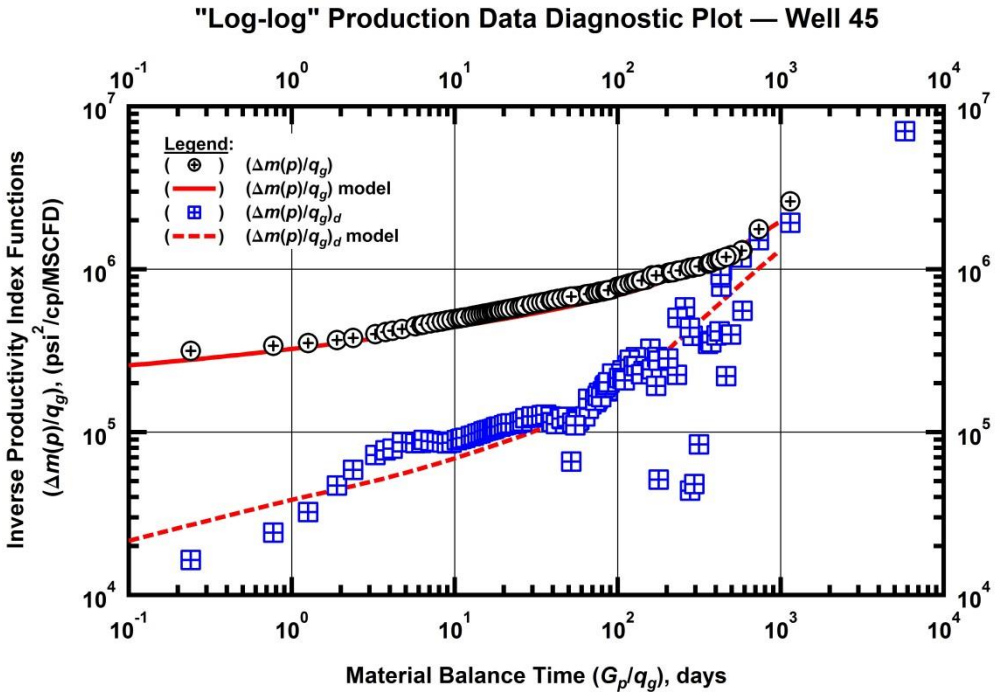

Figure C45 — (Log-log Plot): Production data diagnostic plot — inverse productivity index and its Bourdet derivative functions: data and model matches for Well 45.

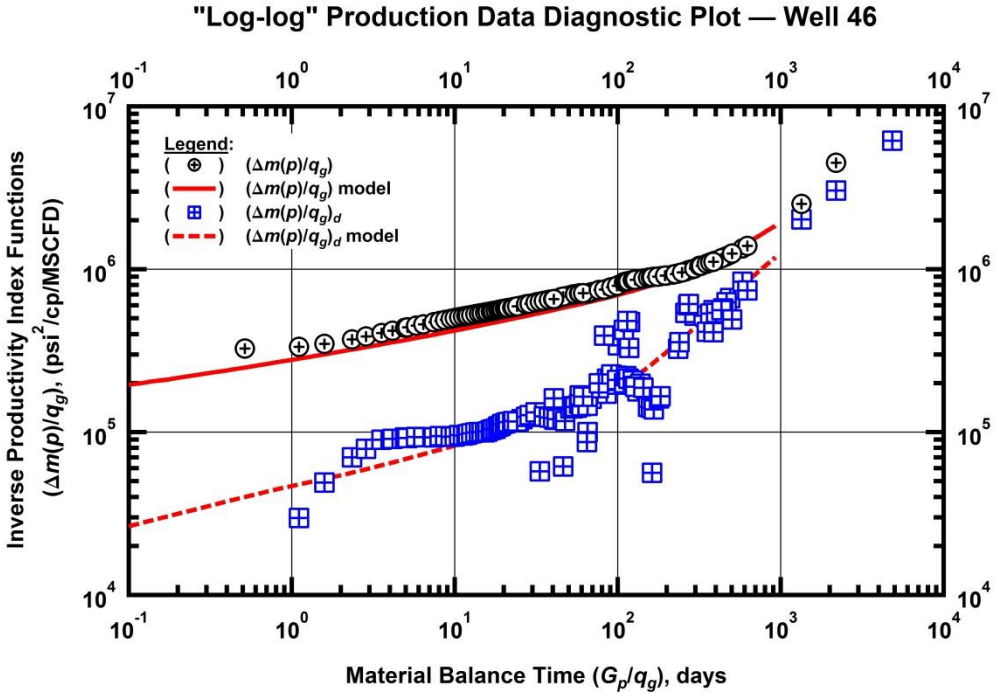

Figure C46 — (Log-log Plot): Production data diagnostic plot — inverse productivity index and its Bourdet derivative functions: data and model matches for Well 46.

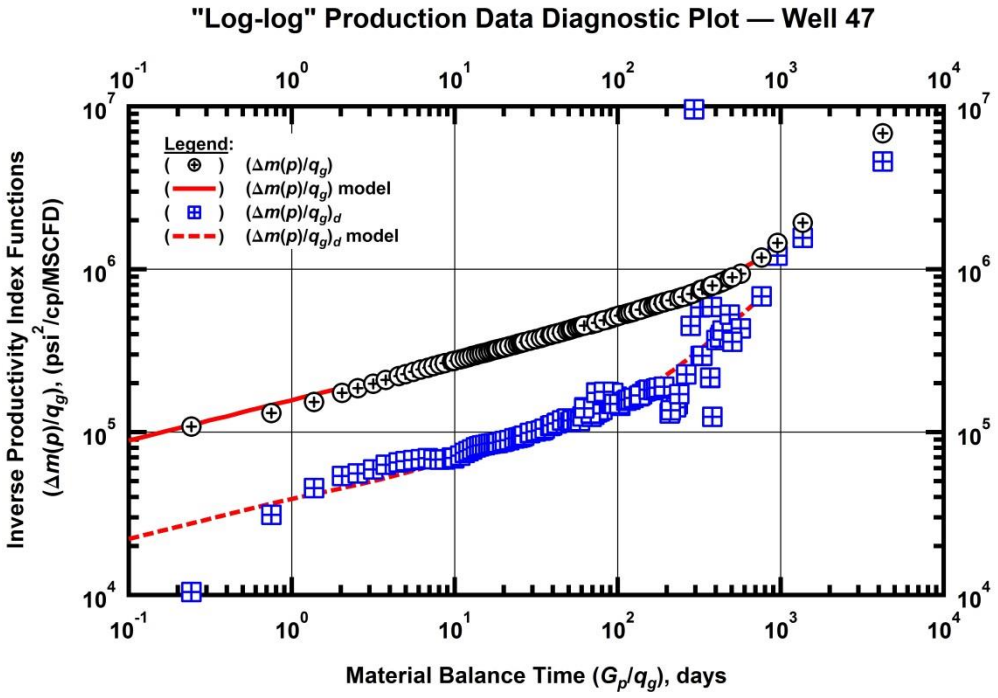

Figure C47 — (Log-log Plot): Production data diagnostic plot — inverse productivity index and its Bourdet derivative functions: data and model matches for Well 47.

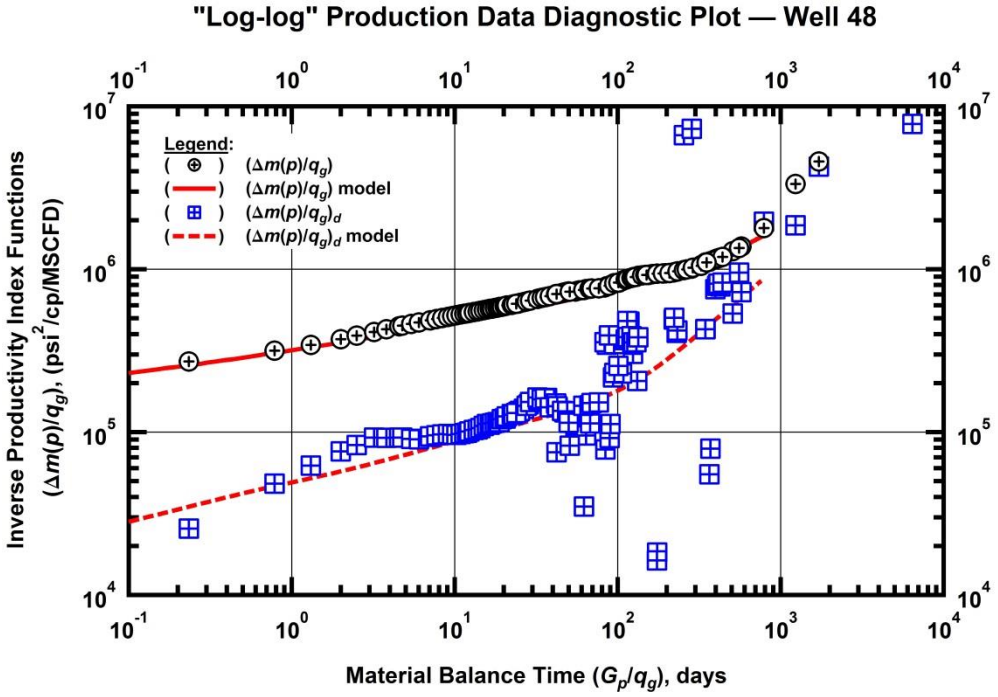

Figure C48 — (Log-log Plot): Production data diagnostic plot — inverse productivity index and its Bourdet derivative functions: data and model matches for Well 48.

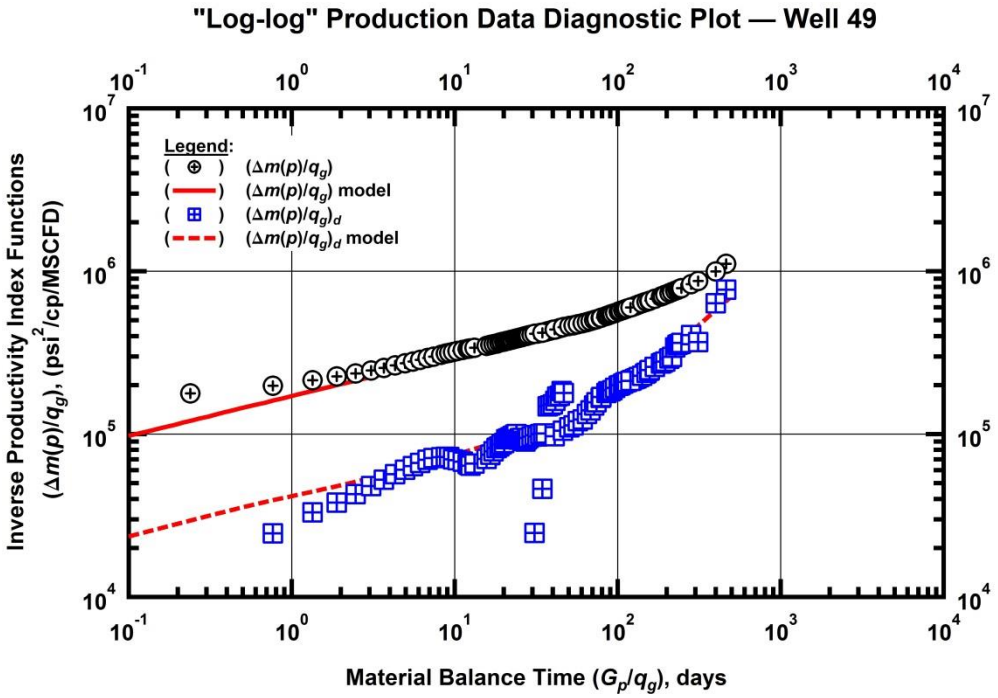

Figure C49 — (Log-log Plot): Production data diagnostic plot — inverse productivity index and its Bourdet derivative functions: data and model matches for Well 49.

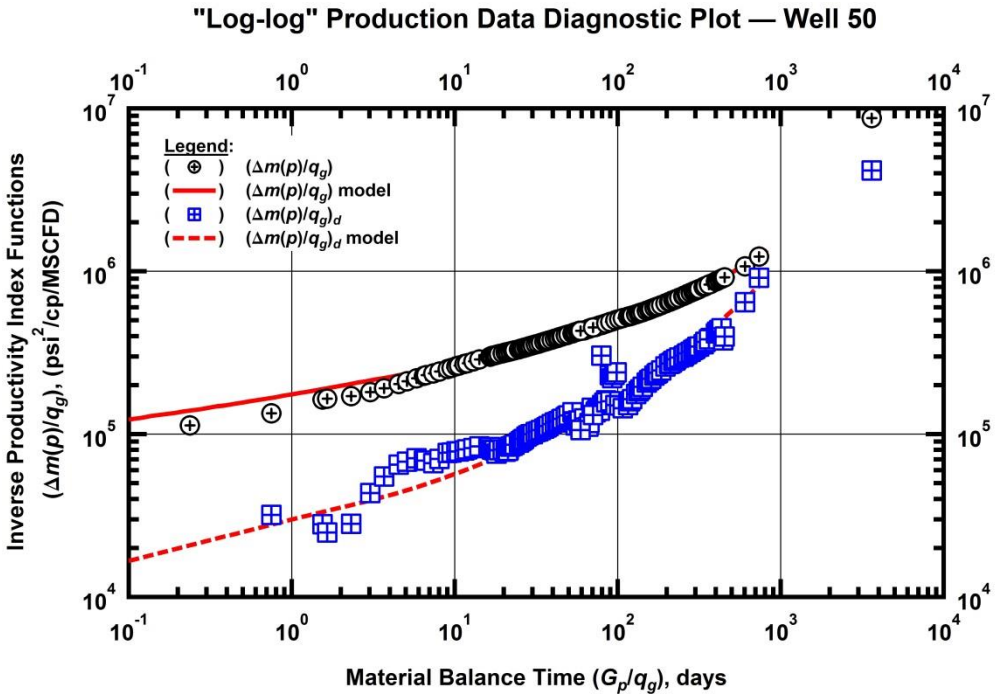

Figure C50 — (Log-log Plot): Production data diagnostic plot — inverse productivity index and its Bourdet derivative functions: data and model matches for Well 50.

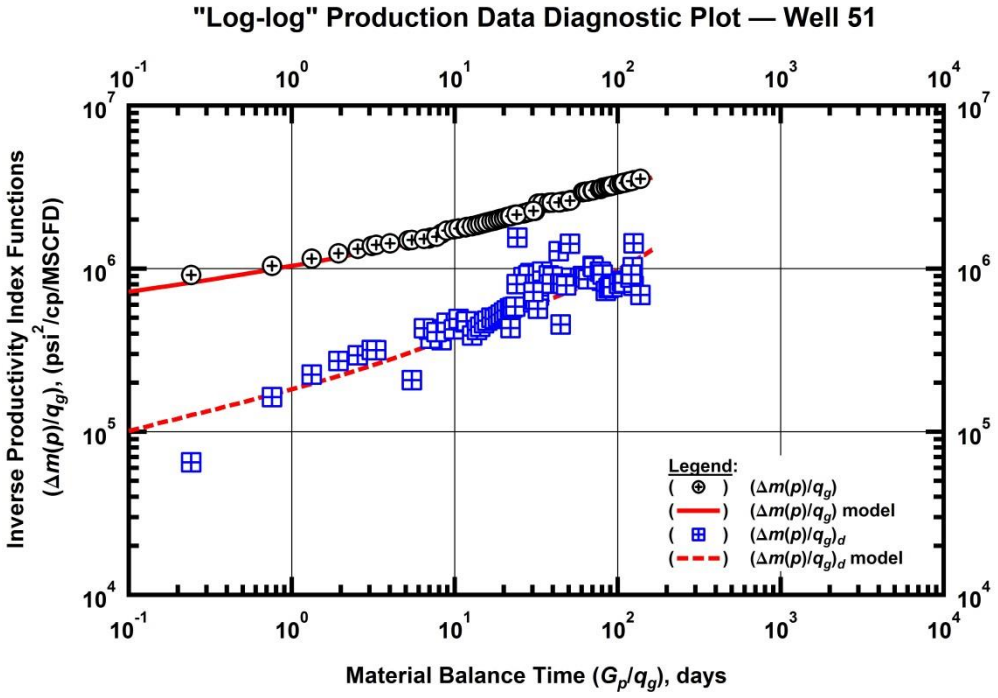

Figure C51 — (Log-log Plot): Production data diagnostic plot — inverse productivity index and its Bourdet derivative functions: data and model matches for Well 51.

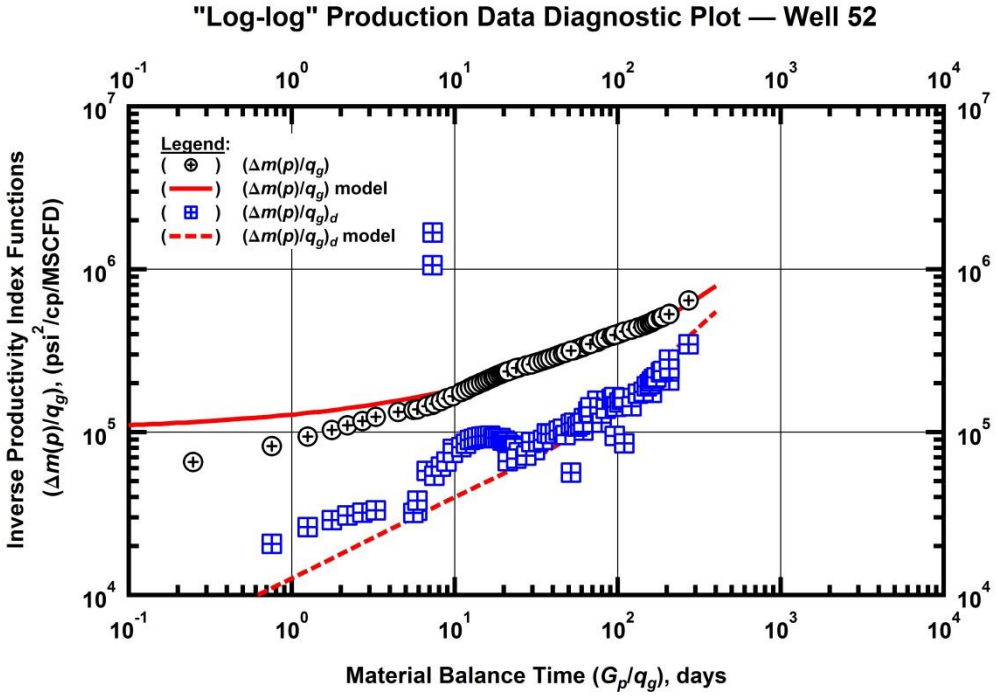

Figure C52 — (Log-log Plot): Production data diagnostic plot — inverse productivity index and its Bourdet derivative functions: data and model matches for Well 52.

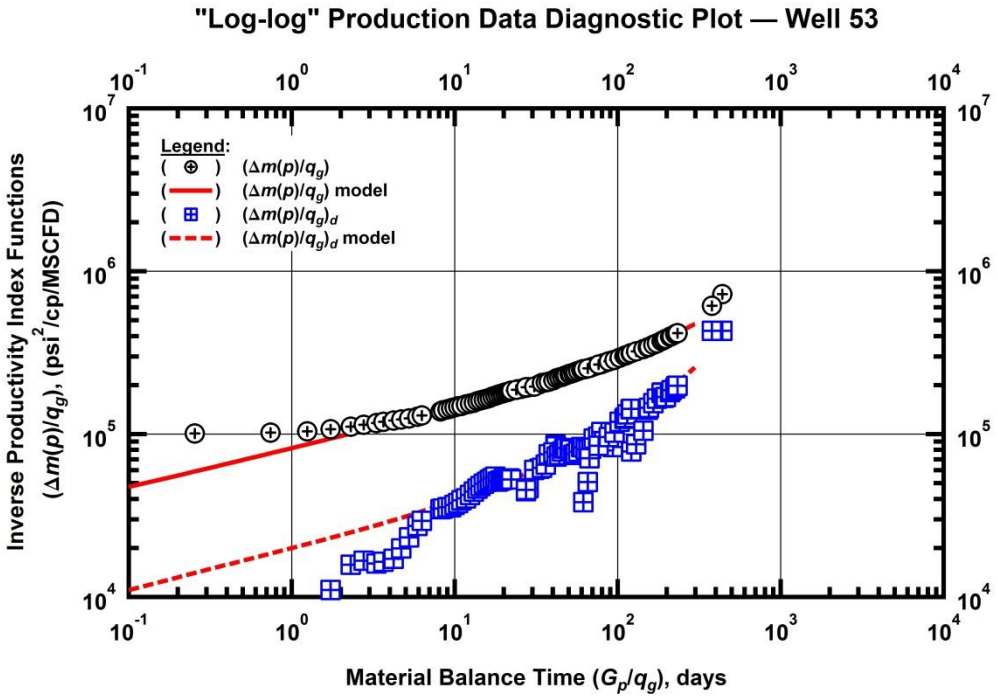

Figure C53 — (Log-log Plot): Production data diagnostic plot — inverse productivity index and its Bourdet derivative functions: data and model matches for Well 53.

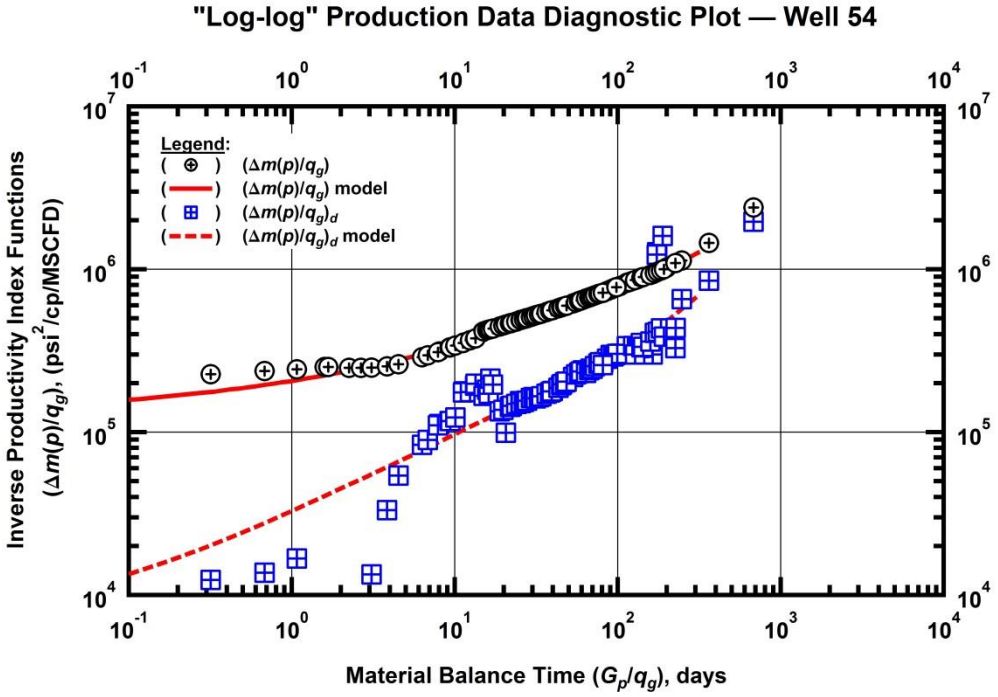

Figure C54 — (Log-log Plot): Production data diagnostic plot — inverse productivity index and its Bourdet derivative functions: data and model matches for Well 54.

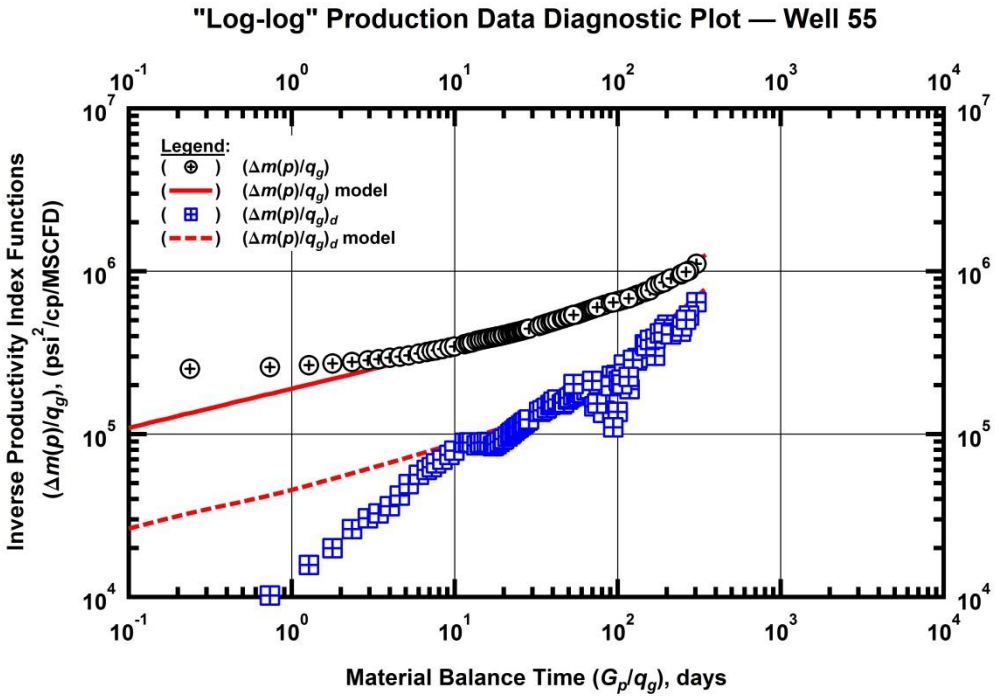

Figure C55 — (Log-log Plot): Production data diagnostic plot — inverse productivity index and its Bourdet derivative functions: data and model matches for Well 55.

APPENDIX D

PRESSURE TRANSIENT ANALYSIS

Included in this appendix is the complete set of pressure buildup diagnostic plots. There are nine cases (**Figs. D1-D9**) in total — three of which are high-frequency bottomhole gauge tests. The remaining six cases are from the surface pressure gauge and they are in daily increments. We presented our rationale for inclusion of these daily surface pressure buildup tests in Chapter VI.

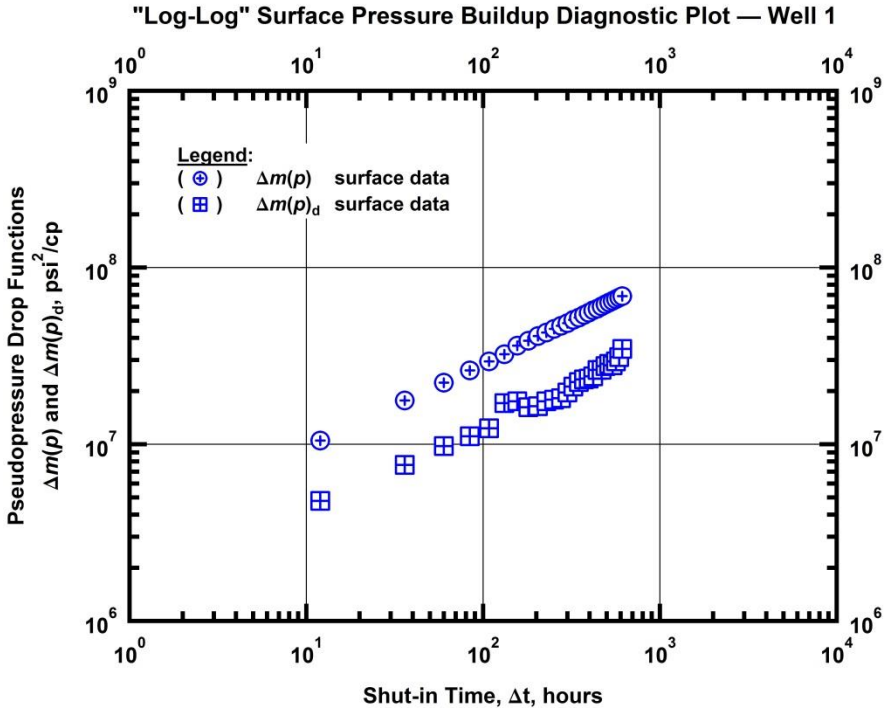

Fig. D1 — (Log-log Plot): Pressure buildup diagnostic plot — daily surface pressure measurement for Well 1.

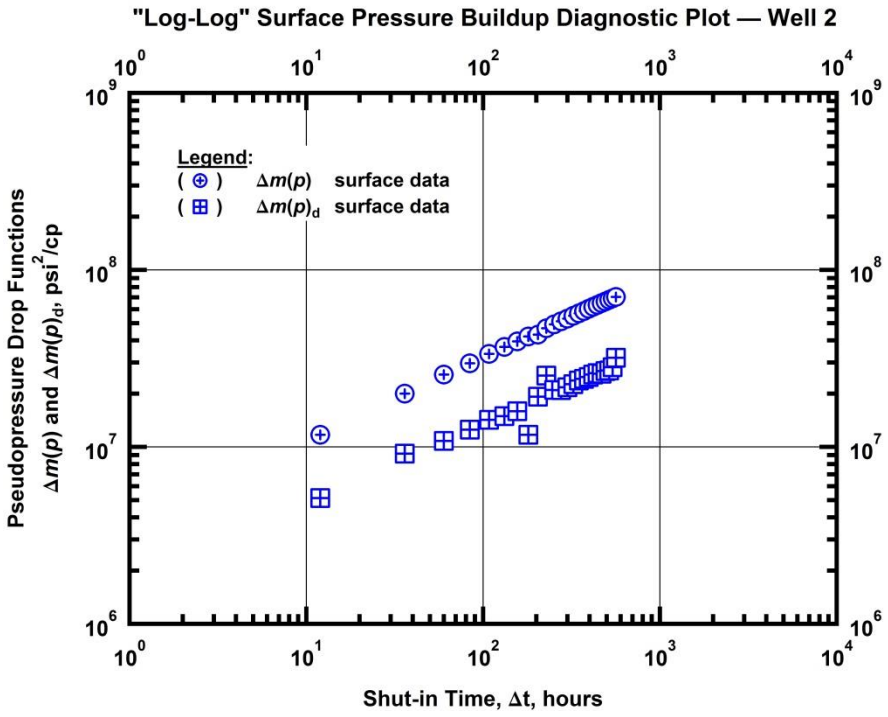

Fig. D2 — (Log-log Plot): Pressure buildup diagnostic plot — daily surface pressure measurement for Well 2.

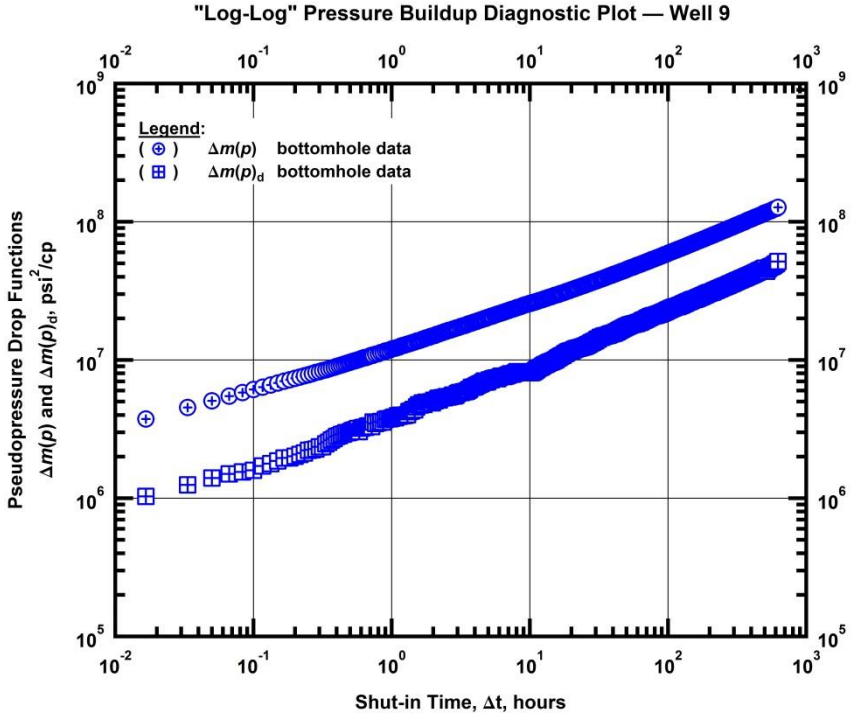

Fig. D3 — (Log-log Plot): Pressure buildup diagnostic plot — high-frequency bottomhole pressure measurement for Well 9.

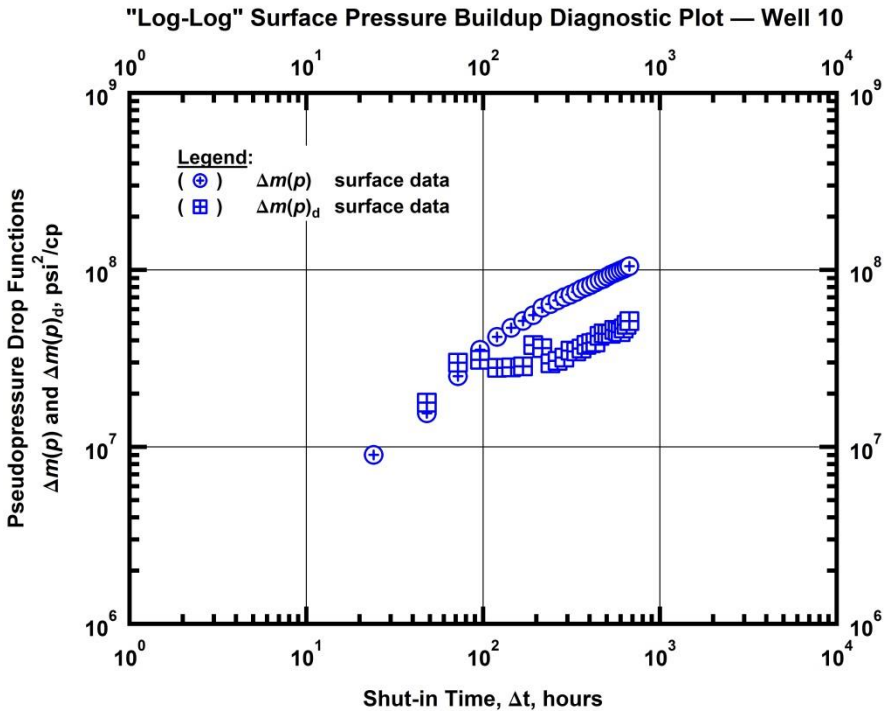

Fig. D4 — (Log-log Plot): Pressure buildup diagnostic plot — daily surface pressure measurement for Well 10.

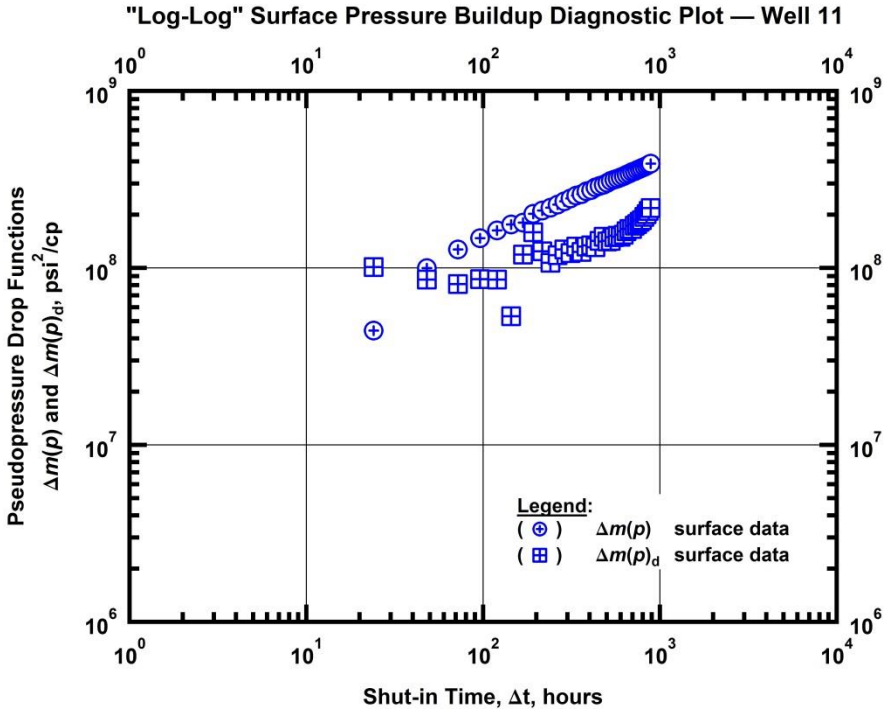

Fig. D5 — (Log-log Plot): Pressure buildup diagnostic plot — daily surface pressure measurement for Well 11.

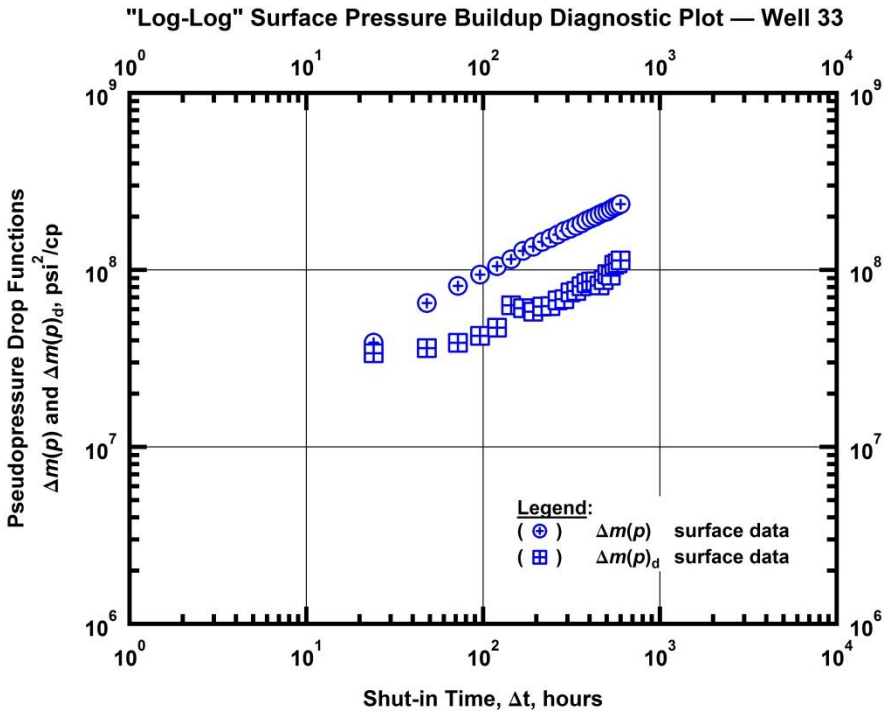

Fig. D6 — (Log-log Plot): Pressure buildup diagnostic plot — daily surface pressure measurement for Well 3.

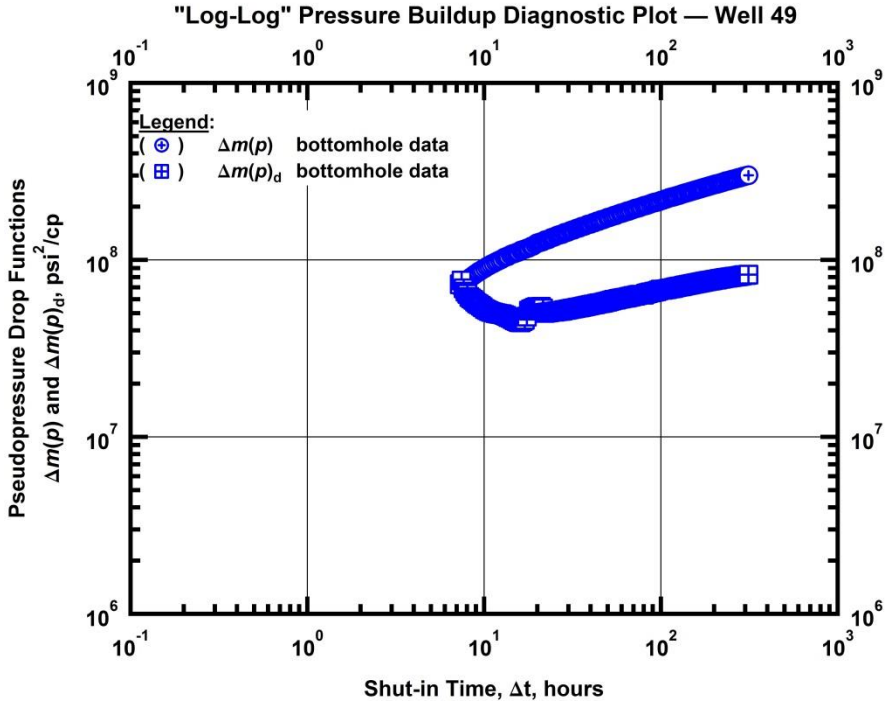

Fig. D7 — (Log-log Plot): Pressure buildup diagnostic plot — high-frequency bottomhole pressure measurement for Well 49.

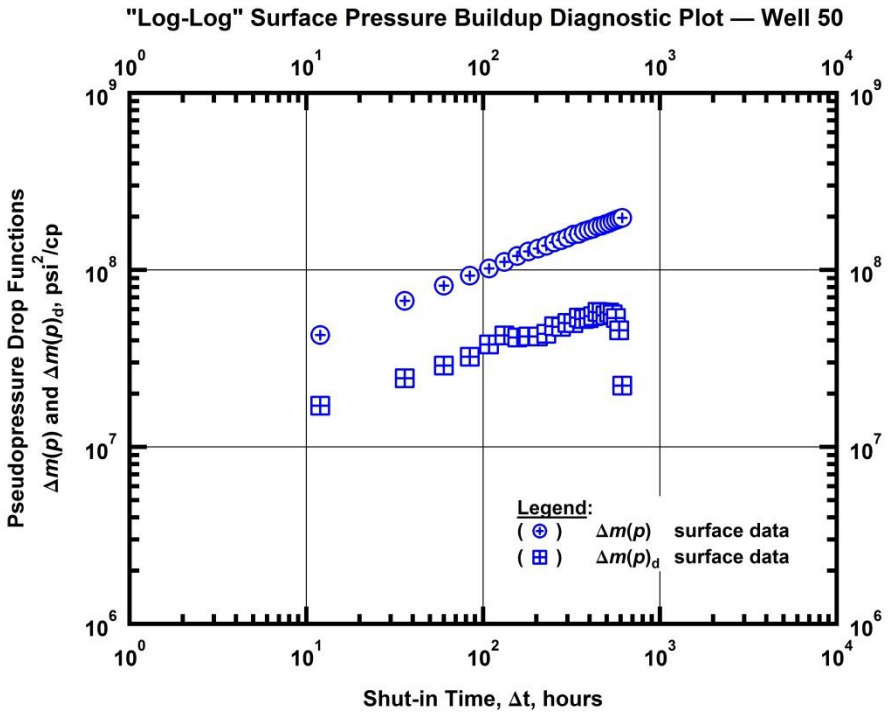

Fig. D8 — (Log-log Plot): Pressure buildup diagnostic plot — daily surface pressure measurement for Well 50.

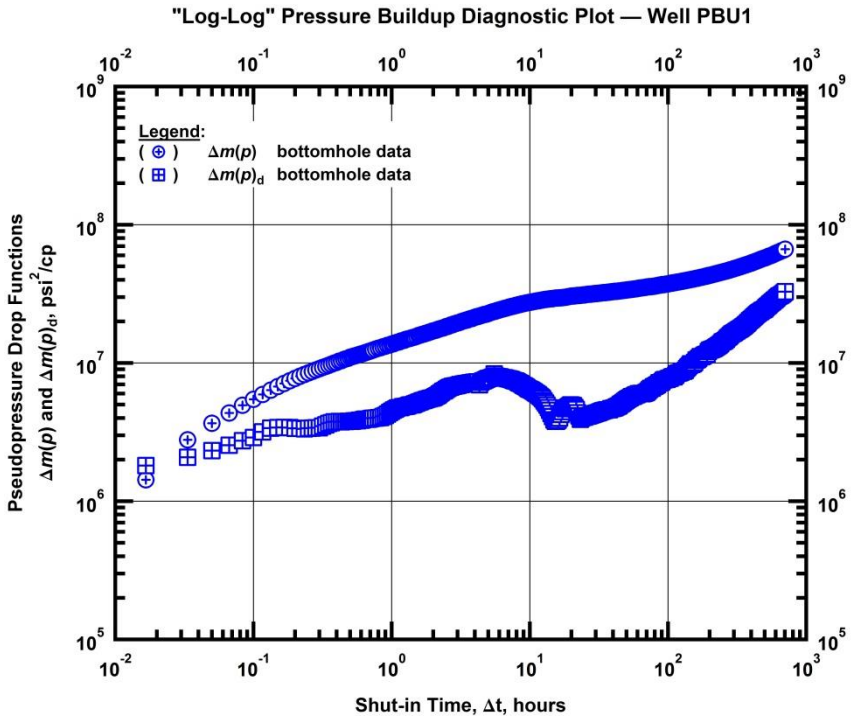

Fig. D9 — (Log-log Plot): Pressure buildup diagnostic plot — high-frequency bottomhole pressure measurement for Well PBU1.